LEABHARLANN CHOLÁISTE NA TRÍONÓIDE, BAILE ÁTHA CLIATH | TRINITY COLLEGE LIBRARY DUBLIN
Ollscoil Átha Cliath | The University of Dublin

Terms and Conditions of Use of Digitised Theses from Trinity College Library Dublin

Copyright statement

All material supplied by Trinity College Library is protected by copyright (under the Copyright and Related Rights Act, 2000 as amended) and other relevant Intellectual Property Rights. By accessing and using a Digitised Thesis from Trinity College Library you acknowledge that all Intellectual Property Rights in any Works supplied are the sole and exclusive property of the copyright and/or other IPR holder. Specific copyright holders may not be explicitly identified. Use of materials from other sources within a thesis should not be construed as a claim over them.

A non-exclusive, non-transferable licence is hereby granted to those using or reproducing, in whole or in part, the material for valid purposes, providing the copyright owners are acknowledged using the normal conventions. Where specific permission to use material is required, this is identified and such permission must be sought from the copyright holder or agency cited.

Liability statement

By using a Digitised Thesis, I accept that Trinity College Dublin bears no legal responsibility for the accuracy, legality or comprehensiveness of materials contained within the thesis, and that Trinity College Dublin accepts no liability for indirect, consequential, or incidental, damages or losses arising from use of the thesis for whatever reason. Information located in a thesis may be subject to specific use constraints, details of which may not be explicitly described. It is the responsibility of potential and actual users to be aware of such constraints and to abide by them. By making use of material from a digitised thesis, you accept these copyright and disclaimer provisions. Where it is brought to the attention of Trinity College Library that there may be a breach of copyright or other restraint, it is the policy to withdraw or take down access to a thesis while the issue is being resolved.

Access Agreement

By using a Digitised Thesis from Trinity College Library you are bound by the following Terms & Conditions. Please read them carefully.

I have read and I understand the following statement: All material supplied via a Digitised Thesis from Trinity College Library is protected by copyright and other intellectual property rights, and duplication or sale of all or part of any of a thesis is not permitted, except that material may be duplicated by you for your research use or for educational purposes in electronic or print form providing the copyright owners are acknowledged using the normal conventions. You must obtain permission for any other use. Electronic or print copies may not be offered, whether for sale or otherwise to anyone. This copy has been supplied on the understanding that it is copyright material and that no quotation from the thesis may be published without proper acknowledgement.

The University of Dublin
Trinity College

Dynamic properties of nanoparticle magnetic systems.

by
Athanasios T. Giannitsis

A thesis submitted for the degree of
Doctor of Philosophy

March 2004

Department of Electronics and Electrical Engineering
University of Dublin-Trinity College

Dublin
Ireland

TRINITY COLLEGE
14 OCT 2004
LIBRARY DUBLIN
THESIS
7426

Declaration

I hereby declare that,

1. This thesis has not been submitted as an exercise for a degree at any other University or Institution;
2. The work contained herein is entirely my own, except where otherwise cited, reference, acknowledged or accredited;
3. I agree that the Library of the University of Dublin-Trinity College may, at their discretion, lend or copy this thesis upon request.

Signed

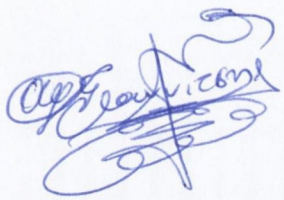

Athanasios T. Giannitsis

Acknowledgements

I am deeply indebted to my supervisor Professor Paul C. Fannin for accepting me as a PhD student to the University of Dublin-Trinity College, funding, supporting and guiding me through all the years of my research. I am thankful to him for introducing me to the subject of the magnetic fluids and the measurement techniques, a subject which broadened my knowledge in the area of magnetism and material science.

My warmest appreciation to Professor Brendan K.P. Scaife from the department of Electrical and Electronic Engineering of Trinity College Dublin for his comments and suggestions on this thesis and also for the many hours of discussion.

My grateful recognition to Professor William T. Coffey of the department of Electrical and Electronic Engineering of Trinity College Dublin for his assistance and advice and for introducing me to special aspects of statistical physics, theory of Brownian motion and polar liquids.

Special acknowledgements to Professor Yury P. Kalmykov from the University of Perpignan, France, for his advice on the subject of nonlinear effects in magnetic and dielectric materials.

Professor Stewart W. Charles from the University of Bangor-North Wales, UK, who supplied some of the ferrofluid samples, is also acknowledged.

Special mention of the support I had from the technical staff of the department namely Shane Hunt, Robert Dempsey and Mark Leach.

Special thank to my colleague and PhD student Colm MacOireachtaigh for his assistance in the laboratory.

Finally, my appreciation to the European Space Agency for part financing of this project.

Dublin, March 2004

Athanasios T. Giannitsis

Dedicated to the loving memory of my mother,
Gioula

Table of contents

Declaration

Acknowledgements

List of symbols iv

List of figures xi

List of tables xiii

Abstract 1

Introduction 3

Chapter 1: Overview of the theory of relaxation and resonance of nanoparticle magnetic systems.

1.1 Introduction 11

1.2 Theory of spectroscopy 11

1.3 The constituents of magnetic liquids 15

1.4 Theory of Debye relaxation 23

1.5 Theory of Néel relaxation and resonance 35

1.6 Conclusions 54

References 55

Chapter 2: Overview of impedance measurement techniques.

2.1 Introduction 58

2.2 Auto-balancing bridge method (low frequencies) 60

2.3 RF-IV method (radio frequencies) 63

2.4 Networking technique (microwave frequencies) 65

2.5 Permeability measurements by using the toroidal technique 68

2.6 Permittivity measurements by using plate and cylindrical capacitor 72

2.7 Permittivity and permeability measurements by means of the coaxial transmission line technique 78

2.8 Conclusions and suggestions for future work 83

References 85

Chapter 3: Brownian relaxation in ferrofluids at frequencies below 1MHz and susceptibility's dependence on polarising field.

3.1 Introduction 88

3.2 Distribution functions with application to Brownian relaxation 90

3.3 Dependence of the static susceptibility in a biasing field. Estimation of the radius of a magnetic nanoparticle by use of the constant frequency method 97

3.4 Dependence of $\chi(\omega)$ in the frequency range 100 Hz-1 MHz on an external polarising constant field. Dependence of the relaxation time on the polarising field 109

3.5 Observation of nonlinear susceptibility in ferrofluids 122

3.6 Application 1: Calculation of the loss factor $\tan\delta$ from the susceptibility data 135

3.7 Application 2: Calculation of heat losses from susceptibility data 138

3.8 Conclusions and suggestions for future work 140

References 141

Chapter 4: Properties of ferrofluids at frequencies above 1 MHz and the dependence on the polarising field of the susceptibility.

4.1 Introduction 144

4.2 A brief review on measurements of χ, in the RF and microwave frequency ranges 144

4.3 Magnetic susceptibility as a function of biasing field in the microwave band 155

4.4 Application 1: Estimation of ferrofluid losses in the microwave frequency range ..168

4.5 Application 2: Estimation of the signal-to-noise ratio in ferrofluids 170

4.6 Conclusions and suggestions for future work 175

References 176

Chapter 5: Electrical equivalent circuits for Debye, Cole-Cole and Landau-Lifshitz equations.

5.1 Introduction 178

5.2 Equivalent electrical circuits for the Debye equation 179

5.3 Equivalent electrical circuits for the Cole-Cole equation 184

5.4 Equivalent electrical circuits for the Landau-Lifshitz equation ..... .188

5.5 Application 1: Permittivity measurement of ferrofluids 188

5.6 Application 2: Estimation of the conductivity of a ferrofluid 193

5.7 Conclusions 195

References 197

Appendix A: Calculation of the magnetic susceptibility using the toroidal technique, and estimation of the susceptibility and permittivity using the transmission line technique.

A.1 Introduction 198

A.2 Calculation of susceptibility by means of the toroidal technique 198

A.3 Calculation of permeability by means of the short circuit transmission line technique 202

A.4 Calculation of permittivity by means of the open circuit transmission line Technique.....205

A.5 Calculation of both μ and ε by means of the short and open circuit transmission line technique 206

References 208

Appendix B: Computational and fitting programs.

B.1 Introduction 209

B.2 Computational and fitting programs 209

B.3 Programming in Matlab 212

B.4 An example of a computational program 217

B.5 Examples of fitting programs 219

B.6 Conclusions 233

References 234

Appendix C: Demagnetising Factor Chart.

The chart 235

List of Symbols

Symbol	Description	S.I. unit
Latin symbols:		
A_{cs}	cross-sectional area	m^2
A_p	electrode area of a plate capacitor	m^2
$B_p(\omega)$	parallel susceptance	Ω^{-1}
$\mathbf{B}$	magnetic flux density	T
B_{eff}	effective magnetic flux density	T
$C(\omega)$	capacitance	F
$C_1(\omega)$	equivalent capacitance of the carrier liquid of a ferrofluid	F
$C_2(\omega)$	equivalent capacitance of the surfactant of a ferrofluid	F
C_0	capacitance of empty capacitor	F
C^{tot}	total equivalent capacitance	F
$C_{tot}(\omega)$	equivalent capacitance of the overall ferrofluid	F
C_p^{tot}	total parallel equivalent capacitance	F
C_s^{tot}	total serial equivalent capacitance	F
C^s	capacitance corresponding to static permittivity	F
C_s^s	series capacitance corresponding to static permittivity	F
C_{fr}	fringe capacitance	F
C^∞	capacitance corresponding to high frequency permittivity	F
c	speed of light equal to 299,792,458	m/s
D	diffusion coefficient	Hz
D'	diffusion coefficient for internal (Néel) relaxation	Hz
d	length	m
d_*	critical diameter for mono-domainness	m
d^*	critical value of the diameter at which resonance appears	m
$\mathbf{E}$	electric field	V/m
e	Euler constant, equal to 2.718281828	-
$\hat{\mathbf{e}}$	unit vector in the direction of the electric field	-
E_0	amplitude of alternating electric field	V/m
$\mathbf{F}$	field (arbitrary)	depends
F	force	N
f	frequency	Hz
f_{max}	frequency corresponding to a maximum peak in the spectrum of χ''	Hz
f_{res}	resonance frequency	Hz
g	Landé factor	-
$G_p(\omega)$	parallel conductance	Ω^{-1}
$\mathbf{h}(t)$	fluctuating field	A/m
h	Planck's constant, equal to 6.6260755×10^{-34}	J s
$\hbar$	normalised Plank's constant, equal to $h/2\pi$	J s

$\hat{\mathbf{h}}$	unit vector in the direction of the external magnetic field	-
$\mathbf{h}_a(t)$	magnetic alternating field	A/m
$\mathbf{h}_a^x$, $\mathbf{h}_a^y$, $\mathbf{h}_a^z$	coordinates of magnetic alternating field	A/m
$\mathbf{H}$	arbitrary magnetic field	A/m
H_0	amplitude of alternating magnetic field	A/m
H_1	value of the static field in which $\chi_\perp - \chi_\parallel$ reaches its maximum	A/m
H_s	biasing static magnetic field	A/m
$\mathbf{H}_A$	internal anisotropy field	A/m
$\mathbf{H}_{cons}$	conservative part of dissipative effective field	A/m
H_R	interaction field	A/m
$\mathbf{H}_s$	strong static field	A/m
I	moment of inertia	kg m^2
$I(r_p)$	particle interaction term	A/m
I(t)	alternating current	A
I_0	amplitude of alternating current	A
I_{in}	input current	A
I_R	current through the conductors of a coaxial cell	A
i	imaginary unit	-
$\mathbf{J}$	total angular momentum of the electron	kg m^2/s
$\mathbf{J}_{diff}$	diffusive current	particles/m^2 s
$\mathbf{J}_d$	drift current	particles/m^2 s
K	anisotropy constant	J/m^3
k_B	Boltzmann constant , equal to1.380658×10^{-23}	J/K
$\mathbf{L}$	orbital angular momentum of the electron	kg m^2/s
L, l, l_1, l_2	lengths	m
L_1	length of the circumference of the toroid minus the length of the slit	m
L_2	length of slit of the toroid core	m
$L(\xi_m)$	Langevin function	-
$L'(\xi_m)$	derivative of the Langevin function	-
$L(\omega)$	inductance	H
L_0	inductance of empty inductor	H
L^s	inductance corresponding to static permeability	H
L^∞	inductance corresponding to high frequency permeability	H
L_{cut}^{empty}	inductance of toroid with empty slit	H
L_{cut}^{full}	inductance of toroid with full slit	H
L_{nocore}	inductance of toroid without core	H
L_{nocut}	inductance of toroid without slit	H
$\hat{\mathbf{m}}$	unit vector in the direction of $\boldsymbol{\mu}_m$ or $\mathbf{M}_s$	-
m_e	mass of the electron, equal to 9.1093897×10^{-31}	kg
m_p	particle mass	kg

$M(\omega)$	complex magnetization	T
$M'(\omega)$	real component of complex magnetization	T
$M''(\omega)$	imaginary component of complex magnetization	T
$\Delta M(t, H_s)$	increment of magnetization	T
$\Delta M_1, \Delta M_2$	increment of the magnetization at several points of the magnetization curve	T
$M_{\parallel}$	longitudinal magnetisation	T
$M_{\parallel}^0$	equilibrium value of longitudinal magnetisation	T
$M_{\perp}$	transverse magnetisation	T
$M_{\perp}^0$	equilibrium value of transverse magnetisation	T
$\mathbf{M}_s$	saturation magnetisation of the material of a ferromagnet	T
M_s^F	saturation magnetisation of a ferrofluid	T
N	density of particles	particles/m^3
$N_{\parallel}$	demagnetizing factor parallel to the direction of the constant field	-
$N_{\perp}$	demagnetizing factor perpendicular to the direction of the field	-
N^e	depolarising factor	-
N_t	number of turns of a winding	-
N_x, N_y, N_z	demagnetising factors (subscript refers to space directions)	-
$\hat{\mathbf{n}}$	unit vector in the direction of uniaxial anisotropy	-
$P(K)$	probability distribution function of anisotropy constant K	-
$P(r_m)$	probability distribution function of magnetic radius r_m	-
$P(x)$	probability distribution function of an arbitrary random variable x	-
$P(\omega)$	complex polarisation	F V/m^2
P_s	polarisation corresponding to ε_s	F V/m^2
P_∞	polarisation corresponding to ε_∞	F V/m^2
q_e	electron charge, equal to $1.60217733 \times 10^{-19}$	Cb
R	resistance	Ω
R_1, R_2	radius	m
R_p	parallel resistance	Ω
R_r	range resistor	Ω
R_s	series resistance	Ω
R_w	DC wire resistance of the toroid	Ω
R_x	resistance of unknown impedance	Ω
$\mathbf{r}$	position vector	m
r_m	magnetic radius of a particle	m
r_p	hydrodynamic radius of the particle (total radius including the surfactant layer)	m
$\mathbf{S}$	angular momentum of the electron spin	kg m^2/s
s	surface area	m^2
S_p	particle surface area	m^2
S_Γ	complex reflection coefficient	-
T	absolute temperature	K

t	time	s
$\tan\delta$	loss factor	-
U	potential energy density	J/m^3
U_A^u	uniaxial anisotropy energy density	J/m^3
U_A^c	cubic anisotropy energy density	J/m^3
$U^{heat}(\omega)$	heat rate energy density	$J/s\ m^3$
$U^{heat}(T)$	heat energy density in the period of one cycle	J/m^3
$u(t)$	unit step function	-
V	potential energy	J
$V(t)$	alternating voltage	V
V_0	amplitude of alternating voltage	V
V_1, V_2	vector voltages	V
V_A^u	uniaxial anisotropy energy	J
V_A^c	cubic anisotropy energy	J
V_A^{sh}	shape anisotropy energy	J
V_A^{su}	surface anisotropy energy	J
V_{DUT}	voltage across device under test (DUT)	V
V_{in}	input voltage	V
V_{inc}	vector voltage of the incident microwave signal	V
V_{ref}	vector voltage of reflected microwave signal	V
V_R	voltage across coaxial cell	V
V_{rr}	voltage across range resistor	V
v_1	fractional volume of the carrier of a ferrofluid	m^3
v_2	fractional volume of the surfactant of a ferrofluid	m^3
v_m	magnetic volume of particle (volume of the magnetic core)	m^3
v_m^*	critical value of magnetic volume at which resonance appears	m^3
v_p	hydrodynamic volume of particle (particle's total volume)	m^3
W	scale parameter of Nakagami distribution function	-
$W(\mathbf{r},t)$	probability density function of the position	-
$W(\vartheta,\phi,t)$	probability density function of the orientations	-
$X(\omega)$	reactance	Ω
X_x	reactance of unknown impedance	Ω
$Y(\omega)$	admittance	Ω^{-1}
$Y_p(\omega)$	parallel admittance	Ω^{-1}
$Y_s(\omega)$	series admittance	Ω^{-1}
Y_{stray}	stray admittance	Ω^{-1}
$Z(\omega)$	impedance	Ω
Z_0	characteristic impedance of a transmission line	Ω
Z_1	characteristic impedance of the part of the line filled with sample	Ω
Z_{in}	input impedance	Ω
Z_{in}^{open}	input impedance of an open terminated transmission line	Ω

Z_{in}^{short}	input impedance of a short terminated transmission line	Ω
Z_L	impedance of a load connected to the coaxial line	Ω
Z_m	measured impedance of device under test (DUT)	Ω
$Z_p(\omega)$	parallel impedance	Ω
Z_R	input impedance of the cell with sample in it	Ω
Z_R^{open}	load impedance of open terminated cell	Ω
Z_R^{short}	load impedance of short terminated cell	Ω
Z_{resid}	residual impedance	Ω
$Z_s(\omega)$	serial impedance	Ω
Z_{sample}	intrinsic impedance of the medium	Ω
Z_x	unknown impedance of device under test (DUT)	Ω
Z_{cut}^{empty}	impedance of toroid with its slit empty	Ω
Z_{cut}^{full}	impedance of toroid with its slit full	Ω

Greek symbols:

α	Cole-Cole parameter alpha	-
$\alpha(\omega)$	complex polarisability	$F\,m^2$
α_0	attenuator factor of a transmission line	-
α_d	damping parameter	-
β	width parameter of Nakagami distribution function	-
β_0	phase coefficient of a transmission line	-
Γ	gamma function	-
$\boldsymbol{\Gamma}$	torque	$N\,m$
γ	gyromagnetic ratio	$T^{-1}s^{-1}$
γ_0	propagation constant of (empty) transmission line	-
γ_1	propagation constant of the part of the line filled with sample	-
γ_g	ratio of L_2 / L_1	-
$\Delta\chi$	susceptibility's increment: polarised χ subtracted from the unpolarised χ	-
$\Delta\chi'$	real component of the susceptibility's increment	-
$\Delta\chi''$	imaginary component of the susceptibility's increment	-
$\Delta\chi_0$	increment of static susceptibility	-
$\varepsilon(\omega)$	relative complex dielectric permittivity	-
$\varepsilon_1(\omega)$	relative permittivity of the carrier	-
$\varepsilon_2(\omega)$	relative permittivity of the surfactant	-
ε_0	dielectric constant of vacuum, equals to $8.854187818\times10^{-12}$	F/m
ε_∞	high frequency ($\omega \to \infty$) permittivity	-
ε_{coax}	relative permitivity of the insulating medium of a coaxial line	-
ε_s	static (at frequency ω=0) dielectric permittivity	-
$\varepsilon_{tot}(\omega)$	overall relative permittivity of a ferrofluid	-

ζ	drag coefficient	N s m
η	damping constant	N/m^3
η_h	hydrodynamic viscosity	$N\ s/m^2$
η_m	magnetic viscosity	$N\ s/m^2$
θ	angle between particle magnetic moment and the easy axis or between the magnetic moment and the field axis	rad
ϑ	polar coordinate	rad
$\hat{\vartheta}$	unit vector of polar coordinate ϑ	-
λ	wavelength	m
$\mu(\omega)$	relative permeability	-
μ_0	absolute permittivity of vacuum, equal to 1.256637061×10^{-6}	H/m
μ_B	Bohr magneton, equal to 1.165×10^{-29}	Wb m
$\boldsymbol{\mu}_e$	electric dipole moment	Cb m
μ_{eff}	effective relative permeability	-
$\boldsymbol{\mu}_m$	magnetic moment of a particle	Wb m
$\mu_m^{\perp}$	component of the particle magnetic moment perpendicular to the external magnetic field	Wb m
$\mu_m^{\parallel}$	component of the particle magnetic moment parallel to the external magnetic field	Wb m
$\mu_m^x, \mu_m^y, \mu_m^z$	coordinates of the magnetic moment of a particle	Wb m
$\boldsymbol{\mu}_s$	magnetic moment of a spinning electron	Wb m
μ_t	relative permeability of toroidal core	-
ξ_1	constant equals to 3.72. It is the value of ξ_m in which $\chi_\perp - \chi_\parallel$ is maximum	-
ξ_e	ratio of the electric energy to the thermal energy	-
ξ_m	ratio of the magnetic energy to the thermal energy	-
σ	ratio of anisotropy energy to the thermal energy	-
$\sigma(\omega)$	conductivity	$\Omega^{-1}m^{-1}$
σ_*	critical value of σ for equalisation of Brownian and Néel relaxation times	-
σ^*	critical value of σ at which resonance appears	-
σ_K	normalised (with respect to the mean K) standard deviation of the anisotropy constant K of a particle	-
σ_r	normalised (with respect to the mean radius) standard deviation of particle radius	-
σ_x	normalised standard deviation of an arbitrary random variable x	-
$\tau_\parallel$	parallel time constant	s
$\tau_\perp$	perpendicular time constant	s
τ_0	decay time of precession	s
τ_0'	Néel prefactor	s
τ_B	Brownian relaxation time	s
τ_D	Debye relaxation time	s

τ'_D	internal rotational diffusion time	s
τ_{eff}	effective relaxation time	s
$\tau_{\perp}^{eff}$	transverse effective relaxation time	s
τ_N	Néel relaxation time	s
τ_p	parallel time constant	s
τ_s	series time constant	s
ϕ	azimuthal coordinate	rad
$\hat{\phi}$	unit vector in the direction of azimuthal coordinate ϕ	-
Φ_B	flux of magnetic flux density **B**	Wb
ϕ_P	phase angle between voltage-current for parallel circuitry	rad
ϕ_s	phase angle between voltage-current for series circuitry	rad
$\chi(\omega)$	complex magnetic susceptibility	-
$\chi'(\omega)$	real component of magnetic susceptibility	-
$\chi''(\omega)$	imaginary component of magnetic susceptibility	-
$\chi'_1(\omega, H_0)$	real part of the fundamental component of the nonlinear susceptibility	-
$\chi''_1(\omega, H_0)$	imaginary part of the fundamental component of the nonlinear susceptibility	-
χ_1, χ_2, χ_3	magnetic susceptibilities for specific points of the magnetization curve	-
$\chi_{\parallel}$	susceptibility parallel to the direction of an external field	-
$\chi_{\perp}$	susceptibility perpendicular to the direction of an external field	-
χ_0	static (at frequency ω=0) magnetic susceptibility	-
χ_{∞}	high frequency ($\omega \rightarrow \infty$) of magnetic susceptibility	-
$\chi_e(\omega)$	complex electric susceptibility	-
χ_0^e	static (at frequency ω=0) electric susceptibility	-
χ_{∞}^e	high frequency ($\omega \rightarrow \infty$) electric susceptibility	-
ψ	angle or phase	rad
ω	angular frequency	rad/s
ω_L	angular Larmor frequency of gyromagnetic resonance	rad/s
ω_{max}	angular frequency corresponding to the maximum of χ''	rad/s
ω_{pre}	precessional angular frequency	rad/s
ω_{res}	angular ferromagnetic resonance frequency	rad/s

SI units

A	Ampere,	Hz	Hertz,	N	Newton,	Ω	Ohm.
Cb	Coulomb,	J	Joule,	s	Second,		
^{0}C	Celsius,	K	Kelvin,	T	Tesla,		
F	Farad,	kg	Kilogram,	V	Volt,		
H	Henry,	m	Meter,	Wb	Weber,		

List of figures

Chapter 1

Figure 1.1 13

Figure 1.2 13-14

Figure 1.3 16

Figure 1.4 21-22

Figure 1.5 32-33

Figure 1.6 44

Figure 1.7 47-49

Chapter 2

Figure 2.1 60

Figure 2.2 66

Figure 2.3 67

Figure 2.4 69

Figure 2.5 71

Figure 2.6 74-75

Figure 2.7 75-76

Figure 2.8 79

Figure 2.9 83

Chapter 3

Figure 3.1 91-92

Figure 3.2 95-96

Figure 3.3 98

Figure 3.4 101

Figure 3.5 103

Figure 3.6 103-104

Figure 3.7 109

Figure 3.8 114-117

Figure 3.9 120-121

Figure 3.10 123

Figure 3.11 129-130

Figure 3.12 130-133

Figure 3.13 137
Figure 3.14 139-140

Chapter 4
Figure 4.1 145
Figure 4.2 148-150
Figure 4.3 150-152
Figure 4.4 158-159
Figure 4.5 160
Figure 4.6 161-163
Figure 4.7 164-165
Figure 4.8 168
Figure 4.9 172-173
Figure 4.10 173

Chapter 5
Figure 5.1 180
Figure 5.2 188
Figure 5.3 190
Figure 5.4 191
Figure 5.5 192
Figure 5.6 194
Figure 5.7 194
Figure 5.8 195
Figure 5.9 196

Appendix B
Figure B.1 214
Figure B.2 220
Figure B.3 225

Appendix C
Figure C.1 235
Figure C.2 236

List of tables

Chapter 1

Table 1.1 42

Chapter 2

Table 2.1 59

Chapter 3

Table 3.1 107

Table 3.2 107

Table 3.3 107

Table 3.4 107

Table 3.5 117

Table 3.6 119

Table 3.7 133

Chapter 4

Table 4.1 154

Table 4.2 154

Table 4.3 154

Table 4.4 169

Chapter 5

Table 5.1 193

Appendix B

Table B.1 213-214

Abstract

This thesis is concerned with the study of the dynamic properties of *ferrofluids*, which are an important class of physical systems where microscopic magneto-mechanical effects can be manifested. There are two processes involved with the dynamic properties of a ferrofluid: (a) the magnetic *relaxation* effect that is due to the rotation of the magnetic moment, $\boldsymbol{\mu}_m$, of the ferroparticle, which can be due to Brownian or Néel relaxation or a combination of both, and (b) the *resonance* effect which is due to the precession of $\boldsymbol{\mu}_m$. The typical frequency range in which the magnetic relaxation appears is below 100 MHz, whilst resonance is detected in the microwave band. The parameter we can quantify is the *complex magnetic susceptibility*, $\chi(\omega,H) = \chi'(\omega,H) - i\chi''(\omega,H)$, which is frequency, ω, and field, $\mathbf{H}$, dependent and can be estimated by impedance measurements. The complex susceptibility provides information on the microscopic parameters of a ferroparticle, namely the particle radius, r_p, the magnetic radius, r_m, the anisotropy constant, K, the internal anisotropy field, H_A, and the gyromagnetic ratio, γ.

Measurements of the complex susceptibility are made on a number of samples. Our study can be summarised in three separate themes, as follows:

(a) To examine the field dependence of the *static*, χ_0, and the *dynamic* susceptibility, $\chi(\omega)$, within the relaxation range by scanning between 10 Hz to 1 MHz and for various values of the *static* polarizing field, $\mathbf{H}_s$, up to 13 kA/m.

(i) The study in the field dependence of χ_0 was performed by *constant frequency measurements* at 10 kHz. At this frequency the value of χ_0 can be approximated very well. The data shows that the dependence of χ_0 on field is in accordance with theory, which predicts that $\chi_{\parallel}(\xi_m) = 3\chi_0 L'(\xi_m)$ and $\chi_{\perp}(\xi_m) = 3\chi_0 L(\xi_m)/\xi_m$, where $\chi_{\parallel}$, $\chi_{\perp}$ are the susceptibilities parallel and perpendicular to $\mathbf{H}_s$, L is the *Langevin function* and $\xi_m = \mu_m H_s / k_B T$.

(ii) The study of the dynamic susceptibility, $\chi(\omega)$, was carried out in the linear and nonlinear regions of the magnetization curve. From the polarised measurements we found that the dynamic susceptibility can be described by an equation which incorporates the frequency dependence (Debye equation), the field dependence of the static susceptibility as mentioned in (i) and also the field dependence of the relaxation time which is in accordance with theory is given by $\tau_{\parallel}(\xi_m) = \tau_B \xi_m L'(\xi_m)/L(\xi_m)$, τ_B being

the relaxation time of the unpolarised susceptibility. In order to fit the data we modified the Cole-Cole equation in order to include the field dependence of χ_0 and $\tau_{\parallel}$. This equation is global and can fit both linear and nonlinear susceptibility. In particular the nonlinear susceptibility data can be also fitted by the equations proposed by Coffey and Paranjape and further modified by Déjardin, who expanded the susceptibility to include higher order $\mathbf{H}_s$. The nonlinear portion of $\chi(\omega)$ is given by the susceptibility increment, $\Delta\chi(\omega)$, which can be detected in our experiments.

(iii) Applications of the available susceptibility data involve estimation of power losses and heat transfer, which can be quantified by use of the tanδ loss parameter and the energy density heat loss.

(b) To examine the field dependence of the dynamic susceptibility, $\chi(\omega)$, within the microwave frequency range between 1 MHz to 20 GHz, for values of the biasing field, $\mathbf{H}_s$, up to approximately 100 kA/m. In the microwave band, magnetic resonance appears. The study in this frequency range is concerned with:

(i) Estimation, by using polarised susceptibility data, of r_m, K, H_A, and γ for two different samples.

(ii) Analysing the field dependence of the Landau-Lifshitz equation and fitting this equation to the susceptibility data by means of Cole-Cole diagrams. It is shown that the Landau-Lifshitz equation can adequately describe the dependence of $\chi(\omega)$ on the biasing field.

(iii) Applications of the available susceptibility data including the estimation of the signal-to-noise ratio in terms of the susceptibility.

(c) To present a theoretical analysis with equivalent electrical circuits which can be used to describe relaxation and resonance in ferrofluids. Equivalent electrical circuits are in common use in the description of absorbing materials, both magnetic and dielectric. Since the Debye and the Landau-Lifshitz equivalent circuits have already been studied our aim was to develop a circuit which can essentially describe the Cole-Cole equation. This can be realized by use of a *constant phase element* which maintains the phase of the circuitry constant.

This thesis also includes an extended review on the theory of ferrofluids and their measurement techniques, and also an extensive range of computer programs designed for computation and fitting.

Introduction

The aim of this project is the study of the dynamic properties of the magnetic liquids, commonly called *ferrofluids*, which are colloidal suspensions of single-domain magnetic particles, dispersed in a carrier liquid and coated by a surfactant layer. The size of a magnetic particle is of the order of some nanometers and it is composed of ferromagnetic or ferrimagnetic material. Each magnetic particle, also called a *ferroparticle*, has a magnetic moment, $\boldsymbol{\mu}_m$, which responds to an external static field, $\mathbf{H}_s$, or to an oscillating field, $\mathbf{h}_a(t)$.

Ferrofluids are an important category of physical systems and have a wide diversity of applications. The research in ferrofluids spans from theoretical mechanics, magnetism, material science, spectroscopy to chemical physics and statistical physics. Their applications have been reported in magneto-electronics, magneto-devices, bioelectronics, heat transfer and medicine.

In particular in electrical engineering ferrofluids are in common use providing enhanced performance of magnetically operated devices such as stepper motors, electromagnets, transformers and loudspeakers. In loudspeakers the ferrofluid fills the gap between the voice coil and the pole pieces where it acts as a cooling agent. This increases the power handling capabilities of the loudspeaker and reduces thermal transient failures. Ferrofluids are also used in ink jet printers, where a small amount of ferrofluid is present in the ink and a small magnetic field applied to a jet of ink deflects the ink in order to draw each character. Ferrofluids are also used in the development of high-density storage media, where spontaneous magnetisation reversal determines the efficiency of the stored information [1].

In industry, the interest in magnetic fluids spans from computer disk drives, where they are used to eliminate harmful dust particles or other impurities, to lubrication, damping and sealing. In rotating shaft seals they behave as a magnetic O-ring and a rotary seal is produced where the shaft of the seal provides hermetic sealing with zero leakage. These rotating shaft seals are found in rotating anode X-ray generators and in vacuum chambers used in the semiconductor industry.

In medicine, ferrofluids find use in biomedical practices where they are employed in selective separation of viruses and bacteria, to the development of biocompatible materials for active targeting of cancer cells with both diagnostic and therapeutic values

[2-4]. For future biomedical applications, researchers are presently attempting to design ferrofluids that can deliver medication to specific locations in the body through the use of applied magnetic fields.

The first reported attempt at producing a ferromagnetic liquid was carried out by Gowan Knight in 1779 [5]. Knight mixed iron filings in water but the dispersion did not have long-term stability. However in 1932 Bitter [6] produced a colloid, for magnetic domain studies, which consisted of a suspension of γ-Fe_2O_3 in ethyl acetate however they were not stable in the long-term. The first stable ferromagnetic liquid was manufactured by Elmore [7] in 1938 at the Massachusetts Institute of Technology. Elmore's magnetic liquid was a water-based colloidal suspension of magnetite (Fe_3O_4) stabilized by soap.

Interest in ferrofluids waned until the mid-1960's when Papell [8] and Rosensweig [9] reported on the practical applications of ferrofluids. Since the mid-1960's technological interest in magnetic fluids has grown rapidly, with a significant increase in theoretical research of ferromagnetic fluid properties. Maiorov [10] appears to be the first to have reported on low frequency-dependant susceptibility measurements, whilst Fannin et al [11,12] made substantial further progress by introducing the toroidal technique and by using network analyzers and auto-balanced bridges.

Today ferrofluids are commercially available but they are also produced in research laboratories. The particles can be made in one of two ways. They can be obtained by precipitating particles of desired size from a solution, or particles of large size can be ground down to achieve the desired particle size.

The high stability of a magnetic fluid is achieved through a combination of particle motion and particle-particle repulsion, both working against Van der Waals and magnetic dipole interactions that tend to stick particles together. Steric repulsion prevents particle agglomeration in surfactant containing magnetic fluids whilst coulombic repulsion accounts for the stability in ionic magnetic fluid [13,14]. In biocompatible magnetic fluids, however, both steric and coulombic repulsion play a very important role in the fluid stability. Actually, in the first step of the synthesis of a biologically active magnetic fluid, an ionic magnetic fluid is used as a chemical precursor to which a buffer-like compound is added [15].

Investigations of the chemical and physical properties of magnetic fluids are of great importance. One of the important tasks in the study of magnetic fluids is the investigation of their magnetic properties, both static and dynamic. The macroscopic

quantity of interest to us is the *complex magnetic susceptibility*, $\chi(\omega)$, which is frequency dependent and can be estimated by impedance measurements. Our experimental method involves the application of a polarising field, $\mathbf{H}_s$, and an alternating field, $\mathbf{h}_a(t)$, the frequency of which varies between 10Hz and 20GHz. This frequency range is realised by means of the combined use of the Hewlett Packard (HP) 4192A (5Hz-13MHz) automatic balanced bridge [16], the HP 4291B (1MHz-1.8GHz) RF impedance vector analyser [17,18], and the HP 8753C, 8722D network analysers, the upper frequency of which can reach 6 GHz and 40 GHz respectively [18].

There are two effects involved with the dynamic properties of a ferrofluid, namely:

(a) The *relaxation* effect, which is related to the rotation of the magnetic moment vector, $\boldsymbol{\mu}_m$, and can be due to Brownian relaxation [19], or Néel relaxation [20], or a combination of both. Brownian relaxation is involved with the physical rotational Brownian motion of the whole ferroparticle, due to thermal agitation whilst the Néel relaxation is related only with the rotation of the moment itself within the ferroparticle which is, again, due to thermal activity. Macroscopically, one can measure the relaxation by measuring $\chi(\omega)$, using impedance measurement techniques. If relaxation is present, a prominent peak appears in the spectrum of $\chi(\omega)$ and one can measure the effective *relaxation time* which is directly related to the average volume of the ferroparticles. Relaxation occurs at low frequencies of the probing alternating field, below 100 MHz.

(b) The *resonance* effect, which is related to the precession of the moment vector about the axis of an effective field. The effective field consists of the ferroparticle's *internal anisotropy field*, $\mathbf{H}_A$, which arises from the crystal's internal potentials, from the random field, $\mathbf{h}(t)$, arising from thermal noise, also called the *stochastic field*, and an external static field, $\mathbf{H}_s$, if polarised measurements are performed. The precession of $\boldsymbol{\mu}_m$ is equivalent to the precession of a mechanical gyroscope, and $\boldsymbol{\mu}_m$ may also change direction. Resonance appears when the frequency of the precession of $\boldsymbol{\mu}_m$ becomes equal to the frequency of a probing alternating field which is used to excite the system. The occurrence of resonance is indicated by the in-phase component of $\chi(\omega)$ switching from a positive to a negative value. This change of sign reflects the reversing of the direction of the moment vector. The precession of $\boldsymbol{\mu}_m$ is characterized by a time constant, τ_0, called the *time of precession*. In real systems τ_0 decays because of damping. In this case τ_0 is defined by a phenomenological expression, $\tau_0 = 1/\alpha_d\omega_{pre}$, where α_d is called the

damping constant and takes on values within the range 0-1. Resonance appears at relatively high frequencies of the alternating probing field, above 500 MHz. Important information can be obtained from the resonant profile of $\chi(\omega)$, including the estimation of the magnetic volume, v_m, of a ferroparticle, the internal anisotropy field, $\mathbf{H}_A$, and the gyromagnetic ratio, γ [21].

In this thesis we will study some of the properties concerned with relaxation and resonance. We perform polarized measurements on a number of ferrofluids where $\mathbf{H}_s$ takes a range of values. In the relaxation region of the spectrum we investigate the dependence of χ on $\mathbf{H}_s$ in the *linear* and *nonlinear* field range of the magnetisation curve. In the resonance region of the spectrum we investigate the field dependence of χ and we demonstrate that the Landau-Lifshitz equation is appropriate to describe this dependence. The contents of each of the chapters, are as follows:

Chapter 1 is an overview of the basic theory of ferrofluids. It introduces the structure of the ferroparticles and constituent parts of a ferrofluid. It also presents in detail the theory of Brownian relaxation, Néel relaxation and resonance. In relaxation process, important equations are the Debye equation [22] and the Cole-Cole equation [23], which are adopted from the theory of polar liquids, but their magnetic analogue is well suited to magnetic liquids. The Debye and the Cole-Cole equations are related to the static susceptibility, χ_0, the frequency, ω, and the effective relaxation time, τ_{eff}. In resonance the important equations are the Landau-Lifshitz [24] and those of Raikher-Shliomis [25], which are simplified by Coffey et al [26].

Chapter 2 reviews the theory of impedance measurements and presents measurement techniques which are used to perform magnetic and dielectric measurements. We detail the equipment used, which consists of an auto-balance bridge and network analysers. The first sections provide a description of the basic principles of the instruments. Following this we introduce the toroid coil technique [11] and the transmission line technique [12], by which one can estimate $\chi(\omega)$. The toroid method is used at frequencies below 1 MHz and requires the use of the auto-balance bridge. The transmission line method is used above 1 MHz and entails the use of network analyzers. In addition, in this chapter we demonstrate how to perform dielectric measurements by the combined use of a cylindrical capacitor and the transmission line over a wideband frequency range.

In chapter 3 we study the field dependence of the static susceptibility, χ_0, and dynamic susceptibility, $\chi(\omega)$, for various values of the polarizing field, $\mathbf{H}_s$. In order to study the field dependence of χ_0 we perform constant frequency measurements [27] at 10 kHz. From measurements at 10 kHz one can closely approximate the value of χ_0. Polarised data shows that the dependence of χ_0 on field is in accordance with theory [27], which predicts that $\chi_{\parallel}(\xi_m) = 3\chi_0 L'(\xi_m)$ and $\chi_{\perp}(\xi_m) = 3\chi_0 L(\xi_m)/\xi_m$, where $\chi_{\parallel}$, $\chi_{\perp}$ are the susceptibilities parallel and perpendicular to $\mathbf{H}_s$, L is the *Langevin function* and $\xi_m = \mu_m H_s / k_B T$. To study the field dependence of the dynamic susceptibility, $\chi(\omega)$, within the relaxation range one must scan between 10Hz and 1 MHz for several values of $\mathbf{H}_s$. These measurements were performed in the linear and nonlinear region of the magnetization curve. The linear region is separated from the nonlinear region at approximately $\mathbf{H}_s$=1 kA/m, according to the information provided by the magnetisation curves of our samples. From polarised measurements of $\chi(\omega)$ we found that the field dependence of $\chi(\omega)$ can be described by $\chi_{\parallel}(\xi_m) = 3\chi_0 L'(\xi_m)$ and also that the relaxation time is field dependent and agrees with the theory of Martsenyuk et al [28] where $\tau_{\parallel}(\xi_m) = \tau_B \xi_m L'(\xi_m)/L(\xi_m)$, τ_B being the relaxation time of the unpolarised susceptibility. To fit the data we modified the Cole-Cole equation in order to include the field dependence of χ_0 and the field dependence of the relaxation time. This equation is global and can fit both linear and nonlinear susceptibility. In particular the nonlinear susceptibility data can be also fitted by the equations proposed by Coffey and Paranjape [29] and modified by Déjardin [30], who expanded the susceptibility to include higher order terms in $\mathbf{H}_s$. The nonlinear portion of $\chi(\omega)$ is given by the susceptibility increment, $\Delta\chi(\omega)$, which can be detected in our experimental data. The chapter concludes with applications involving estimation of power losses and heat transfer.

In chapter 4, we introduce measurements at microwave frequencies where magnetic resonance appears. After a brief summary of the experimental work reported so far on the subject of resonance, we test the Landau-Lifshitz theory [24] to the field dependence susceptibility data by means of Cole-Cole diagrams. In applications one can use the experimental data to estimate power losses and the signal-to-noise ratio by considering the fluid as a signal processing device [25].

In chapter 5, we present a theoretical analysis with equivalent electrical circuits which can be used to describe relaxation and resonance in ferrofluids and polar liquids. The electrical equivalent circuits are in common use in the description of absorbing materials, both magnetic and dielectric. The Debye and the Landau-Lifshitz equivalent circuits have been already studied in the case of magnetic liquids and the case of polar liquids. Our aim is to develop a circuit which can essentially describe the Cole-Cole equation which involves the Cole-Cole parameter, α. This can be realized by use of a *constant phase element* (CPE) which maintains the phase of the circuit constant. With the constant phase element one can realize electrically the distribution function corresponding to the Cole-Cole parameter, α. This chapter concludes with examples of the use of equivalent circuits in relative permittivity, $\varepsilon(\omega)$, measurements. A ferrofluid consists of a polar liquid, the relative permittivity of which can be measured with our equipment, which consists of a capacitor and transmission line. There are two main components that contribute to the polarization of a ferrofluid: its surfactant and its carrier liquid. We can measure the surfactant contribution to $\varepsilon(\omega)$. The equivalent circuits may be used to model the experimental result. Another application involves estimation of the conductivity, $\sigma(\omega)$, of a ferrofluid.

Appendix A provides the mathematical equations that are used to estimate $\chi(\omega)$ from impedance measurements, by using: (a) the toroid technique and (b) the transmission line technique. These models were first published in the articles where these techniques were first reported, see references [11,12].

Appendix B provides examples of the programs which were used to support this work. There are two kinds of programs which were created by the author: computational programs and fitting programs. There is extensive reference to the code of the programs. All the programs were developed in Matlab.

Appendix C provides a chart, whereby one can estimate the demagnetizing factor for various ellipsoids.

References

1. Morup S., Tronc E., *Phys. Rev.Lett.,* **72**, 3278, (1994).
2. Chan D.C.F., Kirpotin D.B. , Bunn P.A.,. *J. Magn. Magn. Mater.* **122**, 374, (1993).

3. Gilchrist R.K., et al.. *Ann. Surgery* **146,** 596, (1957).
4. Lübbe A.S., Bergemann C., Riess H. et al, *Cancer Research*, **56,** 4686, (1996).
5. Wilson B., *Phil. Trans. R. Soc., London,* **69**, 59, (1779).
6. Bitter F., *Phys. Rev.,* **41**, 507, (1932).
7. Elmore W.C., *Phys. Rev.,* **41**, 507 (1932).
8. Papell S.S., *U.S. Patent* 3, **215**, 572 (1962).
9. Rosensweig R.E., *Inst. Sci. Tech.,* **55**, 48 (1996).
10. Maiorov M.M., *Magnetohydrodynamics*, **2**, 21, (1979), (cover-to-cover translation of Magnitnaia Hidrodinamika).
11. Fannin P.C., Scaife B.K.P., Charles S.W., *J. Phys. E., Sci. Instr.*, **19**, 238, (1986).
12. Fannin P.C., Relihan T., Charles S.W., *J. Phys. D, Appl. Phys.*, **28**, 2003, (1995).
13. Massart R., *C.R. Acad.Sci.Paris*, **291C**, 1, (1980).
14. Tourinho F.A., Franck R., Massart R., Perzynski R., *Prog. Colloid. Polym. Sci.,* **79**, 128 (1989).
15. Halbreich A., Roger J., Pons J.N., in: Häfeli U., Schütt W., Teller J., Zborowski M. (Eds.), *Scientific and Clinical Applications of Magnetic Carriers, Plenum Press*, New York, 399, (1997).
16. Agilent Technologies, *PN 4294a New Technologies for Accurate Impedance Measurements (40Hz-110MHz)*, Product Note.
17. Agilent Technologies, *PN 4291-1 New Technologies for Wide Impedance Range Measurements*, Product Note.
18. Agilent Technologies, *Impedance Measurements Handbook*, 2nd edition, (2000).
19. Brown W.F., *Physics Review*, **130**, 1677, (1963).
20. Néel L., *Ann. Geophysics*, **5**, 99, (1949).
21. Fannin P.C., Charles S.W., Relihan T., *J. of Magnetism and Magnetic Materials*, **162**, 319, (1996).
22. Debye P., *Polar molecules*, The Chemical Catalog Co., New York, (1929), Reprinted by Dover, New York.
23. Cole K.S., Cole R.J., *Journal of Chemical Physics*, **9**, 341, (1941).
24. Landau L., Lifshitz E., *Phys. Z. Sowjet.*, **8**, 153, (1935); Collected papers of Landau, Pergamon Press, (1965).
25. Raikher Yu.L., Shliomis M.I., *Sov. Phys. JETP*, **40**, 526, (1974).
26. Coffey W.T., Kalmykov Y.P., Massawe E.S., *Adv. Chem. Phys.*, **85**, 704, (1993).

27. Fannin P.C., Scaife B.K.P., Giannitsis A.T., Charles S.W., *Journal of Physics D: Applied Physics*, **35**, 1305, (2002).
28. Martsenyuk M.A., Raikher Yu.L., Shliomis M.I., *Sov. Phys. JETP*, **38**, 413, (1974).
29. Coffey W.T., Paranjape B.V., *Proceedings of the Royal Irish Academy*, section A, vol **78**, A, num 3, (1978).
30. Déjardin J.L., *Physical Review E*, **68**, 031108, (2003).
31. Fannin P.C., Raikher Yu.L., Giannitsis A.T., Charles S.W., *J. of Magnetism and Magnetic Materials*, **252**, 114, (2002).

Chapter 1

Overview of the theory of relaxation and resonance of nanoparticle magnetic systems.

1.1 Introduction

This thesis is concerned with the study of the dynamic properties of the magnetic fluids. A magnetic fluid consists of magnetic particles dispersed in a carrier liquid. Each particle carries a magnetic moment that arises from the spin motion of the electrons of the atoms which constitute the magnetic particle. The dynamic properties of the magnetic fluids can be studied by applying spectroscopic methods. From the spectrum of the *dynamic susceptibility*, $\chi(\omega)$, of a magnetic fluid one can determine important information about the rotational activity of the magnetic moments of the ferroparticles. In addition one also can estimate the *microscopic* parameters (i.e. size, internal energy density, gyromagnetic ratio, frequency of precession, diffusion time) of the particles.

This chapter is an overview of the theory of the magnetic fluids. It presents the basic concepts of spectroscopy, it follows the structure of the magnetic particles and this is followed by the theory of the rotation of the particle's magnetic moment, which is distinguished between relaxation and resonance. The mechanisms of relaxation and of resonance can be analyzed by using classical mechanics and electrodynamics. The motion of the magnetic particles is affected by thermal energy. Particles perform Brownian motion, thus basic concepts from classical statistical physics (statistical average, diffusion equation, etc) are reviewed.

1.2 Theory of spectroscopy.

Three types of magnetic spectroscopy can be found in the literature:

(a) *microwave* spectroscopy, commonly called *rotational* spectroscopy, which is due to the rotation of the magnetic moment of a magnetic particle due to the influence of an external magnetic field,

(b) *nuclear magnetic resonance* (NMR) spectroscopy, which is due to the interaction of the magnetic moment of the nuclei of the atom with an external field, and

(c) *electronic paramagnetic* resonance (EPR) spectroscopy, which is due to the interaction of the electron spins with an external field.

This thesis is concerned with rotational spectroscopy in the magnetic fluids.

The existence of a permanent magnetic moment in a particle is essential for the appearance of a torque on the particle, which results in its rotation. Based on this concept we can verify if a particle will or will not present a rotational spectrum. The particles with permanent magnetic moments absorb energy from the applied magnetic field. This energy absorption is the result of the interaction of the magnetic moment with the magnetic field. When an oscillating magnetic field, $\mathbf{h}_a(t) = \mathbf{H}_0 \cos(\omega t)$, is applied to the particle, a torque develops which acts on the magnetic moment of the particle and causes it to rotate about the axis which passes through the centre of its mass, thereby causing the magnetic moment vector to align with the magnetic field. This procedure of alignment of the magnetic moment's vector with the magnetic field, takes place any time the field changes direction or phase. When the field and the magnetic moment vector align collinearly, the particle absorbs energy from the magnetic field.

The principle of the rotation of a magnetic particle is illustrated in Fig. (1.1), where the oscillating magnetic field applies a torque to the magnetic moment, $\boldsymbol{\mu}_m$. Likewise, in polar molecules with permanent electric dipolar moment, $\boldsymbol{\mu}_e$, an alternating electric field changes the direction of the molecules about the axis of the propagation of the field (Fig. (1.1)). The rotational spectroscopy, in polar molecules, is a very accurate method to estimate the length of the bonds between the atoms of a molecule. Similarly the rotational spectroscopy is used to estimate the size of the magnetic particles in a magnetic liquid.
The magnetic moment of a magnetic particle is not immobile; it neither aligns right parallel or antiparallel to an arbitrary magnetic field, **H**. The magnetic field causes the moment to deviate by an angle θ and to execute a precessional motion, so that $\boldsymbol{\mu}_m$ curves a conical surface as shown in Fig. (1.2 a). The angular velocity of the precessional motion, ω_{pre}, is called the *Larmor angular velocity*, ω_L, is independent of the angle θ and is proportional to the strength of the magnetic field, **H**, according to the equation

$$\omega_L = \omega_{pre} = \gamma H \qquad (1.2.1)$$

γ is called the gyromagnetic ratio and as will be shown later, γ is the ratio of magnetic moment to the angular momentum of the magnetic particle.

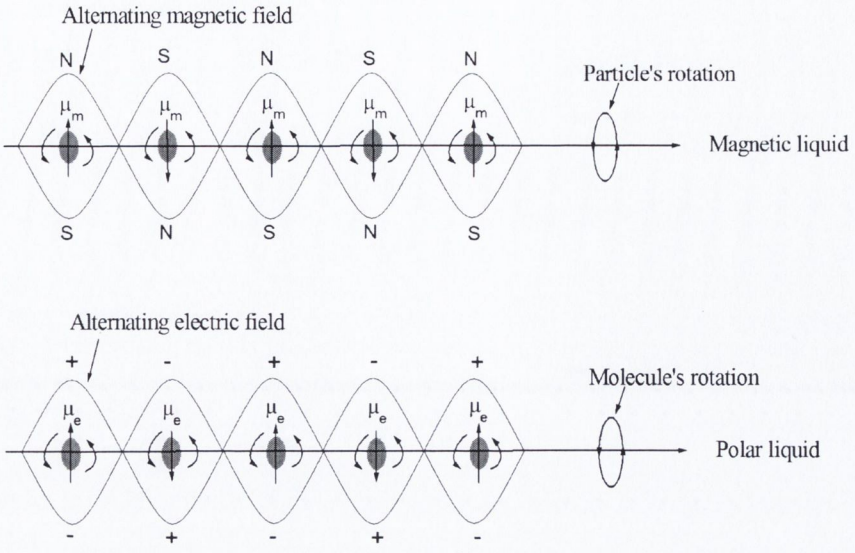

Figure 1.1 The oscillating magnetic field applies a torque to the magnetic moment of the magnetic particle and makes it rotate about the axis of field's propagation (horizontal axis). Similarly the interaction of the electric dipolar moment of a polar molecule with an electric alternating field results in the rotation of the molecule.

Figure 1.2

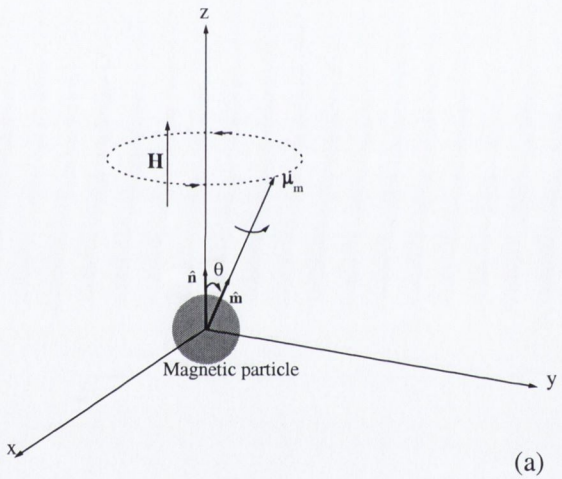

(a)

Figure 1.2 (a) Precession of the magnetic moment of a particle about an arbitrary magnetic field, **H**, which is applied along the z-axis. $\boldsymbol{\mu}_m$ rotates anticlockwise. $\hat{\mathbf{n}}$ is the unit vector along the axis of the field, whilst $\hat{\mathbf{m}}$ is the unit vector on the direction of the magnetic moment.

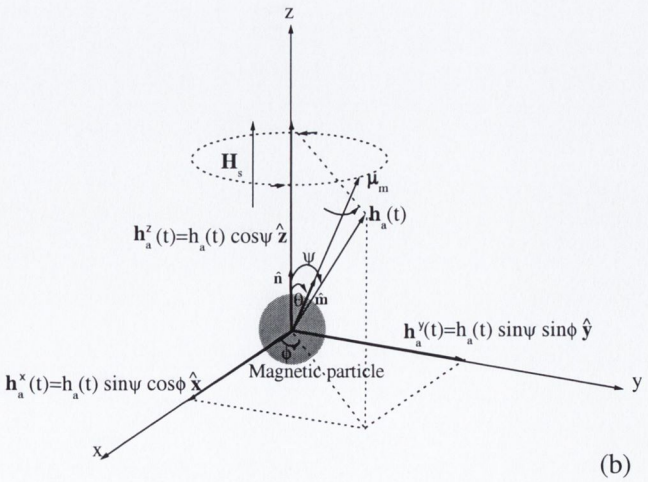

(b)

Figure 1.2 (b) Precession of $\boldsymbol{\mu}_m$ under the influence of a static field, $\mathbf{H}_s$, in conjunction with an alternating field, $\mathbf{h}_a(t)$. On the graph is shown the orientation of the alternating field, $\mathbf{h}_a(t)$, at an arbitrary instant and its components along the three axes of space. The moment rotates anticlockwise.

(Continued).

Figure 1.2

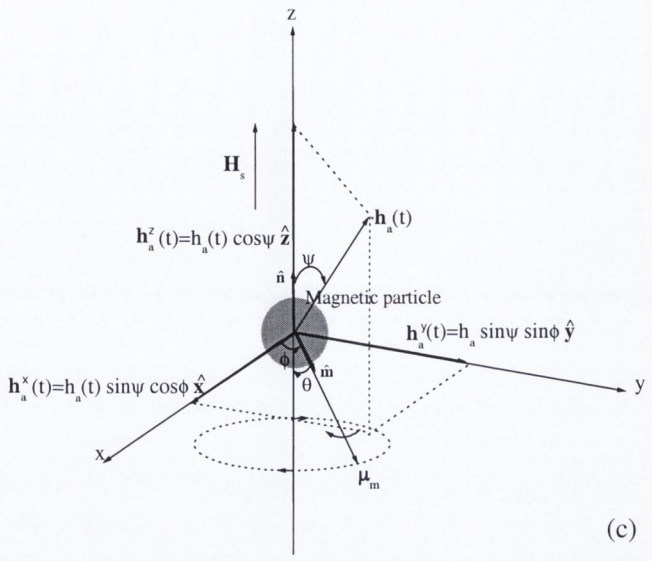

Figure 1.2 (c) When the frequency of the alternating field equals the frequency of moment's precession, the moment jumps to an other energy state, i.e. $\boldsymbol{\mu}_m$ jumps under the x-y plane. The rotation of $\boldsymbol{\mu}_m$ is in the clockwise direction, i.e. $\boldsymbol{\mu}_m$ changes its rotational phase.

One can use the classical theory to describe how a magnetic field can excite (resonate) a magnetic particle. Let us consider a magnetic particle precessing with Larmor angular frequency (frequency of precession), ω_{pre}, about the direction of a static field, $\mathbf{H}_s$, (Fig. (1.2 b)). Let us also consider that initially the vector of the magnetic moment is parallel to $\mathbf{H}_s$. We can change the orientation of $\boldsymbol{\mu}_m$ if we apply an alternating magnetic field, $\mathbf{h}_a(t) = \mathbf{H}_0\cos(\omega t)$, with frequency, ω, which is in the microwave frequency region (GHz). $\mathbf{h}_a(t)$ alternates with frequency ω on the same sense with the precession of the particle, as Fig. (1.2 b) shows. If we can synchronise (resonate) the two frequencies, ω and ω_{pre}, the particle will absorb energy and the magnetic torque will change the particle orientation with respect to the direction of the z-axis. In other words the particle will jump to a state of a higher energy. This procedure of agitating the magnetic particles is called *magnetic resonance*. The particles in the excited state may be de-energized, i.e. to give back the energy that they absorbed, and return to the basic state. The process of de-energization can be recorded by electronic instruments (e.g. spectrometers, analysers). Peaks appear in the spectrum, which denote energy absorption.

We can distinguish between two types of peaks in a rotational spectrum, namely the peaks due to the rotation (relaxation) of the magnetic particles (or polar molecules) and the peaks due to the precession of the particles (molecules). Both types of peaks indicate

absorption of energy, as explained previously. In the rotational spectrum of the polar liquids the peaks appear sharp in shape. This is due to the mono-dispersion of the polar molecules. In the spectra of magnetic liquids the peaks are wide and this is due to the poly-dispersion of the sizes of the particles.

1.3 The constituents of magnetic liquids.

Magnetic liquids, commonly called *ferrofluids*, are suspensions of magnetic particles in a carrier liquid such as water, mineral oil, kerosene, isoparaffin, diester, or toluene. Each particle, also called a *ferroparticle*, consists of a magnetic core of ferromagnetic or ferrimagnetic material of the type m-Fe_2O_4 in which m is a metal from the transition group of the periodic table, such as Fe, Co, Mn, Zn, or Ni. Thus the magnetic core of the ferroparticle may consist of materials such as magnetite (Fe_3O_4), cobalt ferrite ($Co_xFe_{1-x}Fe_2O_4$), manganese ferrite ($Mn_xFe_{1-x}Fe_2O_4$), zinc ferrite ($Zn_xFe_{1-x}Fe_2O_4$), where $x \leq 1$. It is also possible for the core of the magnetic particle to consist of materials which are combinations of these metals in several proportions, such as nickel-zinc ferrite ($Ni_xZn_{1-x}Fe_2O_4$), or cobalt-zinc ferrite ($Co_xZn_{1-x}Fe_2O_4$). The magnetic core is coated in an organic surfactant layer in order to prevent attraction between particles. A single particle has an approximate radius of between 2 and 10 nm of which 2 nm is the thickness of surfactant coating. The surfactant does not always prevent attractions due to the magnetic interaction between particles, especially in high concentrated liquids (with a volume fraction usually larger than 0.06 [1]), and it is possible for *aggregates* to form with arbitrary spheroidal shapes or even chains (Fig. 1.3). The mean radii of aggregates may be 15-100 nm.

The particles are considered to be *single domain* [2]. Single domain means that the volume of the ferromagnet which consists of the particle, the so called magnetic volume, v_m, is composed of one only domain. Domains are areas that are formed in a ferromagnet as a result of energy minimization. Weiss [3,4] was the first to introduce the concept of domains, while Landau and Lifshitz [5] showed that the existence of domains is a consequence of energy minimization.

Frenkel and Dorfman [6] were the first to predict the existence of mono-domain particles. Raikher and Shliomis [7] calculated the critical size for mono-domainness for a typical ferromagnet and obtained a critical diameter of $d_* = 30$ nm.

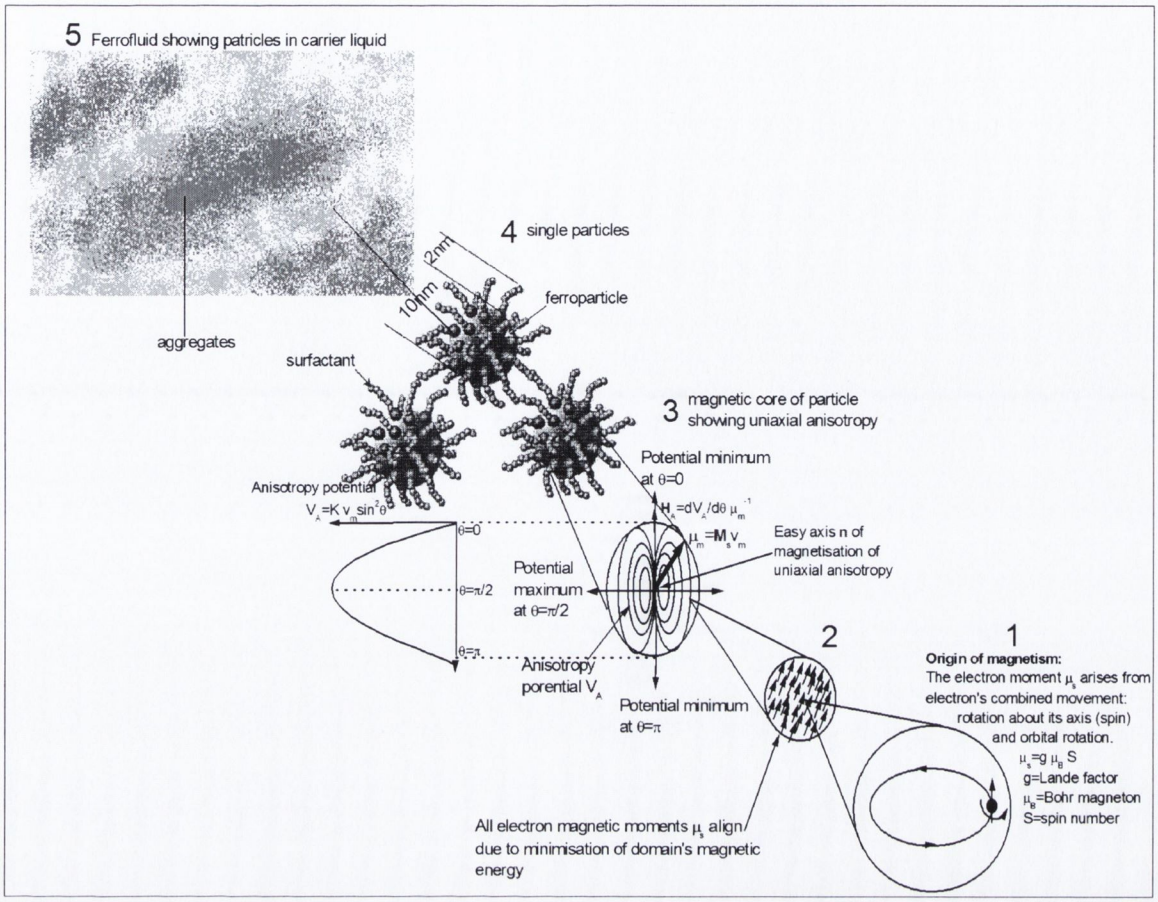

Figure 1.3 Shows a gradual scale-up of the components of a ferrofluid and ferroparticles: At part 1 is shown the origin of the magnetic moment, which arises from the combined rotational motion of the electron about its axis (spin) and around the nuclei. Part 2 is shows how all moments align in the same direction, as short range exchange interaction requires. The sum of all these electron spin moments give the total moment $\boldsymbol{\mu}_m$ of the domain, which is equal to 10^4-10^5 Bohr magnetons (superparamagnetism). Part 3 shows the magnetic part of the particle with its anisotropy (here uniaxial) arising from spin-orbit coupling. Magnetic moment $\boldsymbol{\mu}_m$ may rotate or precess about the direction of potential minimum. This direction is called the easy axis of magnetisation and without any external excitation (such as external field or thermal agitation) $\boldsymbol{\mu}_m$ lies on it. The internal anisotropy field $\mathbf{H}_A$ is given by the differentiation of the potential energy with respect to the angle θ. The maximum potential at $\theta=\pi/2$ is a barrier, which repulses moment $\boldsymbol{\mu}_m$ to a lower potential at $\theta=0$ or π. Part 4 shows the whole particle with the surfactant layer covering the core having a thickness of about 2nm. Surfactant molecules may spread into the carrier liquid without joining particles. Part 5 shows the macroscopic appearance of ferrofluids as an inhomogeneous system. The surfactant may not prevent attractions and aggregates are created acting as big particles.

As shown in Fig. (1.3) the magnetism arises from the combined rotational motion of the electron about its axis (spin) and around the nuclei. The moment arising from the spin, having angular momentum **S**, is strong. The moment arising from the circular rotation, having angular momentum **L**, is weak and it does not contribute much to the total magnetic moment of the electron. If q_e=electron's charge, m_e=electron's mass, μ_0=permittivity of the free space and $\hbar$ the normalised Planck's constant, then the total magnetic moment of the electron is given by [8]

$$\boldsymbol{\mu}_s = g\mu_B \mathbf{J} \tag{1.3.1}$$

where

$$\mathbf{J}=\mathbf{L}+\mathbf{S} \tag{1.3.2}$$

is the vector sum of the vector sum of the two momentums,

$$\mu_B = \mu_0 q_e \hbar / 2m_e \tag{1.3.3}$$

is the Bohr magneton, and

$$g=1+[J(J+1)+S(S+1)-L(L+1)]/2J(J+1) \tag{1.3.4}$$

is the Landé factor which can take values between 1 and 2. The value g=2 is when the magnetic moment is due entirely to the electron spin (paramagnetism) and g=1 when is due entirely to orbital motion (diamagnetism). For ferromagnetic materials g is close to 2.

A single domain particle is characterised by its saturation magnetisation, $\mathbf{M}_s$, which is the vector sum of the electron spin magnetic moments, $\boldsymbol{\mu}_s$, over the volume of the domain (called magnetic volume v_m). The total magnetic moment $\boldsymbol{\mu}_m$ of a single domain ferroparticle is the vector sum of all spin moments, $\boldsymbol{\mu}_s$, or equivalently,

$$\boldsymbol{\mu}_m = \mathbf{M}_s v_m \tag{1.3.5}$$

This is the moment characterising the magnetism of a ferroparticle macroscopically. For ferroparticles $\boldsymbol{\mu}_m$ is about 10^4-10^5 times the Bohr magneton $\mu_B = \mu_0 q_e \hbar / 2m_e$. Strong exchange forces hold the adjacent spins parallel to each other, and the direction of these spins defines the direction of $\boldsymbol{\mu}_m$. These exchange forces fall off very rapidly with distance and only affect nearest neighbour pairs. This short range exchange interaction can be explained by quantum mechanics.

A ferromagnetic crystal is not isotropic since it contains crystallographic axes, usually in uniaxial or cubic disposition. The electron orbits are linked to these axes and by their interaction with the spins (spin-orbit interactions) makes the spins align along these crystallographic axes (Fig. (1.3)). The resulting *anisotropy* is called *magnetocrystalline anisotropy*. Phenomenological expressions for the anisotropy energy can describe some standard anisotropies by expansions in power series that take into account the crystal symmetry.

Uniaxial anisotropy involves only one parameter, the polar angle θ between the z-axis and the direction of magnetisation (Fig. (1.3)). Denoting the unit vector on the z-axis (easy axis) of uniaxial anisotropy by $\hat{\mathbf{n}}$ and that of the magnetisation (and so of moment $\boldsymbol{\mu}_m$) by $\hat{\mathbf{m}}$, we may write the uniaxial anisotropy energy density as,

$$U_A^u = -K\cos^2\theta + K_1\cos^4\theta + \ldots = -K(1-\sin^2\theta) + K_1\cos^4\theta + \ldots \quad (1.3.6)$$

where $\cos\theta$ is the direction cosine of $\hat{\mathbf{m}}$ with respect to $\hat{\mathbf{n}}$. The coefficients $K, K_1, \ldots$ are called anisotropy constants and have dimensions of energy density. In general K_1 is neglected since it is smaller than K. Some authors prefer to write the anisotropy energy as,

$$U_A^u = K\sin^2\theta = K(1-\cos^2\theta) \quad (1.3.7)$$

(K now takes on a different value). For magnetite K has a value between 8000-11,000 J/m^3, for manganese ferrite K$\cong$ 4,000-6,000 J/m^3, for cobalt ferrite K$\cong$ 5,000 J/m^3 and for nickel-zinc ferrite K$\cong$ 3,000 J/m^3. It is convenient to consider the effect of uniaxial anisotropy energy in terms of the internal magnetic field $\mathbf{H}_A$, which is defined by the torque, $\boldsymbol{\Gamma}$, exerted on the magnetic moment $\boldsymbol{\mu}_m$, which is equal to the torque exerted by the anisotropy energy,

$$\boldsymbol{\Gamma} = \boldsymbol{\mu}_m \times \mathbf{H}_A = \frac{\partial V_A^u}{\partial\theta}\hat{\mathbf{u}} = \frac{\partial U_A^u}{\partial\theta} v_m \hat{\mathbf{u}} \qquad (\hat{\mathbf{u}} = \hat{\mathbf{m}} \times \hat{\mathbf{n}}) \quad (1.3.8)$$

V_A^u is the anisotropy energy, U_A^u is the energy density. By substituting Eqs. (1.3.5), (1.3.7), we get,

$$H_A(\theta) = \frac{2K}{M_s}\cos\theta \quad (1.3.9)$$

and when the moment lies on the easy axis,

$$H_A(0) = \frac{2K}{M_s} \quad (1.3.10)$$

This is the value of a coercive field required to reverse the direction of the moment from one easy direction to the other. As shown in Fig. (1.3), the maximum potential is at $\theta=\pi/2$, and is a barrier which forces the moment $\boldsymbol{\mu}_m$ to a lower potential at $\theta=0$ or π. However if the anisotropy barrier is small enough (the barrier energy is always compared with the thermal energy and the dimensionless parameter $\sigma = \frac{Kv_m}{k_B T}$ is usually used for the comparison), then the magnetic moment may be reversed in direction by thermal activation in the absence of any external field.

Cubic-anisotropy, appears in cubic crystals, and the associated energy density is given by

$$U_A^c = K_1 \sum_{\substack{i,j=1 \\ i\neq j}}^{3} m_i^2 m_j^2 + K_2 \prod_{i=1}^{3} m_i^2 + \ldots = \frac{K_1}{2}\left(1 - \sum_{i=1}^{3} m_i^4\right) + K_2 \prod_{i=1}^{3} m_i^2 + \ldots \quad (1.3.11)$$

where i,j=1,2,3≡x,y,z and $m_1 = \sin\theta\cos\phi, m_2 = \sin\theta\sin\phi, m_3 = \cos\theta$, θ is the angle between the magnetisation and the z-axis and φ the azimuthal angle. The cubic-anisotropy energy is obtained by integrating over the whole volume of the ferroparticle, i.e.

$$V_A^c = \int U_A^c dv_m \tag{1.3.12}$$

Any non-spherical particle shape will give rise to *shape anisotropy* arising from the demagnetising fields within the particle. For a spheroid where N_z, N_x are the demagnetising factors in the direction of the major axis and in any direction perpendicular to the major axis, respectively, then the demagnetising energy is given by,

$$V_A^{sh} = \frac{1}{2\mu_0} M_s^2 v_m (N_z \cos^2\theta + N_x \sin^2\theta) \tag{1.3.13}$$

Using Eq. (1.3.8), as before, we find the value of the internal anisotropic field

$$H_A = \frac{1}{\mu_0} M_s (N_x - N_z) \tag{1.3.14}$$

For a general ellipsoid, the demagnetising factors N_x, N_y and N_z lie along the three principle axes and are related by the expression:

$$N_x + N_y + N_z = 1 \tag{1.3.15}$$

For spherical particles $N_x = N_y = N_z = 1/3$, therefore from Eq. (1.3.14), spheres have no shape anisotropy. Shape anisotropy appears only in those ferroparticles which have different demagnetising factors on each direction of space. For the infinitely long cylinder magnetised longitudinally we have $N_x = N_y = 1/2$ and $N_z = 0$, which results in a coercivity of $M_s / 2\mu_0$ and therefore a very large shape anisotropy. In a ferrofluid there exist particles of different shapes and hence, there is a distribution in the values of shape anisotropy ranging between the extremes of perfect spheres, with no shape anisotropy, and infinite cylinders with very large anisotropy.

The electron spin at the surface of a particle has a nearest neighbour on one side and none on the other so that the exchange energy cannot be the same as in the bulk. With reducing particle size, the magnetic contributions from the surface will eventually become more important than those from the bulk of the particle and hence *surface anisotropy* energy will dominate over the magnetocrystalline anisotropy and demagnetising (magnetostatic) energies. In a first approximation, the surface anisotropy energy is proportional to the surface area, S_p, of the particle and is given as [9]:

$$V_A^{su} = K_s S_p \cos^2 \theta' \qquad (1.3.16)$$

where θ' is the angle between this unit vector and the moment.

The rotational movement of ferroparticles in the carrier liquid must be described statistically, since a ferrofluid is an inhomogeneous mixture with particles of several sizes and magnetic moments $\boldsymbol{\mu}_m$. In the case of an externally applied constant field (static case) we can prove that ferrofluids are simply paramagnets: the magnetic energy of a particle under the influence of a constant field $\mathbf{H}_s$ is,

$$-\boldsymbol{\mu}_m \cdot \mathbf{H}_s = -\mu_m H_s \, \hat{\mathbf{m}} \cdot \hat{\mathbf{h}} = -\mu_m H_s \cos\theta, \qquad (\hat{\mathbf{h}} = \mathbf{H}_s / H) \qquad (1.3.17)$$

and in thermal equilibrium, the probability of a particle having an angle θ at a temperature T, according to Boltzmann statistics, is proportional to $e^{\xi_m \cos\theta}$, with $\xi_m = \dfrac{\mu_m H_s}{k_B T}$, thus the average of the direction cosines of the directions of $\boldsymbol{\mu}_m$ with respect to the direction of $\mathbf{H}_s$ is [8],

$$\left\langle \hat{\mathbf{m}} \cdot \hat{\mathbf{h}} \right\rangle = \langle \cos\theta \rangle = \frac{\int_0^{2\pi}\int_0^{\pi} \cos\theta \, e^{\xi_m \cos\theta} \sin\theta \, d\theta \, d\phi}{\int_0^{2\pi}\int_0^{\pi} e^{\xi_m \cos\theta} \sin\theta \, d\theta \, d\phi} = \left(\coth \xi_m - \frac{1}{\xi_m} \right) = L(\xi_m) \qquad (1.3.18)$$

which is the *Langevin function* [10] describing statistically the direction cosines in all paramagnets, and thus in ferrofluids. The Langevin function is the limit of the Brillouin function when the spin number S tends to infinity [9]. The dimensionless field parameter ξ_m is the ratio of the magnetic energy of the particle in the external field to the thermal energy. The induced magnetisation as a function of the field parameter is given by

$$M(\xi_m) = M_s \langle \cos\theta \rangle = M_s L(\xi_m) = M_s \left(\coth \xi_m - \frac{1}{\xi_m} \right). \qquad (1.3.19)$$

This equation describes the magnetisation curve of a ferrofluid system (Fig. (1.4)).

Figure 1.4

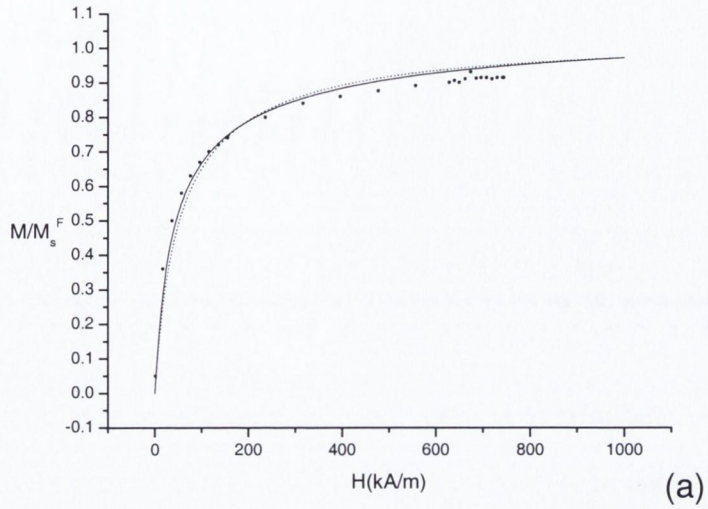

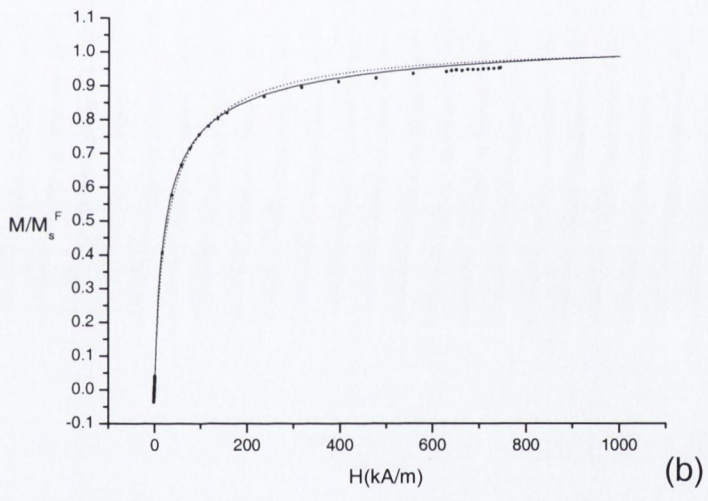

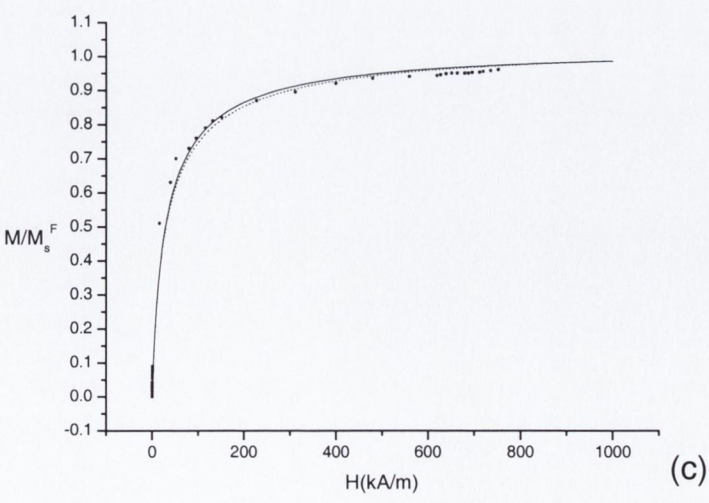

(Continued).

Figure 1.4

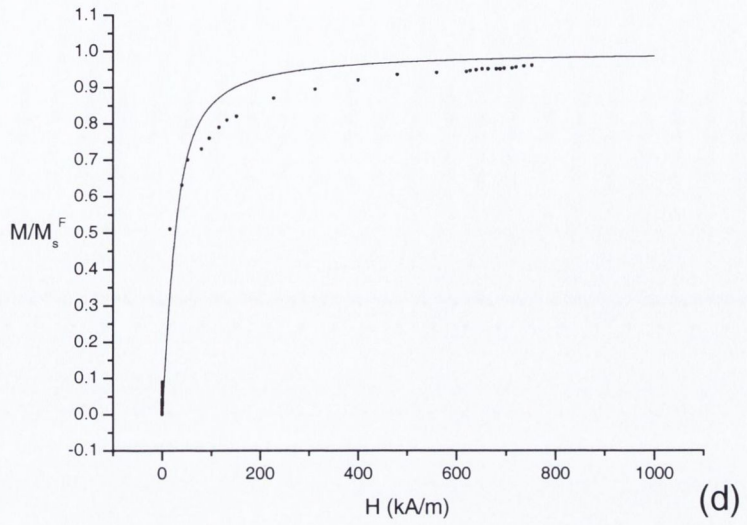

Figure 1.4 Fits of magnetisation curves (as obtained from manufacturer) of (a) magnetite ferrofluid in oil with saturation magnetisation of the fluid M_s^F=340 G (0.034 T), (b) magnetite in water with M_s^F=400 G and (c) magnetite in water with M_s^F=100 G (0.01 T). Data has been fitted with the Langevin equation (1.3.19) modified to include the distribution of the particle's sizes. This is realised by distributing the magnetic radius r_m of the particles by a distribution function such Normal (Gaussian) or Log-Normal. The choice of a distribution is arbitrary but most investigators prefer to use the Normal, Log-Normal or the Nakagami distribution (Normal is a special case of Nakagami distribution, whilst Nakagami is related to Gamma distribution). Since ξ_m is proportional to the cube of r_m it is also distributed, thus the Langevin function accounts for the dispersion of particle size. In the above fits we used the Normal and Log-Normal distributions, the first is denoted by a solid line and the second by a dashed. The parameters used for the fit in each case were: (a) M_s=0.4 T, r_m=4.4 nm, μ_m=1.42x10^{-25} Wb m, σ_r=0.56 (standard deviation) for the Normal distribution and σ_r=0.4 for the Log-Normal distribution, (b) M_s=0.4 T, r_m=5.5 nm, μ_m=2.78x10^{-25} Wb m, and σ_r is 0.6 and 0.45 for Normal and Log-Normal respectively, (c) M_s=0.4 T, r_m=5.5 nm, μ_m=2.78x10^{-25} Wb m, and σ_r is 0.5 and 0.4 for Normal and Log-Normal. (d) shows how the fit (c) would appear if no distribution was applied.

The *Curie law*, which states that the *static susceptibility*, defined as the magnetization divided by the applied static field, is proportional to the inverse of the absolute temperature ($\chi \propto T^{-1}$), may be derived by expanding the Langevin function in a Taylor's series in ξ_m. When $\xi_m << 1$ (valid for normal room temperatures) the expression for $M(\xi_m)$ can be approximated by the first term,

$$M(\xi_m) = M_s \frac{\xi_m}{3} = M_s \frac{\mu_m H_s}{3k_B T} \tag{1.3.20}$$

and thus the static susceptibility,

$$\chi_0 = M_s \frac{\mu_m}{3k_B T} = \frac{C}{T} \tag{1.3.21}$$

The Curie Law, together with the Langevin function, shows that the theory of a paramagnetic gas also holds for ferrofluids.

Because of their size, ferroparticles are treated as Brownian particles. Brownian theory modified by Debye [11,12] for the case of rotational diffusion (in dielectrics) and Néel [13] and Brown [14] for the internal rotational diffusion of moment $\boldsymbol{\mu}_m$, may be used to describe phenomenologicaly the rotational process under the influence of external fields.

1.4 Theory of Debye relaxation

In this section we will introduce the basic theory of relaxation*, which in its original form was developed for the polar liquids, and after we will adopt the final equations to describe relaxation of magnetic liquids. The theory of relaxation entails statistical physics and diffusion.

Einstein's theory [15,16,17] of the *translational Brownian motion*, on which the Debye theory [11,12] of relaxation of an assembly of non interacting polar molecules is essentially based, has as a starting point, the *Fokker-Planck* probability density diffusion equation [16]

$$\frac{\partial W(\mathbf{r},t)}{\partial t} = D\nabla^2 W(\mathbf{r},t) \qquad (1.4.1)$$

where $W(\mathbf{r},t)$ is the three dimensional probability distribution density of finding a particle at position $\mathbf{r}$, at time t and

$$D = \frac{k_B T}{\zeta} \qquad (1.4.2)$$

is the diffusion coefficient which is determined by using the fact that in equilibrium ($\dot{W} = 0$, realised for $t \to \infty$) the solution should be the Maxwell-Boltzmann distribution,

$$W(\mathbf{r}) = A\exp(-\frac{V(\mathbf{r})}{k_B T}) .$$

ζ is the viscous drag coefficient on the Brownian particle, assumed to be a rigid sphere of hydrodynamic radius, r_p, obeying Stokes' law so that, $\zeta\dot{\mathbf{r}} = 6\pi\eta_h r_p\dot{\mathbf{r}}$ is the viscous drag force. Equation (1.4.1) relies on the continuum limit of a discrete time random walk of a very large number of small steps of small duration. The thermal agitation of the particles (Brownian movement) is accounted for by the diffusive current,

* Relaxation is the phenomenon of returning from the polarised state to the original chaotic state.

$$\mathbf{J}_{diff}(\mathbf{r},t) = -D\nabla W(\mathbf{r},t) \tag{1.4.3}$$

Under the influence of an external conservative potential, arising from an applied force

$$\mathbf{F} = -\nabla V(\mathbf{r},t) \tag{1.4.4}$$

a drift current appears and giving rise to the *Smoluchowski equation*

$$\frac{\partial W(\mathbf{r},t)}{\partial t} = -\nabla\cdot\left(\mathbf{J}_d(\mathbf{r},t)+\mathbf{J}_{diff}(\mathbf{r},t)\right) = \nabla\cdot\left(D\nabla W(\mathbf{r},t)+\frac{W(\mathbf{r},t)}{\zeta}\nabla V(\mathbf{r},t)\right) \tag{1.4.5}$$

where the drift current [16]

$$\mathbf{J}_d(\mathbf{r},t) = -\frac{W(\mathbf{r},t)}{\zeta}\nabla V(\mathbf{r},t) \tag{1.4.6}$$

is due to the external force and it is added to the thermal agitation diffusive current, $-D\nabla W(\mathbf{r},t)$. Einstein's equation (1.4.1) is the special case in which the influence of external forces, affecting the system, is neglected ($V(\mathbf{r},t)=0$).

Einstein solved the Fokker-Planck equation (1.4.1) by assuming that each individual particle executes a motion which is independent of the motion of all other particles and the motion of a particle at one instant, t, is independent of its motion at any other instant t′, provided the time interval $\tau = t' - t$ is large enough [16,17]. Assuming the effect of a potential V(x)=Fx, (F=const), he derived an expression for the one dimensional root mean square displacement x(t) for an arbitrary instant t, with the condition that at t=0 the particle was at the beginning of the coordinate system x(0)=0 [16,18]*

$$\sqrt{\langle x^2\rangle} = \sqrt{2Dt} \tag{1.4.7}$$

and a relation between the space interval $\Delta x=x(t')-x(t)=x'-x$ between two sequential observations separated by a time interval τ,

$$\langle \Delta x^2\rangle = 2D\tau \tag{1.4.8}$$

The arguments used for the translational motion may be extended to the rotational motion about the diameter of a particle. Therefore if ϑ is the angular coordinate, the root mean square of change of ϑ at instant t as a result of thermal agitation is

$$\sqrt{\langle \vartheta^2\rangle} = \sqrt{2Dt} \tag{1.4.9}$$

---

* Distinction should be made between the ensemble average denoted hereafter by angular brackets $\langle ... \rangle$ and the time average denoted with overbars.

where the diffusion coefficient is given again by Eq.(1.4.2) but the drag coefficient changes to $\zeta = 8\pi r_p^3 \eta_h$, and the rotational displacement

$$\left\langle \Delta\vartheta^2 \right\rangle = 2D\tau \tag{1.4.10}$$

The method applied by Smoluchowski yields the same result [16,18] as Einstein's method. This method is more direct since the Smoluchowski equation contains the external potential directly.

Solution of differential Eqs.(1.4.1),(1.4.5) is difficult. Adapting Langevin's concept (based on Newtonian mechanics) one can derive the mean square rotational displacement by writing Newton's second law of motion in a polar single angle and for one particle of mass m_p, having moment of inertia I_p,

$$I_p \frac{d^2\vartheta(t)}{dt^2} = -\zeta \frac{d\vartheta(t)}{dt} + \Gamma(t) \tag{1.4.11}$$

with ζ taken (for the rotational case of motion) as $\zeta = 8\pi\eta_h r_p^3$. It is also assumed that the fluctuating torque $\Gamma(t)$ is independent of ϑ and varies very rapidly compared to ϑ and the average satisfies $\left\langle \Gamma(t) \right\rangle = 0$. This rapid variation is expressed by [16,18]

$$\left\langle \Gamma(t)\Gamma(t') \right\rangle = \overline{\Gamma(t)\Gamma(t')} = 2\zeta k_B T \delta(t - t') \tag{1.4.12}$$

where δ is the Dirac delta function and $2\zeta k_B T$ is called the spectral density. Equation (1.4.11) is a *stochastic differential equation*. Following Langevin's concept one can proceed by writing Eq. (1.4.11) as

$$\frac{I_p}{2}\frac{d}{dt}\left(\frac{d\vartheta^2}{dt}\right) - I_p\left(\frac{d\vartheta}{dt}\right)^2 = -\frac{\zeta}{2}\frac{d\vartheta^2}{dt} + \Gamma(t)\vartheta \tag{1.4.13}$$

and averaging over the ensemble in order to include the rotation of all the particles of the system, giving

$$\frac{I_p}{2}\frac{d}{dt}\left(\left\langle \frac{d\vartheta^2}{dt} \right\rangle\right) - I_p\left\langle \left(\frac{d\vartheta}{dt}\right)^2 \right\rangle = -\frac{\zeta}{2}\left\langle \frac{d\vartheta^2}{dt} \right\rangle + \left\langle \Gamma(t)\vartheta \right\rangle \tag{1.4.14}$$

Because the random torque $\Gamma(t)$ is uncorrelated with the rotational displacement then $\left\langle \Gamma(t)\vartheta \right\rangle = 0$, or in other words the motion of a particle at one instant is independent of all other instants, as Einstein stated. When the velocity process has reached equilibrium, the Maxwellian distribution holds, so that

$$\frac{1}{2}I_p\left\langle\left(\frac{d\vartheta}{dt}\right)^2\right\rangle=\frac{1}{2}k_BT \tag{1.4.15}$$

thus Eq. (1.4.14) yields,

$$\frac{I_p}{2}\frac{d}{dt}\left(\left\langle\frac{d\vartheta^2}{dt}\right\rangle\right)+\frac{\zeta}{2}\left\langle\frac{d\vartheta^2}{dt}\right\rangle=k_BT \tag{1.4.16}$$

which has a solution,

$$\left\langle\frac{d\vartheta^2}{dt}\right\rangle=\frac{2k_BT}{\zeta}+Ce^{-\zeta t/I_p} \tag{1.4.17}$$

and ignoring the inertial effects (exponential term equals to zero) we find that

$$\left\langle\frac{d\vartheta^2}{dt}\right\rangle=\frac{2k_BT}{\zeta}\ . \tag{1.4.18}$$

Integration of Eq. (1.4.18) with respect to the time yields,

$$\left\langle\Delta\vartheta^2\right\rangle=\frac{2k_BT}{\zeta}t \tag{1.4.19}$$

which is the same as Eq. (1.4.10) derived by Einstein's method. Thus Langevin's method, based on Newtonian mechanics and averaged over all the particles of the assembly, produces the same result as that obtained by using the diffusion equation. A number of problems associated with magnetic relaxation may be treated both by the Fokker-Planck equation method and equivalently by the Langevin equation. The Fokker-Planck equation is particularly difficult to use for nonaxially symmetric problems involving anisotropy, because of the complicated manipulations of spherical harmonics. It is evident that the Langevin equation provides a much easier and more physical way of treating such problems.

Debye [11,12] in his model of dielectric relaxation (which can also be applied for the case of magnetic liquids) adapted Einstein's theory to the rotational Brownian motion of an assembly of non interacting dipolar molecules each of permanent electric dipole moment $\boldsymbol{\mu}_e$. He considered two models of the process, namely: (a) an assembly of fixed axis rotators subjected to Brownian motion torques having their origin in the background or heat bath and (b) the same assembly with the restriction to fixed axis rotation being removed. Nevertheless the results in both instances are qualitatively the same, since in each case the time-dependent distribution function (if inertial effects are disregarded) depends only on a single space coordinate. In case (a) this is the azimuthal angle ϕ while

in case (b) it is the polar angle ϑ (the colatitude). He accomplished this by simply replacing the Cartesian coordinates of Smoluchowski equation (1.5.5) with the spherical polar coordinates ϑ,ϕ. The electric field in terms of the electric potential is given in spherical coordinates as,

$$\mathbf{E}(\vartheta,\phi,t) = -\nabla V(\vartheta,\phi,t) = -\frac{\partial V(\vartheta,\phi,t)}{\partial \vartheta}\hat{\vartheta} - \frac{1}{\sin\vartheta}\frac{\partial V(\vartheta,\phi,t)}{\partial \phi}\hat{\phi} \qquad (1.4.20)$$

where operator ∇ is now for the polar case. The drift current of Eq. (1.4.6) may be written correspondingly as,

$$\mathbf{J}_d(\vartheta,\phi,t) = -\frac{W(\vartheta,\phi,t)}{\zeta}\nabla V(\vartheta,\phi,t) = -\frac{W(\vartheta,\phi,t)}{\zeta}\left[\frac{\partial V(\vartheta,\phi,t)}{\partial \vartheta}\hat{\vartheta} + \frac{1}{\sin\vartheta}\frac{\partial V(\vartheta,\phi,t)}{\partial \phi}\hat{\phi}\right] \qquad (1.4.21)$$

and the diffusive current Eq. (1.4.3), related to thermal agitation, is written as,

$$\mathbf{J}_{diff}(\vartheta,\phi,t) = -D\nabla W(\vartheta,\phi,t) = -D\left[\frac{\partial W(\vartheta,\phi,t)}{\partial \vartheta}\hat{\vartheta} + \frac{1}{\sin\vartheta}\frac{\partial W(\vartheta,\phi,t)}{\partial \phi}\hat{\phi}\right] \qquad (1.4.22)$$

Smoluchowski equation (1.4.5) finally takes the form,

$$\frac{\partial W}{\partial t} = \frac{1}{\zeta}\left[\frac{1}{\sin\vartheta}\frac{\partial}{\partial\vartheta}\left(\sin\vartheta W\frac{\partial V}{\partial\vartheta}\right) + \frac{1}{\sin^2\vartheta}\frac{\partial}{\partial\phi}\left(W\frac{\partial V}{\partial\phi}\right)\right] + D\left[\frac{1}{\sin\vartheta}\frac{\partial}{\partial\vartheta}\left(\sin\vartheta\frac{\partial W}{\partial\vartheta}\right) + \frac{1}{\sin^2\vartheta}\frac{\partial^2 W}{\partial\phi^2}\right] \qquad (1.4.23)$$

Now in statistical equilibrium $\dot{W} = 0$ and W must reduce to the Maxwell-Boltzmann distribution

$$W(\vartheta,\phi) = A\exp\left(-\frac{V(\vartheta,\phi)}{k_B T}\right) \qquad (1.4.24)$$

By substituting Eq. (1.4.24) into Eq.(1.4.23) we find that the diffusion coefficient D is the same as in the translational case given by Eq. (1.4.2). We define the *Debye relaxation time* by

$$\tau_D = \frac{\zeta}{2k_B T} \qquad (1.4.25)$$

which is the time required for the system to reach its equilibrium (actually 1/e=0.36787 of the value of equilibrium). Following Debye [12] who adapted the Smoluchowski equation to a uniform field **E** applied along the z axis, the potential $V(\vartheta,\phi)$ is reduced to $V(\vartheta) = -\mu_e E\cos\vartheta$. Also from Eq. (1.4.23) we obtain,

$$\frac{\partial W(\vartheta,t)}{\partial t}=\frac{1}{\sin\vartheta}\frac{\partial}{\partial\vartheta}\left[\sin\vartheta\left(\frac{k_BT}{\zeta}\frac{\partial W(\vartheta,t)}{\partial t}+\frac{\mu_eE}{\zeta}\sin\vartheta\frac{\partial W(\vartheta,t)}{\partial t}\right)\right]. \qquad (1.4.26)$$

The general solution of differential Eq. (1.4.26) is written in terms of Legendre polynomials $P_n(\cos\vartheta)$, n=0,1,2,...

$$W(\vartheta,t)=\sum_{n=0}^{\infty}a_n(t)P_n(\cos\vartheta)\ . \qquad (1.4.27)$$

Again in the spirit of the Debye calculations [12] we shall consider two separate cases of dielectric relaxation namely (a) the response following the sudden removal of a constant field (after effect response) and (b) the response to an alternating field which has been applied for a long time so that a steady state has been attained. For the first case in the linear approximation, in which $\mu_eE<<k_BT$ the *after effect* solution, in which the steady field is suddenly switched off at time t=0, of Eq. (1.4.26) is [16]

$$W(\vartheta,t)=A\left(1+\frac{\mu_eE}{k_BT}\cos\vartheta\exp(-\frac{2k_BT}{\zeta}t)\right), \qquad t>0 \qquad (1.4.28)$$

By averaging the mean dipole moment all over the directions yields,

$$\mu_e\langle\cos\vartheta\rangle=\mu_e\frac{\int_0^{2\pi}\int_0^{\pi}W(\vartheta,t)\cos\vartheta\sin\vartheta d\vartheta d\phi}{\int_0^{2\pi}\int_0^{\pi}W(\vartheta,t)\sin\vartheta d\vartheta d\phi}=\frac{\mu_e^2E\exp(-\frac{2k_BT}{\zeta}t)}{3k_BT}\ . \qquad (1.4.29)$$

Similarly for the case of an alternating field,

$$\mathbf{E}=\mathbf{E}_0e^{i\omega t} \qquad (1.4.30)$$

the value of the mean dipole moment is

$$\mu_e\langle\cos\vartheta\rangle=\frac{\mu_e^2}{3k_BT}\frac{E_0}{1+\omega^2\tau_D^2}[(\cos\omega t+\omega\tau_D\sin\omega t)+i(\sin\omega t-\omega\tau_D\cos\omega t)] \qquad (1.4.31)$$

We may modify the above equation to a compact format by extracting the field (in this case the alternating field)

$$\mu_e\langle\cos\vartheta\rangle=\frac{\mu_e^2}{3k_BT}\frac{1-i\omega\tau_D}{1+\omega^2\tau_D^2}E_0e^{i\omega t} \qquad (1.4.32)$$

In using Eq. (1.4.32) it should born in mind that the dipole-moment induced in a single particle by a small external field ($\mu_eE/k_BT<<1$) is minute compared to the fluctuating component in the field direction of the molecular dipole-moment. It is only when we add the coherent induced dipole moments of an extremely large number (say N per unit

volume) of molecules that the total induced dipole-moment greatly exceeds the net fluctuating dipole-moment.

Polarisation of a polar liquid, with particle density N, is equal to N times the average of particle's orientations, so the *complex polarisation*, P(ω), is defined as

$$P(\omega) = P'(\omega) - iP''(\omega) = N\mu_e \langle \cos\vartheta \rangle = \frac{N\mu_e^2}{3k_B T} \frac{1 - i\omega\tau_D}{1 + \omega^2\tau_D^2} E_0 e^{i\omega t} \quad . \tag{1.4.33}$$

Using the complex notation we decompose the polarisation into an in-phase part (the component which is in-phase with the alternating field) and a quadrature part that lags the applied field by π/2 rad. The negative sign of the imaginary part means that the polarisation lags the field. Complex notation can therefore be used to represent the component of the variable which is in-phase and the component which is π/2 rad out-of-phase (delayed), with the field. Such notation is used hereafter for all quantities such as permittivity, permeability, susceptibility etc.

We also define the *complex polarisability*, α(ω), [19] as the average dipole moment divided by the field, with

$$\alpha(\omega) = \alpha'(\omega) - i\alpha''(\omega) = \frac{\mu_e^2}{3k_B T} \frac{1 - i\omega\tau_D}{1 + \omega^2\tau_D^2} = \frac{\mu_e^2}{3k_B T} \frac{1}{1 + i\omega\tau_D} \tag{1.4.34}$$

Electric susceptibility measures the amount of polarisation produced by a particular field. The *complex electric susceptibility* is the polarisation over the alternating field, with

$$\chi_e(\omega) = \chi_e'(\omega) - i\chi_e''(\omega) = \frac{1}{\varepsilon_0} \frac{P'(\omega) - iP''(\omega)}{E_o e^{i\omega t}} = \frac{N\mu_e \langle \cos\vartheta \rangle}{\varepsilon_0 E_o e^{i\omega t}} =$$

$$= \frac{N\mu_e^2}{3\varepsilon_0 k_B T} \frac{1 - i\omega\tau_D}{1 + \omega^2\tau_D^2} = \frac{N\mu_e^2}{3\varepsilon_0 k_B T} \frac{1}{1 + (i\omega\tau_D)} \tag{1.4.35}$$

and the *relative complex dielectric permittivity*

$$\varepsilon(\omega) = \varepsilon'(\omega) - i\varepsilon''(\omega) = \chi_e(\omega) + 1 = \chi_e'(\omega) + 1 - i\chi_e''(\omega) \tag{1.4.36}$$

$$\varepsilon'(\omega) = \chi_e'(\omega) + 1, \qquad \varepsilon''(\omega) = \chi_e''(\omega) \tag{1.4.37}$$

thus

$$\varepsilon(\omega) = \varepsilon'(\omega) - i\varepsilon''(\omega) = \frac{N\mu_e^2}{3\varepsilon_0 k_B T} \frac{1 - i\omega\tau_D}{1 + \omega^2\tau_D^2} + 1 = \frac{N\mu_e^2}{3\varepsilon_0 k_B T} \frac{1}{1 + (i\omega\tau_D)} + 1 \tag{1.4.38}$$

or

$$\varepsilon'(\omega) = \frac{N\mu_e^2}{3\varepsilon_0 k_B T} \frac{1}{1 + \omega^2\tau_D^2} + 1, \qquad \varepsilon''(\omega) = \frac{N\mu_e^2}{3\varepsilon_0 k_B T} \frac{\omega\tau_D}{1 + \omega^2\tau_D^2} \quad , \tag{1.4.39}$$

which is the *Debye equation* defining the spectrum of dielectric permittivity. The *static permittivity*, ε_s, which is the value of permittivity at zero frequency, is the term

$$\varepsilon_s = \frac{N\mu_e^2}{3\varepsilon_0 k_B T} \tag{1.4.40}$$

The Debye equation describes what is sometimes called, anomalous dispersion, based on the concept of *normal diffusion*. Figure (1.5 a) shows a plot of the frequency response of the susceptibility Eq. (1.4.35). The response of permittivity is identical with the response of permeability and the response of magnetic susceptibility, which are defined below. At low frequencies the dipole moments can respond to the applied alternating field so that polarisation is almost completely in phase with this field. Therefore the real part of susceptibility is large and the imaginary is practically zero. However as the frequency increases the polarisation increasingly lags **E** which means that the real part decreases and the imaginary part increases and a point is reached when the imaginary component is a maximum. At higher frequencies, the system cannot respond to the applied alternating field and both real and imaginary susceptibility components decrease to zero. This type of response is characterized as a Debye type response and can accurately describe the behaviour of the system at low frequencies. Equation (1.4.39) was derived by ignoring inertial effects. It is important to notice that Debye theory, without accounting for inertia, is invalid for high frequencies (short observation times). It takes time τ_D for the dipoles to reach equilibrium. It is obvious that if the alternating field is changing in a time smaller than τ_D, the dipoles cannot follow the change. In the limit $\omega >> 1/\tau_D$ (or $\omega \to \infty$) the real and the imaginary parts of the permittivity, Eq. (1.4.39), become zero. This is not totally correct. Since this model works only for low frequencies it ignores other effects which appear in the high frequency region, where the susceptibility may not be zero. A reliable modification of the expression for the susceptibility would take into account its value at the high frequency limit. If we denote this value by χ_∞, then as $\omega \to \infty$, $\chi_e(\omega)$ may be written as [19],

$$\chi_e(\omega) = \chi_e'(\omega) - i\chi_e''(\omega) = (\chi_0^e - \chi_\infty^e)\frac{1 - i\omega\tau_D}{1 + \omega^2\tau_D^2} + \chi_\infty^e \tag{1.4.41}$$

where the static susceptibility equals

$$\chi_0^e = \frac{N\mu_e^2}{3\varepsilon_0 k_B T} \tag{1.4.42}$$

With this modification for $\omega \to 0$, Eq. (1.4.41) predicts $\chi_e(0) = \chi_s^e$ and for $\omega \to \infty$ gives $\chi_e(\infty) = \chi_\infty^e$ (see Fig. (1.5 b)). Since $\chi_\infty^e = \varepsilon_\infty - 1$ the dielectric relative permittivity will take equivalently the form of,

$$\varepsilon(\omega) = \varepsilon'(\omega) - i\varepsilon''(\omega) = (\varepsilon_s - \varepsilon_\infty)\frac{1 - i\omega\tau_D}{1 + \omega^2\tau_D^2} + \varepsilon_\infty = \frac{(\varepsilon_s - \varepsilon_\infty)}{1 + (i\omega\tau_D)} + \varepsilon_\infty$$

$$\varepsilon'(\omega) = \frac{(\varepsilon_s - \varepsilon_\infty)}{1 + \omega^2\tau_D^2} + \varepsilon_\infty, \qquad \varepsilon''(\omega) = \frac{\omega\tau_D(\varepsilon_s - \varepsilon_\infty)}{1 + \omega^2\tau_D^2} \tag{1.4.43}$$

The same theory may be applied to magnetic liquids, by changing the electric terms to magnetic terms. The assumption has to be made that the magnetic particle behaves as a rigid body particle; this means that only relaxation due to Brownian motion is considered, so that the Néel relaxation is blocked. By application of an alternating magnetic field,

$$\mathbf{h}_a(t) = \mathbf{H}_0 e^{i\omega t} \tag{1.4.44}$$

the magnetization will, in accordance with Eq. (1.4.33), be

$$M(\omega) = M'(\omega) - iM''(\omega) = N\mu_m\langle\cos\vartheta\rangle = \frac{N\mu_m^2}{3k_BT}\frac{1 - i\omega\tau_B}{1 + \omega^2\tau_B^2}H_0 e^{i\omega t} \ . \tag{1.4.45}$$

Here we have changed the symbol of Debye time τ_D, defined in Eq. (1.4.25), to τ_B the *Brownian relaxation time*, thus,

$$\tau_B = \frac{\zeta}{2k_BT} = \frac{4\pi\eta_h r_p^3}{k_BT} = \frac{3\eta_h v_p}{k_BT} \tag{1.4.46}$$

The equivalent of the electric susceptibility in magnetism is the *complex magnetic susceptibility* which according to Eq. (1.4.41) will be written as,

$$\chi(\omega) = \chi'(\omega) - i\chi''(\omega) = \frac{(\chi_0 - \chi_\infty)}{1 + i\omega\tau_B} + \chi_\infty$$

$$\chi'(\omega) = \frac{(\chi_0 - \chi_\infty)}{1 + \omega^2\tau_B^2} + \chi_\infty, \qquad \chi''(\omega) = \frac{(\chi_0 - \chi_\infty)\omega\tau_B}{1 + \omega^2\tau_B^2} \tag{1.4.47}$$

with its static value, χ_0, equal to,

$$\chi_0 = \frac{N\mu_m^2}{3\mu_0 k_BT} \ . \tag{1.4.48}$$

The equivalent of the complex permittivity is the *complex permeability*, $\mu(\omega)$, given by

$$\mu(\omega) = \mu'(\omega) - i\mu''(\omega) = (\mu_s - \mu_\infty)\frac{1 - i\omega\tau_B}{1 + \omega^2\tau_B^2} + \mu_\infty = \frac{(\mu_s - \mu_\infty)}{1 + (i\omega\tau_B)} + \mu_\infty$$

$$\mu'(\omega) = \frac{(\mu_s - \mu_\infty)}{1 + \omega^2\tau_B^2} + \mu_\infty, \qquad \mu''(\omega) = \frac{\omega\tau_B(\mu_s - \mu_\infty)}{1 + \omega^2\tau_B^2} \tag{1.4.49}$$

with its static value, μ_s, equal to

Figure 1.5

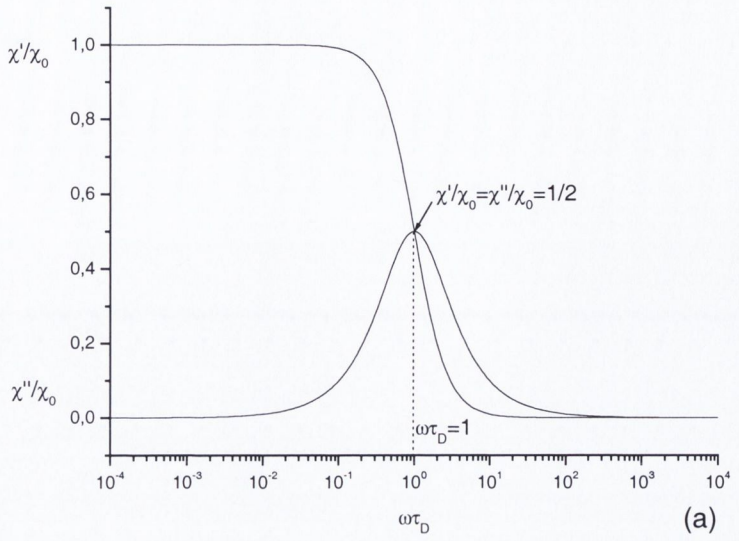

Figure 1.5 (a) Debye type profile of the complex susceptibility showing the real and imaginary components as a function of the frequency ω. Permittivity and permeability have identical susceptibility frequency responses. This plot presents the Debye equation (1.4.47) for magnetic susceptibility with $\chi_\infty = 0$ for mono-disperse case.

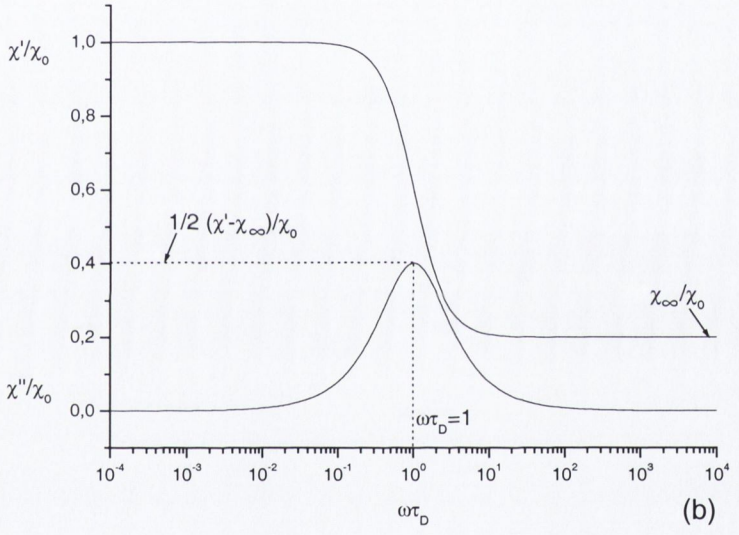

Figure 1.5 (b) Plot of Debye equation (1.4.47) with $\chi_\infty / \chi_0 = 0.2$, for mono-disperse case. χ_∞ gives a correction for the high frequency limit where Debye theory breaks down.

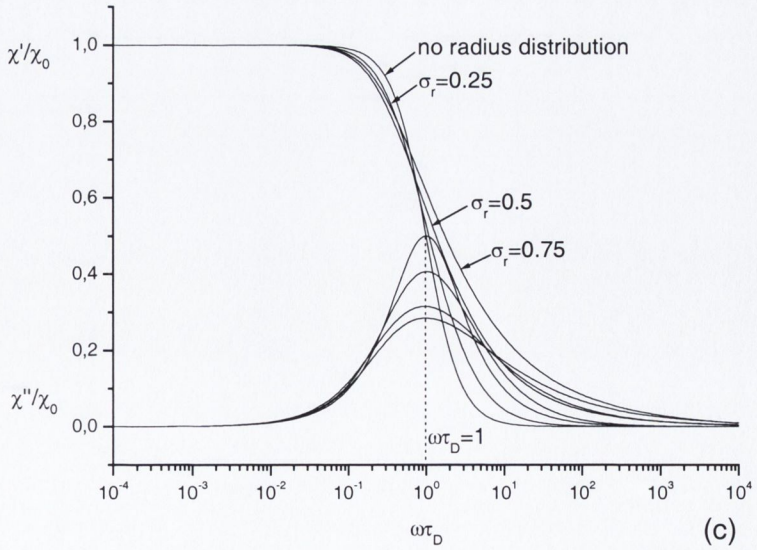

Figure 1.5 (c) Shows the effect of the normal distribution of the radius r_p : by increasing standard deviation, σ_r, the real component inclines from the vertical position and the peak of the imaginary gradually falls with the curve becoming broader.

(Continued).

Figure 1.5

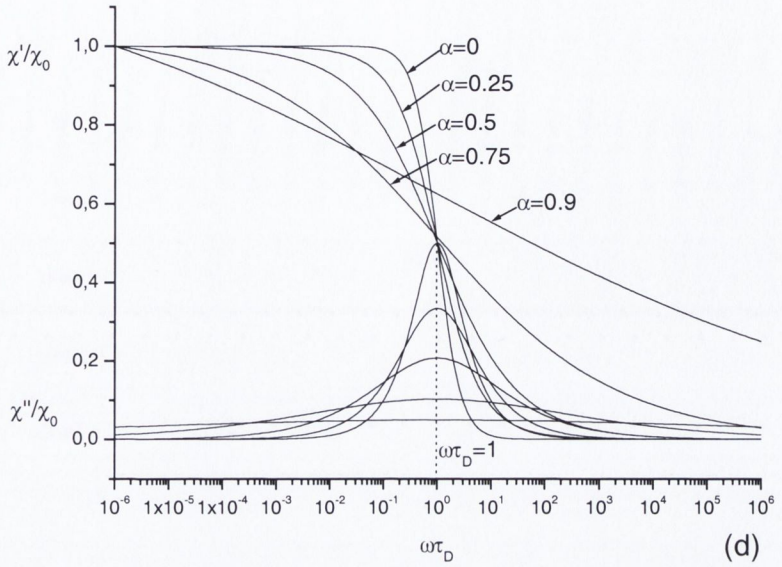

Figure 1.5 (d) Shows the effect of Cole-Cole parameter α. By increasing α, the curve becomes broader, similarly to the (c) case.

$$\mu_s = \frac{N\mu_m^2}{3\mu_0 k_B T} + 1 \ . \qquad (1.4.50)$$

The above theory is valid only for the mono-disperse case. As mentioned in the previous paragraph, magnetic nanoparticles are of several sizes. A distribution, such as normal, log-normal, Nakagami, Cole or Fröhlich, including all possible radii values, r_m, is necessary to be applied with a particular standard deviation σ_r. All distributions give the same effect: by increasing σ_r, the Debye curve become broader with the real component of the susceptibility (or equivalently permittivity, permeability) inclined from the vertical and the magnitude of the imaginary decreased (Fig. (1.5 c)). It is clear that not all radii contribute equally to the susceptibility since the largest number of particles, which are concentrated around the mean $\langle r_p \rangle$, has a greater effect on the value of susceptibility. In order to apply a distribution $P(r_p)$ to the susceptibility it is necessary to calculate the susceptibility of the number of particles $P(r_p)$ corresponding to r_p and then to sum all the susceptibilities over all the range of radii and to average over the total number of particles. Since the system contains an extremely large number of particles, the solution is to integrate over r_p. Thus the susceptibility is given by

$$\chi(\omega) = \frac{\int_{r_{min}}^{r_{max}} \chi(\omega, r_p) P(r_p) dr_p}{\int_{r_{min}}^{r_{max}} P(r_p) dr_p} \qquad (1.4.51)$$

with r_{min}, r_{max} denoting the minimum and maximum possible values of particle radius. For ferromagnetic particles the typical minimum would be 1 nm and the maximum 10 nm.

Cole and Cole [20] modified the Debye equation to take account of the particle size distribution by introducing the parameter α ($0 \le \alpha < 1$), by means of the equation

$$\chi(\omega) = \chi'(\omega) - i\chi''(\omega) = \frac{(\chi_0 - \chi_\infty)}{1 + (i\omega\tau_D)^{1-\alpha}} + \chi_\infty \quad . \qquad (1.4.52)$$

They were concerned with the dielectric case and the equation they modified was Eq. (1.4.43). It is possible to regard the parameter α as a measure of a distribution of relaxation times (Fig. 1.5 d). We may now separate the real and the imaginary parts of Eq. (1.4.52) by using the fact that $i^{1-\alpha} = e^{i\psi} = \cos\psi + i\sin\psi$, $\psi = \frac{\pi}{2}(1-\alpha)$ hence

$$\chi(\omega) = \frac{(\chi_0 - \chi_\infty)}{1 + \cos\psi(\omega\tau_D)^{1-\alpha} + i\sin\psi(\omega\tau_D)^{1-\alpha}} + \chi_\infty =$$

$$= \frac{(\chi_0 - \chi_\infty)}{\left(1 + (\omega\tau_D)^{1-\alpha}\cos\psi\right)^2 + \left((\omega\tau_D)^{1-\alpha}\sin\psi\right)^2} + \chi_\infty - \frac{i(\chi_0 - \chi_\infty)(\omega\tau_B)^{1-\alpha}\sin\psi}{\left(1 + (\omega\tau_D)^{1-\alpha}\cos\psi\right)^2 + \left((\omega\tau_D)^{1-\alpha}\sin\psi\right)^2} \qquad (1.4.53)$$

It is possible to derive the empirical Cole-Cole equation (1.4.52) from an *anomalous diffusion* mechanism describing *anomalous relaxation* [21-24] based on the concept of a continuous time random walk, which in the case of rotation about a fixed axis (one degree of freedom), is described by the diffusion equation [21-24],

$$\frac{\partial W(\phi,t)}{\partial t} = \frac{1}{\tau_D^{-\alpha}} \, {}_0D_t^{1-\alpha}\left(\frac{\partial^2 W(\phi,t)}{\partial\phi^2} + \frac{1}{k_B T}\frac{\partial}{\partial\phi}\left(W(\phi,t)\frac{\partial V(\phi,t)}{\partial\phi}\right)\right) \qquad (1.4.54)$$

where $\tau_D = \frac{\zeta}{k_B T}$, in contrast to τ_D given in Eq. (1.4.25) for rotation in space, and ${}_0D_t^{1-\alpha}$ is defined as ${}_0D_t^{1-\alpha} = \frac{\partial}{\partial t}\,{}_0D_t^{-\alpha}$ with ${}_0D_t^{-\alpha}(W(\phi,t)) = \frac{1}{\Gamma(\alpha)}\int_0^t \frac{W(\phi,t')dt'}{(t-t')^{1-\alpha}}$ being an operator called the Riemann-Liouville fractional derivative [25]. This operator indicates that the system possesses a slowly decaying memory meaning that the process depends on the

history of the system. Equation (1.4.54) constitutes the extension of the classical theory of the Brownian motion, excluding inertial effects, to Cole-Cole behaviour. For $\alpha=1$, Eq. (1.4.54) reduces to the Smoluchowski equation. For the potential $V(\phi) = -\mu_m H_0 e^{i\omega t}\cos\phi$ and the corresponding after effect solution

$$\left\langle \boldsymbol{\mu}_m \cdot \hat{\mathbf{h}} \right\rangle = \frac{\mu_m^2 H_0}{2k_B T} \exp(-\frac{2k_B T}{\zeta} t), \qquad \hat{\mathbf{h}} = \mathbf{H}_s / H_0, \quad t > 0, \tag{1.4.55}$$

equation (1.4.54) yields [22],

$$\left\langle \boldsymbol{\mu}_m \cdot \hat{\mathbf{h}} \right\rangle = \frac{\mu_m^2 H_0}{2k_B T} \frac{e^{i\omega t}}{1+(i\omega\tau_D)^{1-\alpha}} \tag{1.4.56}$$

and

$$\chi(\omega) = \frac{\mu_m^2 N}{2k_B T} \frac{1}{1+(i\omega\tau_D)^{1-\alpha}} \quad . \tag{1.4.57}$$

Similarly, by writing down the equivalent of Eq. (1.4.54) for rotation in space we can prove Eq. (1.4.53) [22]. Titov et al [24] derived a theory for anomalous diffusion including inertial effects.

Several other empirical expressions have been proposed to describe anomalous relaxation, the best known are the Cole-Davidson equation [26-28]

$$\chi(\omega) = \frac{\chi_0 - \chi_\infty}{(1+i\omega\tau_D)^\beta} + \chi_\infty \qquad 0 < \beta \le 1 \tag{1.4.58}$$

and the Havriliak-Negami equation, which is a combination of the Cole-Cole and the Cole-Davidson mechanisms

$$\chi(\omega) = \frac{\chi_0 - \chi_\infty}{\left[1+(i\omega\tau_D)^\alpha\right]^\beta} + \chi_\infty \quad . \tag{1.4.59}$$

1.5 Theory of Néel relaxation and resonance.

Since a ferroparticle has a magnetic moment, $\boldsymbol{\mu}_m$, as described in section 1.3, it is possible for the moment to rotate independently, hence the particle cannot be considered as a rigid body. In section 1.4, where we studied the Debye relaxation, we considered the magnetic vector $\boldsymbol{\mu}_m$ of the magnetic core to be blocked (particle was rotating as one body). The independent internal rotation of $\boldsymbol{\mu}_m$ gives rise to another relaxation effect, called Néel relaxation. The total relaxation is the result of both, Brownian and Néel relaxation. Néel [13] first mentioned this effect for solid state ferromagnets. Brown [14]

set Néel's theory for single domain ferromagnetic particles in the context of the classical theory of the Brownian motion.

The starting point of Brown's treatment of the dynamical behaviour of $\mathbf{M}_s = \boldsymbol{\mu}_m / v_m$ is Gilbert's equation (without thermal agitation) [14, 30]*

$$\frac{\partial \mathbf{M}_s}{\partial t} = \gamma \mathbf{M}_s \times \left(-\partial_M U - \eta \frac{\partial \mathbf{M}_s}{\partial t} \right) \tag{1.5.1}$$

where γ is the ratio of magnetic moment to angular momentum (gyromagnetic ratio), η is a phenomenological damping constant, U is the anisotropy potential magnetic energy density (for example the uniaxial anisotropy energy U_A^u) and ∂_M is the differential vector operator with respect to the coordinates of $\mathbf{M}_s$, with

$$\partial_M = \frac{\partial}{\partial M_x}\hat{\mathbf{x}} + \frac{\partial}{\partial M_y}\hat{\mathbf{y}} + \frac{\partial}{\partial M_z}\hat{\mathbf{z}} \tag{1.5.2}$$

meaning the derivative with respect to the direction of $\mathbf{M}_s$. Equation (1.5.1) has the form of a gyromagnetic equation with the terms in the brackets representing an effective field. The term $\mathbf{H}_{cons} = -\partial_M U$ represents the conservative part and $-\eta \dot{\mathbf{M}}_s$ the dissipative part of the effective field. Brown considered that, in the presence of thermal agitation, the dissipative field $-\eta \dot{\mathbf{M}}_s$ describes only the statistical average of the rapidly fluctuating random forces due to thermal agitation and for an individual particle this term should be,

$$-\eta \dot{\mathbf{M}}_s - \mathbf{h}(t) \tag{1.5.3}$$

where the *fluctuating field* $\mathbf{h}(t)$ has an average value (with respect to the time) equal to zero,

$$\overline{\mathbf{h}(t)} = 0 \tag{1.5.4}$$

and an *autocorrelation function*

$$\overline{h_i(t_1) h_j(t_2)} = \langle h_i(t_1) h_j(t_2) \rangle = \frac{2 k_B T \eta}{v_m} \delta_{ij} \delta(t_1 - t_2) \tag{1.5.5}$$

where $i,j=1,2,3 \equiv x,y,z$, δ_{ij} is the Kronecker's delta and $\delta(t_1 - t_2)$ is Dirac delta function. The overbars in Eqs. (1.5.4), (1.5.5) denotes the statistical average over time. According to statistical physics [18], this time average is equal to the ensemble average.

Brown finally derived, from the above equation of motion, the Fokker-Planck equation for the density of magnetic moment orientations $W(\vartheta, \phi, t)$ finding an

* If an external field $\mathbf{H}_s$ is applied, then this field has to be added to the terms in the bracket.

asymptotic solution for the smallest non vanishing eigenvalue in the limit of very high and very low potential barriers. By using Einstein's argument, as described in section 1.4, it is possible to derive this Fokker-Planck equation from Eq. (1.5.1). Equation (1.5.1) may be written as [16]

$$\dot{\mathbf{M}}_s = \frac{\gamma}{(1+\alpha_d^2)}(\mathbf{M}_s \times \mathbf{H}_{cons}) + \frac{\alpha_d \gamma}{(1+\alpha_d^2)M_s}(\mathbf{M}_s \times \mathbf{H}_{cons}) \times \mathbf{M}_s \qquad (1.5.6)$$

where the dimensionless damping parameter α_d (defined as $\alpha_d = \eta\gamma M_s$) takes values between 0.01 and 0.1 for ferromagnets [31, 32]. Usually it is preferable to write the above equation in a further compact format by using the unit vector $\hat{\mathbf{m}} = \boldsymbol{\mu}_m / \mu_m = \mathbf{M}_s / M_s$ and $g' = \frac{\gamma}{(1+\alpha_d^2)M_s}$, $h' = \frac{\alpha_d \gamma}{(1+\alpha_d^2)M_s} = \alpha_d g'$ (rotary mobility factor). We further write $\mathbf{H}_{cons} = -\partial_M U = -\frac{\partial_{\hat{m}} U}{M_s} = -\frac{\nabla U}{M_s}$ where the operator ∇ is referred to the polar coordinates (its components are $\frac{\partial}{\partial\vartheta}$, $\frac{1}{\sin^2\vartheta}\frac{\partial}{\partial\phi}$). Thus Eq. (1.5.6) is written as

$$\dot{\hat{\mathbf{m}}} = -g' M_s (\hat{\mathbf{m}} \times \nabla U) + h' \hat{\mathbf{m}} \times (\hat{\mathbf{m}} \times \nabla U) \qquad (1.5.7)$$

The rotary mobility factor h', has dimensions of the inverse of the viscosity. Since $\alpha_d << 1$, for ferromagnets, Eq. (1.5.6) is reduced to *Landau-Lifshitz equation* [5]

$$\dot{\mathbf{M}}_s = \gamma(\mathbf{M}_s \times \mathbf{H}_{cons}) + \frac{\alpha_d \gamma}{M_s}(\mathbf{M}_s \times \mathbf{H}_{cons}) \times \mathbf{M}_s \qquad (1.5.8)$$

which is the first proposed equation for the movement of $\boldsymbol{\mu}_m$. In the Landau-Lifshitz equation the first term is the precessional component and the second is the damping component.

The drift current will be given, in polar coordinates, from the expression [16]

$$\mathbf{J}_d(\vartheta,\phi) = W(\vartheta,\phi)\dot{\hat{\mathbf{m}}} \qquad (1.5.9)$$

equivalent to Eq. (1.4.6). To this we add the diffusive current,

$$\mathbf{J}_{diff}(\vartheta,\phi) = -D'\nabla W(\vartheta,\phi) \qquad (1.5.10)$$

which represents the effect of thermal agitation. Accordingly by using Eq. (1.5.7), we have the Fokker-Planck equation [16]

$$\frac{\partial W}{\partial t} = \frac{1}{\sin\vartheta}\frac{\partial}{\partial\vartheta}\left\{\sin\vartheta\left[\left(h'\frac{\partial U}{\partial\vartheta} - \frac{g'}{\sin\vartheta}\frac{\partial U}{\partial\phi}\right)W + D'\frac{\partial W}{\partial\vartheta}\right]\right\} +$$

$$+\frac{1}{\sin\vartheta}\frac{\partial}{\partial\phi}\left[\left(g'\frac{\partial U}{\partial\vartheta}+\frac{h'}{\sin\vartheta}\frac{\partial U}{\partial\phi}\right)W+\frac{D'}{\sin\vartheta}\frac{\partial W}{\partial\phi}\right] \tag{1.5.11}$$

which may be more easily read in the compact vector form, as

$$\frac{\partial W}{\partial t}=g'\hat{\mathbf{m}}(\nabla U\times\nabla W)+h'\nabla\cdot(W\nabla U)+D'\nabla^2 W\ . \tag{1.5.12}$$

The latter equation is called Brown's equation. The term multiplied by g' is the precessional (gyromagnetic) term, it gives rise to *ferromagnetic resonance*, usually in the GHz range for ferromagnets; the term with h' is the alignment term (relaxational) predicting a decay of the precession motion of $\boldsymbol{\mu}_m$ about the effective field with time constant

$$\tau_0=\frac{1}{\alpha_d\omega_{pre}} \tag{1.5.13}$$

where ω_{pre} is the angular frequency of free precession without damping. The effective field doesn't directly cause alignment, but rather it causes a precession of $\boldsymbol{\mu}_m$ about the axis of the field, which along with damping (rising from collisions of the electron spin moments $\boldsymbol{\mu}_s$), produce alignment. The number of the rotations of $\boldsymbol{\mu}_m$ during the relaxation process is $1/\alpha_d$. The angle between $\boldsymbol{\mu}_m$ and the field direction decays exponentially with time constant τ_0 according to the equation,

$$\vartheta(t)=\vartheta_0\exp(-\frac{t}{\tau_0}) \tag{1.5.14}$$

The diffusion coefficient D' is evaluated by requiring that the Maxwell-Boltzmann distribution of orientations should be the stationary (equilibrium) solution of Eq. (1.5.11), so that

$$W_0(\vartheta,\phi)=A\exp(-\frac{V(\vartheta,\phi)}{k_BT}) \tag{1.5.15}$$

with $V(\vartheta,\phi)=U(\vartheta,\phi)v_m$, the internal potential magnetic energy. The imposition of the Maxwell-Boltzmann equilibrium distribution of orientations yields

$$D'=\frac{\eta k_BT}{v_m\left(\frac{1}{\gamma^2}+\eta^2M_s^2\right)}=\frac{\alpha_d\gamma k_BT}{(1+\alpha_d^2)M_s v_m}=\frac{h'k_BT}{v_m}\ . \tag{1.5.16}$$

This is Einstein's formula giving the diffusion coefficient of internal rotation as the mobility factor times the thermal energy per volume, which states the greater the thermal

energy the greater the thermal diffusion. For very low potential barriers, $\sigma << 1$, $\boldsymbol{\mu}_m$ will freely rotate with internal diffusion time

$$\tau_D' = \frac{1}{2D'} = \frac{(1+\alpha_d^2)M_s v_m}{2\alpha_d \gamma k_B T} = \frac{v_m}{2h' k_B T} \quad . \tag{1.5.17}$$

(not to be confused with Debye time τ_D). In both the limits of low ($\alpha_d \to 0$) and of high ($\alpha_d \to \infty$) damping, the internal diffusion time approaches infinity and alignment of $\boldsymbol{\mu}_m$ with the field cannot take place. This is due, for low damping, to infinitely persisting undamped precessional motion and in the case of high damping to the absence of all motion because the mobility of $\boldsymbol{\mu}_m$ is zero. The minimum in τ_D' occurs when $\alpha_d = 1$. In comparison with the Brownian time Eq. (1.4.46), we define the equivalent to viscosity, which is called magnetic viscosity, as

$$\eta_m = \frac{(1+\alpha_d^2)M_s}{6\alpha_d \gamma} = \frac{1}{6h'} \quad . \tag{1.5.18}$$

The nature of this equivalent viscosity is strictly related to the nature of the rotational movement described by the damping parameter (showing how fast $\boldsymbol{\mu}_m$ decays) and the angular momentum (how fast $\boldsymbol{\mu}_m$ rotates).

The probability of $\boldsymbol{\mu}_m$ reversing direction is proportional to exp(σ), where $\sigma = Kv_m / k_B T$. Therefore if the anisotropy barrier is not too large compared with the thermal energy $k_B T$, it is possible for thermal fluctuations to cause the magnetic moment to reverse direction within the particle, (i.e. Néel relaxation). The movement of $\boldsymbol{\mu}_m$ is barely affected by the existence of the potential barrier and the Néel relaxation time is approximately the same as the internal diffusion time τ_D'. However for large σ there is an exponential dependence of Néel time on σ. The relaxation time proposed by Néel is [13]

$$\tau_N = \tau_0 \exp(\sigma) \tag{1.5.19}$$

where τ_0 is the precessional time (called Néel prefactor) and here equals τ_D'. The inverse of τ_N is the average frequency of the switching or flipping of $\boldsymbol{\mu}_m$. From Eq. (1.5.19) it is apparent that for small particles ($\sigma \to 0$) the Néel relaxation time reduces to $\tau_N = \tau_0 = \tau_D'$. For large particles in which $\sigma \to \infty$, the time constant tends to infinity (few years to millions of years). Magnetic tapes and disks which consist of particles on a solid matrix (mechanical Brownian motion is eliminated) consist of relatively large

particles, having large σ, ensuring the absence of Néel relaxation and providing a stable memory of any data written onto them.

Equation (1.5.19) is only a first approximation. Brown [14] criticised Néel's calculation since it relies on a discrete orientation approximation. Néel's theory considers only a single jump from one energy minimum to another without accounting for the time spent by the magnetisation vector in between these energy minima. Brown realised that in the limit $\sigma \to 0$, the Néel time of precession, τ_0, should become equal to τ_D'. He found approximate solutions for the relaxation time for simple uniaxial anisotropy in the limit of high and low potential barriers, so that,

$$\tau_N = \tau_D'(1 + 2\sigma/5) \qquad \text{for } \sigma << 1 \qquad (1.5.20a)$$

and

$$\tau_N = \tau_D' \frac{\sqrt{\pi}}{2\sigma^{3/2}} \exp(\sigma) \qquad \text{for } \sigma > 2 \qquad (1.5.20b)$$

The two equations of Brown are valid only for low and high barriers. They cannot be used for the intermediate values $1 < \sigma < 2$.

Based on the effective eigenvalue technique Coffey et al [33] arrived at the following equation for all values of σ, with

$$\tau_N = \frac{2\tau_D'(\sqrt{\sigma} - D(\sqrt{\sigma})}{D(\sqrt{\sigma})(1 + 2\sigma) - \sqrt{\sigma}} \qquad (1.5.21)$$

where D(x) represents Dawson's integral defined as

$$D(x) = e^{-x^2} \int_0^x e^{t^2} dt \ .$$

An exact (but very lengthy) formula was derived by Coffey et al [34], valid for all values of σ, but it involves calculations of considerable complexity and in view of this fact Eq. (1.5.21) will be used for this work. Yet another useful approximate analytic formula which is valid for all values of σ has been proposed in [35], with

$$\tau_N = \frac{\tau_D'(e^\sigma - 1)}{2\sigma} \left(\frac{1}{1 + 1/\sigma} \sqrt{\frac{\sigma}{\pi}} + 2^{-\sigma - 1} \right)^{-1} . \qquad (1.5.22)$$

So far we have not considered the effect of an externally applied field. Let us consider a constant external field $\mathbf{H}_s$ superimposed on the effective field. Usually the external field, $\mathbf{H}_s$, is comparable to the effective field, $\mathbf{H}_A$. It is easier if Brownian motion (and relaxation) is neglected and only the Néel mechanism operates. Due to

anisotropy, the internal relaxation will depend on the direction of the applied field relative to the direction of the easy axis. When the field is applied parallel to the easy axis there is a tendency for $\boldsymbol{\mu}_m$ to align with the field. When the field is removed the magnetic moment attains thermal equilibrium by jumping over the anisotropy barrier and the magnetisation (called longitudinal) $M_{\parallel}$ tends to zero with time constant τ_N, where

$$M_{\parallel}(t) = M_{\parallel}^0 \exp(-t/t_{\parallel}) = M_{\parallel}^0 \exp(-t/t_N) \tag{1.5.23}$$

(similar expression to Eq. (1.5.14)) therefore τ_N describes the parallel time constant $\tau_{\parallel}$. However when a field $\mathbf{H}_s$ is applied perpendicular to the easy axis the magnetic moment $\boldsymbol{\mu}_m$ deviates in order to respond to the field. The transverse magnetisation $M_{\perp}$ decays with a different time constant when the field is suddenly removed

$$M_{\perp}(t) = M_{\perp}^0 \exp(-t/t_{\perp}) \tag{1.5.24}$$

This transverse time constant is given by Coffey et al [33] by

$$\tau_{\perp} = 2\tau_D' \left[\frac{D(\sqrt{\sigma})(2\sigma+1) - \sqrt{\sigma}}{D(\sqrt{\sigma})(2\sigma-1) + \sqrt{\sigma}} \right] \tag{1.5.25}$$

There is a decrease of $\tau_{\perp}$ with increasing σ. For $\sigma \to 0$, as one would expect, $\tau_{\perp} \to \tau_D'$ and for $\sigma \to \infty$, $\tau_{\perp} \to \tau_D'/\sigma$. The behaviour is opposite to that of $\tau_{\parallel}$ or τ_N which increases exponentially with increasing σ.

So far, we have studied the effect of Brownian (Debye), and Néel, relaxation times separately. In ferroparticles these two effects are combined in one relaxation process. The effective relaxation time will be a function of both. Shliomis [36] estimated that this effective time should be

$$\tau_{eff} = \frac{\tau_N \tau_B}{\tau_N + \tau_B} \tag{1.5.26}$$

The relaxation time which dominates is the smaller one. When one of the relaxation times acquires a large value, compared to the other, the value of τ_{eff} is almost equal to the smaller relaxation time. The Brownian time is a function of the temperature and the hydrodynamic viscosity, while the Néel time is a function of σ and τ_D' which are both related to the temperature, the anisotropy constant and the magnetic volume. When $\sigma < 1$ and since $\eta_m/\eta_h < 10^{-2}$, $\tau_B >> \tau_N \cong \tau_D'$, thus the Néel mechanism dominates. For $\sigma > 10$, $\tau_N >> \tau_B$ so for large particles, relaxation is due to the Brownian mechanism.

The typical value of $\sigma = \sigma_*$ where $\tau_N = \tau_B$ is in the range $5 < \sigma_* < 7$ [36]. In reality a ferrofluid contains a distribution of particle sizes so that some particles may relax or approach thermal equilibrium by the Brownian mechanism and other smaller ones can relax via the Néel mechanism. An observation of the distribution of particle size and relaxation times of a typical ferrofluid is given by Fannin [37] showing that particles having radii greater than 6 nm relax via the Brownian mechanism and those whose radius is less than 6nm via the Néel mechanism. Table (1.1) shows a review of all relaxation times used.

Table 1.1 Summary of relaxation times

Name	Symbol	Equation given	Effect related	Reference
Debye relaxation time	τ_D	$\frac{3\eta_h v_p}{k_B T}$	Brownian relaxation	[11, 12]
Brownian relaxation time	τ_B	$\frac{3\eta_h v_p}{k_B T}$	Brownian relaxation	[11, 12]
Time of precession, or Néel prefactor	τ_0	$\frac{1}{\alpha_d \omega_{pre}}$	Gyromagnetic resonance and Néel relaxation	[13]
Internal diffusion time	τ'_D	$\frac{(1+\alpha_d^2) M_s v_m}{2\alpha_d \gamma k_B T}$	Néel relaxation	[16]
Néel relaxation time	τ_N	$\tau_N = \tau'_D(1+2\sigma/5)$ for $\sigma < 1$ $\tau_N = \tau'_D \frac{\sqrt{\pi}}{2\sigma^{3/2}} \exp(\sigma)$ for $\sigma > 2$ or $\frac{2\tau'_D(\sqrt{\sigma} - D(\sqrt{\sigma})}{D(\sqrt{\sigma})(1+2\sigma) - \sqrt{\sigma}}$ for all σ	Néel relaxation	[14, 33]
Effective relaxation time	τ_{eff}	$\frac{\tau_N \tau_B}{\tau_N + \tau_B}$	Brownian and Néel relaxation	[36]
Parallel time constant	$\tau_{\parallel}$	Same as τ_N	Néel relaxation	[14, 33]
Effective parallel time	$\tau_{\parallel}^{eff}$	Same as τ_{eff}	Brownian and Néel relaxation	[36]
Perpendicular relaxation time	$\tau_{\perp}$	$2\tau'_D \left[\frac{D(\sqrt{\sigma})(2\sigma+1) - \sqrt{\sigma}}{D(\sqrt{\sigma})(2\sigma-1) + \sqrt{\sigma}} \right]$	Ferromagnetic resonance	[33]
Second relaxation time	τ_2	$\frac{\tau'_D}{-\sigma - 2 + \frac{4\sigma(\sqrt{\sigma} - D(\sqrt{\sigma}))}{3\sqrt{\sigma} - (3+2\sigma)D(\sqrt{\sigma})}}$	Ferromagnetic resonance	[33]

In the derivation of the equation (1.3.19) we did not consider the internal anisotropy field. We derive now an expression for the magnetisation with the internal field, $\mathbf{H}_A$, taken into account. Let $\hat{\mathbf{n}}$ be the unit vector along the axis of the uniaxial anisotropy. The magnetic moments respond differently when an external field, $\mathbf{H}_s$, is applied parallel or perpendicular to $\hat{\mathbf{n}}$, due to the uniaxial anisotropy. It is therefore convenient to study the susceptibility in terms of parallel susceptibility, $\chi_\parallel$, when the field is parallel to $\hat{\mathbf{n}}$, and perpendicular susceptibility, $\chi_\perp$, when the field is perpendicular to $\hat{\mathbf{n}}$, components.

For the first case the parallel magnetisation corresponding to $\chi_\parallel$ will be given as in Eq. (1.3.19) with,

$$M_\parallel(\xi_m) = M_s\langle\cos\theta\rangle \tag{1.5.27}$$

where θ is the angle between the field $\hat{\mathbf{h}}$ and moment $\hat{\mathbf{m}}$ directions (Fig. 1.6). The average value of $\cos\theta$ can be evaluated by integrating over the angular distribution as Eq. (1.3.18) shows, but it is necessary to add to the external static field, $\mathbf{H}_s$, the internal anisotropy field which is, according to Eq. (1.3.10), given as,

$$\mathbf{H}_A = 2K/M_s\hat{\mathbf{n}} = 2Kv_m/\mu_m\hat{\mathbf{n}} \tag{1.5.28}$$

Thus the ratio of the total effective magnetic energy to thermal energy is

$$\xi_m\cos\theta - \sigma\sin^2\theta = \frac{\mu_m H\cos\theta - Kv_m\sin^2\theta}{k_B T} \tag{1.5.29}$$

Thus

$$M_\parallel(\xi_m,\sigma) = M_s\langle\cos\theta\rangle = M_s\langle\hat{\mathbf{m}}\cdot\hat{\mathbf{h}}\rangle = M_s\frac{\int_0^{2\pi}\int_0^{\pi}\cos\theta\exp(\xi_m\cos\theta - \sigma\sin^2\theta)\sin\theta d\theta d\phi}{\int_0^{2\pi}\int_0^{\pi}\exp(\xi_m\cos\theta - \sigma\sin^2\theta)\sin\theta d\theta d\phi} \cong$$

$$\cong M_s\xi_m\left(1 - \frac{2\tanh\sigma}{3\sigma}\right) \tag{1.5.30}$$

It is better to use the approximate value because the above integral has a complicated closed form representation. Therefore the parallel susceptibility is

$$\chi_\parallel(\sigma) = \frac{3\chi_0}{\xi_m}\frac{\int_0^{2\pi}\int_0^{\pi}\cos\theta\exp(\xi_m\cos\theta - \sigma\sin^2\theta)\sin\theta d\theta d\phi}{\int_0^{2\pi}\int_0^{\pi}\exp(\xi_m\cos\theta - \sigma\sin^2\theta)\sin\theta d\theta d\phi} \cong 3\chi_0\left(1 - \frac{2\tanh\sigma}{3\sigma}\right) \tag{1.5.31}$$

where χ_0 is the static susceptibility given by Eq. (1.4.48). For small σ, the parallel susceptibility is reduced to χ_0 whilst for large σ it is $3\chi_0$.

For the second case where the field is perpendicular to $\hat{\mathbf{n}}$ lying on the x axis, see Fig. (1.6), the magnetisation in that direction equals,

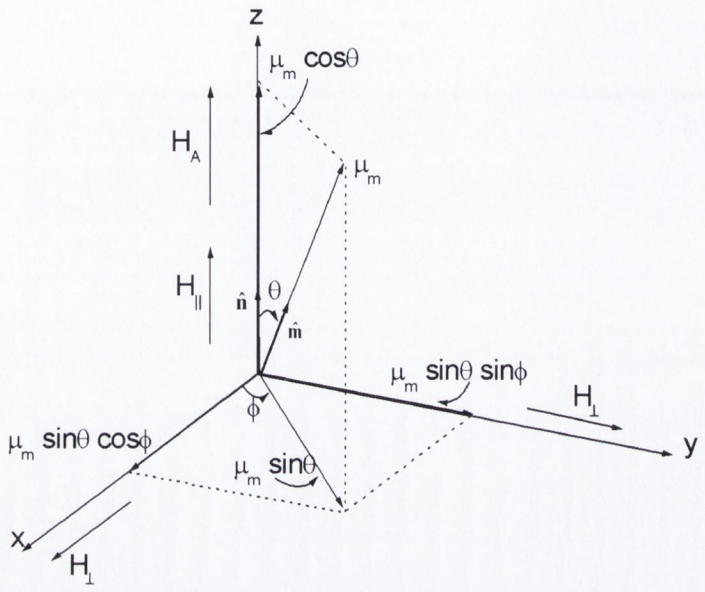

Figure 1.6 The arrangement of the magnetic moment vector and its relation to the field direction. The easy axis is the vertical z axis.

$$M_{\perp}(\xi_m,\sigma) = M_s\langle \sin\theta\cos\phi\rangle = M_s \frac{\int_0^{2\pi}\int_0^{\pi}\sin\theta\cos\phi\exp(\xi_m \sin\theta\cos\theta - \sigma\sin^2\theta)\sin\theta d\theta d\phi}{\int_0^{2\pi}\int_0^{\pi}\exp(\xi_m \sin\theta\cos\theta - \sigma\sin^2\theta)\sin\theta d\theta d\phi} \tag{1.5.32}$$

Closed form solutions are again difficult to obtain, however the above integral can be simplified to a single integral by realising that the internal energy is small compared to the thermal energy so $\xi_m << 1$ hence $\exp(\xi_m \sin\theta\cos\phi) \cong 1 + \xi_m \sin\theta\cos\phi$. Thus, Eq. (1.5.32) becomes

$$M_{\perp}(\xi_m,\sigma) = M_s\langle \sin\theta\cos\phi\rangle = M_s \frac{\int_0^{2\pi}\int_0^{\pi}(\sin^2\theta\cos\phi + \xi_m \sin^3\theta\cos^2\phi)\exp(-\sigma\sin^2\theta)d\theta d\phi}{\int_0^{2\pi}\int_0^{\pi}(\sin^2\theta\cos\phi + \xi_m \sin^3\theta\cos^2\phi)\exp(-\sigma\sin^2\theta)d\theta d\phi} =$$

$$= \frac{M_s}{2} \frac{\int_0^{\pi} \xi_m \sin^3\theta \exp(-\sigma \sin^2\theta) d\theta}{\int_0^{\pi} \sin\theta \exp(-\sigma \sin^2\theta) d\theta} \cong \frac{M_s \xi_m}{3} \frac{\tanh\sigma}{\sigma} \qquad (1.5.33)$$

which corresponds to a susceptibility value

$$\chi_\perp(\sigma) = \frac{3\chi_0}{2\xi_m} \frac{\int_0^{\pi} \xi_m \sin^3\theta \exp(-\sigma \sin^2\theta) d\theta}{\int_0^{\pi} \sin\theta \exp(-\sigma \sin^2\theta) d\theta} \cong \chi_0 \frac{\tanh\sigma}{\sigma} \qquad (1.5.34)$$

For $\sigma \to 0$, the perpendicular susceptibility tends to its static value as is expected since, for almost isotropic particles, the susceptibility is independent of the direction.

Equations (1.5.31) and (1.5.34) for $\chi_\parallel$, $\chi_\perp$ are valid for a static applied field, however in the dynamic case in which an alternating field is applied they will be functions of frequency. If an alternating field is applied in the parallel direction the response of the particles is almost purely relaxational. Debye's equation, which is a function of frequency, as modified to include both relaxation types (τ_D is replaced by $\tau_{eff} = \tau_\parallel^{eff}$), can adequately describe this response. If the alternating field is applied in the perpendicular direction, the response is resonant. Ferromagnetic resonance (or gyromagnetic resonance) [5] occurs when the frequency of the alternating field matches the frequency of precession of $\boldsymbol{\mu}_m$, that is when the atomic magnetic moments precess about an externally applied field with frequency equal to the Larmor frequency ω_L. If the frequency ω of the alternating field is different from ω_{res}, the precessing $\boldsymbol{\mu}_m$ will not seriously be affected since its component in the plane of rotation will pass in and out of phase with the alternating field and there will not be any resultant interaction. However if ω is the same as ω_{res} then moment and field can remain in phase. At this critical point the susceptibility changes sign denoting the change of phase. The value of ω_{res} is associated with the total field $\mathbf{H}_s + \mathbf{H}_A$ and the gyromagnetic ratio, with the relation,

$$\omega_{res} = \frac{d\hat{\mathbf{m}}}{dt} = \gamma \hat{\mathbf{m}} \times (\mathbf{H}_s + \mathbf{H}_A) \qquad (1.5.35)$$

which is the gyromagnetic equation of motion, similar to Eq. (1.5.1) in which $\mathbf{H}_A$ is given as the derivative of anisotropy energy density U in the direction of $\hat{\mathbf{m}}$ (excluding

the dissipative part and thermal agitation but including the external field $\mathbf{H}_s$). The above equation for ω_{res} is simply written for the perpendicular components as

$$\omega_{res} = \gamma(H_s + H_A) \tag{1.5.36}$$

Raikher and Shliomis [7] derived an equation for $\chi_\perp$ basing their analysis on the Landau-Lifshitz equation of motion, Eq (1.5.8), and taking superparamagnetic effects into account but excluding the influence of thermal agitation (it is valid for high σ only). The equation derived for $\chi_\perp$ is called the Landau-Lifshitz equation for dynamic susceptibility and is given by,

$$\chi_\perp(\omega) = \chi_0 \frac{\tanh\sigma}{\sigma} \frac{(1+\alpha_d^2)\omega_{pre}^2 + i\alpha_d\omega\omega_{pre}}{(1+\alpha_d^2)\omega_{pre}^2 - \omega^2 + i2\alpha_d\omega\omega_{pre}} \tag{1.5.37}$$

where $\omega_{pre} = 1/\alpha_d\tau_0$ is the frequency of free precession (Eq. (1.5.13)), so the latter equation may be written in the more suitable form of,

$$\chi_\perp(\omega) = \chi_0 \frac{\tanh\sigma}{\sigma} \frac{1+\alpha_d^2 + i\alpha_d^2\omega\tau_0}{1+\alpha_d^2 - \alpha_d^2\omega^2\tau_0^2 + i2\alpha_d^2\omega\tau_0} \tag{1.5.38}$$

By substituting α_d with $1/\omega_{pre}\tau_0$, the Landau-Lifshitz equation takes the form of,

$$\chi_\perp(\omega) = \chi_0 \frac{\tanh\sigma}{\sigma} \frac{1+\omega_{pre}^2\tau_0^2 + i\omega\tau_0}{1+\omega_{pre}^2\tau_0^2 - \omega^2\tau_0^2 + i2\omega\tau_0} \tag{1.5.39}$$

The latter equation shows that the Landau-Lifshitz equation is a function of two dimensionless parameters. One is $\omega\tau_0$ and is dependent on the frequency and the other is $\omega_{pre}\tau_0$ and is field dependent, because $\omega_{pre} \propto \omega_{res} = \gamma(H_s + H_A)$.

Scaife [38] studied extensively the absorption effects described by the Landau-Lifshitz equation and he proposed the following expression for the precessional decay time,

$$\frac{1}{\tau_0} = \frac{1}{\tau_B} + \frac{1}{2\tau_N} + \alpha_d\omega_{pre} \tag{1.5.40}$$

This precession time involves the time constants of the relaxation, while Eq. (1.5.13) does not. One can split Eq. (1.5.39) into real and imaginary components with,

$$\chi'_\perp(\omega) = \chi_0 \frac{\tanh\sigma}{\sigma} \frac{[1+(\omega_{pre}\tau_0)^2]^2 - \omega^2\tau_0^2(1-(\omega_{pre}\tau_0)^2)}{[1+(\omega_{pre}\tau_0)^2 - (\omega\tau_0)^2]^2 + 4(\omega\tau_0)^2} \tag{1.5.41a}$$

$$\chi''_\perp(\omega) = \chi_0 \frac{\tanh\sigma}{\sigma} \frac{\omega\tau_0[1+(\omega_{pre}\tau_0)^2 + (\omega\tau_0)^2]}{[1+(\omega_{pre}\tau_0)^2 - (\omega\tau_0)^2]^2 + 4(\omega\tau_0)^2} \tag{1.5.41b}$$

Figure 1.7

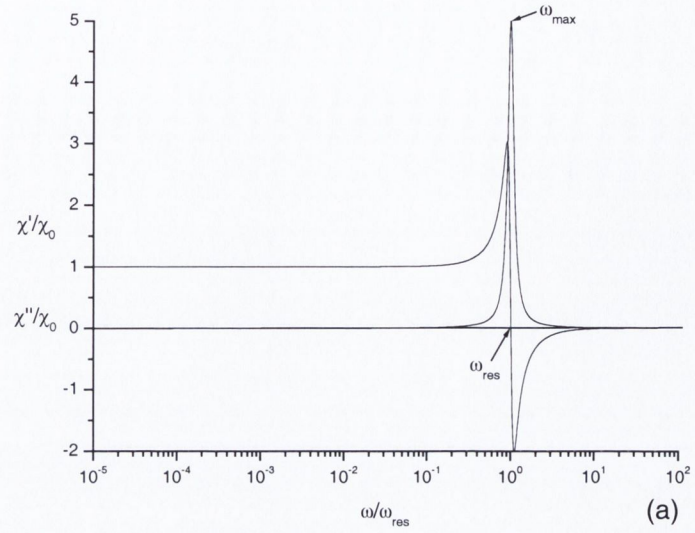

Figure 1.7 (a) Theoretical normalised plot of Landau-Lifshitz equation (1.5.39) without the relaxational (parallel) component. It is indicated the resonance frequency and the frequency where imaginary part has maximum.

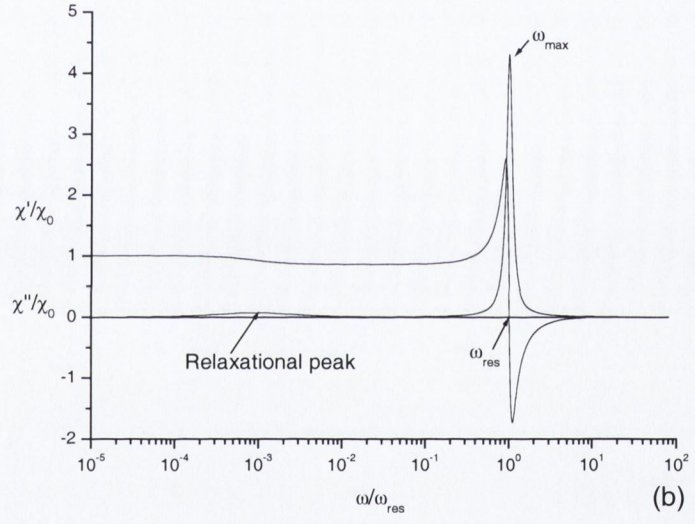

Figure 1.7 (b) The same as (a) but including the relaxational (parallel) part of Eq. (1.5.49). Relaxational behaviour is pronounced on the spectrum with the peak of the imaginary component (energy absorption) of some orders lower compared with the resonance frequency.

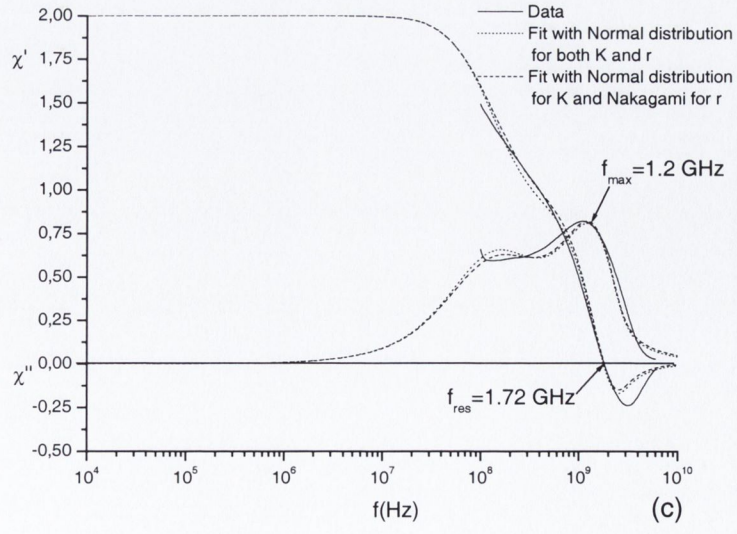

Figure 1.7 (c) Measured susceptibility of magnetite in isoparaffin, 900 G, giving resonance at 1.72GHz and with precessional frequency at 1.2GHz (solid line). Fits have been derived by using the Landau-Lifshitz equation with normal distribution for both radius and K (dotted line) and Nakagami distribution for radius and normal for K (dashed line).

(Continued).

Figure 1.7

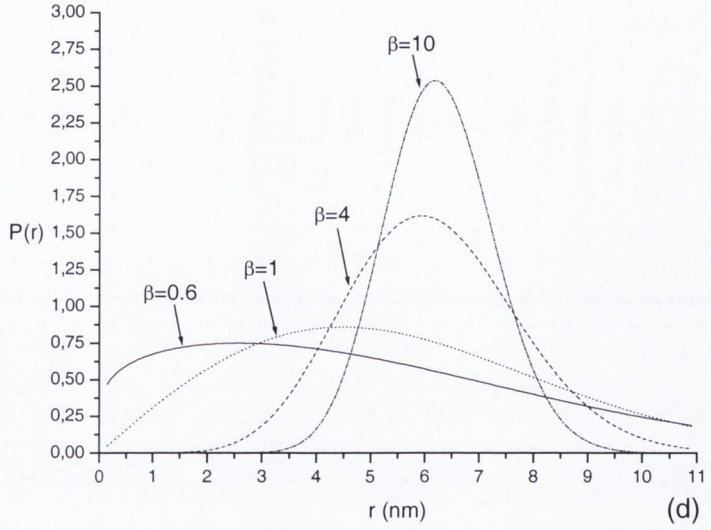

Figure 1.7 (d) Plot of Nakagami distribution for different values of parameter β.

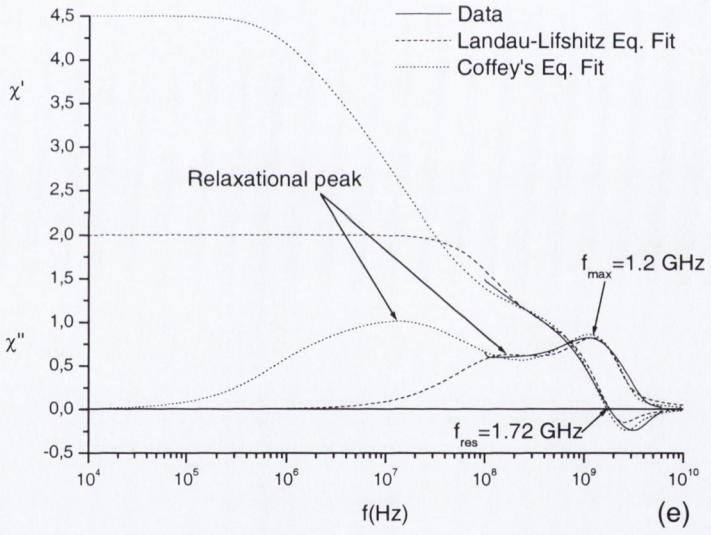

Figure 1.7 (e) Comparison between Landau-Lifshitz equation fit (dashed line) and Coffey's equation fit (1.5.43) appropriately modified to include the parallel susceptibility component as Eq.(1.5.49) states. The data is the same as in (c).

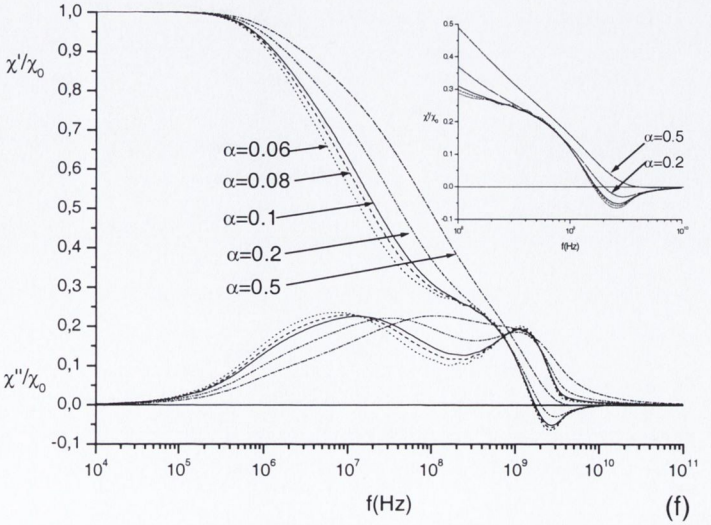

Figure 1.7 (f) Shows how the previous curve, which is the reference (solid line), alters by varying the damping parameter. Inset: the detail of the real component near to the resonance point.

(Continued).

Figure 1.7

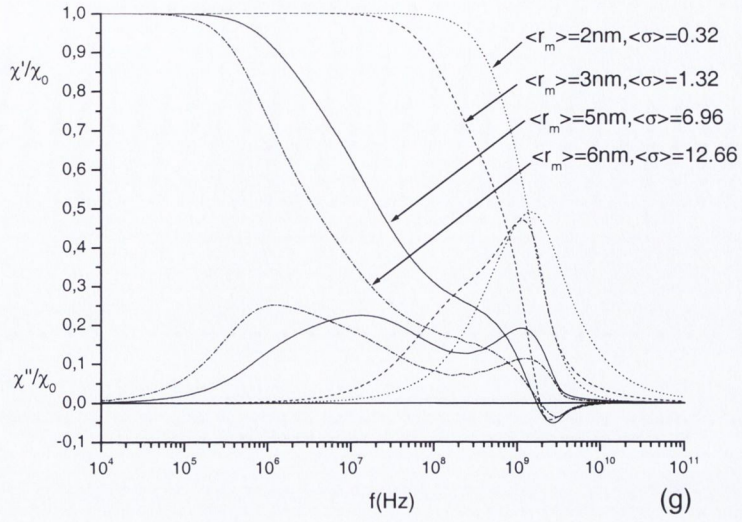

Figure 1.7 (g) Shows the variation of susceptibility curve by changing the mean radius and leaving all other parameters unchanged.

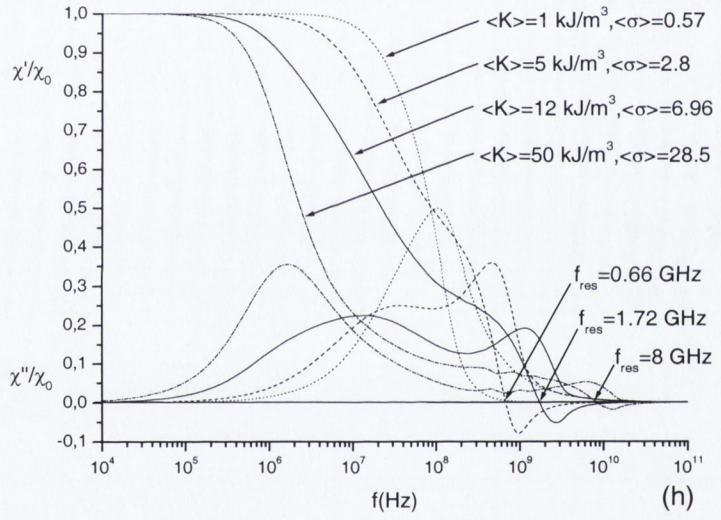

Figure 1.7 (h) Shows the variation of susceptibility by changing K. The resonant frequency is also affected as Eq.(1.5.36) predicts.

For $\omega \to 0$, the Landau-Lifshitz equation reduces to Eq. (1.5.34). It is noticed that $\chi_0 \tanh \sigma / \sigma < \chi_0$, so the magnitude of the resonance component is smaller than the relaxation component. A plot of Eq. (1.5.39) is shown in Fig. (1.7 a). The resonance frequency, ω_{res}, (where χ' reaches zero) and the frequency ω_{max} of absorption (where χ'' becomes a maximum) are clearly indicated. The Landau-Lifshitz equation gives the following value for the resonance frequency

$$\omega_{res} = \frac{1+\alpha_d^2}{\sqrt{1-\alpha_d^2}} \alpha_d \omega_{pre} = \gamma(H_s + H_A) \qquad (1.5.42)$$

calculated by separating real and imaginary parts and observing where the real component changes sign (change of phase). It is required that $\alpha_d < 1$ for resonance to

occur. Since α_d is very small, the precessional frequency is $1/\alpha_d$ times the resonant frequency. If $\alpha_d \to 1$ (no damping) $\omega_{pre} \equiv \omega_{res}$. Coffey et al [33] derived an equation for $\chi_\perp(\omega)$ based on the analysis of Gilbert's equation (1.5.1) which includes the thermal agitation effects (for all values of σ)

$$\chi_\perp(\omega) = \chi_0 \frac{\tanh\sigma}{\sigma} \frac{1 + i\omega\tau_2 + \Delta}{(1 + i\omega\tau_2)(1 + i\omega\tau_\perp) + \Delta} \tag{1.5.43}$$

where

$$\Delta = \frac{\sigma\tau_2(\tau'_D - \tau_\perp)}{\alpha_d^2 \tau'^2_D} \tag{1.5.44}$$

and

$$\tau_2 = \frac{\tau'_D}{-\sigma - 2 + \dfrac{4\sigma(\sqrt{\sigma} - D(\sqrt{\sigma}))}{3\sqrt{\sigma} - (3 + 2\sigma)D(\sqrt{\sigma})}} \tag{1.5.45}$$

is called second relaxation time. The latter equations for $\sigma \to 0$ give $\Delta \to 0$, $\tau_2 \to 0$, $\tau_\perp \to \tau'_D$ and Eq. (1.5.43) is reduced to Debye with relaxation time τ'_D. By increasing σ the resonant character of $\chi_\perp(\omega)$ is more pronounced and when $\sigma \to \infty$ (influence of thermal agitation is very small) then $\tau_2, \tau_\perp \to \tau'_D/\sigma$ and Eq. (1.5.43) yields the Landau-Lifshitz equation (1.5.38). We see that Debye equation and that of Landau-Lifshitz are the two limits for very low and very high σ respectively, since Coffey's equation (1.5.43) covers the whole range of σ values. Equation (1.5.43) can be separated into real and imaginary parts, with

$$\frac{\chi_\perp(\omega)}{\chi_0 \dfrac{\tanh\sigma}{\sigma}} = \frac{(1+\Delta)^2 + \omega^2\tau_2^2 - \Delta\omega^2\tau_2\tau_\perp}{(1 - \omega^2\tau_2\tau_\perp + \Delta)^2 + \omega^2(\tau_\perp + \tau_2)^2} - i\frac{\omega^3\tau_2^2\tau_\perp + \omega\tau_\perp + \omega\tau_\perp\Delta}{(1 - \omega^2\tau_2\tau_\perp + \Delta)^2 + \omega^2(\tau_\perp + \tau_2)^2} \tag{1.5.46}$$

The change of phase happens at the critical point where the real part goes negative at

$$\omega = \omega_{res} = \frac{1 + \Delta}{\sqrt{\Delta\tau_\perp\tau_2 - \tau_2^2}} \tag{1.5.47}$$

For real values of ω_{res} it is required that

$$\Delta = \frac{\sigma\tau_2(\tau'_D - \tau_\perp)}{\alpha_d^2 \tau'^2_D} > \frac{\tau_2^2}{\tau_\perp\tau_2}$$

or

$$\frac{\sigma}{\alpha_d^2} > \frac{\tau_D'^2}{\tau_\perp(\tau_D' - \tau_\perp)} \tag{1.5.48}$$

When $\alpha_d < 0.1$ the condition for resonance is approximately $\sigma^2 > 5\alpha_d^2$. The critical value of σ at which ferromagnetic resonance disappears is $\sigma^* = \sqrt{5}\alpha_d$. This equation also determines the critical volume of the ferromagnetic particle, namely $v_m^* = \sigma^* k_B T / K$ at which the characteristic frequency of precession of the magnetic moment vanishes. For $\alpha_d = 0.1$ we find that $\sigma^* \cong 0.22$. The first investigators to arrive at this result were Raikher and Shliomis [7] who showed that the critical diameter, d^*, of the ferroparticle usually varies from 3 nm to 12 nm.

The total susceptibility will be the average over the spatial three dimensions (Fig. (1.6)), that is,

$$\chi(\omega) = \frac{1}{3}(\chi_\parallel(\omega) + 2\chi_\perp(\omega)) \tag{1.5.49}$$

in which the best expression for $\chi_\perp(\omega)$ is the resonance equation (1.5.43) and the Debye equation for the purely relaxational $\chi_\parallel(\omega)$ part. Consequently

$$\chi(\omega) = \frac{1}{3}\left(\frac{3\chi_0\left(1 - \frac{2}{3}\frac{\tanh\sigma}{\sigma}\right)}{1 + i\omega\tau_\parallel^{eff}} + 2\chi_0 \frac{\tanh\sigma}{\sigma} \frac{1 + i\omega\tau_2 + \Delta}{(1 + i\omega\tau_2)(1 + i\omega\tau_\perp) + \Delta} \right) \tag{1.5.50}$$

Let us investigate the properties of the models described above to see how realistic they are. This can be shown by fitting the theoretical equations to experimental data. We first show the necessity of using the combined form of susceptibility with both relaxation and resonance components. In Fig. (1.7 b) is shown a plot of susceptibility given by Eq. (1.5.49) with the Landau-Lifshitz equation (1.5.39) describing the perpendicular part and the Debye equation the parallel part. The relaxational absorption peak is indicated on the spectrum and it is some orders lower than ω_{res} and ω_{max}. Since σ is not zero, the magnitude of the resonance part $(\chi'/\chi_0 = \tanh\sigma/\sigma)$ is smaller than that of the relaxational component $\chi'/\chi_0 = 1$. The plots of Figs.(1.7 a-b) are for the monodisperse case. Such curves do not correspond to a realistic system, in which the radius and anisotropic energy varies from particle to particle, and cannot fit the data.

We now show the necessity of using probability distribution functions to describe both radius and anisotropic energy distributions. In Fig. (1.7 c) (solid line), is presented

the susceptibility spectra of a measured ferrofluid magnetite sample in an isoparaffin carrier with M_s^F=900 G. Measurement is obtained by use of the transmission line technique (see Chapter 2). It is impossible to fit such a susceptibility curve if the distributions of radii and anisotropic constants are not accounted for. Since particles are of several sizes and shapes, the internal anisotropy energy varies from particle to particle and this fact has to be reflected in the distribution of K. The different shape anisotropies in each individual particle, arising from the demagnetising fields, result in the existence of a distribution of K. Susceptibility is estimated in a manner analogous to that described in section 1.4 for the distribution of the Debye equation. Similarly to Eq. (1.4.51) we write

$$\chi(\omega) = \frac{\int_{r_{min}}^{r_{max}} P(r_m) \int_{K_{min}}^{K_{max}} \chi(\omega, K, r_m) P(K) dK dr_m}{\int_{r_{min}}^{r_{max}} P(r_m) \int_{K_{min}}^{K_{max}} P(K) dK dr_m} \qquad (1.5.51)$$

The distributions $P(r_m)$ and $P(K)$ result in the elimination of the sharpness of the curve and ensure a sufficient width. As has been said before, the choice of the distribution is such as to give an appropriate fit with sensible values of parameters.

We investigate now which is the appropriate distribution function to describe $P(r_m)$ and $P(K)$. The optimum choice is given from the best possible fit. Normal (gaussian) distribution is usually preferred for its simplicity and because it is close to the natural Boltzmann distribution. The dotted line fit in Fig. (1.7 c) is developed by distributing both K and r_m with normal probability function. The radius and viscosity parameters used in this fit are in accordance with those given by the manufacturer [39], having values of 5nm and 60 mPascal respectively. Saturation magnetisation of the magnetite material is M_s=0.4 T (320,000 A/m) and its gyromagnetic ratio 1.76×10^{11} Hz/T (220,000 Hz m/A) and anisotropy constant of 10 kJ/m^3. Distribution parameters (standard deviation) have to be adjusted to obtain the best fit, as close as possible to the data. By evaluating $\langle r_m \rangle$=5 nm and r_m in the range 0.16-10nm with a normalised standard deviation (for normal distribution) of σ_r=0.3 and $\langle K \rangle$= 0.8 kJ/m^3 with K in the range 0.18-16 kJ/m^3, with σ_K=0.6 and $\alpha_d = 0.25$, we get the fit of Fig. (1.7 c) (dotted line) which is close to the data.

The distribution of radii sometimes requires to have a bigger population of particles with radius different than the mean. This is possible by using the Nakagami distribution function which, as shown in Fig (1.7 d), is not symmetrical (as the normal distribution) and gives a maximum below or above $\langle r_m \rangle$ depending on the width parameter β*. For small β (i.e. 0.6, 1) the maximum is below $\langle r_m \rangle$=5 nm denoting that the smaller particles contribute more to the susceptibility due to their bigger population. For larger β (i.e. 4, 10) $\langle r_m \rangle$ is above 5nm. The normal distribution function is symmetric and always has a maximum at the central value. The Nakagami probability function is a more appropriate means of describing particle size distribution and will be used hereafter. A fit with Nakagami distribution for $\langle r_m \rangle$ is plotted in Fig. (1.7 c) (dashed line) with β=0.8 and keeping all other parameters the same as in the previous fit (dotted line); it is obviously not very different from the previous fit.

Let us now compare the two models described previously, namely Landau-Lifshitz (Eq. (1.5.39)) and Coffey's (Eq.(1.5.43)). The ratio of anisotropy energy to thermal energy used for the previous fits has a mean value of $\langle \sigma \rangle = \langle K \rangle \langle v_m \rangle / k_B T = 1.35$, which is small. Thus Coffey's equation (1.5.43) is, as stated before, more adequate for fitting since the Landau-Lifshitz equation is appropriate for $\sigma \to \infty$. Another reason for preferring Eq.(1.5.43) is that the value of α_d (=0.25), used for the previous fit, is relatively large and outside the range (0.01-0.1) commonly quoted [31, 32]. By fitting Eq. (1.5.50) to the data and by using the more realistic α_d=0.1 and $\langle K \rangle$= 1.2 kJ/m^3 and leaving all the other parameters the same as before, we get a more accurate fit, see Fig. (1.7 e) (dotted line). The Landau-Lifshitz fit is shown on the same graph for comparison (dashed line). The difference in the relaxation peak is due to the different value of $\langle K \rangle$ used for each fit and thus different σ which effects $\tau_{\parallel}^{eff}$. Another difference is the susceptibility's magnitude at lower frequencies which is small according to the Landau-Lifshitz model. The fit obtained by using Eq.(1.5.50) yields a low frequency susceptibility which agrees with the datasheet of the fluid. It is obvious that Coffey's modified equation (1.5.50) is more suitable to describe the resonance effect and will be used hereafter. But as we will show

* For further comment on the Nakagami distribution function, and all other probability functions used here, see Chapter 3

in Chapter 4, the Landau-Lifshitz equation is more suitable for describing the field dependence of the susceptibility.

It is of interest to study how Coffey's equation (1.5.43) behaves by varying α_d, $\langle r_m \rangle$ and $\langle K \rangle$ parameters. We will study three cases, namely: (a) varying α_d and leaving $\langle r_m \rangle$=5nm and $\langle K \rangle$=1.2 kJ/m^3 unchanged (for comparison), (b) varying $\langle r_m \rangle$ and leaving α_d=0.1 and $\langle K \rangle$=1.2 kJ/m^3 unchanged, (c) varying $\langle K \rangle$ and leaving $\langle r_m \rangle$=5nm and α_d=0.1 unchanged. It is apparent that, by changing either $\langle r_m \rangle$ or $\langle K \rangle$, the parameter σ is strongly affected.

(a) In Fig. (1.7 f) it is shown that by increasing α_d there is a transition from pure resonance to relaxation. The solid line is identical to the fit of Fig.(1.7 e) and it is the reference. All other parameters have been kept the same. By decreasing α_d resonance is more prominent.

(b) The variation of $\langle r_m \rangle$ causes a variation in $\langle \sigma \rangle$ which sequentially effects $\langle \tau_N \rangle$ and $\langle \tau_{\parallel}^{eff} \rangle$. The bigger $\langle \sigma \rangle$ the bigger $\langle \tau_{\parallel}^{eff} \rangle$, causing a shift of the relaxation peak to the left, as is shown in Fig.(1.7 g) where $\langle r_m \rangle$ takes the value of 2, 3, 5, 6 nm resulting in $\langle \sigma \rangle$=0.32, 1.32, 6.96, 12.66, respectively. All the other parameters remained the same as in the fit of Fig.(1.7 e). For $\langle r_m \rangle$=2nm ($\langle \sigma \rangle$=0.32) the susceptibility is purely relaxational. When $\langle r_m \rangle$=3nm ($\langle \sigma \rangle$=1.32) the resonance and relaxational peaks are split. For $\langle r_m \rangle$=5nm ($\langle \sigma \rangle$=6.96), which is the same curve as the fit of Fig.(1.7 e), we have the two effects seperated. For $\langle r_m \rangle$=6nm ($\langle \sigma \rangle$=12.66) relaxation absorption occurs lower and it tends to have a Brownian rather than a Néel character.

(c) Variation of $\langle K \rangle$ effects $\langle \sigma \rangle$ and the resonant frequency as indicated by Eq. (1.5.36). When $\langle K \rangle$=1 kJ/m^3 ($\langle \sigma \rangle$=0.57) the susceptibility has a relaxation nature only (see Fig.(1.7 h)). For $\langle K \rangle$=5 kJ/m^3 ($\langle \sigma \rangle$=2.8) resonance appears but f_{res} is lower than the f_{res} corresponding to $\langle K \rangle$=10 kJ/m^3, which is the reference (solid line). Finally for $\langle K \rangle$=50 kJ/m^3 ($\langle \sigma \rangle$=28.5) f_{res} is higher.

1.6 Conclusions

In this chapter we presented the basic theory of ferrofluidic systems with a detailed description of the inner and exterior part of a ferropraticle including the possible cases of anisotropy arising from crystal's structure and shape. Phenomenological models for relaxation (both Brownian and Néel) and resonance of the magnetic moment, have been specified. Debye and Cole-Cole equations (1.4.47), (1.4.52) which are adopted from the dielectric relaxation theory, based on statistical physics concept for normal and anomalous rotational diffusion respectively, are the underlying models used to describe the particle's relaxation and to explain the susceptibility's spectroscopic profile. Substituting Debye's relaxation time with the effective relaxation time can extend the model to include the combined effect of Brownian and Néel relaxation. Ferromagnetic resonance, arising from the moment's precession, is described by Coffey's equation (1.5.43) which includes the effect of thermal agitation, in contrast with the simpler Landau-Lifshitz equation (1.5.39) which is the limit for large magnetic to thermal energy ratio. Under the influence of an external alternating field, both relaxation and resonance can be accounted for by considering the particle's rotational movement as being pure relaxational in a direction parallel to the field and pure precessional in the perpendicular direction. Accordingly, the magnetic susceptibility is given as the average of the directional susceptibilities $\chi_{\parallel}$, $\chi_{\perp}$ as Eq. (1.5.49) states.

References:

1. Shliomis M.I., Pshenichnikov A.F., Mozorov K.I., Shurubor Yu.I., *J. of Magnetism and Magnetic Materials*, **85**, 40, (1990).
2. Jiles D., *Introduction to Magnetism and Magnetic Materials*, Chapman & Hall, 2nd edition, (1998).
3. Weiss P., *Compt. Rend.* **143**, 1136, (1906).
4. Weiss P., *J. Phys.*, **6**, 661, (1907).
5. Landau L., Lifshitz E., *Phys. Z. Sowjet.*, **8**, 153, (1935); Collected Papers of Landau, Pergamon Press, (1965).
6. Frenkel J, Dorfman J., *Nature*, **126**, 274, (1930).
7. Raikher Yu.L., Shliomis M.I., *Sov. Phys. JETP*, **40**, 526, (1974).
8. Levy R.A., *Principles of Solid State Physics*, Academic Press, (1968).

9. Aharoni A., *Introduction to the Theory of Ferromagnetism*, Oxford Publications, (1996).
10. Langevin P., *Ann. Chem. et Phys.*, **5**, 70, (1905).
11. Debye P.,*Ver. Deut. Phys. Gesell.* **15**, 777, (1913); reprinted (1954) in collected papers of Peter J.W. Debye Interscience New York.
12. Debye P., *Polar Molecules*, The Chemical Catalogue Co. New York (1929), Reprinted by Dover, New York.
13. Néel L., *Ann. Geophys*, **5**, 99, (1949).
14. Brown W.F., *Physical Review*, **130**, 1677, (1963).
15. Mazo R. *Brownian Motion: Fluctuations, Dynamics and Applications*, Oxford University Press, Oxford (2002).
16. Coffey W.T., Kalmykov Yu.P., Waldron J.T., The Langevin Equation, World Scientific (1996).
17. Einstein A., in Fürth R. H., Ed., *Investigations on the Theory of the Brownian Movement,* Methuen, London, 1926; reprinted by Dover, New York, 1954.
18. Coffey W. T., *Adv. Chem. Phys.* **63**, 69, (1985).
19. Scaife B.K.P., *Principles of Dielectrics*, Oxford Publications, (1998).
20. Cole K.S., Cole R.J., *Journal of Chemical Physics* , **9**, 341, (1941).
21. Dédjardin J.L., *Physical Review E*, **68**, 031108, (2003).
22. Coffey W. T., Kalmykov Yu. P., Titov S. V., *J. Chem. Phys.*, **116**, No 15, 6422, (2002).
23. Coffey W.T., Theory of anomalous dielectric relaxation, *Proc. NATO Workshop Ustron Katowice Poland*, (2003). NATO Conference Series, Ed. S.J. Rzoska.
24. Titov S. V., Kalmykov Yu. P., Coffey W. T., *Phys. Rev. E*, **69**, 031114, (2003).
25. Oldham K.B., Spanier J., The Fractional Calculus, Academic, New York, (1974).
26. Davidson D., Cole R., *J. Chem. Phys.*, **19**, 1484, (1951).
27. Havriliak S., Negami S., *J. Polym. Sci.* C, **14**, 99, (1966).
28. Fannin P.C., *Adv. Chem. Phys.*, **104**, 181, (1998).
29. Cole K.S., *Permeability and Impermeability of Cell Membrane of Ions*, Cold Spring Harbor Sympos Quant Biol, **8**, 110, (1940).

30. Gilbert T.L., *Phys. Rev.*, **100**, 1243, (1955).

31. Shliomis M.I., Raikher Y.L., *IEEE Trans. Magn.*, **MAG-16**, 237, (1980).

32. Anderson J.C., Donovan B., *Proc. Phys. Soc.*, **B75**, 149, (1960).

33. Coffey W.T., Kalmykov Y.P., Massawe E.S., *Adv. Chem. Phys.*, **85**, 704, (1993).

34. Coffey W.T., Crothers D.S.F., Kalmykov Y.P., Massawe E.S., Waldron J.T., *Phys. Rev.*, **49**, 1869, (1994).

35. Coffey W.T., Cregg P.J., Crothers D.S.F., Waldron J.T., Wickstead A.W., *J. Magn. Magn. Mater.*, **131**, L301, (1994).

36. Shliomis M.I., Stepanov V.I., *Adv. In Chem. Phys.*, **87**, 1, (1994).

37. Fannin P.C., J. *Magn. Magn. Mater.*, **136**, 49, (1994).

38. Scaife B.K.P., *Adv. Chem. Phys.*, **109**, 1, (1999).

39. FerroTec Data Table, EMG Ferrofluid, (1998).

Chapter 2

Overview of impedance measurement techniques.

2.1 Introduction

Permittivity and permeability as functions of frequency can be easily determined by means of impedance measurements. The impedance of a material is measured at several frequencies by using auto-balance bridges, vector meters and impedance analysers. No single method of measurement can cover the frequency range, from a few Hz up to microwave frequencies. Each method has a range of frequencies for which it is most appropriate [1,2]. The ranges of frequencies should overlap, enabling a complete coverage to be obtained. Conventional bridges may be used over a range of approximately 5 Hz to 100 MHz. The RF I-V [2] method is suitable for a rather higher band of frequencies from 1 MHz to 3 GHz. At frequencies exceeding 50 MHz permittivity and permeability can be determined from measurement of the velocity and attenuation of electromagnetic wave propagation in the material. Below 40 GHz the wave is propagated in a coaxial transmission line. At higher frequencies the wave is propagated in free space but this technique is not applied for our measurements. The maximum frequency we are able to use with our experimental set up is, approximately, 20 GHz. In Fig. (2.1 a-e) is shown the arrangements of the several methods commonly used (from low frequencies up to microwave region) and in Table (2.1) a summary of the advantages/disadvantages of each method.

The *bridge method* is a common bridge as Fig. (2.1 a) shows. When no current flows through the detector (D), the value of the unknown impedance is obtained by $Z_x = Z_1 Z_3 / Z_2$. Various kinds of bridge, employing combinations of R, L, C, components as the bridge elements, are used for various applications.

The *auto-balancing bridge method* is shown in Fig.(2.1 b). The current which flows through Z_x, also flows through range resistor R_r. The potential at point L is maintained at zero volts (virtual ground), because the current through R_r balances with the Z_x current by operation of the I-V converter amplifier. Z_x is calculated using voltage measurement at the high terminal and that across R_r.

In the *I-V method* (Fig.(2.1 c)) the unknown impedance Z_x can be calculated from measured voltage and current values. Current is calculated using the voltage measurement across an accurately known low value resistor R. In practice a low loss transformer is used in place of R to prevent the effects caused by placing a low value resistor in the circuit. The transformer, however, limits the high frequency end of the measurement.

The *RF I-V method* (Fig.(2.1 d)) is based on the same principle as the I-V method, but it is configured in a different way by using an impedance matched measurement circuit (50 Ω) and a precision coaxial test port for operation at higher frequencies. There are two types of arrangements, which are suitable for low and high impedance measurements. Z_x is derived from measured voltage and current values. The current that flows through Z_x is calculated from a voltage measurement across a known value resistor R. In practice a transformer is used instead of R but it limits the low end of the applicable frequency range.

Table 2.1 Summary of impedance measurement methods.

Method	Advantages	Disadvantages	Applicable frequency range
Bridge method	-High accuracy (<1%). -Wide frequency coverage by different types of bridge.	-Manually balanced. -Narrow frequency coverage with a single instrument.	DC-300 MHz
Auto-balancing bridge	-High accuracy. -Wide frequency range with one instrument.	-Very high frequency range is not available.	5 Hz-100 MHz
I-V method	-Suitable to probe type test needs.	-Operating frequency range is limited by transformer used in probe.	10 kHz-100 MHz
RF I-V method	-High accuracy (<1%). -Wide impedance range.	-Operating frequency range is limited by transformer used in test head.	1 MHz-3 GHz
Network analyser	-High frequency range.	-Narrow impedance range (Z_x needs to be close to characteristic impedance).	50 MHz and above.

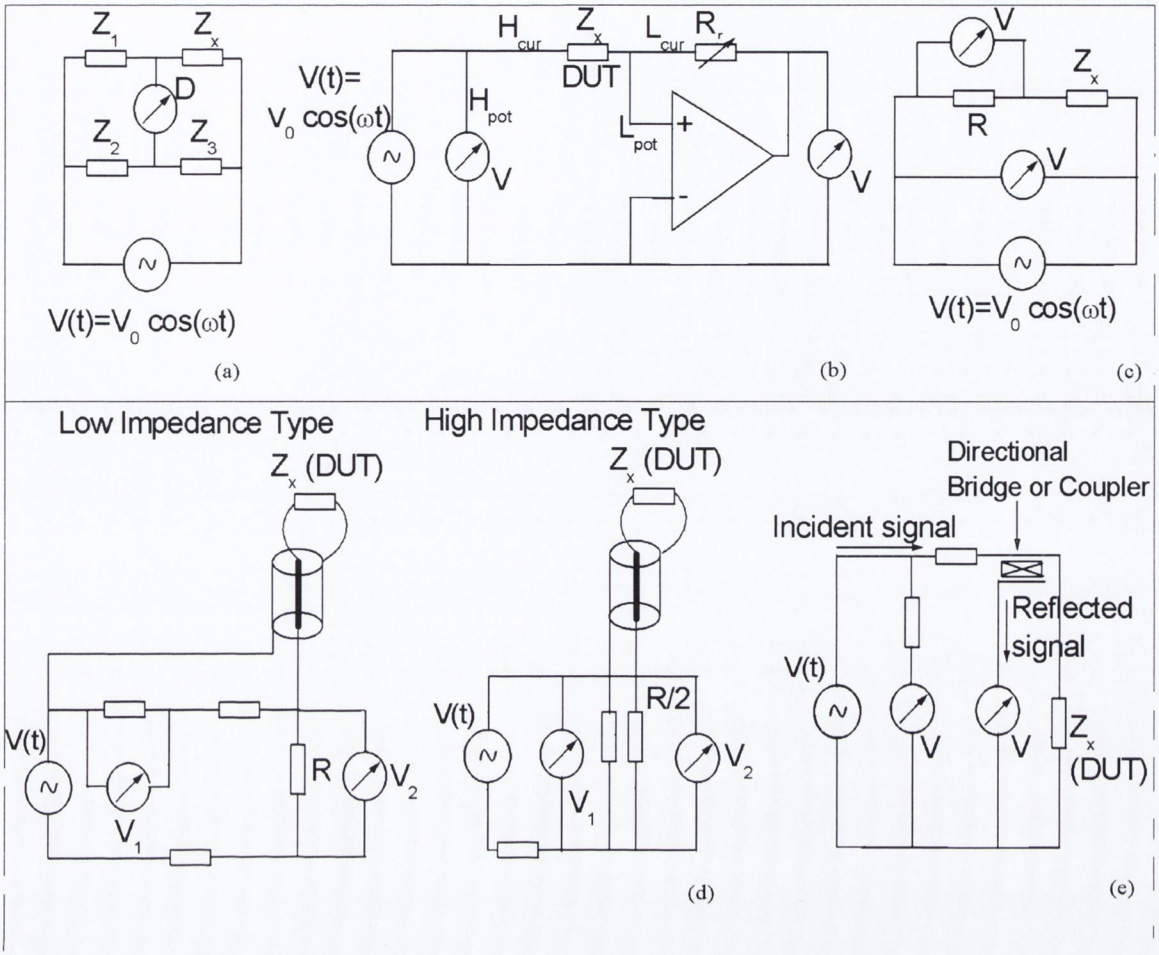

Figure 2.1 (a) Common bridge method. When the current through the detector D is zero, the bridge balances and the unknown impedance is equal to $Z_x = Z_1 Z_3 / Z_2$, (b) The Auto-balancing bridge method is based on the elimination of the current through Z_x. The unknown value of the load is given by $Z_x = R_r V_{DUT} / V_{rr}$, (c) The common I-V method is based on the measurement of the source voltage and the calculation of the current through R by measuring the voltage across R, (d) The RF I-V method is principally the same as the I-V method but the output impedance matches the impedance of port extension. There are two arrangements, one for high impedance DUT and one for low impedance DUT, (e) The Networking technique is based on the measurement of the reflected coefficient S_Γ; that is the ratio of the reflected to the incident wave.

The principle of the network analysis method is illustrated in Fig.(2.1 e). The reflection coefficient is obtained by measuring the ratio of the incident signal to the reflected signal. A directional bridge or coupler is used to detect the reflected signal and a network analyser is used to supply and measure the signals.

2.2 Auto-balancing bridge method (low frequencies).

The auto-balancing bridge method is appropriate for lower frequencies (5 Hz-100 MHz). Hewlett Packard's (HP) 4192A LF Impedance Analyser [3] (5 Hz-13 MHz) can cover most of the measurement range by adapting a suitable fixture to its four-terminal

pair output (H_{cur}, H_{pot}, L_{cur}, L_{pot}). For magnetic measurements the fixture can be an inductor, usually a toroidal coil with core [4], fed with an alternating current of constant amplitude and for dielectric measurements, the fixture can be a plate or cylindrical capacitor fed with an alternating constant amplitude voltage. The frequency resolution is high (1 mHz) and the range of signal level is 5 mV-1.1 V with a resolution of 5 mV. This auto-balanced bridge can measure loads with a reading accuracy 0.08% in an impedance range 3 mΩ-500 MΩ.

The circuitry of HP 4192A bridge (Fig. 2.1 b) is divided into three sections, the *signal source* which generates the source signal applied to the unknown load, the *auto-balance bridge section* which balances the current through the range resistor R_r with the current through the device under test (DUT) Z_x, to maintain a zero potential at the low (L) terminal, and the *vector ratio detector* which measures two vector voltages across DUT (V_{DUT}) and range resistor R_r (V_{rr}). The range resistor R_r is a switch array of several resistors (50 Ω, 400 Ω, 3.2k Ω, 25.6k Ω) each of them is selected by the instrument to suit to the measurement range according to DUT's impedance. The range boundary is specified at two points to give an overlap between adjacent ranges. In the auto-balancing section the + input of the operational amplifier (see Fig. (2.1 b)) detects the potential at the low (L) terminal and controls both magnitude and phase of the oscillator at the output of the operational amplifier, so that the detected potential becomes zero. In more detail, when the bridge is unbalanced a null detector detects an error current and a phase detector separates it into 0^o and 90^o vector components. The output signals go throughout integrators and are applied to a modulator to drive both component signals. The resultant signal is amplified and fed back through the range resistor R_r to cancel the current through Z_x, therefore no error flows into the null detector (+ input). This balancing operation is performed automatically over the full frequency range. Z_x is evaluated by $Z_x = R_r V_{DUT} / V_{rr}$. The output source resistor is 50 Ω and oscillating signal is applied directly to Z_x from the H_{cur} terminal. This source resistor must be taken into consideration especially when measuring low values of impedance (low inductance or high capacitance). The oscillator level should be set as high as possible to obtain a good signal to noise ratio (S/N) for the vector ratio detector section. However when measuring cores care must be taken to ensure that the oscillator voltage level does not give rise to saturation effects.

Since measured loads (inductors or capacitors) are frequency dependent the actual signal level (voltage or current) at their terminals is not the same for all frequencies as the signal produced by the source (oscillator). The instrument is equipped with an *auto-level-control function*, which can automatically maintain a constant test signal level. By comparing the monitored signal level with the test signal level setting value, this function adjusts the oscillator output voltage until the monitored level meets the setting value. The test signal voltage is monitored at the high (H) terminal and the test signal current is calculated from the value of range resistor R_r and the voltage across it.

The measured loads are not directly connected to the four terminal pair of the bridge, because they do not geometrically fit to the shape of the terminal. Various types of test fixtures are utilised to ease connection of the DUT to the measurement terminal. Usually these fixtures short the pairs (H_{cur}-H_{pot} and L_{cur}-L_{pot}). As a result a variety of errors (such as residual impedance, stray admittance, electrical length, etc) are involved in the circuit between the DUT and the terminals. The induced errors are dependent upon test frequency, test fixture, leads, DUT connection configuration, and surrounding conditions of the DUT. The instrument's open/short *calibration function* eliminates the effects of the test fixture's residuals. When the terminals are open, the stray admittance Y_{stray} is measured, because the residual impedance Z_{resid} is negligible. When the terminals are shorted, then the residual impedance Z_{resid} is measured. As a result each residual parameter is known and the impedance Z_x of the DUT is given by,

$$Z_x = \frac{Z_m - Z_{resid}}{1-(Z_m - Z_{resid})Y_{stray}} \qquad (2.2.1)$$

where Z_m is the actual measured impedance. The procedure to perform calibration is a key technique to obtain accurate measurement results.

With the HP 4192A bridge one only adjusts the oscillator voltage and not the current. If the current amplitude needs to be maintained constant (e.g., for the measurement of an inductor) it is necessary for a pre-measurement to be completed and for the calculation of the voltage level (which will produce the desired current) to be performed in order for the analyser to adjust the voltage to that level. The analyser controller does not have this capability, so an external controller is necessary to perform these calculations. The external controller can be any common computer connected to the bridge under use of the HP Interface Bus (HP-IB) protocol [5-8], which is equivalent to the General Purpose Interface Bus (GPIB) and to the IEEE 488 interface communication

protocol. This communication is also necessary for another reason, to store the measurement data to a computer's disc, since HP 4192A does not have own storage facility.

2.3 RF I-V method (radio frequencies).

The RF I-V method is an advanced and accurate technique for measurements beyond the frequency coverage of the automatic bridge and below the frequency coverage of the transmission line technique, however it provides better accuracy. The HP 4291B RF impedance/material analyser [9] is the instrument we use to perform measurements between 1 MHz-1.8 GHz. This analyser provides a test head extended to a cylindrical fixture (short transmission line), which behaves as a capacitor or an inductor depending on the load (open or short) applied. For the type of measurements we are performing, the sample covers the whole volume of the cylindrical cell. The way that a measurement is taken is dependent on the impedance of the load, thus there is circuitry for low impedance measurement and for high impedance measurement. A simplified diagram for both means is illustrated in Fig. (2.1 d). This circuitry has three main parts:

(a) The *signal source section*, which generates RF test signals applied to the unknown device. Generally, a frequency synthesizer is used to meet frequency accuracy, resolution and sweep function needs. The amplitude of the signal source output is adjusted to the desired test level by the output attenuator. The source section has an impedance of 50 Ω. The oscillator output level can be controlled to change the test signal level applied to the DUT. The HP 4291B is equipped with a level monitor function, which can display the test signal level and measurement results.

(b) The *test head section*. The measurement circuit is matched to the characteristic impedance of 50 Ω to ensure optimum accuracy at high frequencies. The test port also employs a precision coaxial connector of 50 Ω characteristic impedance. Because the measurement circuit impedance is fixed at 50 Ω, all measurements are made with reference to 50 Ω without ranging operation. There are two signals measured: V_1, which represents the voltage across the DUT, and V_2, which represents the current flowing through the DUT.

(c) The *vector ratio detector section*. The two vector voltages V_1 and V_2 are measured with an identical ratio detector to avoid tracking errors. Each vector voltage is converted into digital data by an A/D converter and is digitally separated into 0^o and 90^o vector components. The impedance of the unknown device can be determined from the

ratio of the two voltages; for the low impedance type test head the DUT impedance is given as $Z_x = 2R/(V_2/V_1 - 1)$ and for the high impedance type test head, Z_x is given as $Z_x = R(V_1/V_2 - 1)/2$.

The HP 4291B, as with all analysers, requires *calibration* each time a measurement is initiated or each time the setup is changed. At radio frequencies, a change in the instrument operating conditions, such as, environmental temperature, humidity, frequency setting, etc, can have a great effect on measurement accuracy. In addition, measurement circuits have some error terms (such as stray admittance and residual impedance) whilst the four resistances R in the measurement circuit do not have exactly the same impedance value. In fact, the impedance values calculated from the previous equations for Z_x do not correspond with the actual impedance value of the DUT. The nature of an RF vector measurement makes it difficult to sufficiently maintain the calibrated measurement performance over a long period of time. Thus, users have to periodically perform calibration. Calibration is executed in reference to three standard terminations, open, short and load, and all three must be performed. The two vector voltmeters can measure at two different points, in the linear circuit. In this case, the DUT impedance can be expressed by the measured voltage values V_1 and V_2 using a bilinear form as follows [9]

$$Z_x = a\frac{1 + b(V_1/V_2)}{1 + c(V_1/V_2)} \tag{2.3.1}$$

where a, b, c are complex constants. By using the measurement impedance value Z_m instead of the voltage ratio and modifying the equation, Z_x can also be expressed using the following bilinear form

$$Z_x = A\frac{Z_m - B}{1 - CZ_m} \tag{2.3.2}$$

where A, B and C are complex constants (calibration coefficients) related to the circuit. If three standards that have known impedance value are measured, these three constants can be calculated. The coefficient B represents residual impedance when the circuit is perfectly shorted and C represents stray admittance when the circuit is perfectly open.

Compensation reduces the effect of error sources existing between the DUT and the instrument calibration plane. Compensation is not the same as calibration and cannot replace calibration. The measurements required for compensation depend on the calibration accuracy, so compensation must be performed after calibration has been

completed. The measuring circuit (fixture) connecting a test sample to the test port actually becomes part of the sample that the instrument measures. Diverse parasitic impedances, existing in the measuring circuit between the test port and the unknown device, affect the measurement result (the measurement error is increased because of the additional impedance). For eliminating the errors due to fixture residual and stray factors, an open/short/load compensation is provided. As in the case of the calibration, three unknown constants values have to be estimated [9],

$$Z_x = A_{compen} \frac{Z_m - B_{compen}}{1 - C_{compen} Z_m} \tag{2.3.3}$$

2.4 Networking technique (microwave frequencies).

Measurements up to microwave frequencies are realised by the combined use of the HP 8753C (3 MHz-6 GHz) and the HP 8722D (50 MHz-40 GHz) network analysers [12,13]. A simplified diagram showing the principle of networking technique is illustrated in Fig.(2.1 e). The port of a network analyser is connected to a coaxial line through which microwaves can be transmitted. Most of the analysers support a second port, which works as an individual channel. It is possible for microwaves to be transmitted from the first port and to be detected at the second. It is also possible for a signal to be transmitted from one port, to be totally reflected and, finally, to be detected at the same port. Hence there are two possible means by which a measurement can be obtained: with transmission or with reflection. The transmission method is complex in terms of its setup, cell specifications, calibration (requires two individual calibrations, one for each channel) and calculations to derive the permittivity and permeability from the measured impedance [15]. The reflection technique [16] is the method used here.

The ratio of the reflected to the incident voltage is the reflection coefficient S_Γ and it is a complex quantity, given by

$$S_\Gamma = \frac{V_{ref}}{V_{inc}} = |S_\Gamma|(\cos\psi + i\sin\psi) = |S_\Gamma| \angle \psi \tag{2.4.1}$$

where V_{ref} is the vector (complex) voltage of the reflected wave, V_{inc} is the vector voltage of the incident wave and ψ the polar angle of the S_Γ complex number. For the case when the line is open, $S_\Gamma = 1$, and for shorted case, $S_\Gamma = -1$, (Fig. (2.2)). For the case when a 50 Ω load is connected $S_\Gamma = 0$; this means no reflection since the impedance of the 50 Ω load is equal to the characteristic impedance of the line. It is evident that

$-1 \leq S_\Gamma \leq 1$. In general the reflection coefficient S_Γ is correlated with the arbitrary unknown impedance Z_x with,

$$S_\Gamma = \frac{Z_x - Z_0}{Z_x + Z_0} \tag{2.4.2}$$

(Z_0 =50 Ω is the characteristic impedance) or by solving for Z_x yields,

$$Z_x = Z_0 \frac{1+S_\Gamma}{1-S_\Gamma} \tag{2.4.3}$$

The network analyser automatically calculates Z_x and displays on two screens the trace of the real and imaginary components. Thus, the trace of R_x versus frequency is illustrated on one screen consisting of a sequence of points, each one corresponding to an individual frequency, and on the other screen the analyser illustrates the trace of X_x versus frequency. The analyser saves temporarily the measured data in a tabular format into its memory and sends them later, via the HP-IB, to a computer for storage.

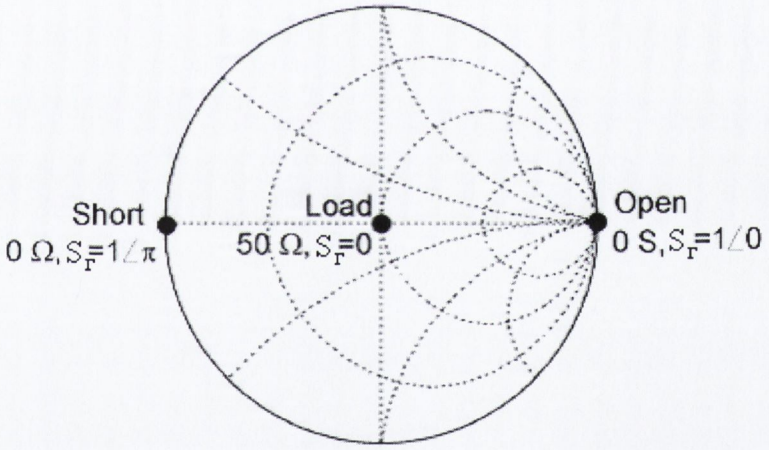

Figure 2.2 Smith chart showing the value of the reflection coefficient for open, short and 50 Ω load adapted to the end of the transmission line. The analyser is capable of presenting on its screen a Smith chart with the trace of the impedance of the load being measured. For a frequency sweep this trace appears as a sequence of individual points.

It is necessary to achieve calibration with three standards (open, short, load), as in the case of RF I-V method, and the equation which relates the calibration coefficients is Eq.(2.3.2). The calibration technique is the same as the one described in section 2.3.

The cylindrical cell, in which the sample is placed, is the end section of the coaxial line. The diameter of the inner conductor is 3mm and the diameter of the outer conductor 7mm. To obtain good accuracy, the sample depth must be large enough to ensure that there is sufficient interaction of the incident radiation with the sample material (unknown load), but on the other hand the sample depth must be small enough to ensure the absence of dimensional effects [17]. In general the lower the operating frequency the larger the

sample depth must be to attain the same accuracy in the results. However in practice one single sample depth can be used over three decades of frequency range. The transmission line method, however, has its limitations, due to the fact that the sample depth has to be small in comparison to the operating wavelength, materials with high values of ε or μ require very thin samples to take measurements up to GHz frequencies. Furthermore the method is not very accurate for the measurement of low loss materials, which require thick samples (i.e., a good fraction of a wavelength, to measure the loss component accurately). Kerosene-based and isoparaffin-based ferrofluids, have relatively low dielectric constants ($\varepsilon \cong 2\text{-}3.5$) with large loss components in their permeabilities throughout the frequency spectrum, and the transmission line method gives satisfactory measurements up to 20 GHz. For water-based ferrofluids, which have a large value of permittivity (approximately 65-80), the transmission line technique is limited to a frequency of 3GHz. These results and their reliability will be examined later (see section 2.7).

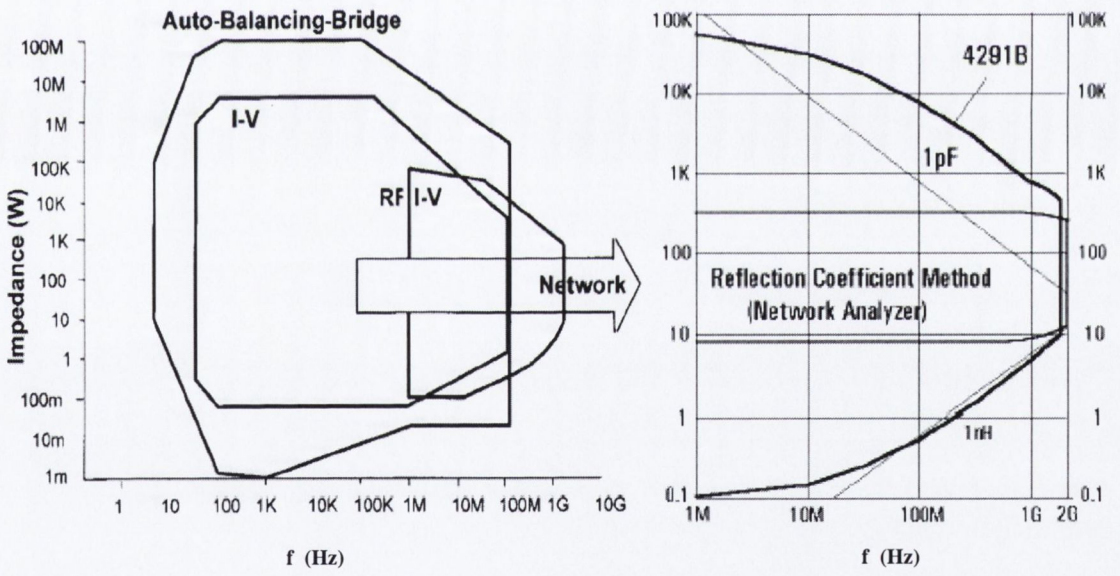

Figure 2.3 Comparison of the four techniques for low (auto-balancing bridge), intermediate (I-V and RF I-V) and high (networking) frequency ranges. The auto-balancing technique provides the best measurement accuracy and broadest impedance coverage, but its frequency range is limited. With the RF I-V method it is possible to cover a frequency range up to 2-3 GHz, but it cannot measure very big and very small impedances as the auto-balanced method does. The networking technique has the broadest frequency range and it is the only technology that can measure at microwave frequencies, but the accurate impedance measurement range is limited to those impedance values that are close to the characteristic impedance of the transmission line (50 Ω). Graphs have been taken from [10,11].

We now want to compare the three measurement methods in terms of frequency and impedance restrictions: as was previously stated, by increasing the frequency capability

the impedance measurement range is gradually reduced. This is exemplified in Fig. (2.3) where a comparison of all the methods described above is shown. The auto-balancing bridge measures a wide impedance range, since in the RF I-V method the impedance range is less broad and in the networking is thinner (close to 50 Ω).

2.5 Permeability measurements by using the toroid technique.

The method used to measure the complex permeability, μ, with the HP 4192A auto-balanced bridge, for frequencies between 10 Hz-100 kHz, involves placing the magnetic sample into an inductor and measuring its complex inductance, where

$$L(\omega) = L'(\omega) + iL''(\omega) = R(\omega)/\omega + iL(\omega) \qquad (2.5.1)$$

$R(\omega)$ is the resistive part of the inductor and $L(\omega)$ its inductance. The complex permeability, $\mu(\omega)$, is given by the ratio of the full to the empty value of the complex inductance (or impedance),

$$\mu(\omega) = \mu'(\omega) - i\mu''(\omega) = \frac{L'_{full}(\omega) + iL''_{full}(\omega)}{L'_{empty}(\omega) + iL''_{empty}(\omega)} = \frac{Z_{full}}{Z_{empty}} \qquad (2.5.2)$$

since $R(\omega) + i\omega L(\omega) = \omega(L'(\omega) + iL''(\omega))$. There are several types of inductors, such as cylindrical, coil and wound toroid, but the optimum choice is that which gives an accurate measured value of inductance (impedance). If the impedance of the inductor is small, then the error of the measurement increases causing uncertainty in the value of μ. Permeability, as a function of frequency, may also be affected by the capacitance of the inductor, which may limit the measurable frequency range due to the circuit's resonance effect.

Consider the case of a *cylindrical inductor* of length l, carrying an alternating current, I(t), with the radius of the internal and external conductors being R_1 and R_2, respectively. When the inductor is empty, by using Ampere's law, we calculate the magnetic flux density between the two conductors, which, by considering polar coordinate system $\hat{\vartheta}$, $\hat{\phi}$, $\hat{z}$ with z parallel to the axis of the cylinder, is

$$\mathbf{B}(\mathbf{r}, t) = \frac{\mu_0 I(t)}{2\pi r}\hat{\vartheta} \qquad (2.5.3)$$

with $R_1 \le r \le R_2$ (outside this region the field is zero). The field is extended concentricly to the cylinder's axis. The total magnetic flux is given by integrating over the rectangular area l dr, thus

$$\Phi_B(t) = \int d\Phi_B = \int \mathbf{B}(\mathbf{r},t)\cdot(l d\mathbf{r}) = \frac{\mu_0 I(t) l}{2\pi}\int_{R_1}^{R_2}\frac{dr}{r} = \frac{\mu_0 I(t) l}{2\pi}\ln\frac{R_2}{R_1} \qquad (2.5.4)$$

The inductance (empty) will be given by,

$$L = \frac{\Phi_B(t)}{I(t)} = \frac{\mu_0 l}{2\pi}\ln\frac{R_2}{R_1} \qquad (2.5.5)$$

For the cylindrical cell, used in this work, R_1=1.5 mm, R_2=3.5 mm, $l \leq 10\,cm$. Then, cell's inductance is, approximately, 1.7×10^{-8} H, which is minute in comparison with the values that the bridge can measure (order of mH). Even for a relatively high frequency (1 kHz), for this sort of method, the measured impedance is not more than 1 mΩ which is the lowest possible impedance that the instrument can measure. Although it is easy to calculate L, the cylindrical cell cannot be used at such low frequencies. The cylindrical inductor can be used for the RF I-V and networking techniques, where the frequency range is extended from 1 MHz and over.

A more adequate method of determining the frequency dependent complex magnetic susceptibility of a ferrofluid is to insert the fluid into the alternating magnetic field of a *coil*, which has a much bigger inductance, and observe the changes in its inductance, $\Delta L(\omega)$, and resistance, $\Delta R(\omega)$, as the frequency is varying. The ratio $\Delta L(\omega)/L(\omega)$ is proportional to $\chi'(\omega)$, while $\chi''(\omega)$ is proportional to $\Delta R(\omega)/\omega L$ [4]. However, the coil technique requires the use of a large inductance which, with the associated capacitance, restricts the frequency range over which measurements can be made.

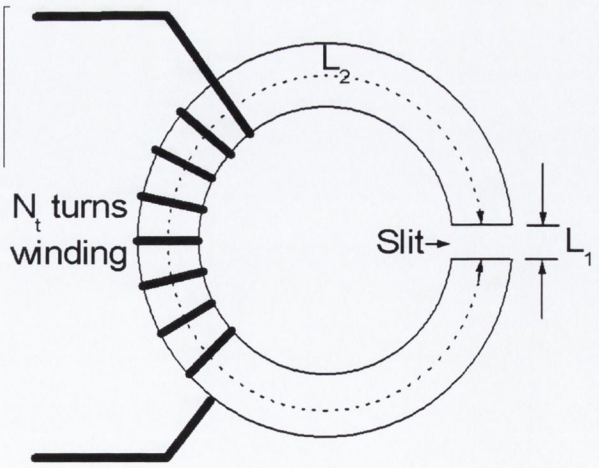

Figure 2.4 Experimental toroid

A more convenient and efficient method is to use the *toroidal technique* of Fannin et al [4]. This technique involves placing the fluid in an alternating magnetic field which is generated within a high permeability (e.g., mu-metal or similar magnetic alloy) toroidal core. A narrow slit is cut in the toroid (Fig. (2.4)) and the fluid is inserted into the slit. The slit's length, L_1, is tiny in comparison to the remaining length, L_2, of the circumference, L_1+L_2, ($\gamma_g = L_1/L_2 << 1$). Consider, now, that the winding has N_t turns and a cross-sectional area A_{cs}. The permeability can be written in terms of $\tilde{A}$, $\tilde{B}$, $\tilde{U}$, $\tilde{V}$ (see Appendix A, section A.2) as,

$$\mu' - i\mu'' = \frac{(-\tilde{A} - i\tilde{B})(\tilde{U} - i\tilde{V})}{\tilde{U}^2 + \tilde{V}^2} \tag{2.5.6}$$

where $\tilde{A}$, $\tilde{B}$, $\tilde{U}$ and $\tilde{V}$ are given by Eqs. (A.2.26)-(A.2.29),

$$\tilde{A} = \gamma_g (R_{cut}^{empty} R_{cut}^{full} + R_w^2 - R_w R_{cut}^{full} - R_w R_{cut}^{empty} - X_{cut}^{empty} X_{cut}^{full} \tag{2.5.7}$$

$$\tilde{B} = \gamma_g (-R_w X_{cut}^{empty} - R_w X_{cut}^{full} + R_{cut}^{full} X_{cut}^{empty} + R_{cut}^{empty} X_{cut}^{full}) \tag{2.5.8}$$

$$\tilde{U} = \gamma_g R_w R_{cut}^{full} + \gamma_g R_w R_{cut}^{empty} + \gamma_g X_{cut}^{full} X_{cut}^{empty} - \gamma_g R_w^2 - \gamma_g R_{cut}^{full} R_{cut}^{empty} + \omega L_{nocore} (X_{cut}^{empty} - X_{cut}^{full}) \tag{2.5.9}$$

$$\tilde{V} = \gamma_g R_w X_{cut}^{full} - \gamma_g R_{cut}^{empty} X_{cut}^{full} - \gamma_g R_{cut}^{full} X_{cut}^{empty} - \gamma_g R_w R_{cut}^{empty} + \omega L_{nocore} (-R_{cut}^{empty} + R_{cut}^{full}) \tag{2.5.10}$$

R_w is the dc wire resistance of the winding, L_{nocore} is the inductance of the toroid coil without the core and is given by Eq. (A.2.8). $R_{cut}^{full}, R_{cut}^{empty}, X_{cut}^{full}, X_{cut}^{empty}$ are the resistances and reactances when the slit of the toroid is full/empty (the subscript "cut" stands for the core with slit). It is obvious that $\tilde{A}$, $\tilde{B}$, $\tilde{U}$ and $\tilde{V}$ can be evaluated by measuring $R_{cut}^{full}, R_{cut}^{empty}, X_{cut}^{empty}, X_{cut}^{full}$ and by knowing γ_g, L_{nocore} which are given by the geometrical characteristics of the toroid, that is L_1, L_2, N_t and A_{cs}. From Eq. (2.5.6) we can calculate the components of the permeability, which are

$$\mu' = -\frac{\tilde{A}\tilde{U} + \tilde{B}\tilde{V}}{\tilde{U}^2 + \tilde{V}^2}, \qquad \mu'' = \frac{\tilde{B}\tilde{U} + \tilde{A}\tilde{V}}{\tilde{U}^2 + \tilde{V}^2} \tag{2.5.11}$$

Susceptibility is, then, given as

$$\chi' = \mu' - 1 = -\frac{\tilde{A}\tilde{U} + \tilde{B}\tilde{V}}{\tilde{U}^2 + \tilde{V}^2} - 1, \qquad \chi'' = \mu'' = \frac{\tilde{B}\tilde{U} + \tilde{A}\tilde{V}}{\tilde{U}^2 + \tilde{V}^2} \tag{2.5.12}$$

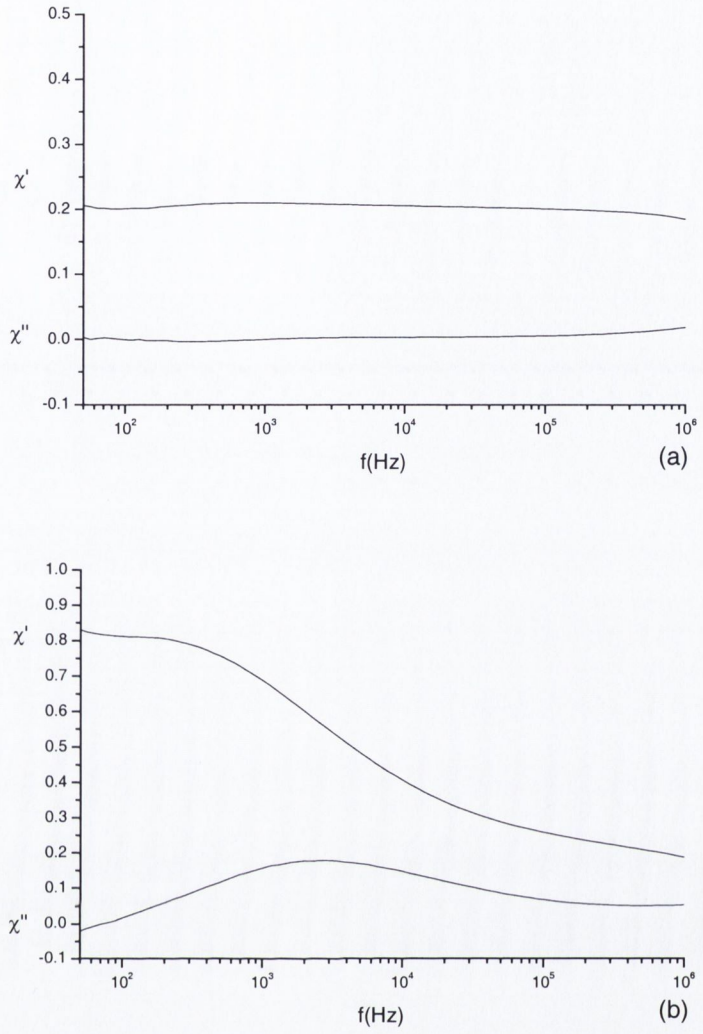

Figure 2.5 Magnetic susceptibility of magnetite in water measured in frequency range 50 Hz-1 MHz: (a) without absorption peak, (b) with absorption peak. An absorption peak, at such low frequencies, denotes aggregation.

We calculate the susceptibility by evaluating Eq. (2.5.12) by importing the measured data ($R_{cut}^{full}, R_{cut}^{empty}, X_{cut}^{full}, X_{cut}^{empty}$) into a computer program, written in Matlab*. In Fig. (2.5 a-b) we show examples of magnetic susceptibility of measured ferrofluids, both magnetites in water, with the toroid technique, in a frequency range 50 Hz-1 MHz. The fluid of Fig (2.5 a) has saturation magnetisation M_s^F=411 G and no Brownian loss peak is observed. The susceptibility of the fluid of Fig. (2.5 b) has an absorption Brownian peak at low frequency (2,500 Hz), which means the relaxation time of the particle is

* Matlab is a high-performance language for technical computing developed by The Math Works Inc. It integrates computation, visualisation and programming. The main features of this programming language and examples of the computational and the fitting programs written and used for this work are given to Appendix B.

large. Large relaxation times denote agglomeration, since aggregated particles rotate slowly, having a characteristic profile like that of Fig.(2.5 b). The toroid, which is used for both measurements, has number of turns N_t=20 and winding resistance R_w=0.05 Ω. The core has circumference 150 mm, cross-sectional area A_{cs}=9.52×9.52 mm^2=90.7 mm^2 and the length of the slit is L_1=0.3 mm. Above 1 MHz measurement is prohibited because the toroid resonates. For measurements below 50 Hz another toroid with bigger inductance (N_t=80) is more suitable, since the bridge cannot observe the changes of the impedance below this frequency.

2.6 Permittivity measurements by using plate and cylindrical capacitor.

We can measure the dielectric relative permittivity of a sample by using a plate or a cylindrical capacitor adapted to the HP 4192A bridge. It is necessary to measure the capacitance with the cell empty and full. Unfortunately this technique is limited by the highest impedance value (100 MΩ) that the instrument can measure. Because the capacitance of both, plate and cylindrical, capacitors is small (approximately 0.1-0.5 pF), the associated impedance is large and exceeds the limit of 100 MΩ for frequencies below 50 kHz. The inductance of such capacitors is small and has little effect on the value of the total impedance. Thus the capacitor is not causing resonance at high frequencies and it is measuring accurately up to 13 MHz (instrument's highest possible frequency).

Fannin et al [18] investigating the magneto-dielectric effect of ferrofluids in the frequency range 50 kHz-1 MHz, used a parallel plate capacitor of area 0.25 cm^2 and 10 μm separation. It is not easy to use a capacitor with a so small a slit and extra care should be taken when the sample is inserted into the slit in order for the whole gap to be covered by the fluid. A more adequate plate capacitor is the HP 16451B dielectric test fixture [19,20]. It is possible to adapt a variety of electrodes of several dimensions and shapes on this fixture. A micrometer, which is adjusted by a rotating knob, moves the guarded electrode, allowing the user to adjust the distance between the electrodes. The accuracy of the micrometer is 10 μm and the maximum distance between the electrodes can be 1 cm. The active area of the electrode, which is used for our measurements, is a circular disc of diameter 10 mm. Concentrically to the active area there is a guard ring, separated from the active area by a tiny air gap. The purpose of the existence of this guard ring is to keep the electrical field uniform at the edge of the active area and, thus, to eliminate the stray capacitance. A method of parallelism of the guarded electrode with respect to the

unguarded electrode is applied before calibration. This method is based on an optical observation together with an electrical measurement of the capacitance value of the empty cell [19]. After parallelism, an open/short calibration has to be performed. The HP 16451B fixture has an extension cable, which shorts the guarded electrode to the H_{cur} and H_{pot} terminals of the HP 4192A bridge and the unguarded electrode to the L_{cur}, L_{pot} terminals. The HP 16457B fixture is designed to measure solid materials but it is possible to measure liquids by inserting the liquid into a sample holder. The sample holder is a non-electrically conducting (plastic) cylindrical cell with diameter bigger than the diameter of the electrode's active area (10 mm), so that it does not affect the measurement. The capacitance without the sample under test is given by

$$C_0 = \varepsilon_0 \frac{A_p}{d} \tag{2.6.1}$$

where A_p = active area of the plate and d= the length between the plates. The electrode used in this work using has a diameter of 10 mm, so $A_p = 7.85\times10^{-5}\,m^3$, and the depth was chosen to be 9.5mm for measuring the dielectric liquids (for solid films, d equals the thickness of the film). Hence the capacitance of the unfilled cell is 7.31×10^{-14} F. The capacitance with the sample in the cell is given by

$$C(\omega) = \varepsilon'(\omega)\varepsilon_0 \frac{A_p}{d} \tag{2.6.2}$$

where $\varepsilon'(\omega)$ is the real component of the relative permittivity of the sample. By dividing the two capacitances we can calculate $\varepsilon'(\omega)$. The imaginary component of ε, which denotes absorption, is given in association with the resistive part of the device, that is $\varepsilon''(\omega) = C''d/\varepsilon_0 A_p = -d/\varepsilon_0 \omega R A_p$, where C'' is the imaginary capacitance. In Fig. (2.6) are shown typical results obtained for solid and liquid dielectrics, in the frequency range between 50 kHz-13 MHz, with the technique described above. Fig. (2.6 a-b) shows the relative permittivity of Si and borosilicate glass films of thickness 0.5 mm. Relative permittivity was measured 3.3 for Si and 52 for borosilicate glass. Fig. (2.6 c) shows the permittivity of a Teflon disc of thickness 0.8 mm, which is 2.1. Fig. (2.6 d-e) shows the result of measuring liquid isoparaffin and liquid propanol, which agree with the expected values, 2.1 and 18 respectively. The gradual fall of $\varepsilon''(\omega)$ of Si and propanol at frequencies below 1 MHz is due to their conductance.

Figure 2.6 Typical dielectrics measured with the HP 16451B plate capacitor:

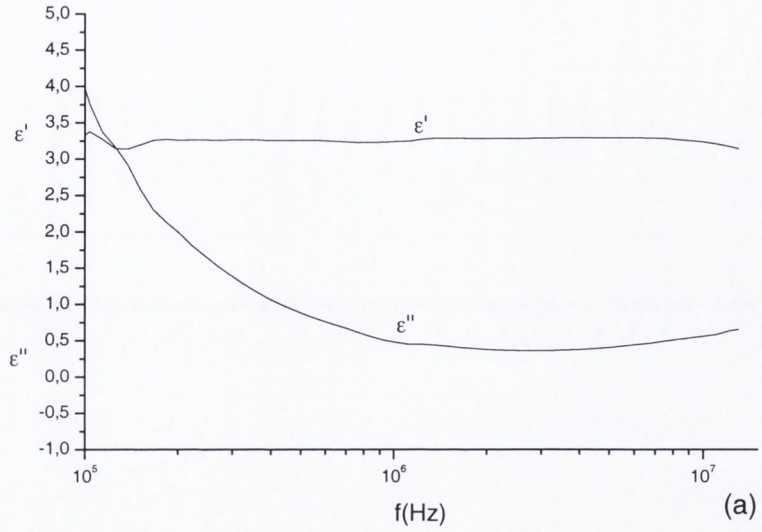

Figure 2.6 (a) Relative permittivity of Si film of thickness 0.5 mm.

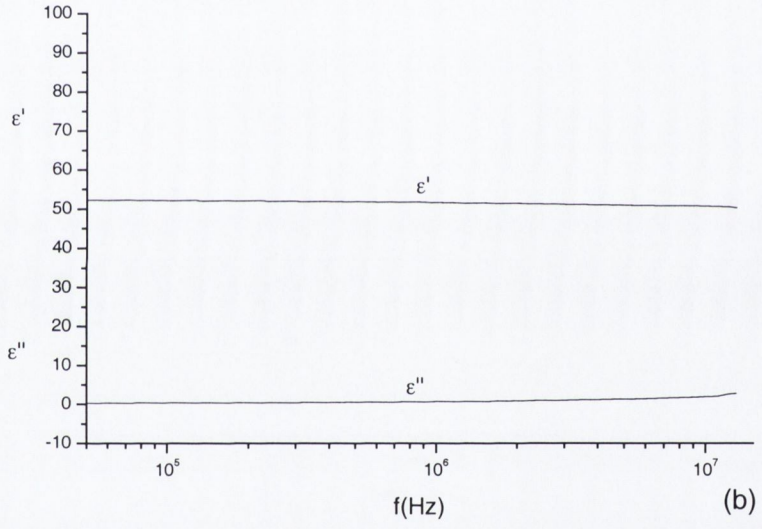

Figure 2.6 (b) Relative permittivity of borosilicate glass film of thickness 0.5 mm.

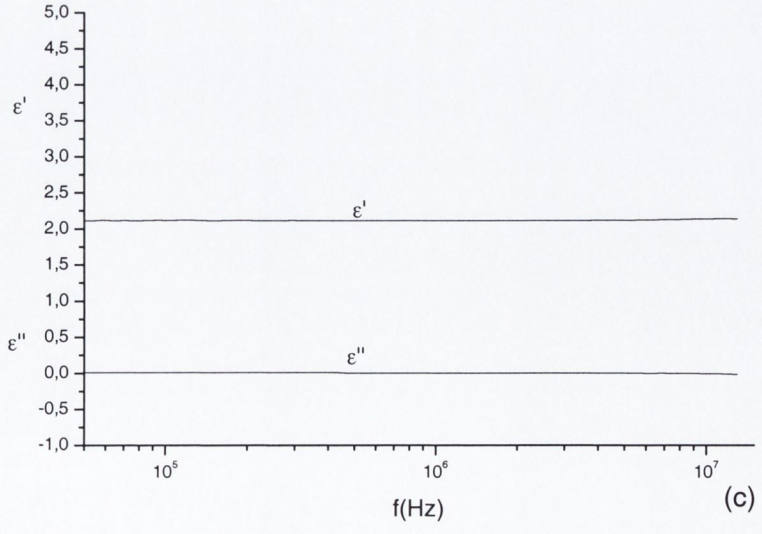

Figure 2.6 (c) Relative permittivity of Teflon of thickness 0.8 mm.

(Continued).

Figure 2.6 Typical dielectrics measured with the HP 16451B plate capacitor:

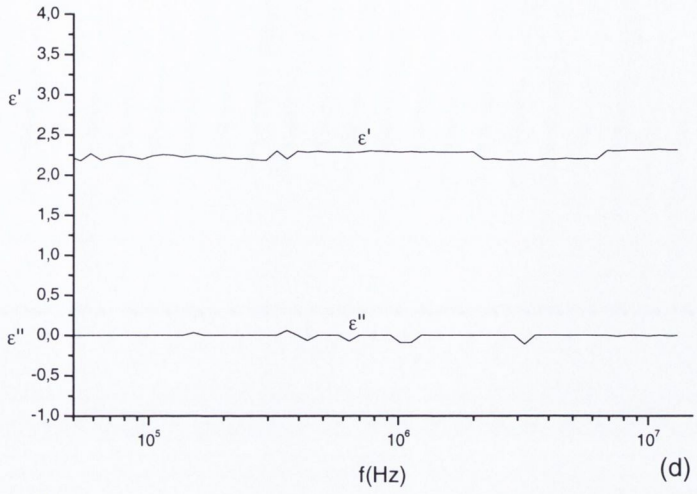

Figure 2.6 (d) Relative permittivity of liquid isoparaffin.

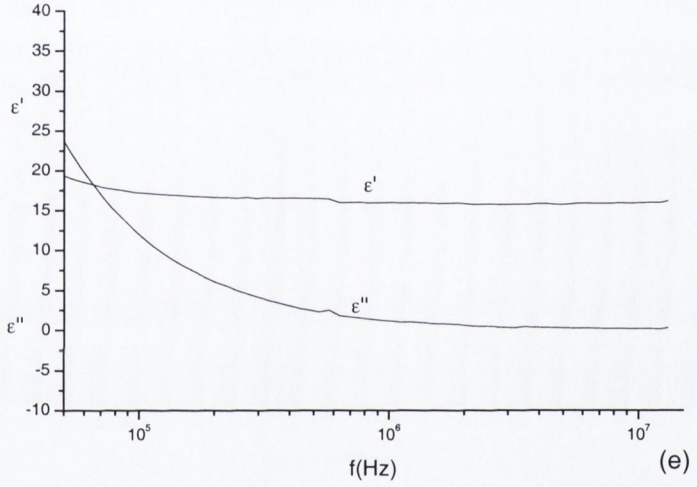

Figure 2.6 (e) Relative permittivity of liquid propanol. All samples were measured at room temperature (20°C).

Figure 2.7 Typical liquid dielectrics measured with the cylindrical capacitor:

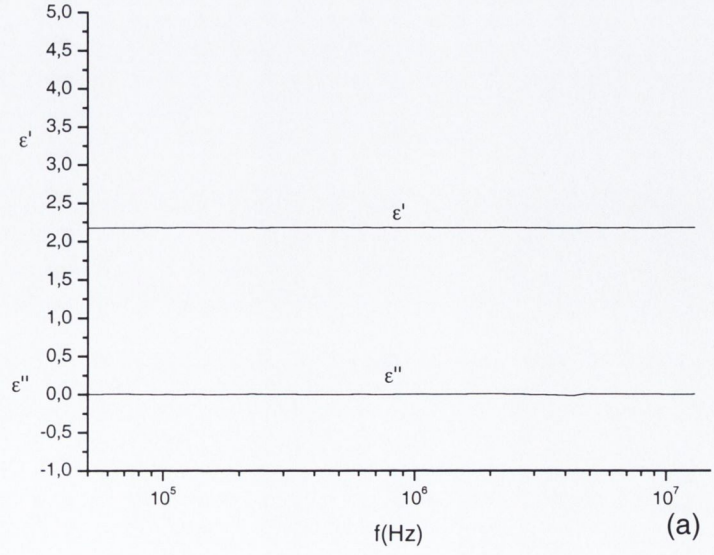

Figure 2.7 (a) Relative permittivity of isoparaffin.

(Continued).

Figure 2.7 Typical liquid dielectrics measured with the cylindrical capacitor:

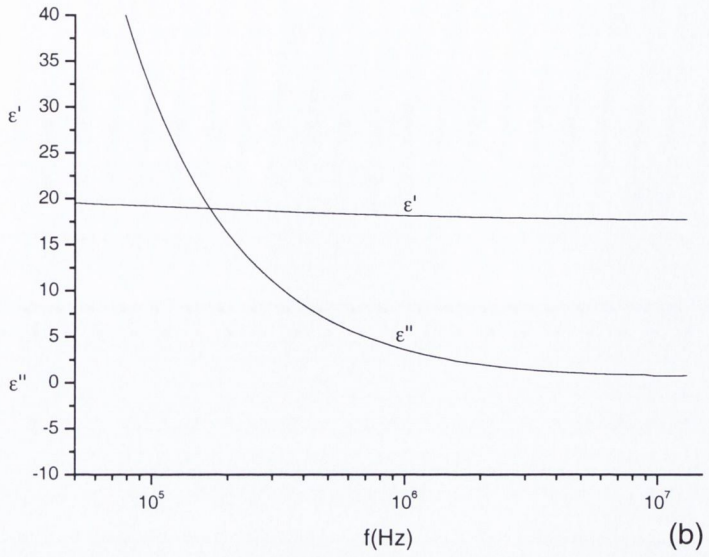

Figure 2.7 (b) Relative permittivity of Propanol.

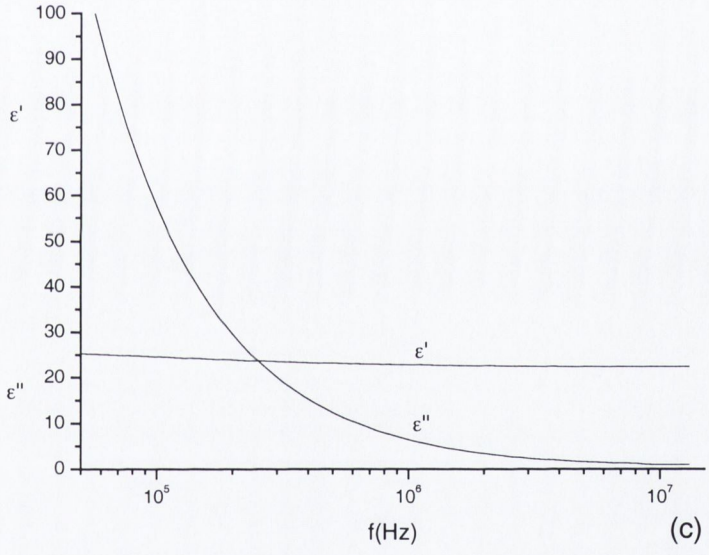

Figure 2.7 (c) Relative permittivity of Ethanol.

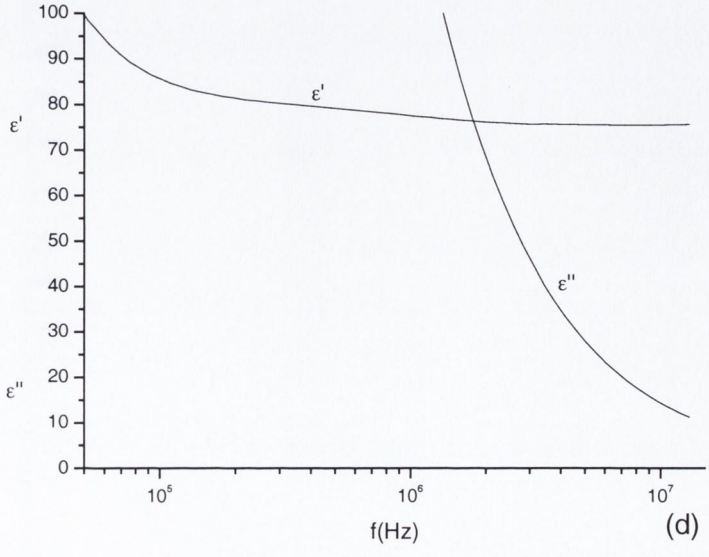

Figure 2.7 (d) Relative permittivity of water. All measurements at room temperature (20°C).

It is also possible to use a cylindrical cell, forming a *cylindrical capacitor*, as a fixture. The measurement of liquids becomes simpler, compared to the method using the plate capacitor, because no sample holder is needed, since the cell itself forms the holder. The cylindrical cell cannot be used for measuring solids and films. The electrical field, $\mathbf{E}(\mathbf{r},t)$, in an empty cylindrical capacitor, of length l, is easily calculated by using Gauss's law (by considering a cylindrical and closed surface concentric to the cell's axis), which yields

$$\mathbf{E}(\mathbf{r},t) = \frac{q_c(t)}{2\pi r l \varepsilon_0}\hat{\mathbf{r}} \tag{2.6.3}$$

where q_c = charge on capacitor. $\mathbf{r}$ is the distance between the axis of the capacitor and the point on which we calculate the field. If the radius of the internal and the external conductor is R_1 and R_2 respectively, then $R_1 \le r \le R_2$. Outside this region the field is zero. The potential difference between the two conductors is found by integration of Eq. (2.6.3) over the distance $R_1 \le r \le R_2$, hence

$$V_{R_1-R_2}(t) = \int_{R_1}^{R_2}\mathbf{E}(\mathbf{r},t)\cdot d\mathbf{r} = \frac{q_c(t)}{2\pi l\varepsilon_0}\int_{R_1}^{R_2}\frac{dr}{r} = \frac{q_c(t)}{2\pi l\varepsilon_0}\ln\frac{R_2}{R_1} \tag{2.6.4}$$

The capacitance, C_0, will be the instantaneous charge divided by the potential difference, hence

$$C_0 = \frac{q_c(t)}{V_{R_1-R_2}(t)} = \frac{2\pi l\varepsilon_0}{\ln\dfrac{R_2}{R_1}} \tag{2.6.5}$$

For a cylindrical capacitor with l=9.5 mm and inner and outer conductor radii of 1.5 mm and 3.5 mm respectively, $C_0 = 6.234\times10^{-13}\,\mathrm{F}$. The capacitance of the cylinder full of dielectric is

$$C(\omega) = \frac{2\pi l\varepsilon(\omega)\varepsilon_0}{\ln\dfrac{R_2}{R_1}} \tag{2.6.6}$$

By dividing the two capacitances we calculate the real relative permittivity. The imaginary component of ε is proportional to the imaginary capacitance $C'' = -1/\omega R$. To connect the cylindrical cell to the four-port terminal of the bridge it is necessary to adapt the HP 16085B four-terminal to a 7mm (APC-7)* connector which connects the inner

* APC-7 connector is a standard Hewlett Packard cylindrical connector with 7mm diameter.

conductor of the cylindrical cell to the H_{cur} and H_{pot} terminals and the outer conductor to the L_{cur} and L_{pot} terminals. It is interesting to compare the permittivity of isoparaffin and propanol measured with the plate capacitor (Fig. (2.6 d-e)) with the permitivities of the same samples measured with the cylindrical capacitor shown in Fig. (2.7 a-b). In Fig. (2.7 c-d) the permittivity of two other typical dielectrics is illustrated: ethanol (ε'=23) and water (ε'=80). The pronounced high values of the imaginary component of permittivity, in all liquid samples measured, is due to the combined effect of *high conductance* and the *double layer* formed by ions on the electrodes.

2.7 Permittivity and permeability measurements by means of the coaxial transmission line technique.

A cylindrical cell, like the one described in the previous sections, may be used for broadband measurements. When the cell behaves as an inductor, capacitance does not contribute much because it is small compared to the inductance and when the cell behaves as a capacitor, inductance does not contribute for the same reason. Again, it is not possible for one cell with the same depth to be used for measurements covering the whole spectrum, from RF to microwaves, however such a wide band may be covered by the combined use of three cells of three different depths. Experimentally we found that a cylindrical inductor with R_1=1.5 mm, R_2=3.5 mm and depth l=9.5 mm is sufficient for magnetic measurements between 1 MHz-1 GHz. A similar inductor, however with length l=1.8 mm, is sufficient for coverage between 100 MHz-6 GHz. For the range 1 GHz-20 GHz it is found that a cell with l=1 mm is adequate. Similar cells cover, approximately, the same bands that are used for dielectric measurements.

The cylindrical cell forms the end of the transmission line. Calibration is performed on the upper plane of the cell. So the reference is taken at the end of the coaxial line, thus the remaining part of the line is considered as a part of the port, and its associated impedance (50 Ω) does not contribute to the measured impedance. The cell behaves as an inductor when the internal and external cylindrical conductors are shorted and it behaves as a capacitor when the conductors are open circuited. Hewlett Packard supports short and open adaptors, for the 7 mm connector, operating sufficiently up to 40 GHz. The short adaptor ensures a perfect connection between the conductors. The open adaptor ensures that no stray capacitance appears on the edge of the open cell. In Fig. (2.8 a) a cross-section of the transmission line is shown with the sample holder of length l. The distance between the port and the cell is denoted by x. This transmission line has an

equivalent electrical circuit (Fig. (2.8 b)) consisting of inductors L in series and capacitors C in parallel. This LC combination has a characteristic impedance $Z_0 = \sqrt{L/C}$ =50 Ω. Only the cell of length l can behave as a pure inductor or a pure capacitor, depending on the termination. The rest of the line (length x) is both inductive and capacitive. In Fig. (2.8 c-d) the equivalent circuits of the line are shown, when the cell is filled with the sample. Since the sample (DUT) has different inductive and capacitive properties than the properties of the line, the section of length l has different values of impedance, $R_{DUT} + i\omega L_{DUT}$ for short circuit and $R_{DUT}/(1 + i\omega R_{DUT} C_{DUT})$ for open circuit. This is the impedance which is measured by the analyser.

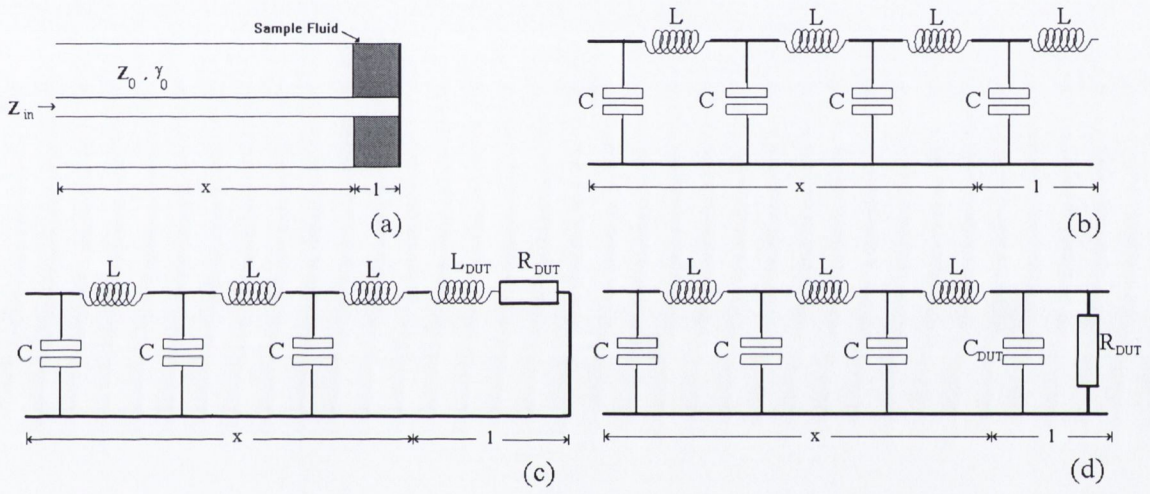

Figure 2.8 (a) Transmission line, incorporating a cell, (b) Equivalent circuit of lossless transmission line, (c) Equivalent circuit of shorted transmission line with the fluid in the cell, (d) Equivalent circuit of open transmission line with the fluid in the cell.

As stated in section 2.4, the reflection method is preferable to the transmission method [14,15]. There are two basic approaches to the determination of μ and ε from the reflection coefficient S_Γ: (a) methods that have used equivalent circuit description and (b) methods that attempt a rigorous solution of the electromagnetic field equations appropriate for the coaxial line. The relative simplicity of the former treatment accounts for its great popularity [27] and the latter approach has been largely restricted to a theoretical development of the forward problem, which is the derivation of S_Γ from known values of μ and ε, and the inverse problem which is the inverse solution of the latter based on a point-matching theory. Several experimentalists have applied the equivalent circuit description, such as Nicolson and Ross [21, 22] who applied a method

with equations connecting μ and ε directly to the reflection coefficient, which is calculated by time-domain reflection measurement or alternatively by frequency-domain reflection measurement. But this model has its disadvantages, namely: (a) an ambiguity in phase must be resolved at each frequency by matching the calculated and measured group delay, (b) this procedure does not work well at frequencies where the sample length is a multiple of one-half wavelength [14]. Scott et al [23] presented a function to map the admittance of the line to the permittivity (and the inverse) by using an open-circuited coaxial line of general length. He demonstrated this by measuring typical dielectric materials. A summary and a criticism of coaxial line reflection methods, of several configurations and terminations, is reviewed by Stuchly et al [24]. They gave general equations applying to all the line terminations they describe.

The model employed in this thesis relates the permittivity and permeability of the material under test (MUT) to the impedance of the filled cell. The instrument itself calculates this impedance from a reflection coefficient measurement, as is described in section 2.4. What is needed are equations that are stable over the frequency range of interest and not dependent on the position of the calibration reference plane. Our method is based on the pioneering work of Roberts and von Hippel [25]. This model requires that the cell be filled completely by the ferrofluid with no air gaps existing between the sample and the holder (the measurement of an MUT with arbitrary shape is also possible by using the fine element method in conjunction with the Newton-Raphson method [26]). We want to derive an expression for μ as a function of the input impedance of the section of the line which is after the calibration plane. We distinguish between two cases: (a) when the termination of the cell is shorted and (b) when the cell is terminated in an open circuit. A full derivation is presented in sections A.3 and A.4 of Appendix A. These models do not take into account the dielectric characteristics of the material. A combined theory, which correlates μ and ε is presented, in section A.5.

Case (a), *cell's termination is a short circuit* (see section A.3): The starting point is to write the input impedance, Z_{in}, at the plane where the transmission line is connected to the port of the analyser (Eq. (A.3.1)) in terms of the characteristics of the line [28] and the input impedance, Z_R, of the cell which is located at distance x from the port of the analyser (Eq. (A.3.9)), in terms of MUT μ and cell's dimensions. By combining these two expressions we can determine the permeability in terms of the input impedance of the line, $Z_{in} = R_{in} + iX_{in}$, as it is described by Eqs. (A.3.13) and (A.3.14), that is

$$\mu' = \frac{\lambda}{2\pi l}\frac{R_{in}^2 \tan(\beta_0 x) + (X_{in} - Z_0 \tan(\beta_0 x))(X_{in} \tan(\beta_0 x) + Z_0)}{(R_{in} \tan(\beta_0 x))^2 + (X_{in} \tan(\beta_0 x) + Z_0)^2} \qquad (2.7.1)$$

and

$$\mu'' = \frac{\lambda}{2\pi l}\frac{R_{in}(X_{in} \tan(\beta_0 x) + Z_0) - (X_{in} - Z_0 \tan(\beta_0 x))R_{in} \tan(\beta_0 x)}{(R_{in} \tan(\beta_0 x))^2 + (X_{in} \tan(\beta_0 x) + Z_0)^2} \qquad (2.7.2)$$

where $\beta_0 = 2\pi/\lambda$ is the phase coefficient of the line (line is approximately lossless, thus the attenuation $\alpha_0 = 0$). The above equations are referred to the case when the calibration plane is in an arbitrary position, x, far from the analyser's port. In our setup the calibration plane is the termination (upper face) of the cell, thus $x = -l$. $Z_{in} = R_{in} + iX_{in}$ can also be taken as the impedance measured by the instrument on the calibration plane, since the rest of the line is part of the port. We can calculate μ by importing the data into a computer program, developed in Matlab, which applies Eqs. (2.7.1), (2.7.2) for $x = -l$=length of the cell.

Case (b), *cell's termination is an open circuit* (see section A.4): By following a similar procedure we are able to derive the expression of ε, uncorrelated to μ. The termination of the cell, here, is open. This ensures that the electric field is large and the magnetic field is small within the sample, provided that the wavelength within the sample is much greater than the sample thickness. As it is shown in section A.4 we can express the permittivity as

$$\varepsilon' = \frac{\lambda}{2\pi l}\frac{(Z_0 + X_{in} \tan(\beta_0 x))(Z_0 \tan(\beta_0 x) - X_{in}) - R_{in}^2 \tan(\beta_0 x)}{(R_{in} \tan(\beta_0 x) - X_{in})^2 + R_{in}^2} \qquad (2.7.3)$$

and

$$\varepsilon'' = \frac{\lambda}{2\pi l}\frac{(Z_0 + X_{in} \tan(\beta_0 x))R_{in} + (Z_0 \tan(\beta_0 x) - X_{in})R_{in} \tan(\beta_0 x)}{(R_{in} \tan(\beta_0 x) - X_{in})^2 + R_{in}^2} \qquad (2.7.4)$$

The equations derived above for μ and ε are valid only under the assumption that the wavelength is much greater than the sample thickness. This assumption is not usually true for high frequencies, thus abnormal behaviour occurs above 100 MHz. Dimensional resonance takes place when the depth is an odd multiple of quarter wavelengths. For example at f=1 GHz the wavelength in the water is approximately (for ε=80, μ=1) $\lambda = 1/(f\sqrt{\varepsilon\varepsilon_0\mu\mu_0})$ =3.3 cm, giving λ/4=8.5 mm which is comparable to the cell's depth. Thus, a sequence of resonances appear on the spectrum every $f = 4/(n\lambda\sqrt{\varepsilon\varepsilon_0\mu\mu_0})$ (Hz), n=1, 3, 5, ... For the case of water, resonance will occur at 1, 3, 5 ... GHz

approximately. The reduction of the sample depth enables reliable results to be obtained at higher frequencies. However for water a much smaller sample depth, approximately 0.1 mm, would have to be used to obtain reliable results up to 6GHz. Such a small depth is difficult to realise in practice. Fortunately for non-water based ferrofluids, such as these based on paraffin or kerosene, μ and ε are small thus the propagation velocity is large and the resonance frequency one order higher than water-based fluids.

For satisfactory experimental results we develop our model in a manner in which μ and ε will contribute simultaneously to the calculation. Even here there will still be restrictions, which will limit the measurement up to 20 GHz. This is the highest we can go by using the fixed cell depths stated before. To improve the model, we notice that when the depth of the sample becomes an appreciable fraction of the wavelength then, for a short circuited line, the electrical field is not eliminated, as we considered before. When this happens it is no longer possible to determine μ independently of ε and vice versa. Two sets of impedance measurements have to be taken: one with the sample short circuited and one with the sample open circuited. Both sets of impedance measurements are cast as a set of two simultaneous equations in a computer program where μ and ε are determined. The combined expressions have been derived in section A.5 of Appendix A and they are given by

$$\mu = \sqrt{(\tilde{P} + i\tilde{Q})(\tilde{X} + i\tilde{Y})} \tag{2.7.5}$$

and

$$\varepsilon = \sqrt{\frac{\tilde{X} + i\tilde{Y}}{\tilde{P} + i\tilde{Q}}} \tag{2.7.6}$$

where $\tilde{P}$ and $\tilde{Q}$ denote the real and the imaginary parts as defined by Eq. (A.5.10) and $\tilde{X}$ and $\tilde{Y}$ represent the real and imaginary components as given in Eq. (A.5.14). All the parameters $\tilde{P}$, $\tilde{Q}$, $\tilde{X}$ and $\tilde{Y}$ can be determined from the impedance measurements.

Figure (2.9) shows the magnetic susceptibility and permittivity measurement obtained for a ferrofluid sample of magnetite in isoparaffin with a fluid with M_s^F=525 G and particle radius 4.3 nm by using the transmission line technique. The accurate Eqs.(2.7.5), (2.7.7) were used to calculate χ and ε. Two different impedance measurement techniques were used: the RF I-V method (HP 4291B analyser) with a cell of 9.5 mm depth and the networking method (HP 8753C analyser) with a cell of 1.8 mm depth. The first was used for frequencies between 1 MHz-1.8 GHz and the second in the range 100

MHz-6 GHz. The frequency at which the data was combined was 500 MHz. The resonance frequency, f_{res}, was 1.8 GHz and the frequency of maximum absorption, f_{max}, was 1.2 GHz, which are typical values for magnetites. The permittivity of this ferrofluid has a value of ε=4.25 at 1 MHz and it shows a relaxational (Brownian) behaviour in the GHz range, giving a Debye peak at f_{max} =1.6 GHz.

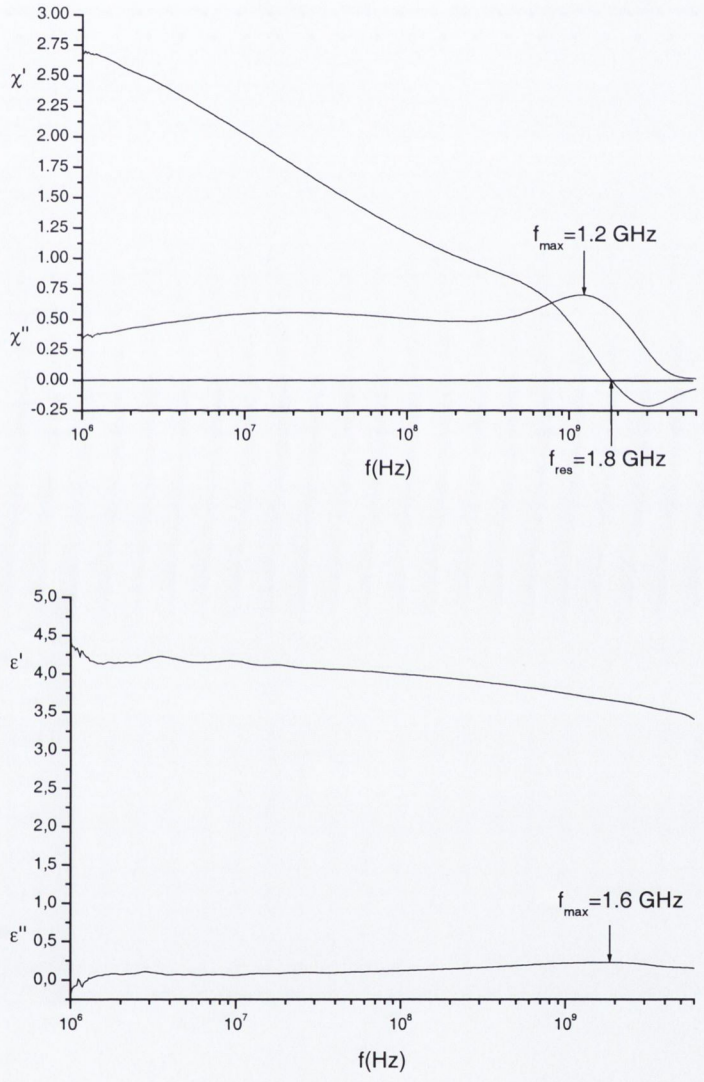

Figure 2.9 Spectrums of χ and ε of an isoparaffin-based ferrofluid with magnetite particles in a frequency range 1 MHz-6 GHz. The resultant spectra are obtained by combining the data of two independent measurements: one with a 9.5 mm cell depth and one with a 1.8 mm cell.

2.8 Conclusions and suggestions for future work

Impedance measurement techniques, which are used for frequencies between 10 Hz-20 GHz for permeability measurements and 50 MHz-30 GHz for permittivity measurements, have been presented. Impedance measurements are realised by the combined use of an auto-balanced bridge (HP 4192A, 5 Hz-13 MHz), a vector meter

analyser concerned to the RF I-V method (HP 4291B, 1 MHz-1.8 GHz) and two network analysers (HP 8753C, 3 MHz-6 GHz, and HP 8722D, 50 MHz-40 GHz). The auto-balanced method is based on the principle of the balanced bridge, with the instrument automatically covering a wide frequency band. This is the most accurate of all the methods considered here and it also covers the widest impedance range. The RF I-V method is based on digital analysis of the vector voltage measured across the MUT and the vector current passing through the MUT. This method can be extended up to 3GHz with reduced impedance range. The networking technique extends up to the microwave frequencies but the MUT's impedance should be close to the characteristic impedance of the coaxial line. To realise permeability measurements with the auto-balanced bridge method it is necessary to use a toroid with sufficient dimensions and number of turns in order to ensure an adequate inductance measurement, in accordance with the capability of the instument. It is required that the toroid is measured full and empty. The measurement frequency limits are strongly dependent on the toroid's characteristics. A toroid for coverage between 50 Hz-1 MHz has number of turns N_t=20 and winding resistance R_w=0.05 Ω. The core of the toroid has a circumference of 150 mm, cross-sectional area A_{cs}=9.52×9.52 mm^2=90.7 mm^2; the length of the slit is L_l=0.3 mm. For below 50 Hz a bigger winding (80 turns) should be used. The model which evaluates the magnetic susceptibility from impedance's data is given by Eqs.(2.5.6)-(2.5.12). For permittivity measurements, either a plate or a cylindrical capacitor can be used. Empty and full measurement of impedance are required, and the model which evaluates ε is expressed by Eq.(2.6.2) for the plate capacitor and Eq.(2.6.6) for the cylindrical capacitor. In the RF I-V and networking methods μ and ε are estimated by the model described in section 2.7, the final form of which is given by Eqs.(2.7.39), (2.7.40). There are three different cells, of 9.5 mm, 1.8 mm and 1mm depth, to be used for three measurement frequency ranges, namely, 1 MHz-1 GHz, 100 MHz-6 GHz and 1 GHz-20 GHz. The resultant values μ and ε is obtained by combining the three spectra corresponding to the three frequency ranges. Dimensional resonance does not permit complete measurements above 20 GHz with the coaxial cell method.

Alternative experimental techniques, for measurements outside the frequency range considered in this thesis, exist in the literature. For permeability measurements below 10 Hz the magneto-optical method [29, 30] is strongly recommended. This method has been compared with Fannin's toroidal technique at frequencies 1 Hz-10 kHz [29]. Both

methods give identical results in the frequency range beyond 100 Hz, but below 100 Hz the magneto-optical method is more accurate. This inaccuracy of the toroid method is due to the limited measuring accuracy of the bridge (even 1% uncertainty on impedance is giving a significant error in μ). To extend the measuring capabilities to frequencies above 20 GHz, the only way forward appears to be with free space propagation, which can be realised by means of antennas [31-33].

References:

1. Scaife B.K.P., *Complex Permittivity*, English University Press, London, (1971).
2. Agilent Technologies, *Impedance Measurement Handbook*, 2nd Edition, (2000).
3. Hewlett Packard, Operational and Service Manual, HP 4192A LF Impedance Analyser, (1982).
4. Fannin P.C., Scaife B.P.K., Charles S.W., *J. Phys. E., Sci. Instrum.*, **19**, 238, (1986).
5. Hewlett Packard, *Using the HP-IB Interface with Microsoft Windows*, (1991).
6. Hewlett Packard, *Using the HP-IB Interface and Command Library with DOS*, (1991).
7. Hewlett Packard, *Programmer's Guide, HP 8719D/20D/22D Network Analyser*, (1997).
8. Hewlett Packard, *HP 4291B RF Impedance/Material Analyser Programming Manual*, (1998).
9. Hewlett Packard, *HP 4291B RF Impedance/Material Analyser Operational Manual*, (1998).
10. Agilent Technologies, *PN 4294a New Technologies for Accurate Impedance Measurements (40Hz-110MHz)*, Product Note.
11. Agilent Technologies, *PN 4291-1 New Technologies for Wide Impedance Range Measurements to 1.8GHz*, Product Note.
12. Hewlett Packard, *HP 8753C Network Analyser, User's Guide and Quick Reference*, 2nd edition, (1990).
13. Hewlett Packard, *HP 8719D/8720D/8722D Network Analyser User's Guide*, (1997).

14. Baker-Jarvis J., Vanzura E.J., Kissick W.A., *IEEE Transactions on Microwave Theory and Techniques*, Vol **38**, No 8, 1096, (1990).
15. Vincent D., Jorat L., Monin J., Noyel G., *Meas. Sci. Technol.*, **5**, 990, (1994).
16. Fannin P.C., Relihan T., Charles S.W., *J. Phys. D, App. Phys.*, **28**, 2003, (1995).
17. Brockman F.G., Dowling P.H., Steneck W.G., *Phys. Rev.*, **77**, NO. 1, 85, (1950).
18. Fannin P.C., Scaife B.K., Charles S.W., *Journal of Magnetism and Magnetic Materials*, **122**, 168, (1993).
19. Hewlett Packard, *HP 16451B Dielectric Test Fixture, Operational and Service Manual*, (1992).
20. Hewlett Packard, *Dielectric Constant Measurement of Solid Materials*, Application Note 380-1, (1989).
21. Nicolson A.M., *IEEE Transactions on Instrumentation and Measurement*, Vol **IM-17**, No 4, 395, (1968).
22. Nicolson A.M., Ross G.F., *IEEE Transactions on Instrumentation and Measurement*, Vol **IM-19**, No 4, 377, (1970).
23. Scott W.R., Smith G.S., *IEEE Transactions on Instrumentation and Measurement*, Vol **IM-35**, No 2, 130, (1986).
24. Stuchly M.A., Stuchly S.S., *IEEE Transactions on Instrumentation and Measurement*, Vol **IM-29**, No 3, 176, (1980).
25. Roberts S., von Hippel A.R., *J. App. Phys.*, **17**, 610, (1946).
26. Deshpande M. D., Reddy C.J., *Application of FEM to Estimate Complex Permittivity of Dielectric Material at Microwave Frequency Using Waveguide Measurements, NASA Technical Report*, CR-198203, pp. 24, (1995).
27. Athey T.W., Stuchly M.A., Stuchly S.S., *IEEE Trans. Microw. Theory Tech.*, **MTT-30**, 82, (1982).
28. Kraus J.D., *Electromagnetics*, McGraw-Hill, 4th Edition, (1992).
29. Payet B., Siblini A., Blanc-Mignon M.F., Noyel G., *IEEE Transaction on Magnetics*, Vol **35**, No 3, 2018, (1999).
30. Hasmonay E., Depeyrot J., Sousa M.H., Tourinho F.A., Barci J.C., Perzynski R., *Journal of Magnetism and Magnetic Materials*, **201**, 195, (1999).
31. Scott W.R., Smith G.S., *IEEE Transactions on Antennas and Propagation*, Vol **AP 34**, No 7, (1986).

32. Smith G.S., Scott W.R., *IEEE Transactions on Antennas and Propagation*, Vol **AP 35**, No 8, (1987).
33. Garcia-Ruiz I., Aviles-Castro C.D., Jardon-Aguilar H., *Applied Microwave and Wireless*, **Vol 13**, No 6, 56, (2001).

Chapter 3

Brownian relaxation in ferrofluids at frequencies below 1MHz and susceptibility's dependence on polarising field.

3.1 Introduction

The magnetic susceptibility is strongly dependent on the polarising field as the magnetisation curves of Fig. (1.4) demonstrate. There are two ways of studying this dependence: (a) by varying the amplitude of the alternating exciting magnetic field, $\mathbf{h}_a$, and (b) by superimposing an alternating field, $\mathbf{h}_a$, on a biasing static field, $\mathbf{H}_s$, and varying the latter. The field dependence of χ can be easily understood from the profile of the magnetisation curve. The magnetisation curve of a paramagnetic system is described by the Langevin function. The magnetic susceptibility, which is given by the derivative of magnetisation with respect to the instant field (alternating or bias or both), changes gradually with the field. The tangent of the magnetisation curve is a decaying function thus we expect that the susceptibility will decrease with increasing field. For the case of a biasing static field, $\mathbf{H}_s$, the magnetisation vector is trying to align in the $\mathbf{H}_s$ direction. For an alternating field the magnetisation vector tries to follow the oscillations. In both cases the susceptibility is dependent on the relative direction of the external field and the direction $\hat{\mathbf{h}} = \mathbf{H}_A / |\mathrm{H}_A|$ of the anisotropy axis which, when the moment is blocked, tries to align itself in the direction of the external field. If both alternating and static fields are simultaneously applied, with the condition that the alternating field is much smaller than the static field, then the magnetic moment vector, $\boldsymbol{\mu}_m$, is orientated in the direction of $\mathbf{H}_s$, because $\boldsymbol{\mu}_m$ is blocked, and at the same time is agitated (deviates) away from this direction, due to the influence of the small alternating field. In this case the susceptibility is dependent on the relative direction of the external fields. Thus we define the parallel susceptibility, $\chi_{\parallel}(\mathrm{H}_s + \mathrm{h}_a)$, where both the alternating field component and the static field are oriented in the same direction and the perpendicular susceptibility,

$\chi_{\perp}(H_s + h_a)$, where the alternating field component is oriented transversely to the biasing field direction. This situation is similar to that described in section 1.4 which described the case of static and high frequency applied fields in perpendicular and parallel directions with respect to internal anisotropic field, $\mathbf{H}_A$, direction (easy axis). In the following study we will neglect the effect of the internal anisotropy field, by considering that the $\boldsymbol{\mu}_m$ vector is blocked, which means that the particle behaves as if it were rigid. This can happen only when high potential-barriers ($\sigma \rightarrow \infty$) appear in the magnetic core. The result is that the Néel relaxation mechanism does not operate. This consideration is realistic since the relaxation we observe below 1MHz, is mainly Brownian. The assumption that $\boldsymbol{\mu}_m$ is blocked solves a lot of computational problems and simplifies the averaging procedure and the relevant integral equations.

The functions $\chi_{\parallel}(H_s + h_a)$ and $\chi_{\perp}(H_s + h_a)$ are decay functions of the biasing static field, H_s. Both susceptibilities gradually decrease by increasing the biasing field. Their difference, $\chi_{\perp} - \chi_{\parallel}$, has a maximum value of $\xi_m = \mu_m H_s / k_B T = \xi_1 = 3.72$. From that value of ξ_m we are able to estimate the magnetic moment, μ_m, and consequently the magnetic radius of the nanoparticle. This method is valid only for non-aggregated ferrofluids (a single magnetic volume is not defined for the case of agglomerated particles). Measurements of $\chi_{\parallel}(H_s + h_a)$, $\chi_{\perp}(H_s + h_a)$ and $\chi_{\perp} - \chi_{\parallel}$ are shown in section 3.3.

The functions $\chi_{\parallel}(H_s + h_a)$ and $\chi_{\perp}(H_s + h_a)$ can also be easily combined with the Debye theory in such a way that the modified Debye equation describes both the biasing field dependence and the alternating field dependence. The static biasing field affects the value of the static susceptibility, χ_0, and the transverse and longitudinal relaxation times, whilst the alternating field affects the dispersion according to the Debye theory. Experimental evidence is incorporated in section 3.4.

The Debye theory can be expanded to take into account the nonlinear effect of the relative permeability. Coffey and Paranjape [1] have shown theoretically that there are higher order terms of the external field which should be added in the Debye expression. They show, for the dielectric case, a relaxation due to the nonlinear behaviour of the dielectric. The magnetic analogue of the latter theory is well suited for the case of the ferrofluids, in which we are able to observe the nonlinear effects (section 3.5).

Appropriate fits to the measured susceptibility data show the accuracy of the models. It is necessary to take account of the distribution of particle sizes. Because of the importance of applying the distributions to the natural quantities, we start the next section by introducing the various kinds of distribution functions with application to Brownian relaxation.

3.2 Distribution functions with application to Brownian relaxation.

The distribution of a natural quantity, such as a particle's radius or the anisotropy constant, of a chaotic ensemble of particles must be inversely exponentially dependent on the ratio of the deviation of their values from their mean to their standard deviation. This inversely exponential form makes the distribution have the same shape as the natural Maxwell-Boltzmann distribution in which the probability function is inversely proportional to the ratio of the internal kinetic energy of the system to its thermal energy (mean energy). These kinds of distributions have a characteristic "bell" shape and they can be symmetrical or asymmetrical about the mean. Normal (gaussian) and Cole-Cole distributions are symmetrical. Other distributions, such as log-normal and Nakagami, are not symmetrical and the usefulness of this property is that the most probable value (maximum peak) is different from the mean (average) value. Distributions of other shapes, such as the Fröhlich distribution which is rectangular, may also be used but they do not describe the system naturally.

As is already stated in the previous chapter, the appropriate distribution is that which obtains the best possible fit. Thus, only after repeated fitting of several distributions, can we be able to decide which one can adequately describe the system. It is possible for two different distributions to attain the same good fit. In this case both distributions are sufficient and either can be used.

The distributions involved are functions of a free variable, x, which represents a natural quantity (e.g. radius or anisotropy constant), the mean, $\langle x \rangle$, and one more parameter which usually effects the broadness of the function's curve. This parameter is usually the normalised standard deviation, σ_x, with respect to the mean value $\langle x \rangle$. σ_x is defined, for the discrete case, as

$$\sigma_x = \frac{\sqrt{\sum_{i=1}^{n} (x_i - \langle x \rangle)^2}}{\langle x \rangle} \qquad (3.2.1)$$

where n is the number points of the distribution. n is the number of parameter's individual values which is extremely large so it can be considered to tend to infinity. Thus the previous expression of σ_x can be written in the continuum limit as

$$\sigma_x = \frac{\sqrt{\int_{x_{min}}^{x_{max}} (x - \langle x \rangle)^2 dx}}{\langle x \rangle} \qquad (3.2.2)$$

where x_{min} and x_{max} are the minimum and maximum values that the natural variable x can take.

Figure 3.1 Distribution functions of an arbitrary random variable x:

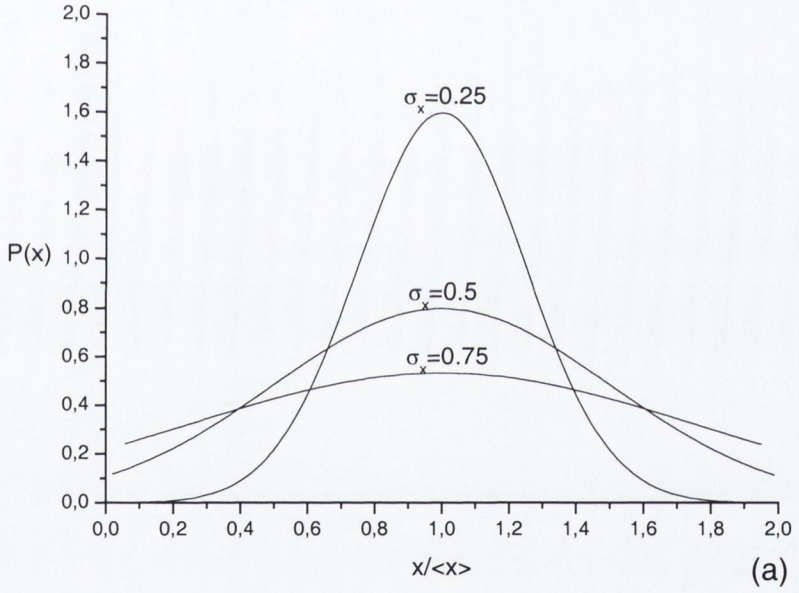

Figure 3.1 (a) normal distribution.

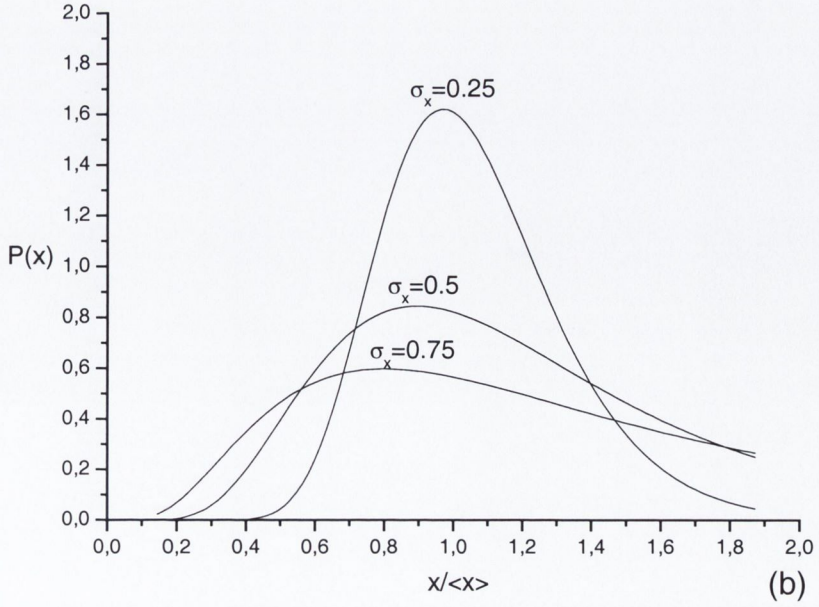

Figure 3.1 (b) log-normal distribution.

(Continued).

Figure 3.1 Distribution functions of an arbitrary random variable x:

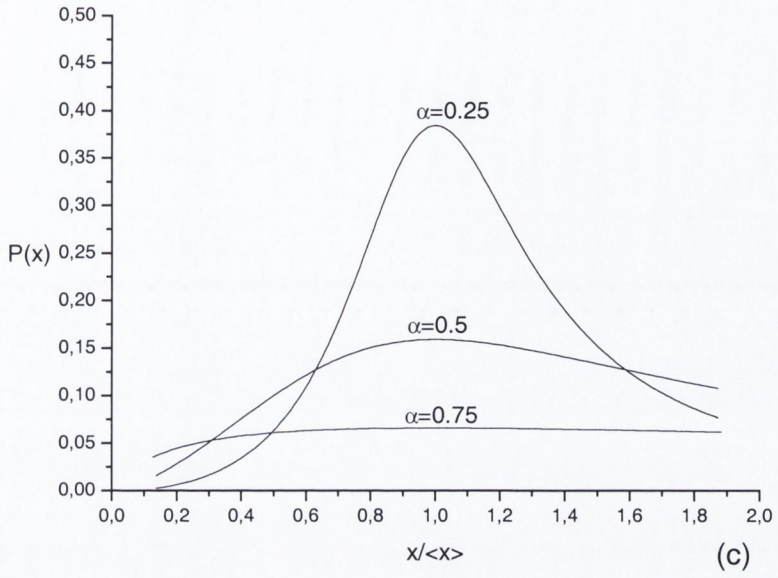

Figure 3.1 (c) Cole-Cole distribution.

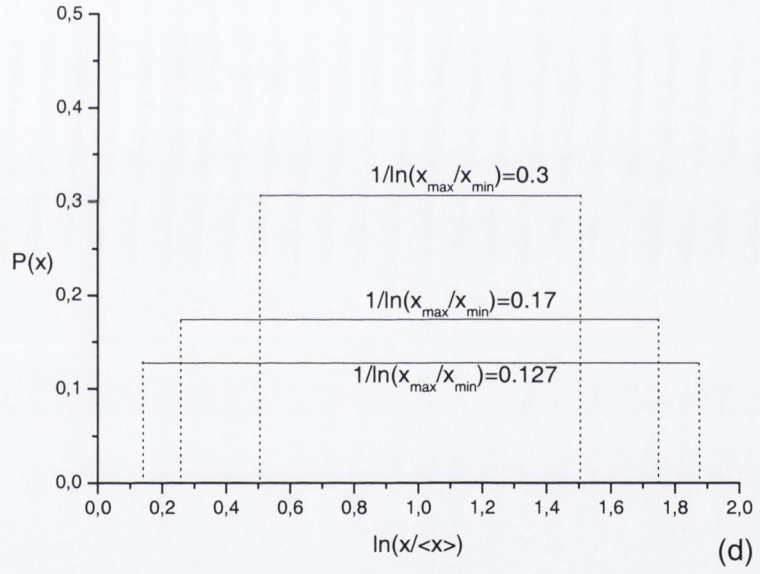

Figure 3.1 (d) Fröhlich distribution.

The normal (gaussian) distribution [2] is by far the most popular due to its simplicity and its symmetry. The symmetry ensures that if the natural parameter is, for example the radius, then the particles with bigger radii than the mean radius have the same probability of occurrence as the particles with radii smaller than the mean. The normal distribution of an arbitrary variable x with mean value $\langle x \rangle$ and normalised (to the mean) standard deviation σ_x is given by the expression,

$$P(x) = \frac{1}{\sigma_x \sqrt{2\pi}} \exp\left[-\frac{1}{2} \left(\frac{\frac{x}{\langle x \rangle} - 1}{\sigma_x} \right)^2 \right] \qquad (3.2.3)$$

A plot of the above equation for several values of σ_x is presented in Fig. (3.1 a). The normal distribution is symmetrical about $\langle x \rangle$, the point at which the function's maximum appears. As seen from the graph, increasing σ_x results in the decrease of the maximum peak and the widening of P(x).

The following equation describes the log-normal distribution function [2], which is the natural logarithm of x, normally distributed:

$$P(x) = \frac{1}{\sqrt{2\pi\sigma'_x}} \exp\left[-\frac{1}{2} \frac{(\ln x - \ln(x/\sqrt{\sigma_x^2 + 1})^2}{\sigma'_x} \right] \qquad (3.2.4)$$

where $\sigma'_x = \ln(1 + \sigma_x^2)$. The usefulness of the log-normal distribution is that it does not allow x to have negative values. Negative values are prohibited for the sort of natural quantities we encounter (i.e. r_p and K). A plot of log-normal distribution is shown in Fig. (3.1 b) for various values of σ_x.

The Nakagami distribution [3], a plot of which has been shown in Fig.(1.7 d) for various values of the width parameter β, is described by the following relation

$$P(x) = \frac{2\beta^\beta}{\Gamma(\beta) W^\beta} x^{2\beta-1} \exp(-\beta x^2 / W) \qquad (3.2.5)$$

where the scale parameter, W, is defined as

$$W = \frac{1}{n} \sum_{i=1}^{n} x_i^2 \qquad (3.2.6)$$

with n=number of distribution points. Both the scale parameter, W, and the width parameter, β, affect the broadness of the curve. The Nakagami distribution is asymmetrical. This asymmetry is effected by β which for small values (β<1) moves the peak to the left of $\langle r_p \rangle$ and for bigger values (β>3) moves the peak to the right of $\langle r_p \rangle$.

The Cole-Cole distribution [4] (not to be confused with the Cole-Cole exponent parameter, $1-\alpha$, described in section (1.4)) does not contain any exponential term, but it does have a "bell" shape. The equation describing this distribution is:

$$P(x) = \frac{\sin(\pi\alpha)}{2\pi(\cosh(1-\alpha)\ln[(x/\langle x \rangle)^m] - \cos(\pi\alpha))} \qquad (3.2.7)$$

where $0 \leq \alpha \leq 1$ is the Cole-Cole parameter. The exponent m denotes that the logarithm may be dependent on a power of the distributed physical quantity x. For example if x is considered to be the volume, v_p, or the relaxation time, τ_B, of the nanoparticle then m=1, but if it is considered to be the radius, r_p, then m=3. That means that by choosing any parameter we want (v_p, τ_B, or r_p) the effect on the distribution remains the same since they are all related the same way (logarithms of v_p and τ_B which are proportional to r_p^3). The shape of the Cole-Cole distribution is shown in Fig.(3.1 c) for several values of α. The maximum (most probable) is always the mean $\langle x \rangle$.

We now introduce the Fröhlich distribution [5] which is a rectangular distribution, which means that all values are equally probable, thus the mean is given by $\langle x \rangle = (x_{max} - x_{min})/2$. The Fröhlich distribution is described by

$$P(\ln x) = \begin{cases} \dfrac{1}{\ln[(x_{max}/x_{min})^m]} & x_{min} < x < x_{max} \\ 0 & 0 < x < x_{min},\ x_{max} < x < \infty \end{cases} \qquad (3.2.8)$$

where the exponent m plays the same role as described before. A plot of (3.2.8) is shown in Fig. (3.1 d) for different values of the parameter $1/\ln[(x_{max}/x_{min})^m]$ with m=1.

To demonstrate an application and the significance of combining the distributions with the Debye model, according to what Eq. (1.4.51) states, we consider the measurement of two different magnetic liquids: (a) a water-based magnetite ferrofluid with M_s^F=100 G (0.01 T) and (b) a water-based ferrofluid with cobalt ferrite particles with M_s^F=300 G (0.03 T). Both fluids have been measured with the toroid technique in the range 50Hz-1MHz:

(a) *Magnetite in water carrier (100 G)*: the data of the water-based magnetite are denoted by a solid line in Figs. (3.2 a-c). The peak of χ'' at frequency f_{max}=4.68 kHz corresponds to a relaxation time $\tau_B = 3.4 \times 10^{-5}$ s from which we are able to calculate the mean particle radius, r_p: for room temperature 300°K and viscosity 10^{-4} N/m^2, r_p=48 nm, which denotes aggregation. By using the Cole-Cole equation (1.4.52) with α=0.9 we get the fit (dotted line) of Fig (3.2 a). Comparable fits to the data (solid line) are obtained by using Normal, Log-normal or Nakagami distribution, as Fig. (3.2 b) shows. Below 1 kHz these fits give more accurate results for both, real and imaginary, components than these obtained with the Cole-Cole fit.

Figure 3.2

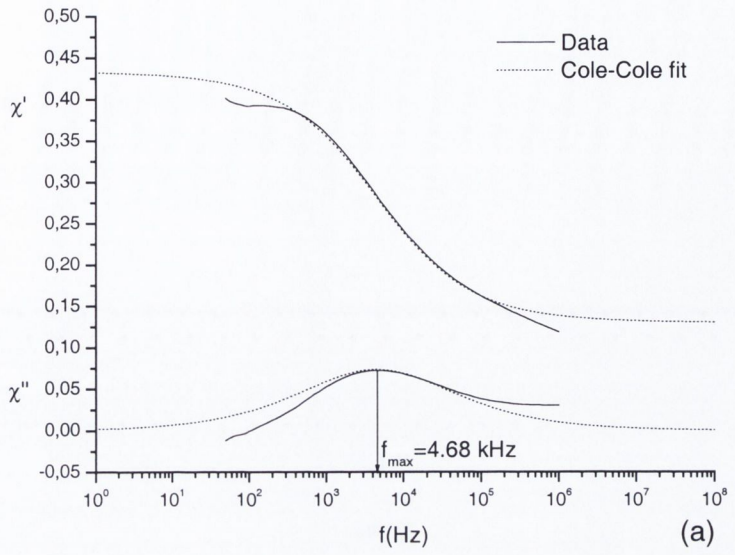

Figure 3.2 (a) Ferrofluid data of 100 G magnetite in water (solid line) fitted with Cole-Cole equation (dotted line).

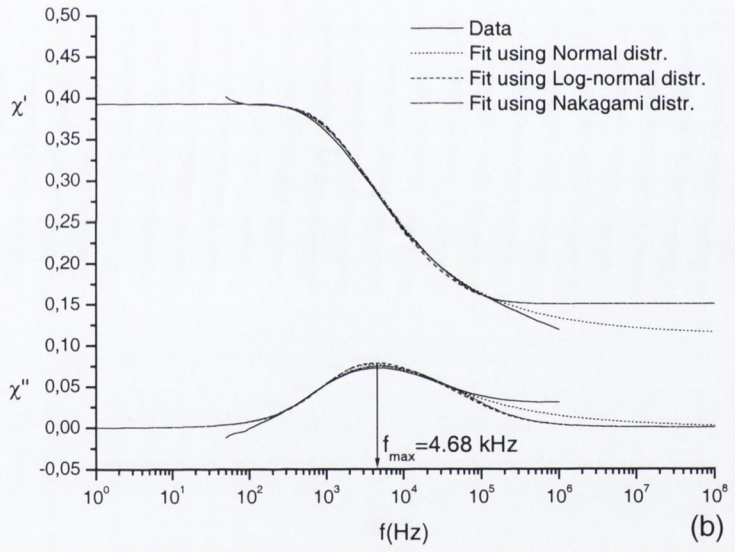

Figure 3.2 (b) The same data of magnetite (solid line) fitted with Debye equation modified to include Normal (dotted line), Log-normal (dashed line) and Nakagami (dot-dash) distribution.

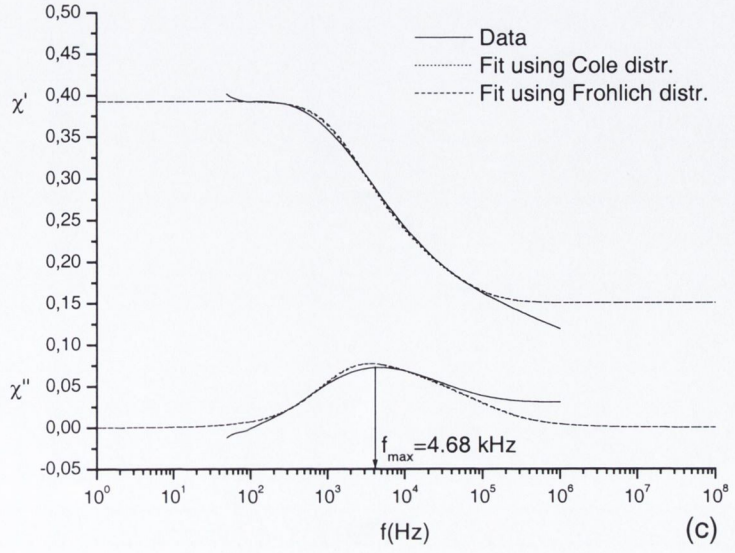

Figure 3.2 (c) The same data of magnetite (solid line) fitted with the Debye equation modified to include Cole (dotted line) and Fröhlich (dashed line) distribution.

(Continued).

Figure 3.2

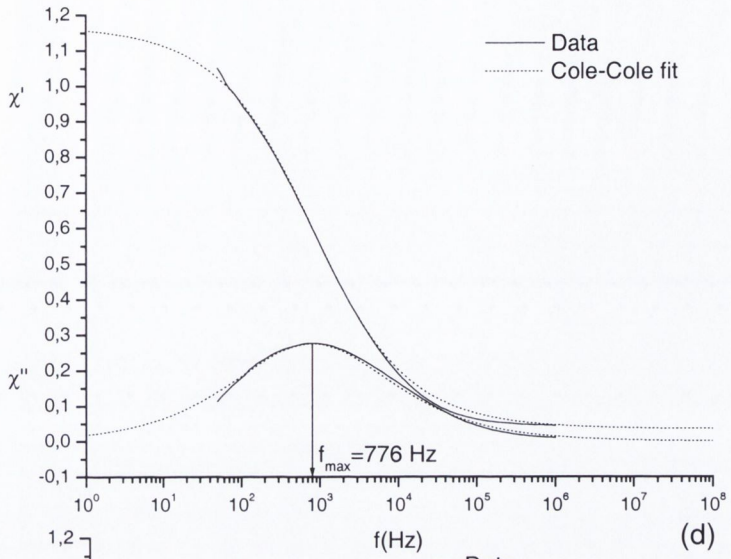

Figure 3.2 (d) Ferrofluid data of 300 G cobalt ferrite in water (solid line) fitted with Cole-Cole equation (dotted line).

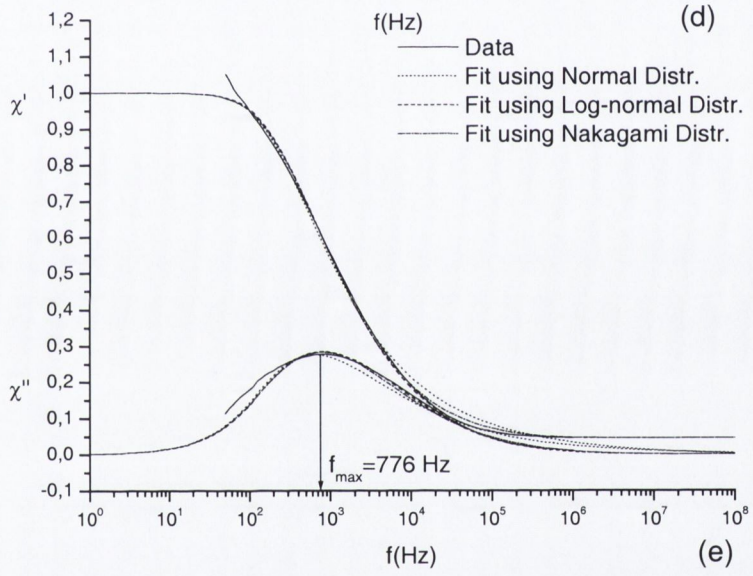

Figure 3.2 (e) The same data of cobalt ferrite (solid line) fitted with Debye equation modified to include Normal (dotted line), Log-normal (dashed line) and Nakagami (dot-dash) distribution.

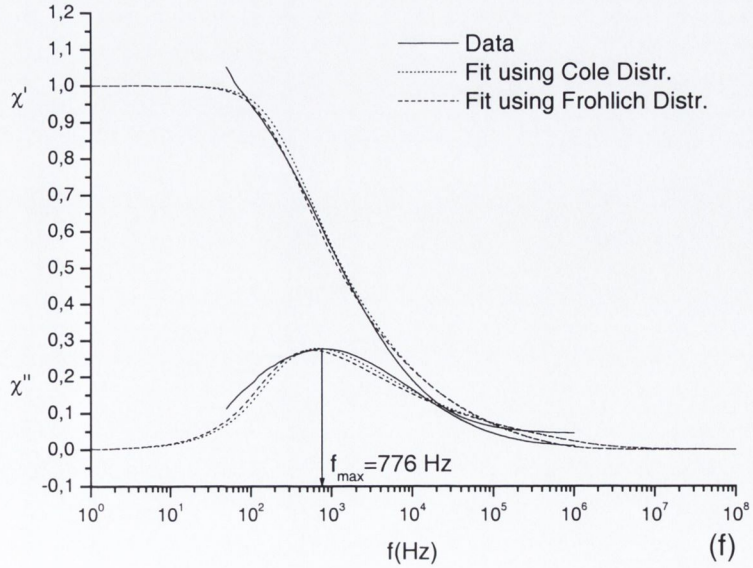

Figure 3.2 (f) The same data of cobalt ferrite (solid line) fitted with the Debye equation modified to include Cole (dotted line) and Fröhlich (dashed line) distribution.

The normalised standard deviation, σ_r, used for the Normal distribution fit (dotted line) was 0.9, for the Log-normal (dashed line) σ_r=0.9 and the width parameter β for the Nakagami distribution (dot-dash) was 0.6. We get comparable good fits by using the Cole-Cole distribution and the Fröhlich distribution as shown in Fig. (3.2 c). The α parameter used, for the Cole-Cole fit (dotted line), was α=0.9, agreeing with the Cole-Cole exponential parameter, $1-\alpha$, of the fit of Fig. (3.2 a). The height of Fröhlich distribution (dashed line) used was $\ln(\tau_{max}/\tau_{min})$=0.201. All fits gave the same value of static susceptibility with χ_0=0.3925, except the fit obtained with the Cole-Cole equation in which χ_0=0.43. This difference, together with the inaccuracy below 1 kHz, is due to the different way of distributing r_p when the Cole-Cole equation is used. In the Cole-Cole case the relaxation time is distributed rather than r_p, but by applying Eq. (1.4.52) we can distribute r_p directly.

(b) *Cobalt ferrite in water (300 G)*: The data of the water based cobalt ferrite is shown in Figs. (3.2 d-f) with a solid line. The Brownian peak is observed at f_{max}=776 Hz corresponding to a hydrodynamic radius r_p= 87 nm. The Cole-Cole equation is used for fitting, see dotted line in Fig. (3.2 d), with χ_0=1.17 and α=0.5. The Debye equation including Normal, Log-normal and Nakagami distributions, is fitted by using σ_r=0.9, σ_r=0.9 and β=1 respectively (Fig.(3.2 e)). Very close fits were achieved by use of Cole-Cole and Fröhlich distributions (Fig.(3.2 f)).

3.3 Dependence of the static susceptibility in a biasing field. Estimation of the radius of a magnetic nanoparticle by use of the constant frequency method.

The susceptibility of a magnetic liquid is a function of the polarising field and can be measured by varying an external biasing static field, H_s. In this section measurements and analysis are presented of the incremental magnetic susceptibilities $\chi_{\parallel}(H_s)$ and $\chi_{\perp}(H_s)$, of magnetic ferrofluids subjected to a strong external polarising static field, H_s, superimposed on a small alternating field, $h_a(t) = H_0 \cos(\omega t)$. The alternating field is so weak as to cause only *linear behaviour* in the response to that field. This requires the magnetic liquid to have low losses, i.e. χ'' must be approximately zero at the frequency

of the probing alternating field. Usually the frequency of measurement is chosen to be relatively low (i.e. 1 kHz or 10 kHz) which for non-aggregated ferrofluids is far below the frequency f_{max} of the absorption peak. To perform longitudinal and transverse polarisation it is necessary to place the coil in a position parallel and perpendicular to the axes of the poles of an electromagnet. A cylindrical coil is used, with sufficient dimensions and number of turns in order to achieve optimum measurement at the frequency of the alternating probing field. The sample holder is a cylinder, which suit the dimensions of the cylindrical coil so that the inner diameter of the winding is the same as the outer diameter of the holder. The holder is filled with the sample and is placed into the winding. This technique was named the *constant frequency method* [6]. So far, we have only shown how to estimate the *hydrodynamic volume* of the ferroparticle by measuring the magnetic susceptibility as a function of frequency by means of the toroid technique. With the constant frequency method it is possible to estimate the *magnetic volume* of the ferroparticle.

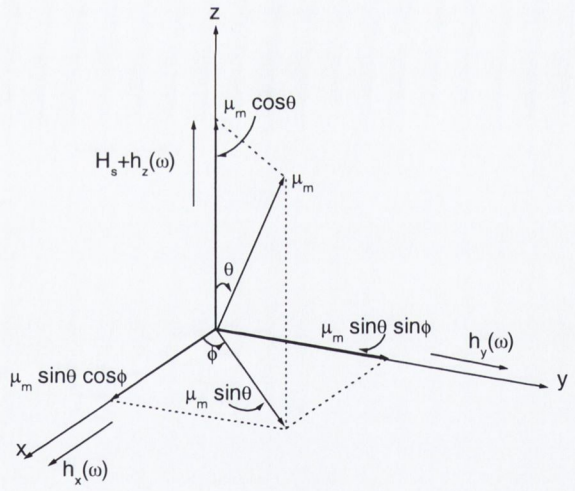

Figure 3.3 Relative directions of magnetic moment, μ_m, biasing field, $\mathbf{H}_s$, and constant frequency alternative field, $\mathbf{h}_a(t)=\mathbf{H}_0\cos(\omega t)$. The alternating magnetic field, $h_a(t)$, can propagate in all directions of space.

Closed form expressions can be obtained in terms of the Langevin function for the longitudinal and transverse susceptibility and the corresponding relaxation times (for the parallel and perpendicular relaxation times see next section 3.4). Based on statistical averaging calculations, it can be shown that $\chi_\perp$, $\chi_\parallel$ and $\chi_\perp - \chi_\parallel$ are given by the expressions [6],

$$\chi_{\parallel}(H_s) = \frac{N\mu_m^2}{\mu_0 k_B T}\left[1 - \coth^2(\mu_m H_s / k_B T) + \frac{1}{(\mu_m H_s / k_B T)^2}\right] = 3\chi_0 L'(\xi_m) \quad (3.3.1)$$

$$\chi_{\perp}(H_s) = \frac{N\mu_m^2}{\mu_0 k_B T}\left[\frac{\coth(\mu_m H_s / k_B T)}{\mu_m H_s / k_B T} - \frac{1}{(\mu_m H_s / k_B T)^2}\right] = 3\chi_0 \frac{L(\xi_m)}{\xi_m} \quad (3.3.2)$$

$$\chi_{\perp}(H_s) - \chi_{\parallel}(H_s) = \frac{N\mu_m^2}{\mu_0 k_B T}\left[-1 + \coth^2(\mu_m H_s / k_B T) - \frac{2}{(\mu_m H_s / k_B T)^2} + \frac{\coth(\mu_m H_s / k_B T)}{\mu_m H_s / k_B T}\right] \quad (3.3.3)$$

where N=particle number density, $\xi_m = \mu_m H_s / k_B T$ and $L'(\xi_m)$ is the derivative of the Langevin function. These equations have been derived by excluding the particles internal anisotropy, or in other words, by assuming that $\boldsymbol{\mu}_m$ is blocked (Néel relaxation is avoided). Such an assumption, which is realistic for the frequency of observation, can simplify the calculations since one will not have to take into the account the anisotropy field, $\mathbf{H}_A$. The moment vector, $\boldsymbol{\mu}_m$, which is aligned with the easy axis, follows the orientation of $\mathbf{H}_s + \mathbf{h}_a$. The arrangement of Fig. (3.3) shows the relative position of the moment and the external applied fields. The alternating field is in general a non-planar wave and can be decomposed in its three components $\mathbf{h}_a^x$, $\mathbf{h}_a^y$ and $\mathbf{h}_a^z$. The effect of the combined field on the components of the moment ($\boldsymbol{\mu}_m^x = \mu_m \sin\theta\cos\phi\,\hat{\mathbf{x}}$, $\boldsymbol{\mu}_m^y = \mu_m \sin\theta\sin\phi\,\hat{\mathbf{y}}$ and $\boldsymbol{\mu}_m^z = \mu_m \cos\phi\,\hat{\mathbf{z}}$; θ, ϕ are the polar angles) will cause a different value for the susceptibility. Since x and y directions are equivalent (they are affected by the same field), then $\mu_m^x = \mu_m^y = \mu_m^{\perp}$ correspond to $\chi_{\perp}$. Similarly $\mu_m^z = \mu_m^{\parallel}$ corresponds to $\chi_{\parallel}$. Notice that when Eqs. (3.3.1) and (3.3.2) are substituted in the equation for the total susceptibility, $\chi = \frac{1}{3}(\chi_{\parallel} + 2\chi_{\perp})$ give

$$\chi = \chi_0 = \frac{N\mu_m^2}{3\mu_0 k_B T} \quad (3.3.4)$$

which is as expected.

Equations (3.3.1), (3.3.2) can also be derived from the concept of the random walk. Coffey et al [7], used *linear response theory* [8,9] to derive expressions for the transient rise of the magnetisation which follows the application of a small dc field, H(t), superimposed on a large static field, H_s, which is applied for very long time. The linear response theory has been presented by Scaife in [8,9]. This method is essentially based on the notion that if the increment due to the small dc field, H(t), is very small relatively to

the H_s bias field, then the response to a weak alternating field, h_a, superimposed on the bias field can be found from the response to the increment of the dc field. The starting point of Coffey's et al method is Brown's equation (1.5.11), which has been presented in section 1.5. The potential energy density, which was substituted in Eq. (1.5.11), has the form [7]: $U(\vartheta) = -(H_s M_s + H M_s u(t))\cos\vartheta$, where the small dc field, H, can be applied longitudinally or transversely to the strong static field, H_s, and u(t) is the unit step function. Unfortunately the formalism which describes Coffey's method, is quite complex and is not adapted here.

The theoretical plots of $\chi_\perp$, $\chi_\parallel$ and of the difference $\chi_\perp - \chi_\parallel$ as functions of the ξ_m parameter, as they are described by Eqs. (3.3.1), (3.3.2), (3.3.3), are shown in Fig. (3.4 a). The difference $\chi_\perp - \chi_\parallel$ has a pronounced peak at ξ_1=3.72 which can be estimated by requiring that the derivative $d(\chi_\perp - \chi_\parallel)/d\xi_m$=0. This derivative can be easily calculated by recalling that the derivative of $\coth\xi_m$ equals to $1-\coth^2\xi_m$, hence [6]

$$\frac{1}{\chi_0}\frac{d(\chi_\perp(\xi_m)-\chi_\parallel(\xi_m))}{d\xi_m} = \frac{d}{d\xi_m}\left[-1+\coth^2\xi_m - \frac{2}{\xi_m^2} + \frac{\coth\xi_m}{\xi_m}\right]$$

$$= \frac{1}{\xi_m} + \frac{4}{\xi_m^3} - \coth\xi_m\left(\frac{1}{\xi_m^2} - 2\right) - \coth^2\xi_m\left(\frac{1}{\xi_m} + 2\coth\xi_m\right) \qquad (3.3.5)$$

Numerically we find that the root of this function is ξ_1=3.72. A plot of Eq. (3.3.5) is shown in Fig. (3.4 b). By plotting the measured $\chi_\perp - \chi_\parallel$ data versus the biasing field, H_s, and finding what value of H_s corresponds to the peak of the $\chi_\perp - \chi_\parallel$ curve, we are able to determine the value of the magnetic moment and furthermore the magnetic volume of the nanoparticle if the saturation magnetisation of the material is known. A plot of the derivative of $\chi_\perp - \chi_\parallel$ with respect to ξ_m is shown in Fig. (3.4 b). The root ξ_1, is where the curve cuts the zero axis.

When H_s takes large values, $\coth\xi_m$ can be expanded in a series as follows [6],

$$\coth\xi_m = 1 + 2\left(\frac{1}{e^{2\xi_m}} + \frac{1}{e^{4\xi_m}} + \frac{1}{e^{6\xi_m}} + \ldots\right) \qquad (3.3.6)$$

so that, if $e^{\xi_m} >> 1$, then

$$\coth\xi_m \cong 1 \qquad (3.3.7)$$

By using this simplification Eqs.(3.3.1), (3.3.2) may be approximated by

$$\chi_{\parallel}(H_s) \cong \frac{N}{\mu_0}\frac{k_B T}{H_s^2} \tag{3.3.8}$$

and

$$\chi_{\perp}(H_s) \cong \frac{N}{\mu_0}\left(\frac{\mu_m}{H_s} - \frac{k_B T}{H_s^2}\right) \tag{3.3.9}$$

Similarly Eq. (3.3.3), for large values of H_s, can be simplified to

$$\chi_{\perp}(H_s) - \chi_{\parallel}(H_s) \cong \frac{N}{\mu_0}\left(\frac{\mu_m}{H_s} - \frac{k_B T}{H_s^2}\right) \tag{3.3.10}$$

Figure 3.4

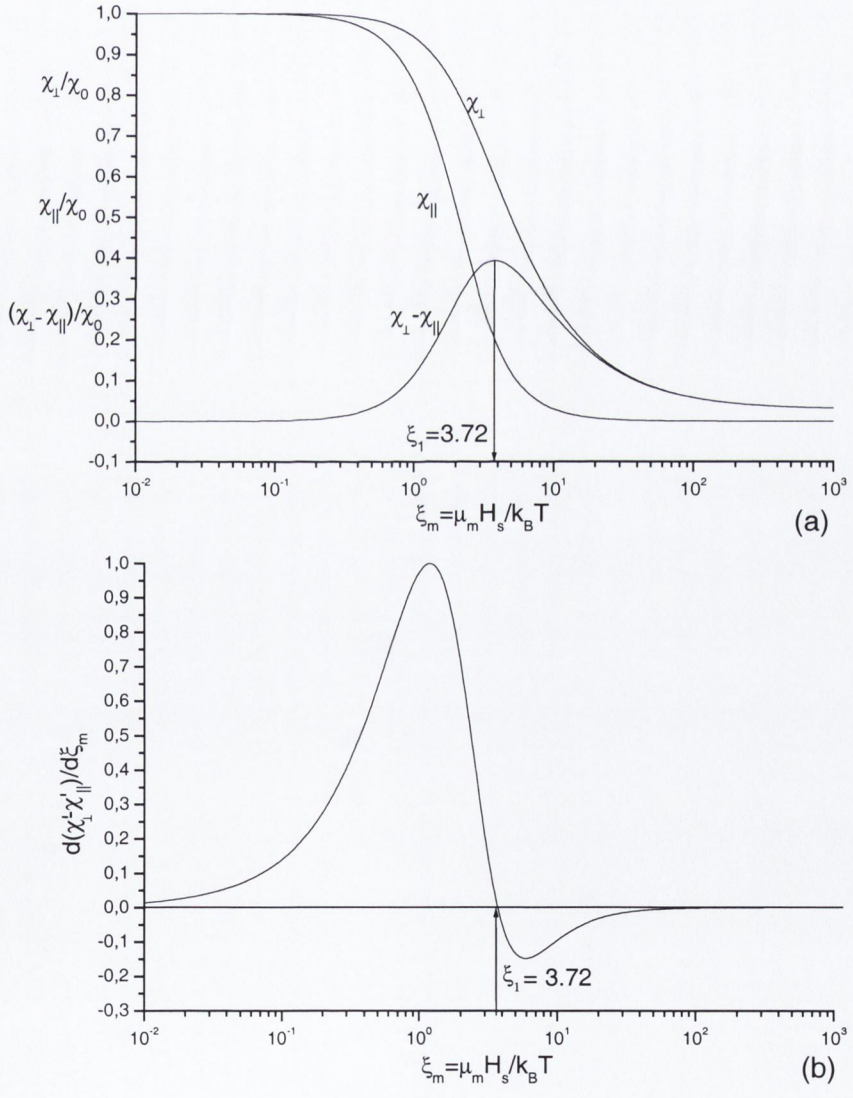

Figure 3.4 (a)

A theoretical normalised plot of parallel and perpendicular susceptibilities and their difference as they are given by Eqs. (3.3.1), (3.3.2), (3.3.3).

Figure 3.4 (b)
Theoretical plot of the derivative of $\chi_{\perp} - \chi_{\parallel}$ given by Eq. (3.3.5).

Because of the dispersion of particle size it is necessary to distribute r_m, which affects μ_m and hence ξ_m. This means that both the free parameters, r_m and ξ_m, are distributed. For a specific value of the bias field, H_s, the value of ξ_m which corresponds to a specific point of the $\chi_\perp$, $\chi_\parallel$ and $\chi_\perp - \chi_\parallel$ curves is dependent on r_m, since $\xi_m = 4M_s \pi r_m^3 H_s / 3k_B T$. It is obvious that when r_m reduces, the parameter ξ_m becomes smaller and thus it shifts the $\chi_\perp$, $\chi_\parallel$ and $\chi_\perp - \chi_\parallel$ curves to the left. The opposite happens when r_m increases. This is shown in Figs. (3.5 a-c) in which $\chi_\perp$, $\chi_\parallel$ and $\chi_\perp - \chi_\parallel$ are plotted as functions of both r_m and ξ_m. The curvature of the trace of $\chi_\perp - \chi_\parallel$ on the cross-sectional x-y plane is noticeable: for small values of r_m the maximum peak of $\chi_\perp - \chi_\parallel$ is shifted very much to the left of the ξ_m axis. Due to the dependence of ξ_m on r_m, the root ξ_1 does not equals 3.72 for any arbitrary value of r_m. Hence, ξ_1 is dependent on r_m. This fact is shown in Fig. (3.5 d) which illustrates how the values of ξ_1 varies as function of r_m, for those values of r_m taken for the distribution.

For the experiment a cylindrical coil with a winding of 30 turns, length 2.6 cm and diameter 1.2 cm, is used. The inductance of the coil measured at low frequency (close to zero) is 4 μH. Measurements are obtained at a constant low frequency f=10 kHz, which is the optimum frequency since it is close to dc and much lower than the f_{max}, where the absorption peak appears. The HP 4192A auto-balanced bridge was used to measure the inductance L and resistance R of the coil with the sample holder full and empty. The ratio $\Delta L / L$ is proportional to χ', whilst χ'' is proportional to $\Delta R / \omega L$, where Δ denotes the difference between empty and full.

The result of measuring an isoparaffin-based magnetite of M_s^F=400 G (0.04 T) is shown in Fig. (3.6 a) with dots, whilst Fig. (3.6 b) illustrates the derivative of the $\chi_\perp - \chi_\parallel$ data (dots) with respect to H_s. The values of the static magnetic field, H_s, used in this experiment are approximately: 15.1, 21.6, 32.9, 44.6, 57, 69.6, 83.2, 97.6, 110.1, 123.5, 135.4, 149.7, 162.1, 174, 186.5, 197.4 kA/m. The continuous lines in Fig. (3.6 a) represent the fits obtained by use of Eqs. (3.3.1)-(3.3.3) modified to include several distributions of the magnetic radius, namely: log-normal (solid line), normal (dotted line) and Nakagami (dashed line). The particle radii were varied in 38 steps of 0.2 nm over the

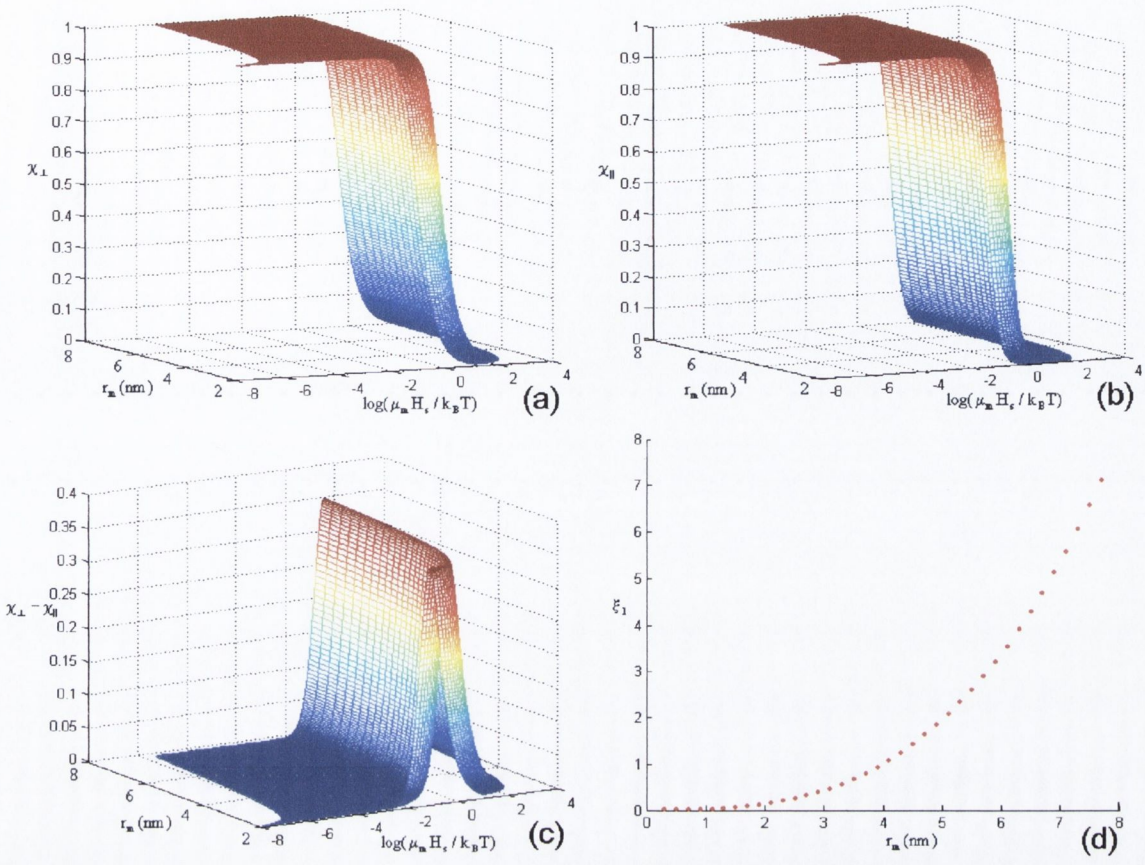

Figure 3.5 Shows how, when applying a log-normal distribution for the magnetic radius, the ξ_m parameter is effected which results in a shift of the points of **(a)** the susceptibility in the perpendicular direction, **(b)** the susceptibility in the parallel direction, **(c)** susceptibility's difference $(\chi_\perp - \chi_\parallel)$, **(d)** shows the dependence of ξ_1, which corresponds to the peak of $\chi_\perp - \chi_\parallel$, on the values that the particle magnetic radius takes for the distribution.

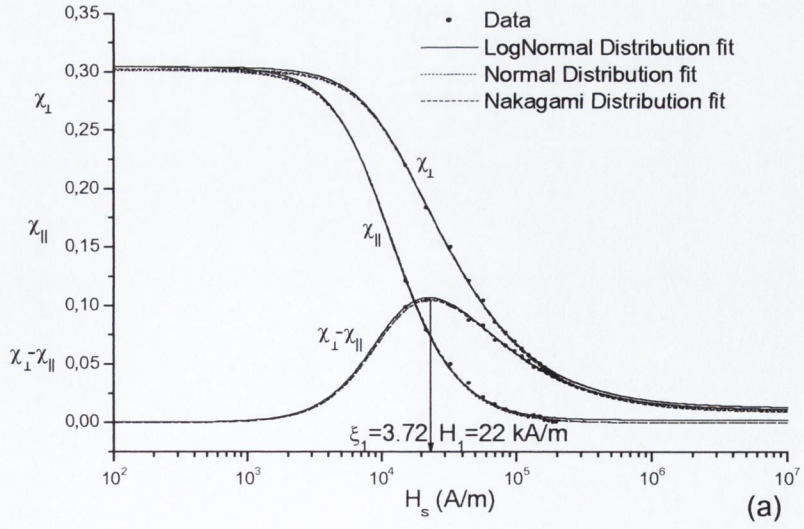

Figure 3.6 (a) Experimental data (dots) of a 400 G magnetite in isoparaffin carrier versus constant magnetic field. The solid line is the fit obtained by using Eqs. (3.3.1)-(3.3.3) modified to include a log-normal distribution of the magnetic radius, the dotted line is the fit obtained by using the normal distribution and the dashed line is the fit obtained by using the Nakagami distribution.

(Continued).

Figure 3.6

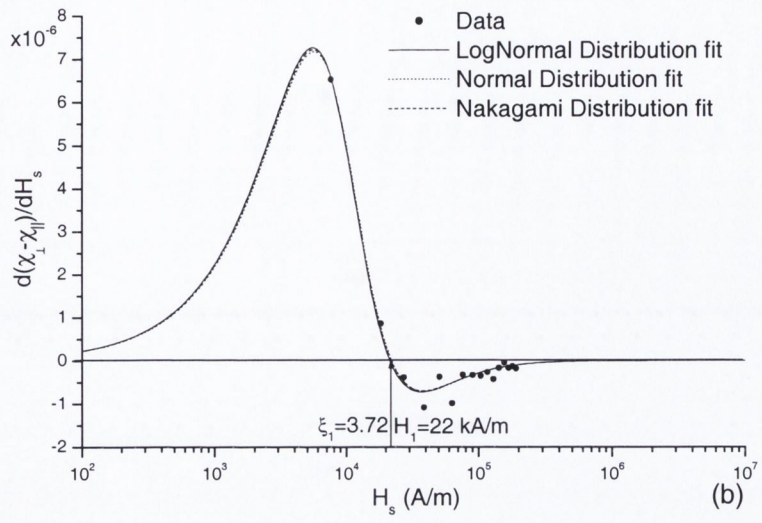

Figure 3.6 (b) Illustrates the derivative $d(\chi_{\perp} - \chi_{\parallel})/dH_s$ of the data (dots) and the fits by using Eq. (3.3.5) for the case of log-normal (solid line), normal (dotted line) and the Nakagami (dashed) distributions. This graph helps to give an accurate estimation of the H_s value, which corresponds to $\xi_1 = 3.72$.

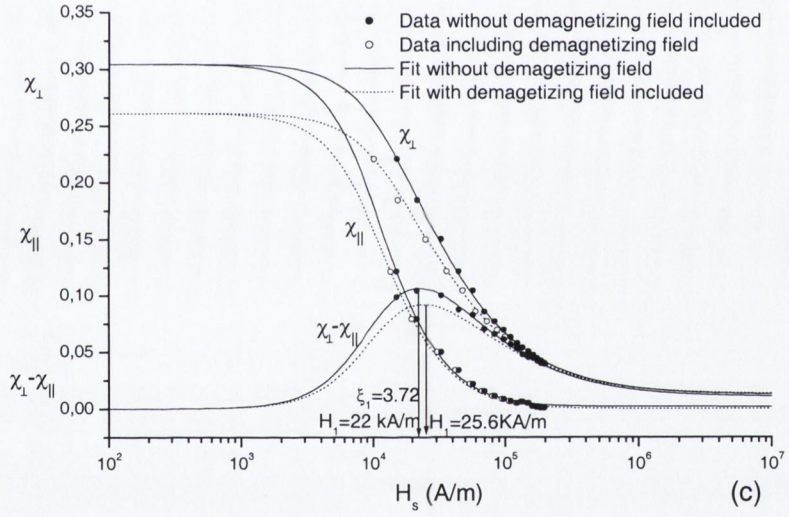

Figure 3.6 (c) The empty dots are the modified data when demagnetising field is accounted for. The corrected data points are shifted to the left. The $\chi_{\perp} - \chi_{\parallel}$ curve cannot be presented because of the mismatching between the perpendicular susceptibility corrected data and the parallel susceptibility corrected data. The dotted line is the fit for the corrected data. The value of H_1, now, can be estimated only from the fit.

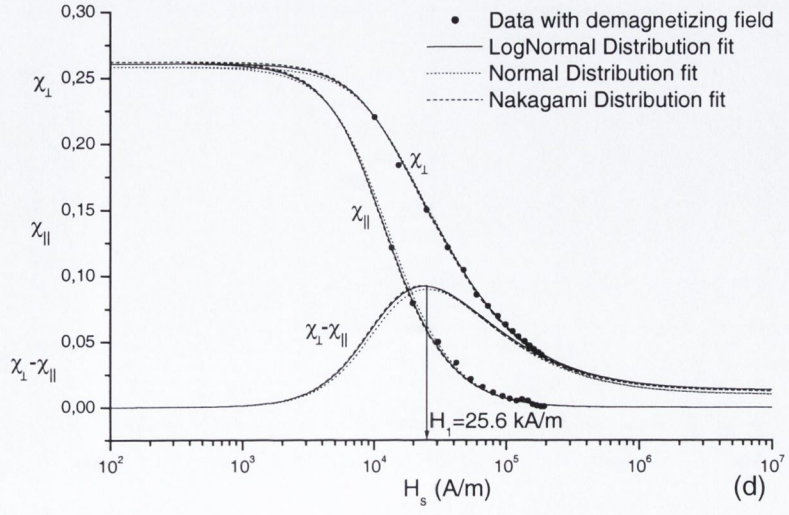

Figure 3.6 (d) Accurate fits, which are corresponding to the corrected data, are obtained by applying log-normal (solid line), normal (dotted line) and Nakagami (dashed line) distribution of the magnetic radius.

range 3.2-10.8 nm with the mean being 7 nm. The static value of the susceptibility, for zero field, was measured and found to be 0.3. This value was used for the fit, which in the limit of low H_s approaches 0.3. The actual form of the equations used for the distribution were

$$\chi_{\parallel}(r_m, H_s) = N \times 5.4 \times 10^{26} r^6 \left[1 - \coth^2(4 \times 10^{20} r_m^3 H_s) + \frac{6.1 \times 10^{-42}}{(r_m^3 H_s)^2} \right] \qquad (3.3.11)$$

$$\chi_{\perp}(r_m, H_s) = N \times 5.4 \times 10^{26} r_m^6 \left[\frac{\coth(4 \times 10^{20} r_m^3 H_s)}{4 \times 10^{20} r_m^3 H_s} - \frac{6.1 \times 10^{-42}}{(r_m^3 H_s)^2} \right] \qquad (3.3.12)$$

(r_m in m, H_s in A/m). For each value of H_s, r_m is distributed over its 38 different values. The fitting parameters which were used, are: M_s=0.4 Tesla, $\langle \mu_m \rangle = 5.74 \times 10^{-25}$ Wb m, $\langle r_m \rangle$=7 nm; for the normal distribution fit σ_r=0.45, for the log-normal distribution fit σ_r=0.32 and for the Nakagami distribution fit β=0.8 and $W = 2.83 \times 10^{-17}$. Figure (3.6 b) shows the fits obtained using Eq. (3.3.5). The maximum peak of the $\chi_{\perp} - \chi_{\parallel}$ curve is observed at H_1=22 kA/m (0.025 T). By using the relation $\xi_1 = \mu_m H_1 / k_B T$, as the theory describes, we can easily calculate the *effective moment* which is found to be $\mu_m = 7 \times 10^{-25}$ Wb m. The saturation magnetisation of the magnetite ferroparticle is M_s=0.4 T (320 kA/m), thus the *effective magnetic radius* was found to be 7.4 nm, which is close to the mean particle radius calculated from the fit.

As the sample is cylindrical in shape, the demagnetising field, H_D, [10-12] of the sample must be taken into account for both the perpendicular and parallel orientations. The effect of the demagnetizing field is to change the value of the actual field within the sample. The corrected field is the superposition of H_s and the demagnetizing field, which is dependent on the shape characteristics of the sample. The demagnetizing field is estimated by considering the demagnetizing factors. There are two demagnetizing factors involved with the cylindrical sample: $N_{\parallel} = N_z$ is for the case where the major long axis of the sample is parallel to the polarizing field, H_s, whilst $N_{\perp} = N_x = N_y$ is the demagnetizing factor when the long axis of the sample is perpendicular to H_s. Both demagnetizing factors are related to each other by

$$N_{\perp} = (1 - N_{\parallel})/2 \qquad (3.3.13)$$

The demagnetizing fields in both directions are given in relation to the particular magnetization $M(H_s)$ of the sample, hence the parallel demagnetizing field is given by

$$H_{\parallel}^{D}(H_s) = N_{\parallel}M(H_s) \tag{3.3.14}$$

and the demagnetizing field for the perpendicular orientation is,

$$H_{\perp}^{D}(H_s) = N_{\perp}M(H_s) \tag{3.3.15}$$

To estimate the magnetization, $M(H_s)$, value for each applied field, H_s, we need to have the magnetization curve of the sample. Usually the normalized magnetization curves have the same profile for similar ferrofluids (e.g. for all paraffin-based magnetites). According to this fact it is enough to know, in order to estimate the demagnetizing field, only the normalized magnetization curve of the family in which the fluid belongs. The demagnetizing factors, $N_{\parallel}$ and $N_{\perp}$, can be calculated theoretically. There are expressions for most geometrical arrangements [10] but this subject is more for theoretical interest rather than practical application. Practically, by use of charts (see Appendix C, Fig. (C.1)), one can estimate $N_{\parallel}$ and $N_{\perp}$ accurately. From the chart we can estimate both parallel and perpendicular demagnetizing factors for several material shapes (cylinders and ellipsoids) as a function of the ratio, m, of the dimensions of the material. For a cylindrical shape the parameter m is the ratio of the length of the cylinder's long axis to the cylinder's diameter. For the cell we use, the long axis is 2.6 cm and the diameter 1.2 cm, thus m= 2.16. By projecting m=2.16 on the curve which corresponds to low permeability (μ=10) we find $N_{\parallel}$=0.12 (see Appendix C, Fig. (C.2)). The perpendicular demagnetizing factor is easily calculated from Eq. (3.3.5) and it is found to be $N_{\perp}$=0.44.

The demagnetizing field arises from the combined magnetization of the magnetic particles and it is oriented opposite to the direction of H_s. Hence the *effective field*, which actually acts on the ferroparticles, is given for the parallel direction as,

$$H_s - H_{\parallel}^{D}(H_s) = H_s - N_{\parallel}M(H_s) \tag{3.3.16}$$

and for the perpendicular, by

$$H_s - H_{\perp}^{D}(H_s) = H_s - N_{\perp}M(H_s) \tag{3.3.17}$$

By using the latter expressions we are able to perform a correction to the experimental $\chi_{\perp}$ and $\chi_{\parallel}$ data points. Since the actual field is smaller than H_s, as Eqs. (3.3.16), (3.3.17) predict, the data points will slightly shift to the left. This movement of the data

Table 3.1 The actual fields applied to the 400 G fluid.

Externally applied Field	Corrected field in parallel direction	Corrected field in perpendicular direction
H_s (kA/m)	$H_s - N_{\parallel}M$ (kA/m)	$H_s - N_{\perp}M$ (kA/m)
0	0	0
15.1	13.6	10,1
21.6	19.8	15,4
32.9	30.6	25,3
44.6	42.1	36,1
57	54.3	47,8
69.6	66.8	59,9
83.2	80.2	73,1
97.6	94.5	87,1
110.1	10.7	99,4
123.5	120.2	112,5
135.4	132.1	124,3
149.7	146.4	138,4
162.1	158.7	150,7
174	170.6	162,5
186.5	183.1	174,9
197.4	193.9	185,7

Table 3.2 Fitting parameters for 400 G fluid.

Normal distribution parameters	Log-normal distribution parameters	Nakagami distribution parameters
M_s=0.4 T	M_s=0.4 T	M_s=0.4 T
$\langle\mu_m\rangle$=5.74 $\times 10^{-25}$Wbm	$\langle\mu_m\rangle$=5.74 $\times 10^{-25}$Wbm	$\langle\mu_m\rangle$=5.74 $\times 10^{-25}$Wbm
$\langle r_m\rangle$=7 nm	$\langle r_m\rangle$=7 nm	$\langle r_m\rangle$=7 nm
r_{min}=3.2 nm	r_{min}=3.2 nm	r_{min}=3.2 nm
r_{max}=10.8nm	r_{max}=10.8nm	r_{max}=10.8nm
step=0.2 nm	step=0.2 nm	step=0.2 nm
σ_r=0.45	σ_r=0.45	β=0.8

Table 3.4 Fitting parameters for 250G fluid.

Normal distribution parameters	Log-normal distribution parameters	Nakagami distribution parameters
M_s=0.4 T	M_s=0.4 T	M_s=0.4 T
$\langle\mu_m\rangle$=9.2 $\times 10^{-25}$Wbm	$\langle\mu_m\rangle$=9.2 $\times 10^{-25}$Wbm	$\langle\mu_m\rangle$=9.2 $\times 10^{-25}$Wbm
$\langle r_m\rangle$=8 nm	$\langle r_m\rangle$=8 nm	$\langle r_m\rangle$=8 nm
r_{min}=4.2 nm	r_{min}=4.2 nm	r_{min}=4.2 nm
r_{max}=11.8nm	r_{max}=11.8nm	r_{max}=11.8nm
step=0.2 nm	step=0.2 nm	step=0.2 nm
σ_r=0.33	σ_r=0.4	β=2.1

Table 3.3 The actual fields applied to the 250 G fluid.

Externally applied Field	Corrected field in parallel direction	Corrected field in perpendicular direction	Externally applied Field	Corrected field in parallel direction	Corrected field in perpendicular direction
H_s (kA/m)	$H_s - N_{\parallel}M$ (kA/m)	$H_s - N_{\perp}M$ (kA/m)	H_s (kA/m)	$H_s - N_{\parallel}M$ (kA/m)	$H_s - N_{\perp}M$ (kA/m)
0	0	0	24,9	23,6	20,7
5,1	4,8	3,9	35,7	34,2	30,7
5,5	5,2	4,3	45,9	44,2	40,5
6,2	5,8	4,8	56,8	55,1	51
6,9	6,53	5,4	69,2	67,3	63,1
8,3	7,8	6,5	80,3	78,4	74,1
9,8	9,2	7,7	91,1	89,1	84,6
11,4	10,6	8,9	102,4	100,4	95,7
12,0	11,3	9,5	114,1	112,1	107,3
12,8	12,1	10,1	124,7	122,6	117,8
14,3	13,4	11,3	135,4	133,3	128,5
15,2	14,2	12,1	147,1	145,7	140,1
19,5	18,4	15,7	158,3	156,2	151,1
			168,4	166,3	161,2

points results in a shift of the maximum peak of $\chi_\perp - \chi_\parallel$ and corrects the value of H_1. We remark that since Eqs. (3.3.16), (3.3.17) predict different values for the corrected field, the shift of the parallel data points will be smaller compared with the shift of the perpendicular data points. This indicates that after the correction both sets of data do not correspond to the same fields. Thus, we cannot subtract them. The $\chi_\perp - \chi_\parallel$ curve will be derived by fitting the $\chi_\perp$ and $\chi_\parallel$ data points first and then subtracting the fit lines. A fundamental element in the use of this procedure is to perform a good fit to the $\chi_\perp$ and $\chi_\parallel$ data points, which assures a correct prediction for the maximum peak of $\chi_\perp - \chi_\parallel$.

In Fig. (3.6 c) we see the $\chi_\perp$ and $\chi_\parallel$ original data points (full dots) and the corrected data points (empty dots) for the 400 G magnetite ferrofluid in isoparaffin. The solid line represents the fit for the original data, whilst the dotted line is the fit for the corrected data. The corrected values for both fields, in parallel and perpendicular directions, are represented in Table (3.1). From the fit we find that H_1=25.6 kA/m, which is slightly higher than the corresponding value (22 kA/m) for the case when the demagnetising field was not accounted for. According to the theory described above the corrected value of the effective magnetic moment will be 6×10^{-25} Wb m from which, for M_s=0.4 T, we derive $\langle r_m \rangle$=7.1 nm, which is closer to the correspondent value (7 nm) which is obtained from the fit. The fitting parameters used to fit the corrected data are given in Table (3.2) and they are not far from the fitting parameters used to fit the original data.

Figure (3.7 a-b) shows another example of measurement with the constant frequency method. The ferrofluid consists of magnetite ferroparticles in a water carrier. The saturation magnetisation of this sample is M_s^F=250 G (0.025 T). More points for the polarizing field are taken. The values of the polarizing field, for this experiment, are shown in Table (3.3) together with the corrected values for the parallel and perpendicular field when the demagnetising field is considered. The fit obtained for several distributions is illustrated in Fig. (3.7 b). The solid line corresponds to the log-normal distribution, the dotted line to the normal and the dashed to the Nakagami distribution. The fitting parameters for the three fits are given on Table (3.4). The maximum peak occurs at H_1=16.7 kA/m which corresponds to an effective moment 9.2×10^{-25} Wb m. The effective radius is estimated at 8.1 nm, which is close to the radius estimated from the fit (8 nm, see Table (3.4)).

The constant frequency method, together with the measurements of the spectrum of the susceptibility, is an accurate and easy to use technique for estimating the magnetic and hydrodynamic radius of the ferroparticles.

Figure 3.7

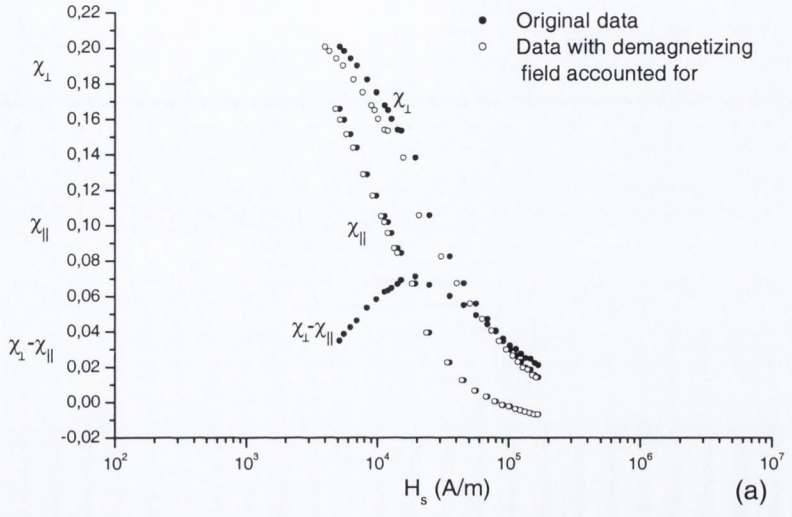

Figure 3.7 (a) Experimental data of the 250 G magnetite in water sample. Empty dots denote the original data and the filled dots the modified data which include the effect of the demagnetising field.

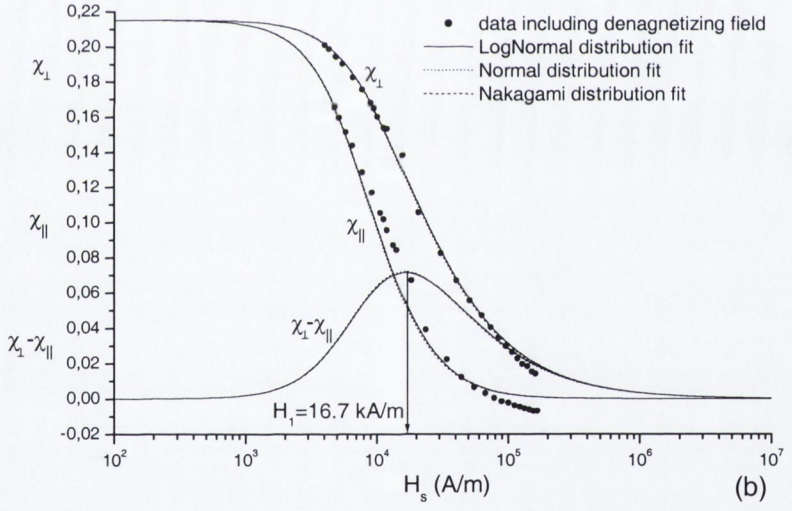

Figure 3.7 (b) Shows fits obtained by using Eqs. (3.3.1), (3.3.2). Solid line denotes the fit with the log-normal distribution, dotted line is the fit with the normal distribution and the dashed line is the fit with the Nakagami distribution.

3.4 Dependence of $\chi(\omega)$ in the frequency range 100 Hz-1 MHz on an external polarising constant field. Dependence of the relaxation time on the polarising field.

The dependence of the magnetic susceptibility of a ferrofluid on an external polarising field, H_s, superimposed on a weak alternating field, $h_a(t) = H_0 \cos(\omega t)$ (studied in section 3.3) is reflected in the static susceptibility. Again, the alternating field, h_a, is so weak that only linear behaviour is considered. The static susceptibility, χ_0, corresponds to zero frequency (dc) and its response, which is given by Eq. (3.3.1) or Eq.

(3.3.2), depends on the relative direction of the static polarising field. The effect of H_s on χ_0 results in the dependence of H_s on the susceptibility for all individual frequencies, since the complex susceptibility is directly dependent on χ_0. Coffey et al [7] explained this effect theoretically by solving first Brown's equation (see Eq. (1.5.11)), by expanding the solution in spherical harmonics (Eq. (1.4.27)), and afterwards used the linear response theory to derive the ac response from the response of a weak constant (dc) field, H, applied together with the strong H_s field. The expression they derived for the parallel susceptibility, $\chi_{\parallel}(\omega,\xi_m)$, appropriately modified to include the high frequency effects which are incorporated in the χ_∞ term, is

$$\chi_{\parallel}(\omega,\xi_m)=\frac{3\chi_0 L'(\xi_m)-\chi_\infty}{1+i\omega\tau_{\parallel}}+\chi_\infty=\frac{3\chi_0(1-\coth^2(\xi_m)+1/\xi_m^2)-\chi_\infty}{1+i\omega\tau_{\parallel}}+\chi_\infty \qquad (3.4.1)$$

whilst the perpendicular susceptibility, $\chi_{\perp}(\omega,\xi_m)$, is

$$\chi_{\perp}(\omega,\xi_m)=\frac{3\chi_0 L(\xi_m)/\xi_m-\chi_\infty}{1+i\omega\tau_{\perp}}+\chi_\infty=\frac{3\chi_0(\coth(\xi_m)/\xi_m-1/\xi_m^2)-\chi_\infty}{1+i\omega\tau_{\perp}}+\chi_\infty \qquad (3.4.2)$$

In the above equations $L'(\xi_m)$ is the derivative of the Langevin function and ξ_m in this case is $\mu_m(H_s+h_a)/k_BT$. Equations (3.4.1) and (3.4.2) were also reported, but without derivation, by Shliomis and Raikher [14] for the Debye relaxation of ferrofluid particles.

The externally applied biasing field, H_s, results in one additional effect: the blocking of the large particles. By increasing H_s, the blocking gets stronger, thus a smaller number of big particles contribute to the relaxation phenomenon. This has a great effect on the relaxation time, which now varies in accordance with H_s. The contribution of the smaller particles increases by increasing H_s, which results in an increase in rotational mobility, leading to the effective relaxation time being smaller because the smaller particles (smaller relaxation times) dominate in the relaxation effect. This effect was predicted theoretically by Martsenyuk et al [13]. Coffey at al [7] gave analytical closed form expressions for the relaxation times, which are dependent on the relative orientation of the fields. They derived the relaxation times by means of a method, which combines linear response theory and the *effective eigenvalue method* [15,16]. The parallel relaxation time, $\tau_{\parallel}(\xi_m)$, is given by,

$$\tau_{\parallel}(\xi_m) = \tau_B \frac{\xi_m L'(\xi_m)}{L(\xi_m)} = \tau_B \frac{\xi_m \left[1 - 2L(\xi_m)/\xi_m - L^2(\xi_m)\right]}{L(\xi_m)} \tag{3.4.3}$$

where τ_B is the usual Brownian relaxation time, given by Eq. (1.4.46), for the case of no external bias field. The Néel relaxation mechanism is not operating. This is appropriate for the measurements we present below, since the relaxation appears to be purely Brownian [17]. Wnen Néel relaxation is involved in the observed relaxation (this would be if the absorption peak appears in the MHz range) $\tau_{\parallel}$ would be given by Eq. (1.5.21) in conjunction with Eq. (1.5.26) and $\tau_{\perp}$ by Eq. (1.5.25) for the case of no external biasing field and by Eqs. (6.82)-(6.84) of [7] when H_s is active.

For small values of ξ_m the Langevin function can be approximated by

$$L(\xi_m) = \xi_m / 3 \tag{3.4.4}$$

and so for small ξ_m we find, from Eq. (3.4.3), that $\tau_{\parallel}(\xi_m) = \tau_B$, as expected. If higher terms of ξ_m are retained in the Langevin function, we have

$$L(\xi_m) = \xi_m / 3 - 2\xi_m^2 / 45 \tag{3.4.5}$$

which results in

$$\tau_{\parallel}(\xi_m) = \tau_B (1 - 2\xi_m^2 / 15) \tag{3.4.6}$$

For the other limit of large ξ_m, the predicted relaxation is virtually instantaneous, the asymptotic behaviour being

$$\tau_{\parallel}(\xi_m) = \tau_B / \xi_m \tag{3.4.7}$$

The perpendicular relaxation time, according to [7], is given by

$$\tau_{\perp}(\xi_m) = \tau_B \frac{2L(\xi_m)}{\xi_m - L(\xi_m)} \tag{3.4.8}$$

In the limit $\xi_m << 1$ we find, as expected, that the perpendicular relaxation time is simply the Brownian relaxation time. For small values of ξ_m, retaining higher order terms in the Langevin function, we obtain the low field approximation

$$\tau_{\perp}(\xi_m) = \tau_B (1 - \xi_m^2 / 10) \tag{3.4.9}$$

For large values of ξ_m, the Langevin function approaches unity and so we have the asymptotic solution

$$\tau_{\perp}(\xi_m) = 2\tau_B / \xi_m \tag{3.4.10}$$

Equations (3.4.3) and (3.4.8) coincide precisely with the formulae obtained by Martsenyuk et al [13] (Eq. (28) of their paper). It is of interest to note that the field dependence of the relaxation times $\tau_{\parallel}$ and $\tau_{\perp}$ is identically the same as for polar dielectrics under the influence of an electric field [18,19]. Thus, Eqs. (3.4.3) and (3.4.8) predict the same field dependencies of the relaxation times $\tau_{\parallel}$ and $\tau_{\perp}$ for both a ferrofluid and a polar fluid. This is not unexpected because from a physical point of view the behavior of a suspension of fine ferromagnetic particles in a constant magnetic field is similar to that of a system of electric dipoles (polar molecules) in a constant electric field.

Equations (3.4.1), (3.4.3) and Eqs. (3.4.2), (3.4.8) can be combined in a manner so that the resultant expression for the susceptibility predicts both a decrease of the susceptibility's magnitude and a shift of the Brownian peak as a function of H_s. This is realized if $\tau_{\parallel}$ in Eq. (3.4.1) is substituted by $\tau_{\parallel}$ from Eq. (3.4.3) and $\tau_{\perp}$ in Eq. (3.4.2) is replaced by $\tau_{\perp}$ which is given by Eq. (3.4.8). It is necessary to consider a distribution of particle radii (or distribution of the relaxation times), since the above expressions for the field dependence refer to the mono-disperse case. We proved in section 3.2 that any of the distribution functions presented there can be used since they give the same good fit for the Debye relaxation data curves. We can use any of them for distributing the expressions given by Eqs. (3.4.1), (3.4.2), but we prefer the Cole-Cole exponential parameter, $1-\alpha$, due to its simplicity. Thus, the final expressions for the modified Debye model which includes the effect of the polarizing field H_s for both the susceptibility's magnitude and relaxation time, and accounts for the particle's poly-dispersion, can be written as

$$\chi_{\parallel}(\omega,\xi_m)=\frac{3\chi_0 L'(\xi_m)-\chi_\infty}{1+(i\omega\tau_{\parallel}(\xi_m))^{1-\alpha}}+\chi_\infty=\frac{3\chi_0(1-\coth^2(\xi_m)-1/\xi_m^2)-\chi_\infty}{1+(i\omega\tau_{\parallel}(\xi_m))^{1-\alpha}}+\chi_\infty \qquad (3.4.11)$$

$$\chi_{\perp}(\omega,\xi_m)=\frac{3\chi_0 L(\xi_m)/\xi_m-\chi_\infty}{1+(i\omega\tau_{\perp}(\xi_m))^{1-\alpha}}+\chi_\infty=\frac{3\chi_0(\coth(\xi_m)/\xi_m-1/\xi_m^2)-\chi_\infty}{1+(i\omega\tau_{\perp}(\xi_m))^{1-\alpha}}+\chi_\infty \qquad (3.4.12)$$

We will show now experimental evidence, which proves the validity of Eq. (3.4.11). Two ferrofluids have been tested under the influence of a polarizing field. The first ferrofluid consists of cobalt-ferrite particles in water with saturation magnetisation M_s^F=300 G (0.03 T). The second ferrofluid is a water-based magnetite with M_s^F=100 G (0.01 T). The toroidal technique in conjunction with the HP 4192A auto-balanced bridge was used for the measurements. A secondary winding of three turns was wound on the

toroidal core, and it was fed with a constant current from a constant-current source. Care has been taken to avoid transformer effects between the two windings on the toroid. The interaction of the current-source's impedance with the rest of the circuit can be eliminated by choosing a large output impedance. A meter was connected between the current source and the secondary winding in order to read the current flow. The constant magnetic field, H_s, which flows into the slit of the toroid can be easily calculated by

$$H_s = \frac{N_t I}{L_1} \tag{3.4.13}$$

where I is the constant current (in A), N_t is the number of turns of the secondary winding (in our experiment N_t=3) and L_1 is the length of the slit of the toroid (for the toroid we use, L_1=0.33 mm). The polarising field, H_s, is given in A/m. The constant-current level was varied between 0.1-1.5 A with increments of 0.1 A. The values of the biasing field H_s, which correspond to these current levels, are presented in the first column of Table (3.5). The magnitude of H_s is very much larger than the amplitude of the alternating magnetic field which doesn't exceed the value of 60 A/m. This ensures that the technique works in the linear region. It is evident that both, alternating and biasing magnetic fields are orientated in the same direction. Therefore the susceptibility, which can be measured with this method, is the parallel susceptibility.

The results for the cobalt-ferrite ferrofluid are presented in Figs. (3.8) and those for the magnetite ferrofluid in Figs. (3.9) with dots:

(a) *Cobalt-Ferrite in water (300 G)*: The real and the imaginary components of the cobalt-ferrite parallel susceptibility are shown in Figs. (3.8 a-b) with dots, for the polarising fields of Table (3.5), whilst the fits obtained by using Eqs. (3.4.11), (3.4.12) are presented with solid lines. χ_0 and χ_∞ have the values which are indicated in the last two columns of Table (3.5). χ_0 decrease gradually with increase of the polarising field, whilst χ_∞ remains the same. From the fit we found that this gradual fall was in accordance with that predicted by Eq. (3.3.1). From the χ'' graph we see a shift to the right (increase) of the frequency f_{max} of the absorption peak. The values of f_{max} are signified in the second column of the Table (3.5). This increase of f_{max} corresponds to a decrease in the parallel relaxation time, $\tau_{\parallel} = 1/2\pi f_{max}$, the values of which are indicated in the third column of the Table (3.5). Furthermore, we can determine the contribution of

Figure 3.8 Cobalt-ferrite in water (300 G) polarised measurement:

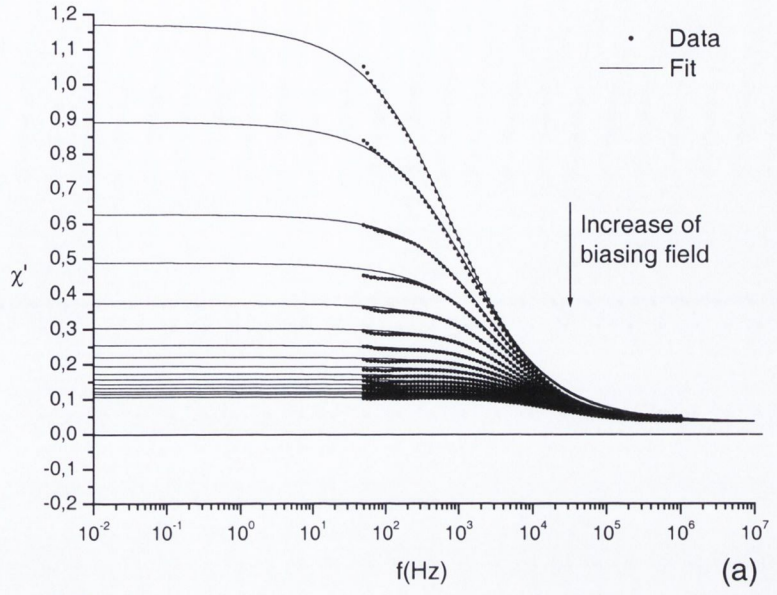

Figure 3.8 (a) Plot of parallel susceptibility (real component) for the H_s values of Table (3.5). Dots are the data and the solid line is the fit obtained by using Eq. (3.4.11).

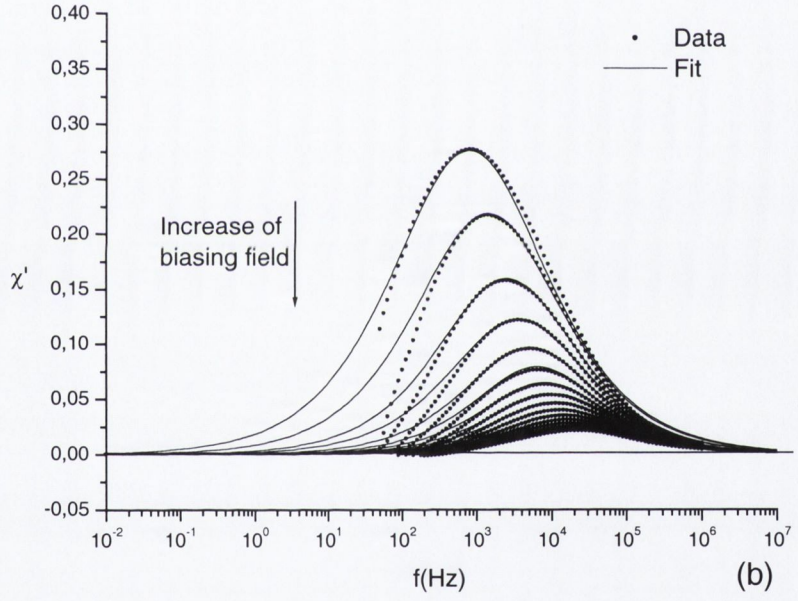

Figure 3.8 (b) the same, but for χ''.

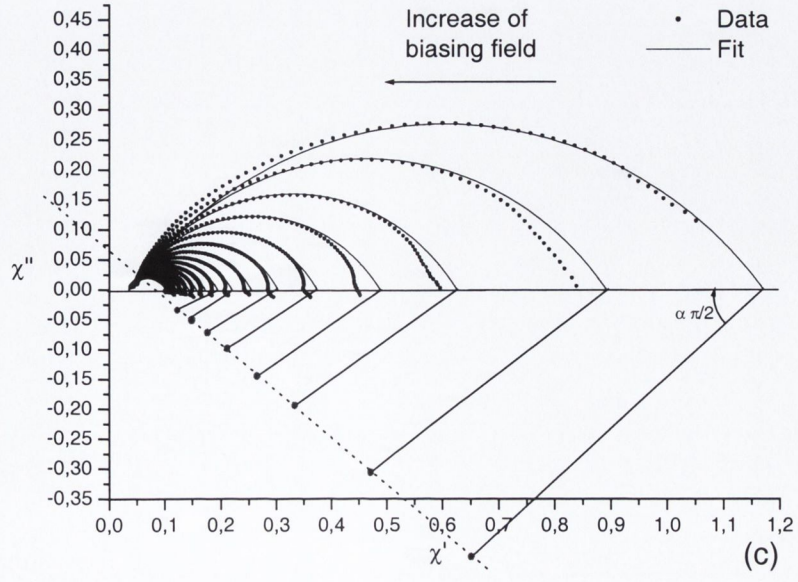

Figure 3.8 (c) Cole-Cole curves, corresponding to the various H_s values.

(Continued).

Figure 3.8 Cobalt-ferrite in water (300 G) polarised measurement:

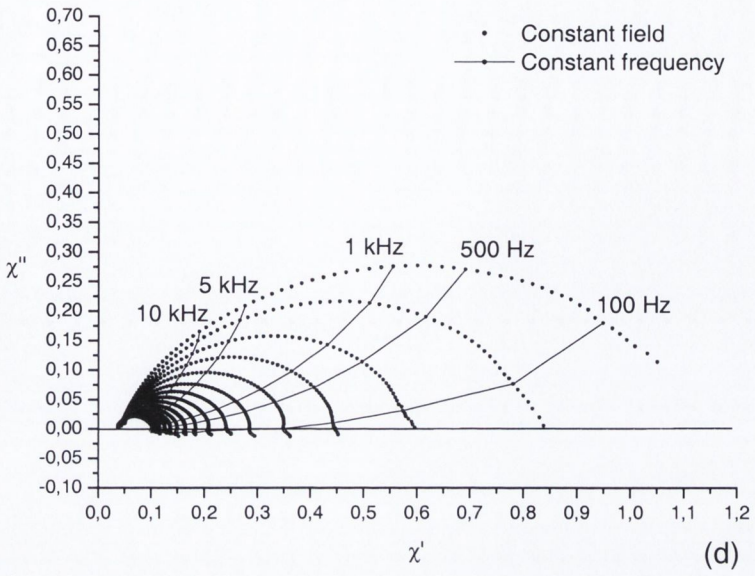

Figure 3.8 (d) Cole-Cole curves (solid lines) corresponding to constant frequencies.

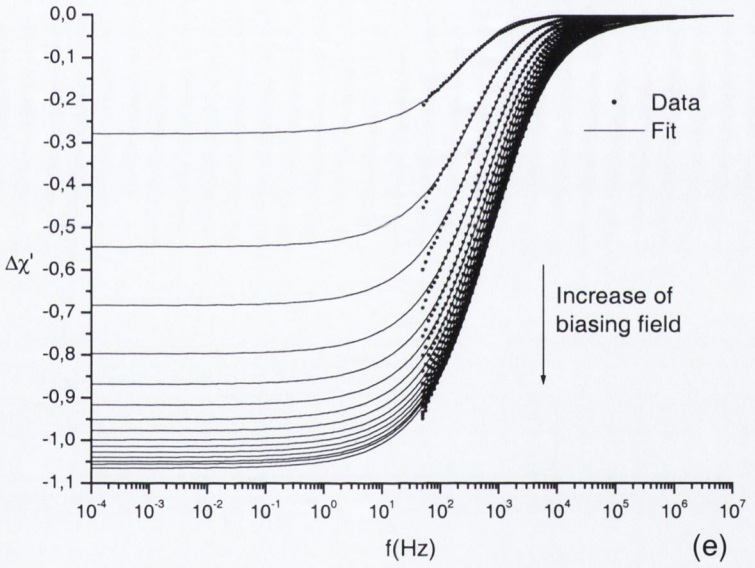

Figure 3.8 (e) $\Delta\chi'$ which is the unpolarised data subtracted from the polarised data.

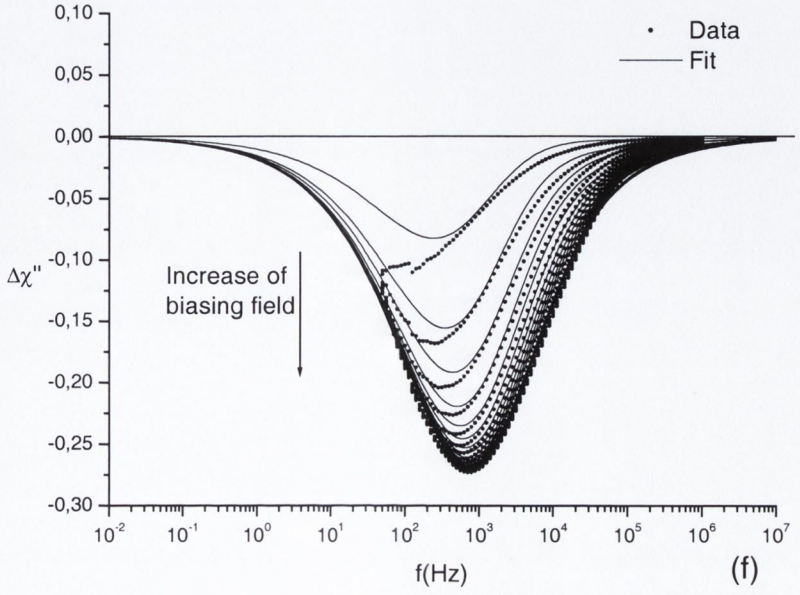

Figure 3.8 (f) the same for $\Delta\chi''$.

(Continued).

Figure 3.8 Cobalt-ferrite in water (300 G) polarised measurement:

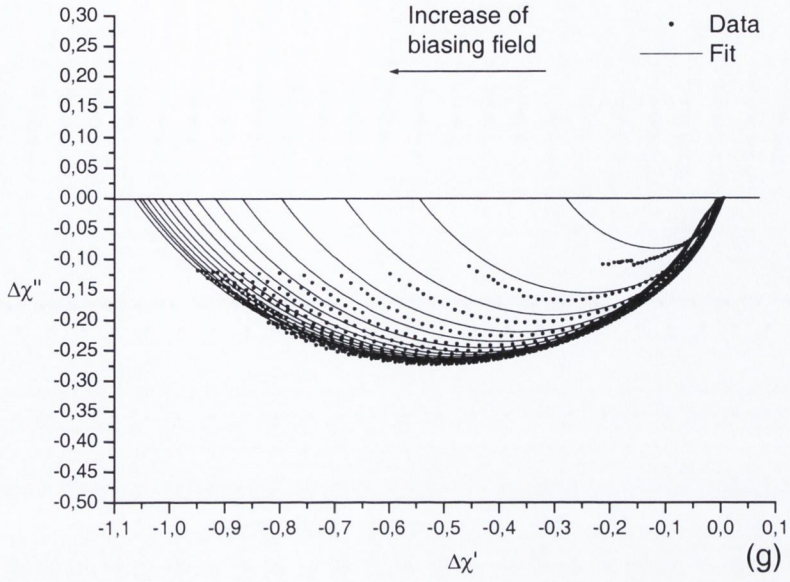

Figure 3.8 (g) Cole-Cole plot of $\Delta\chi'$ versus $\Delta\chi''$.

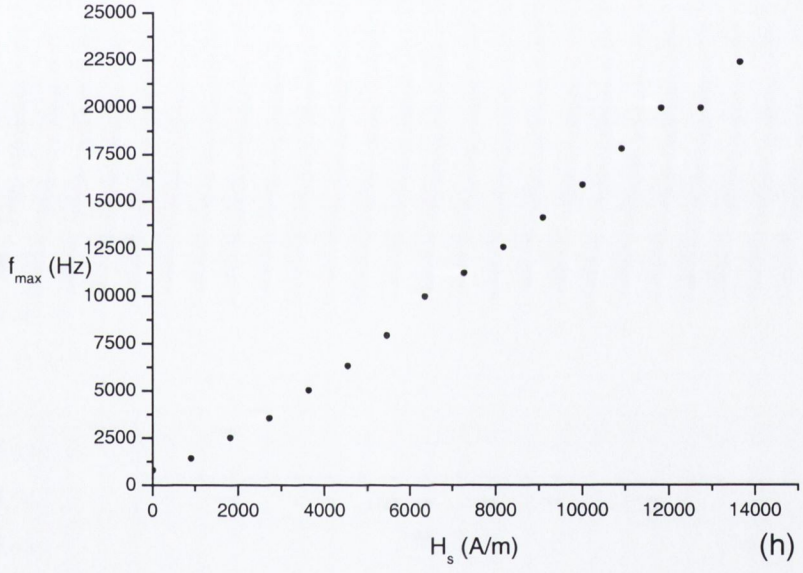

Figure 3.8 (h) f_{max} as a function of H_s (linear dependence).

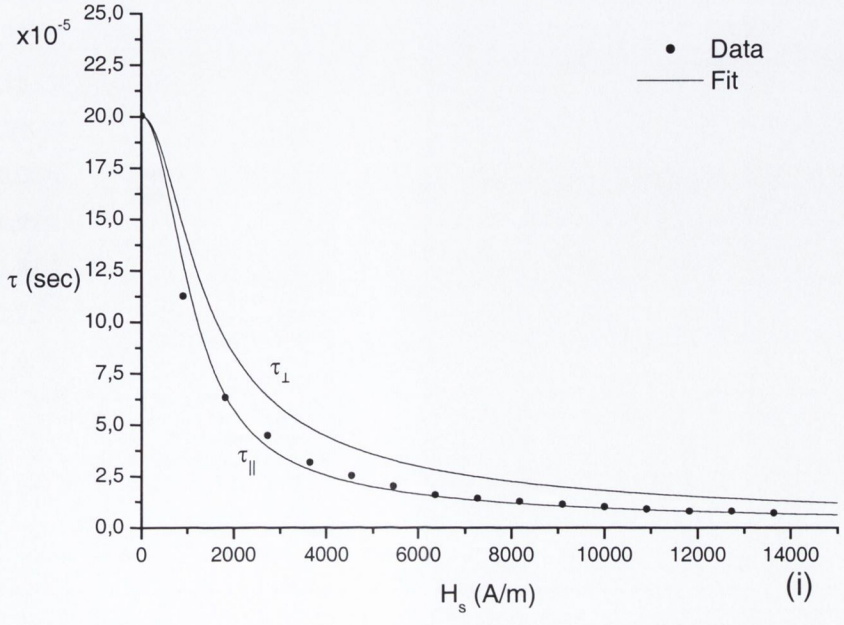

Figure 3.8 (i) $\tau_{\|}$ versus H_s. The fit (solid lines) are obtained by using Eq. (3.4.3),

(Continued).

Figure 3.8 Cobalt-ferrite in water (300 G) polarised measurement:

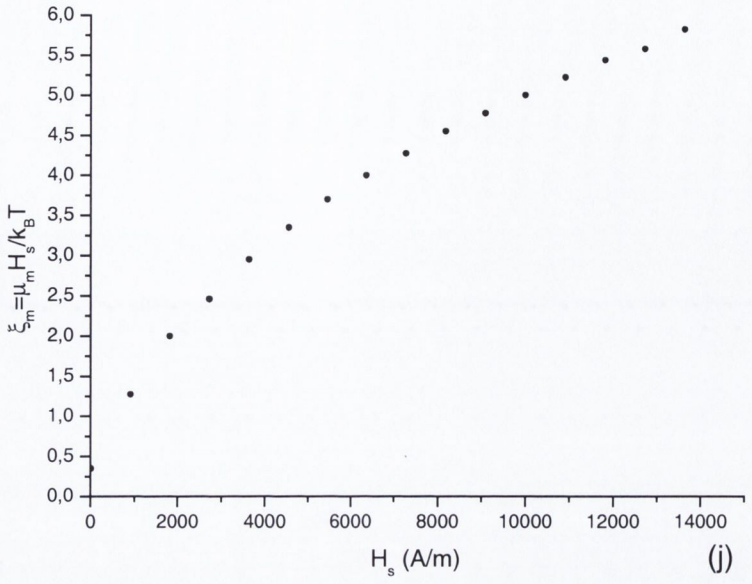

Figure 3.8 (j) Plot of the ξ_m parameter values used for the fit.

Table 3.5 Cobalt ferrite in water (300 G): parameters calculated from the measured data.

Polarising field	Frequency of Brownian peak	Parallel relaxation time	Hydrodynamic radius	Ratio of field energy to thermal energy	Static susceptibility	High freq/cy susc/lity
H_s (A/m)	f_{max} (Hz)	$\tau_{\parallel}$ (sec)	r_h (nm)	$\xi_m = \mu_m H_s / k_B T$	χ_0	χ_∞
0	794	2.003×10^{-4}	87.1	0.35	1.172	0.035
909.09	1,412	1.126×10^{-4}	71.8	1.275	0.891	0.035
1,818.2	2,511	6.336×10^{-5}	59.3	2	0.627	0.035
2,727.3	3,548	4.485×10^{-5}	52.8	2.46	0.489	0.035
3,636.4	5,011	3.175×10^{-5}	47.1	2.95	0.373	0.035
4,545.5	6,309	2.522×10^{-5}	43.6	3.35	0.303	0.035
5,454.5	7,943	2.003×10^{-5}	40.4	3.7	0.252	0.035
6,363.6	10,000	1.591×10^{-5}	37.4	4	0.219	0.035
7,272.7	11,220	1.418×10^{-5}	36	4.275	0.193	0.035
8,181.8	12,589	1.264×10^{-5}	34.6	4.55	0.171	0.035
9,090.9	14,125	1.126×10^{-5}	33.3	4.775	0.157	0.035
10,000	15,848	1.004×10^{-5}	32.1	5	0.143	0.035
10,909	17,782	8.949×10^{-6}	30.8	5.22	0.132	0.035
11,818	19,952	7.976×10^{-6}	29.7	5.435	0.12	0.035
12,727	19,952	7.976×10^{-6}	29.7	5.575	0.118	0.035
13,636	22,387	7.109×10^{-6}	28.6	5.82	0.106	0.035

the particle's sizes to the susceptibility, for each value of polarizing field, by calculating the *effective hydrodynamic radius* from Eq. (1.4.46). From the values in Table (3.5) we see that with increase of the polarizing field the smaller are the particles which contribute to the relaxation effect.

The fits in Figs. (3.8 a-b) are obtained by choosing optimum values for ξ_m and α for each individual curve. The Cole-Cole parameter α used here is 0.36 and it doesn't change significantly for several values of biasing field. This is demonstrated by the *Cole-Cole diagram* of Fig. (3.8 c) in which we plot χ'' versus χ'. In a Cole-Cole diagram the data appear to form a semicircle with the centre under the horizontal axis. Each semicircle corresponds to a different field and each data point to a different frequency. If we connect all the data-points which correspond to the same frequency, but to different polarizing fields, we get the Cole-Cole diagram for constant frequency. Figure (3.8 d) shows where the constant frequency curves (solid line) intersect the constant field curves (dots). The angle, ψ, formed between the radius and the horizontal axis, in Fig. (3.8 c), is equal to $\psi=\alpha\pi/2$ [20]. For the case of mono-dispersion $\alpha=0$ ($\psi=0$), and the Cole-Cole diagram is a complete semicircle. For our data we found that for each individual data curve, $\psi=0.565$ rad. Thus, the radii of all the circles are parallel and the circle's centres lie on the same line.

To obtain optimum fits the ξ_m parameter took the values which are denoted in Table (3.5). The χ_0 value in Eq. (3.4.11) was set equal to 1.172, which is the χ_0 value of the unpolarized susceptibility (top curve in Fig. (3.8 a)), and τ_B was set equal to 0.2003 ms which corresponds to the f_{max} value of the unpolarised χ''. It is obvious that the fits of the Figs. (3.8 a-b) are very close to the data and they show the validity of the theory used to explain our experiments. To achieve more accuracy in the fitting we subtracted the unpolarised data-curve from each polarised data-curve. The differences $\Delta\chi'$ and $\Delta\chi''$ are plotted as a function of the frequency in Figs. (3.8 e-f). Now, by increasing the polarising field $\Delta\chi'$ and $\Delta\chi''$ become more negative. Figure (3.8 g) shows the Cole-Cole diagram of $\Delta\chi''$ versus $\Delta\chi'$. From the latter three figures it is much easier to inspect visually the error between the data and the fit.

To show the accuracy of Eq. (3.4.3) for the parallel relaxation time we may fit Eq. (3.4.3) to the values of $\tau_{\parallel}$ given in Table (3.5). We plot first f_{max} versus H_s, Fig (3.8 h). The dependence is linear. We plot after $\tau_{\parallel} = 1/2\pi f_{max}$ versus H_s and we attain the fit by

use of Eq. (3.4.3). As Fig. (3.8 i) shows, the fit is very close. Thus, the theory of Martsenyuk et al can describe our results.

(b) *Magnetite in water (100 G)*: In Figs. (3.9 a-b) are presented, with dots, the components of the parallel susceptibility of a magnetite in water ferrofluid. The biasing fields used for this measurement are denoted in Table (3.6). The behaviour of the fluid is identically the same as that of the cobalt-ferrite and agrees completely with the model, which is described by Eq. (3.4.11). The f_{max} and $\tau_{\parallel}$ values are presented in Table (3.6). For the fit we used the values of ξ_m which are described in the same table. The Cole-Cole parameter α was 0.45 for all cases, showing a broader dispersion in the distribution of the size of the ferroparticles, as compared to that of the cobalt-ferrite sample. $\Delta\chi'$ and $\Delta\chi''$ are shown in Figs. (3.9 c-d). The values of the dimensionless parameter ξ_m, which were used for the fit, are denoted in Table (3.6) and plotted in Fig. (3.9 e). A fit of Martsenyuk's et al Eq. (3.4.3) for the parallel relaxation time, $\tau_{\parallel}$, is presented in Fig. (3.9 f). The unpolarized value of the Brownian relaxation time, that is 35.63 μsec, was used for this fit. The estimated effective hydrodynamic radius for the magnetite is much smaller than the radius of the cobalt-ferrite. This is why the calculated relaxation times are bigger for the cobalt-ferrite (one order).

Table 3.6 Magnetite in water (100 G): parameters calculated from the measured data.

Polarising field	Freq/ncy of Brownian peak	Parallel relaxation time	Effective hydrodyna-mic radius	Ratio of field energy to thermal energy	Static susce-ptibility	High frequency susc/lity
H_s (A/m)	f_{max} (Hz)	$\tau_{\parallel}$ (sec)	r_h (nm)	$\xi_m = \mu_m H_s / k_B T$	χ_0	χ_∞
0	4,466	3.563×10^{-5}	31.62	0.128	0.435	0.13
909.1	5,623	2.830×10^{-5}	11.426	0.548	0.409	0.12
1,818.2	7,079	2.248×10^{-5}	11.427	1.097	0.346	0.115
2,727.3	10,000	1.591×10^{-5}	11.31	1.6	0.278	0.113
3,636.4	12,589	1.264×10^{-5}	11.07	2	0.226	0.1
4,545.5	14,125	1.126×10^{-5}	10.85	2.35	0.187	0.095
5,454.5	15,848	1.004×10^{-5}	10.62	2.65	0.159	0.085
6,363.6	17,782	8.949×10^{-6}	10.4	2.9	0.139	0.083
7,272.7	19,952	7.976×10^{-6}	10.17	3.1	0.124	0.077
8,181.8	21,032	7.571×10^{-6}	10.03	3.35	0.11	0.07
9,090.9	21,200	7.511×10^{-6}	9.82	3.485	0.102	0.067

Figure 3.9 Magnetite in water (100 G) polarised measurement:

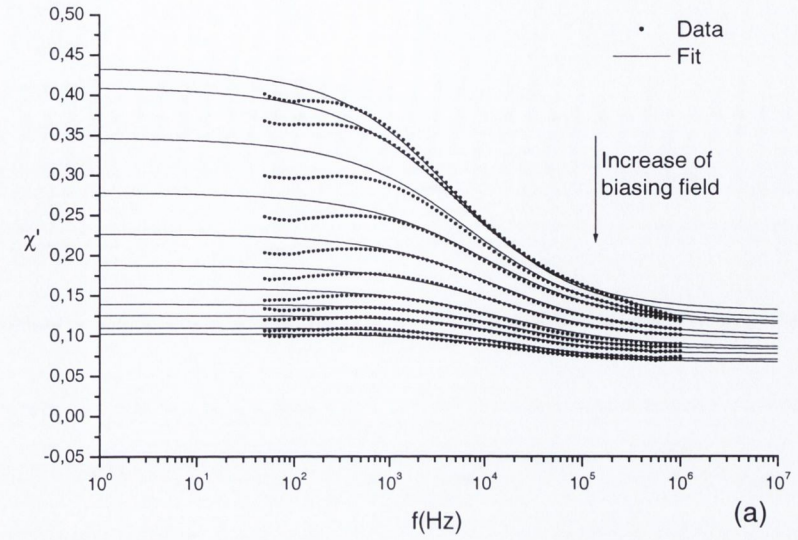

Figure 3.9 (a) Plot of parallel susceptibility (real component) for the values of the polarizing field of Table (3.6). Dots are the data and the solid line is the fit obtained by using Eq. (3.4.11).

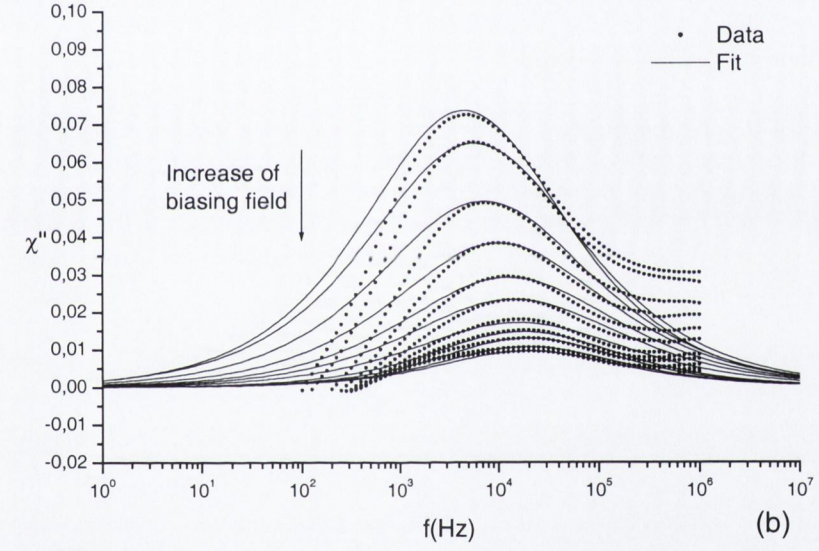

Figure 3.9 (b) The same as in (a), but for χ''.

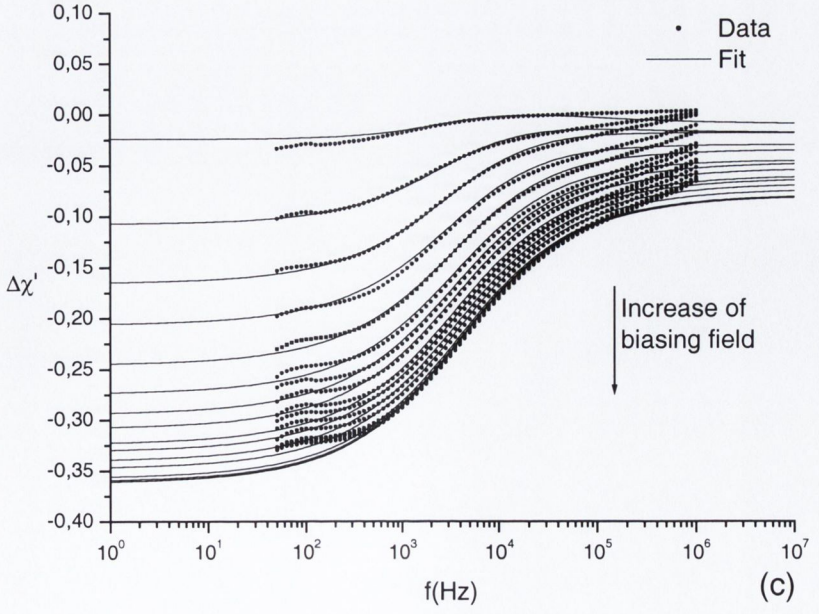

Figure 3.9 (c) Shows the difference, $\Delta\chi'$, of the unpolarised data subtracted from the polarised data.

(Continued).

Figure 3.9 Magnetite in water (100 G) polarised measurement:

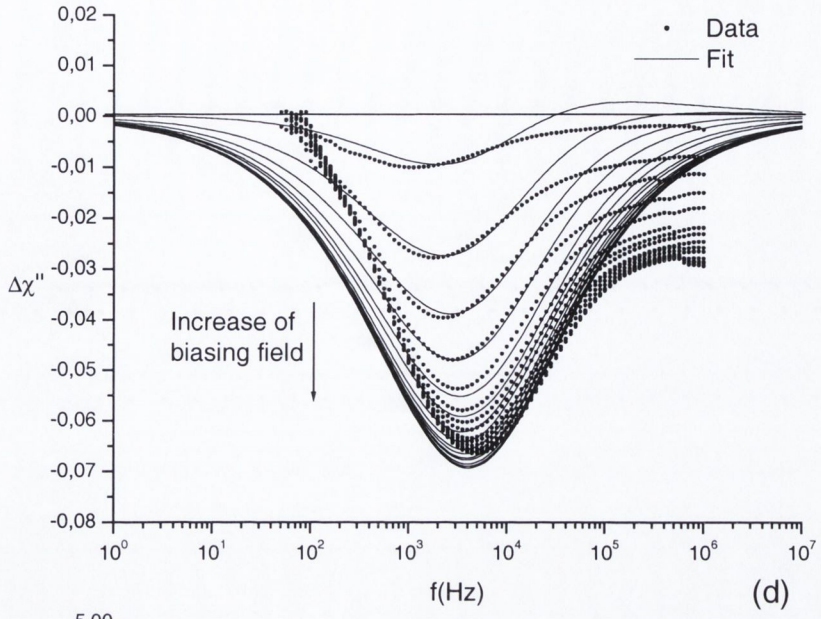

Figure 3.9 (d) The same as in (c), but for $\Delta\chi''$.

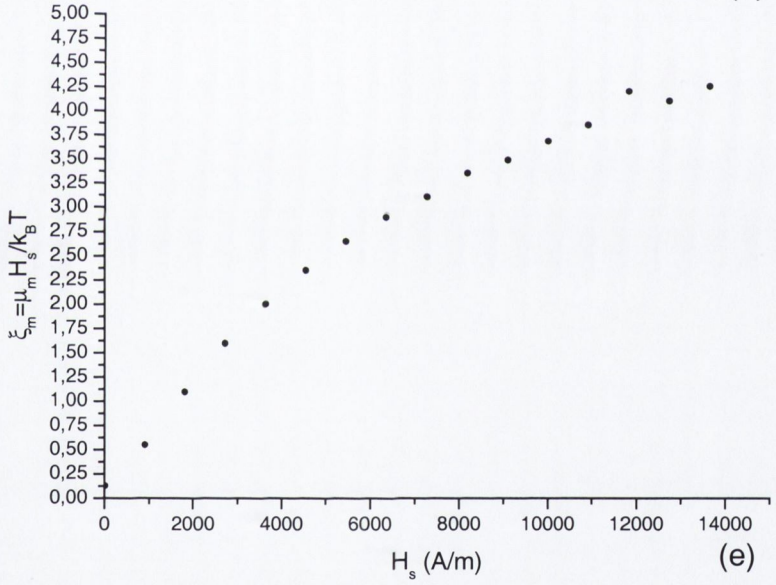

Figure 3.9 (e) Plot of the ξ_m parameter values used for the fit.

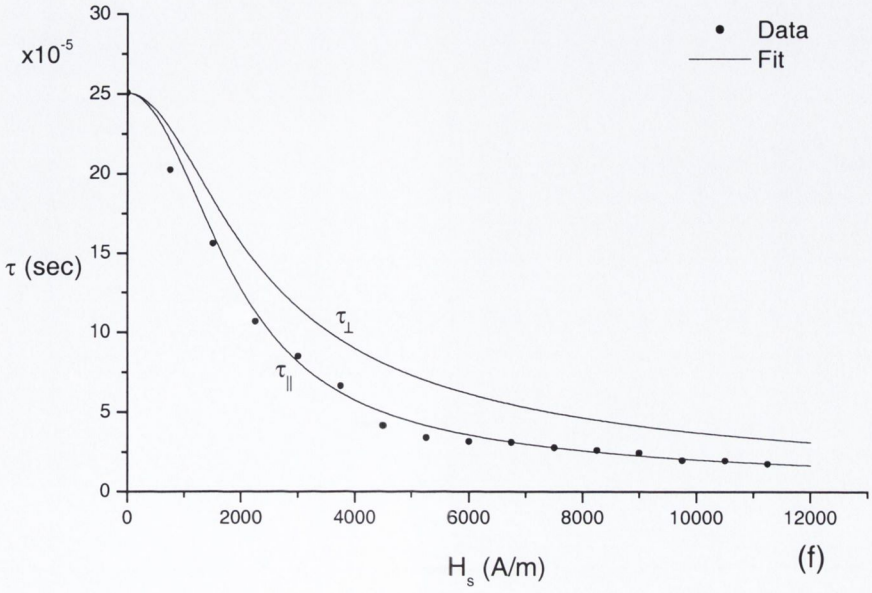

Figure 3.9 (f) $\tau_{\parallel}$ versus H_s. The fit (solid lines) are obtained by using Eq. (3.4.3). $\tau_{\perp}$ is also plotted, estimated from (3.4.8).

3.5 Observation of nonlinear susceptibility in ferrofluids.

We have measured so far only the behaviour of the ferrofluids in the linear region of the magnetization curve. The linear region of a magnetization curve is considered to be the field range in which the tangent of the curve, which determines the susceptibility, does not significantly change. This is the low field region, usually below 1 kA/m for typical ferrofluids. Beyond this range nonlinearity gradually becomes significant.

The nonlinear behaviour of the susceptibility is due to the nature of the magnetization curve; that is, due to its Langevin profile. At high fields the susceptibility, which is given by $\chi = dM/dh_a$ (all the quantities here are complex), decreases because the slope of the magnetization curve gradually decreases due to the incremental decrease in $\Delta M \rightarrow dM$, see Fig. (3.10 a). We can measure the nonlinear susceptibility if the alternating field h_a is strong enough to observe the incremental non-uniform changes of ΔM. The minimum value of h_a which is required for nonlinear observations is dependent on which region of the magnetization curve we are working in. The most nonlinear part is the region between the points A and B of Fig. (3.10 a) in which the slope changes rapidly. In this region it is not necessary to apply a particularly large h_a but we do need an additional large static field, H_s, which is able to shift the total magnetic strength to the right. With total field, $H_s + h_a(t)$, one can observe the non-uniform changes of ΔM even for small changes of h_a but the required value of H_s is difficult to reach experimentally. The region of the curve within the points B and B′ ($\pm$ 15 kA/m) is straighter, as is shown in the magnified Fig. (3.10 b), but we can still observe ΔM deformations. Here, the required value of H_s can be easily obtained, but the optimum value of h_a is larger, compared to what it was for the region between A and B. This is the region where we performed the polarised measurements presented in section 3.4, but in these measurements h_a was so small (approximately 60 A/m) that it could observe only uniform changes of ΔM. Finally, there is a region close to zero (CC′ in Fig. (3.10 c)) where the magnetization curve is straight and only linear effects appear. This is the region where we perform the unpolarised measurements.

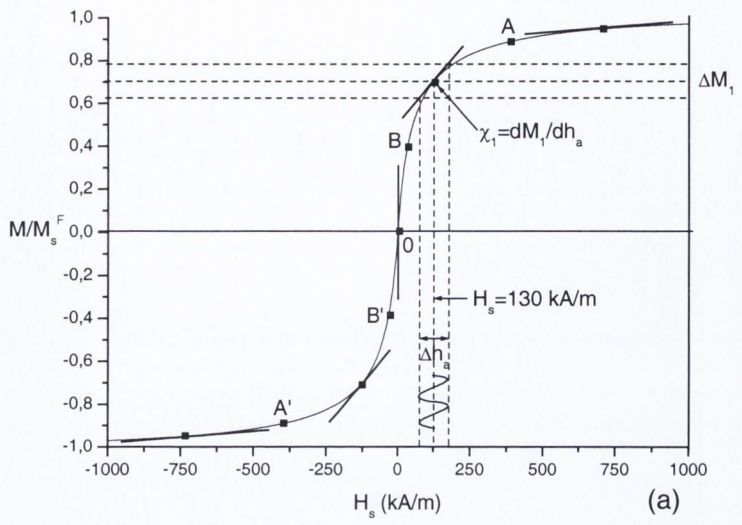

Figure 3.10 (a) Normalised magnetisation curve of a magnetite in water, ferrofluid, similar to the one presented in Fig. (1.4 b) in section 1.3. It shows the Langevin profile of the curve for positive and negative values of the applied biasing field, H_s. The tangent value to a specific point of the curve determines the susceptibility. The gradual change of the slope is due to the nature of the magnetisation curve and gives rise to nonlinear effects in the ferrofluids. This division of the magnetisation curve exceeds by far the usual values of the polarising field H_s (below 15 kA/m), which is used for the polarising measurements with the toroid coil.

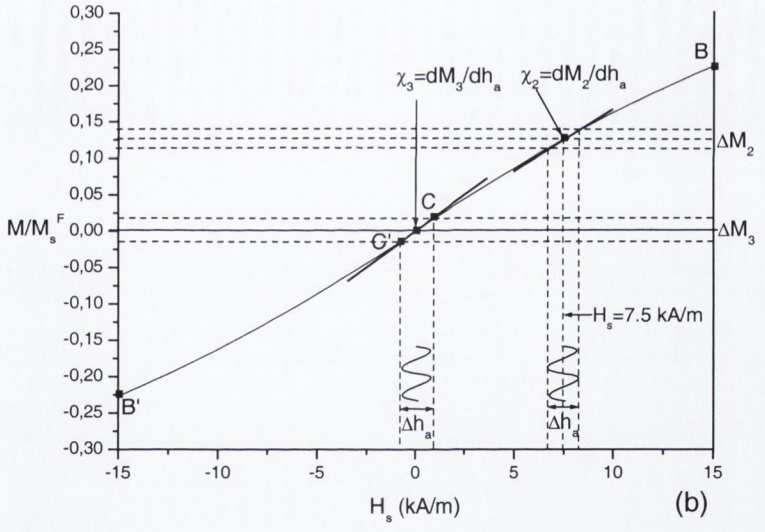

Figure 3.10 (b) Magnification of the magnetisation curve to the field range which is used for polarizing measurements with the toroid technique. The curvature is still significant for H_s above 1 kA/m and a relatively large oscillating field, h_a, can detect the nonlinearity.

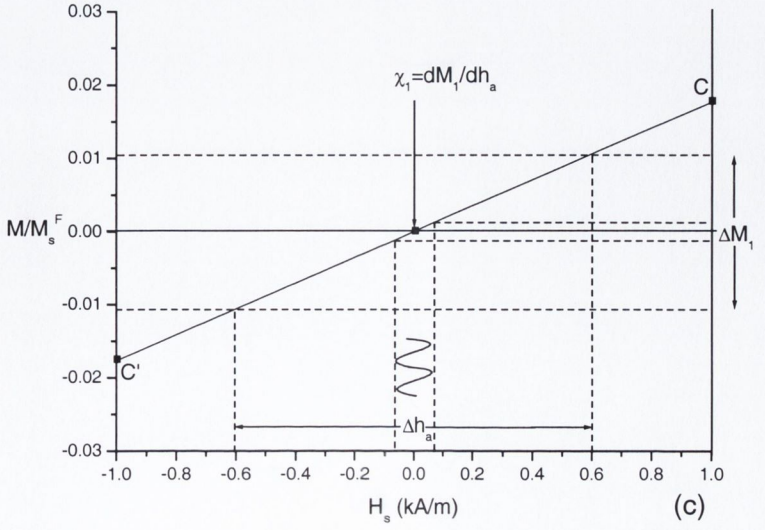

Figure 3.10 (c) Further enlargement (H_s is below 1 kA/m) shows the linear region of the magnetization curve. Here the detected susceptibility is independent of the value of the oscillating field, h_a. By increasing the oscillating field (by more than 1 kA/m) it is possible to reach the nonlinear region.

It is also possible to operate in the nonlinear region (beyond ± 1kA/m), without use of the auxiliary field H_s, by simply using a large value of oscillating field, h_a. This can be realised by means of a big enough toroidal core wound with a large number of turns. A winding of 80 turns, fed by 10 mA, can create approximately a value of h_a =2.5 kA/m, in contrast to 60 A/m which is created by the 20 turns winding which was used for the linear measurements. It is obvious that in both cases, whether experimenting with the combined field $H_s + h_a(t)$ or whether with h_a only, the amplitude of h_a is the important parameter, which lets us measure the linear or the nonlinear behaviour of the susceptibility.

The dependence of the magnetization's increment, ΔM, on the field is a complicated function but ΔM can be expanded in: (a) a series of powers of H_s, for the case of $H_s + h_a(t)$, or (b) in a series of powers of h_a when a strong alternating field is the only source of external excitation. Coffey and Paranjape [1] derived a theory for nonlinear relaxation in dielectric systems, the magnetic analogue of which, as shown here, can be easily applied for the case of ferrofluids. From an experimental point of view it is easier to observe both nonlinear effects and frequency dependent effects, such as magnetic relaxation, for a ferrofluid than for a polar dielectric fluid because of the far lower fields and probe frequencies required. Experimental evidence of dielectric nonlinear relaxation has been given recently for several polar dielectric liquids, namely hexyl-cyanobiphenyl in benzene [21,22], solutions of pentyl-cyanobiphenyl in cyclohexane and in squalane [23], polyvinil acetate [24] and trifluoroethylene-rich copolymers [25]. There are experimental verifications of the validity of Coffey and Paranjape's model for nonlinear susceptibility in dielectrics. It is our aim to present experimental evidence for the validity of this model in ferrofluids. For convenience we will present the magnetic analogue of the model.

The main differentiation between Coffey and Paranjape's consideration and Debye's [26] derivation was the notion that there is no longer the connection between the aftereffect and the alternating-field solutions seen in the linear approximations. The ratio of the response to stimulus (transfer function or impulse response) now depends on the form of the applied field, and is not independent of it, as in the linear case. The starting point of Coffey and Paranjape's theory was the Smoluckowski equation (1.4.5) for a planar rotator (they considered only the ϑ coordinate). They considered two cases for the external potential, namely:

Case (a): when only a strong alternating field, $h_a(t) = H_0 \cos(\omega t)$, is applied. This field results in a potential $V(\vartheta, t) = -\mu_m H_0 \cos(\omega t)\sin\vartheta$, and

Case (b): when a strong biasing and a relatively small alternating field ($H_0 / H_s << 1$) are superimposed, giving a total field $H(t) = H_s + H_0 \cos(\omega t)$. This field results in a potential

$$V(\vartheta, t) = -\mu_m [H_s + H_0 \cos(\omega t)]\sin\vartheta = -\mu_m H_s [1 + (H_0 / H_s)\cos(\omega t)]\sin\vartheta .$$

For each individual case they solved the Smoluckowski equation by using spherical harmonics (Eq. (1.4.27)) and they derived the corresponding polarisability in terms of powers of H_0 for case (a) and H_0 / H_s for case (b). In practice, one need only go as far as terms H_0 and H_0^3 for the case (a) and as far as $(H_0 / H_s)^2$ for the case (b), since the higher-order field terms make negligible contributions to the susceptibility.

For case (a) the solution contains terms of two angular frequency components, ω and 3ω. The component of the susceptibility having angular frequency ω may be written in the form [1]

$$\chi_1'(\omega, H_0) = \frac{N\mu_m^2}{3\mu_0 k_B T} \frac{1}{1+\omega^2\tau_B^2} \left[1 - \left(\frac{\mu_m H_0}{k_B T} \right)^2 \frac{(27 - 13\omega^2\tau_B^2)}{540(1+\omega^2\tau_B^2)(1+4\omega^2\tau_B^2/9)} \right] \tag{3.5.1}$$

$$\chi_1''(\omega, H_0) = \frac{N\mu_m^2}{3\mu_0 k_B T} \frac{\omega\tau_B}{1+\omega^2\tau_B^2} \left[1 - \left(\frac{\mu_m H_0}{k_B T} \right)^2 \frac{(21 + \omega^2\tau_B^2)}{270(1+\omega^2\tau_B^2)(1+4\omega^2\tau_B^2/9)} \right] \tag{3.5.2}$$

The ω and 3ω components of the susceptibility can be separated experimentally [24,25]. Notice the field dependence of the susceptibility on the amplitude, H_0, of the alternating field. The terms independent of H_0 are those obtained by Debye in his treatment of relaxation, whilst the terms dependent on H_0 represent relaxation due to the nonlinear behaviour.

For case (b) the solution for the magnetization is given in terms of both biasing field and the amplitude of the alternating field; it is described by the expression [1],

$$M(t, H_s) = \frac{N\mu_m^2 H_s}{3\mu_0 k_B T} \left\{ 1 - \frac{1}{15}\left(\frac{\mu_m H_s}{k_B T} \right)^2 + \frac{(H_0/H_s)}{1+\omega^2\tau_B^2} \left[1 + \left(\frac{\mu_m H_s}{k_B T} \right)^2 \frac{(2\omega^4\tau_B^4 - \omega^2\tau_B^2 - 27)}{15(1+\omega^2\tau_B^2)(9+\omega^2\tau_B^2)} \right] \cos(\omega t) \right.$$

$$\left. + \frac{\omega\tau_B (H_0/H_s)}{1+\omega^2\tau_B^2} \left[1 - \left(\frac{\mu_m H_s}{k_B T} \right)^2 \frac{(\omega^4\tau_B^4 + 19\omega^2\tau_B^2 + 42)}{15(1+\omega^2\tau_B^2)(9+\omega^2\tau_B^2)} \right] \sin(\omega t) + O((H_0/H_s)^2) \right\} \tag{3.5.3}$$

In this instance, provided that the higher order field terms $O((H_0/H_s)^2)$ may be neglected, only the fundamental frequency is present. The first two terms in Eq. (3.5.3) represent the expansion of the Langevin function for the magnetization in the strong constant field H_s. The components of the last two terms that are independent of $\frac{\mu_m H_s}{k_B T}$ are those due to the relaxation in the field $h_a(t) = H_0 \cos(\omega t)$ alone, whereas the two components prefixed by $\left(\frac{\mu_m H_s}{k_B T}\right)^2$ represent magnetic relaxation induced by the nonlinear coupling between the constant field and the alternating field. Equation (3.5.3) may be rearranged to read as follows:

$$\Delta M(t, H_s) = M(t, H_s) - M_{const} = [\chi'(\omega, H_s) - i\chi''(\omega, H_s)]H_0 \exp(i\omega t) \qquad (3.5.4)$$

where M_{const} denotes the constant portion of Eq. (3.5.3) and where

$$\chi'(\omega, H_s) = \frac{N\mu_m^2}{3\mu_0 k_B T} \frac{1}{1+\omega^2\tau_B^2}\left[1 + \left(\frac{\mu_m H_s}{k_B T}\right)^2 \frac{(2\omega^4\tau_B^4 - \omega^2\tau_B^2 - 27)}{15(1+\omega^2\tau_B^2)(9+\omega^2\tau_B^2)}\right] \qquad (3.5.5)$$

$$\chi''(\omega, H_s) = \frac{N\mu_m^2}{3\mu_0 k_B T} \frac{\omega\tau_B}{1+\omega^2\tau_B^2}\left[1 - \left(\frac{\mu_m H_s}{k_B T}\right)^2 \frac{(\omega^4\tau_B^4 + 19\omega^2\tau_B^2 + 42)}{15(1+\omega^2\tau_B^2)(9+\omega^2\tau_B^2)}\right] \qquad (3.5.6)$$

The increment $\Delta M(t, H_s)$ may be regarded as the magnetization arising from the alternating field and from the interaction of the alternating field with the constant field. The nonlinear terms of Eqs. (3.5.5) and (3.5.6) are regarded as the increment of the susceptibility, $\Delta\chi$, due to the nonlinear response, thus we may write

$$\Delta\chi'(\omega, H_s) = \frac{\chi_0}{1+\omega^2\tau_B^2}\left(\frac{\mu_m H_s}{k_B T}\right)^2 \frac{(2\omega^4\tau_B^4 - \omega^2\tau_B^2 - 27)}{15(1+\omega^2\tau_B^2)(9+\omega^2\tau_B^2)} \qquad (3.5.7)$$

$$\Delta\chi''(\omega, H_s) = -\frac{\chi_0\omega\tau_B}{1+\omega^2\tau_B^2}\left(\frac{\mu_m H_s}{k_B T}\right)^2 \frac{(\omega^4\tau_B^4 + 19\omega^2\tau_B^2 + 42)}{15(1+\omega^2\tau_B^2)(9+\omega^2\tau_B^2)} \qquad (3.5.8)$$

The term $\Delta\chi$ is the susceptibility difference between a polarised and an unpolarised measurement; it may also be represented in its complex form of $\Delta\chi = \Delta\chi' - i\Delta\chi''$. It is an important factor and can be represented graphically by subtracting the unpolarised data from the polarised data.

Other, later, attempts of estimation of the nonlinear susceptibility in *polar liquids* were made by Morita and Watanabe [27,28], who proposed a general formal perturbation

theory of the nonlinear response, Raikher et al [29], who solved the equation for the orientational distribution function by expansion in Legendre polynomials and harmonics, and Déjardin and Kalmykov [30,31], who proposed an exact solution in terms of matrix continued fractions. From the latter solution more general expressions for the first and third harmonics of the nonlinear susceptibility can be derived (see Eqs. (2.37)-(2.44) of [32]), which may be written in terms of the fields (both alternating and biasing) and a dimensionless parameter κ which measures the contribution of the induced dipole moment with respect to the permanent one (for polar nonpolarizable molecules $\kappa=0$, while for nonpolar polarizable molecules $\kappa=\pm\infty$). In spite of the generality of these expressions, we will adhere to the original Coffey and Paranjape's calculations which is sufficient to describe our experimental results.

The above expressions for nonlinear susceptibility are just normalised expressions and refer to the mono-dispersed case. To apply them to a realistic system we have to introduce χ_∞ into the expressions, and to account for the particle distribution. The distribution functions described in section 3.2 may be used, and applied to the nonlinear susceptibility expressions. The Cole-Cole parameter α can also be used but it is necessary to derive an expression of the nonlinear susceptibility, which includes α. To derive such an expression it is necessary to solve the diffusion equation (1.4.54), which describes anomalous diffusion, for both (a) and (b) cases. By extending the linear response solution originally given by Coffey et al [32] to the nonlinear case in the manner originally used by Coffey and Paranjape, Déjardin [33] solved the problem theoretically for both cases (note that in his paper $1-\alpha$ is denoted by α):

For case (a) he arrived at the following expression for the fundamental harmonic χ_1, with

$$\chi_1(\omega,H_0)=\frac{N\mu_m^2}{3\mu_0 k_B T}\frac{1}{(1+(-i\omega\tau_B)^{1-\alpha})}\left\{1-\left(\frac{\mu_m H_0}{k_B T}\right)^2\frac{1}{60(1+(-i\omega\tau_B)^{1-\alpha})}\right.$$

$$\left.\times\left[\frac{2\left[1+(\omega\tau_B)^{1-\alpha}\cos\left(\frac{\pi(1-\alpha)}{2}\right)\right]}{1+(i\omega\tau_B)^{1-\alpha}}+\frac{3}{3+(-2i\omega\tau_B)^{1-\alpha}}\right]\right\} \qquad (3.5.9)$$

For $\alpha=0$ the latter expression reduces to the complex form of Eqs. (3.5.1) and (3.5.2) [33], which is in agreement with the results in [1].

For case (b) he proposed the following expression for the increment of the nonlinear susceptibility, $\Delta\chi$, where,

$$\Delta\chi(\omega, H_s) = -\frac{\chi_0}{(1+(i\omega\tau_B)^{1-\alpha})}\left(\frac{\mu_m H_s}{k_B T}\right)^2 \frac{1+(1+(i\omega\tau_B)^{1-\alpha})(2+\frac{1}{3}(i\omega\tau_B)^{1-\alpha})}{15(1+(i\omega\tau_B)^{1-\alpha})(1+\frac{1}{3}(i\omega\tau_B)^{1-\alpha})} \qquad (3.5.10)$$

For α=0 the latter equation is the complex form of the nonlinear increment of susceptibility, Eqs. (3.5.7) and (3.5.8). Others [24] have proposed empirical expression, based on the Havriliak-Negami expression (Eq.(1.4.59)), which involve $\Delta\chi$ and the parameter α. But such an expression does not have any physical importance since it is not derived from the principle of the random walk and the concept of the anomalous diffusion.

Experimentally we are able to measure the nonlinear term $\Delta\chi$ by operating in the nonlinear region BB′ of the magnetization curve with a sufficiently high alternating field. The experimental setup is the same as the one described in the previous section: for case (a) use of a toroid with a large number of turns, it is possible to create an alternating field of some kA/m, and for case (b) use of a secondary winding carrying a sufficient constant current which creates a strong enough biasing field. The results of the measurement of a 100 G (0.01 T) magnetite in water sample, which was measured in section 3.4, is shown in Fig. (3.11) for case (a), and in Fig. (3.12) for case (b). Let us study both cases individually:

Case (a): The amplitudes of the alternating magnetic fields, under which the sample was tested, were approximately 250 A/m, 730 A/m, 1.2 kA/m and 1.6 kA/m. These fields were generated by a toroidal coil of 80 turns, fed by various currents. The current source was the HP 4192A auto-balanced bridge. The result, in Fig. (3.11 a-b), shows a gradual reduction in the magnitude of χ' and χ'' (more significant at the lower frequencies) with increasing oscillating field. The susceptibility curves, which match to the 250 and 730 A/m field values, correspond to the linear response. Both curves converge on each other. The other two susceptibility curves correspond to the nonlinear response. The susceptibility's increment $\Delta\chi$ can be calculated by subtracting the linear from the nonlinear curve, see Fig. (3.11 c). The $\Delta\chi$ response shows a frequency at which $\Delta\chi'$ becomes positive. This is a resonance point (change of the phase). The corresponding frequency has a value of f_{max}=1.4 kHz. This change of sign in $\Delta\chi'$ is characteristic of nonlinear behaviour. Coffey and Paranjape's solution predicts the change of sign: at low

Figure 3.11

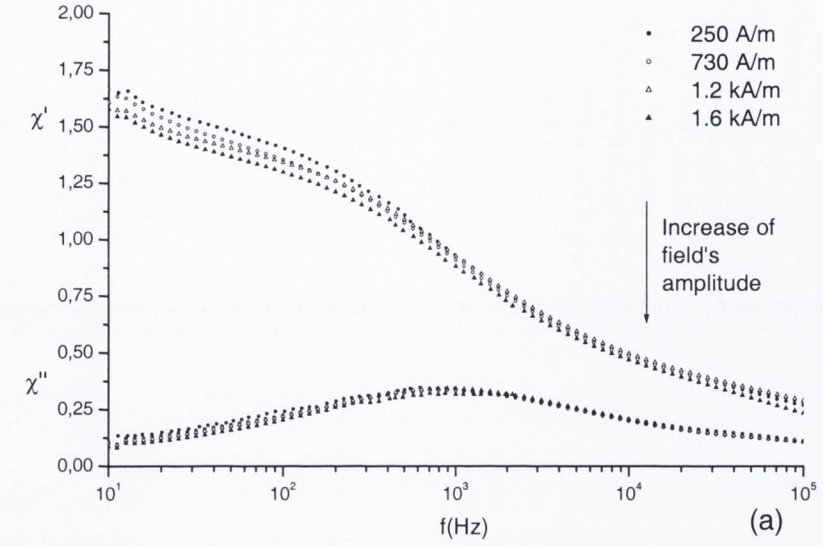

Figure 3.11 (a) The susceptibility's response as a function of the frequency and the oscillating field. The fields applied were 250 A/m, 730 A/m, 1.2 kA/m and 1.6 kA/m approximately. The latter two fields were operating in the nonlinear region. The difference between the linear response (250 and 730 A/m) and the nonlinear response (1.2 and 1.6 kA/m) is more pronounced at the lower frequencies.

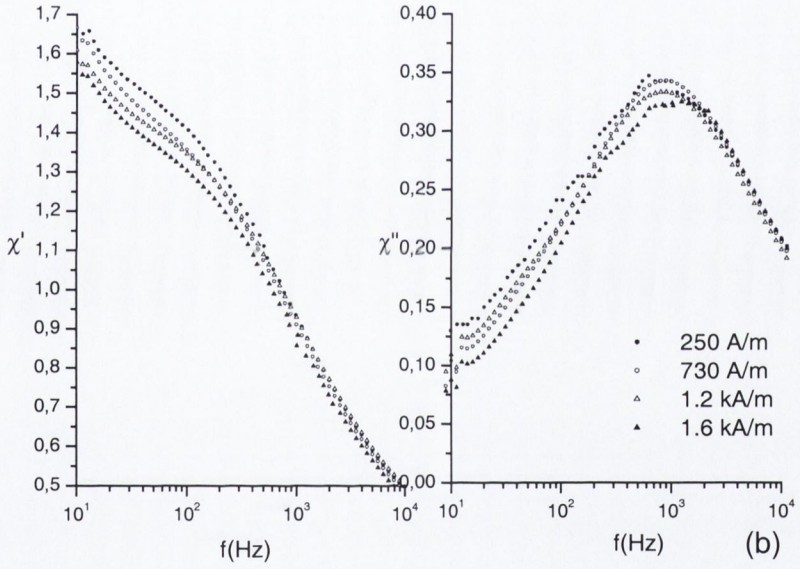

Figure 3.11 (b) Magnification of real and imaginary component of χ.

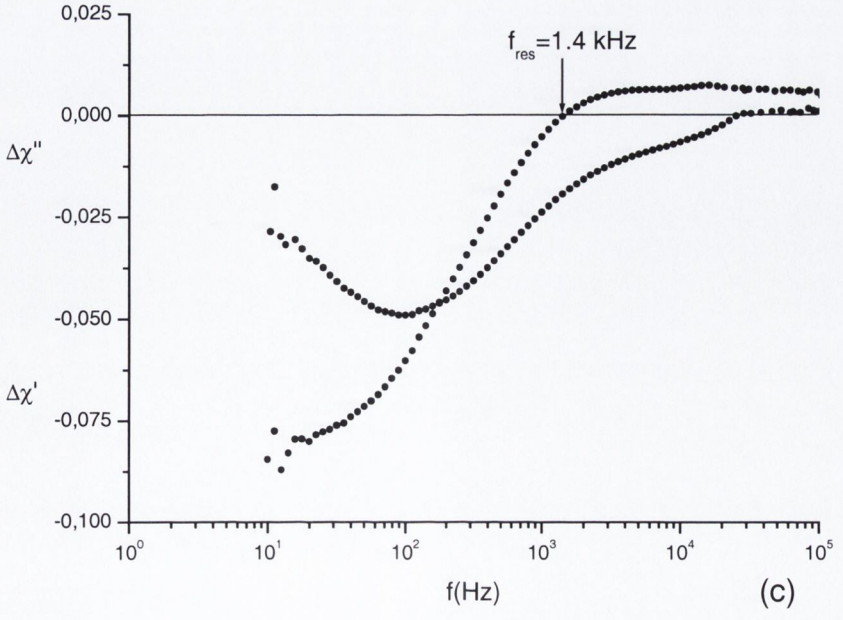

Figure 3.11 (c) Shows the susceptibility's increment $\Delta\chi$ between the linear response (250 A/m) and the nonlinear response (1.6 kA/m). The manifested resonance point at f_{res}=1.4 kHz, which is predicted by Coffey and Paranjape's model, is a characteristic of the nonlinear behaviour.

(Continued).

Figure 3.11

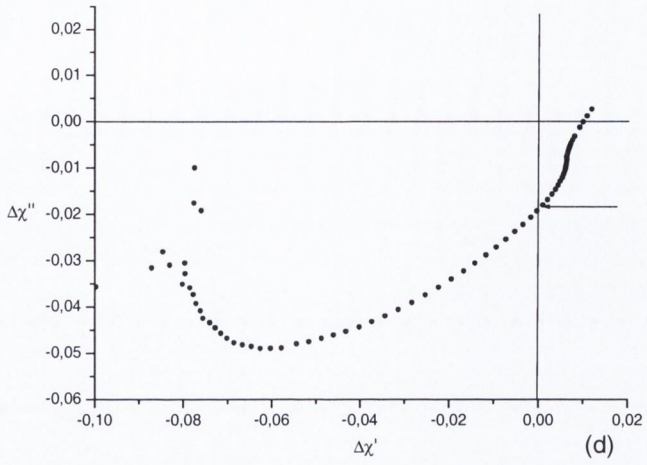

Figure 3.11 (d) The Cole-Cole diagram of $\Delta\chi$ components. The arrow shows the point at which $\Delta\chi$ becomes positive.

Figure 3.12

Shows the data of the linear (unpolarised) and the nonlinear (polarised) susceptibility for various biasing fields.

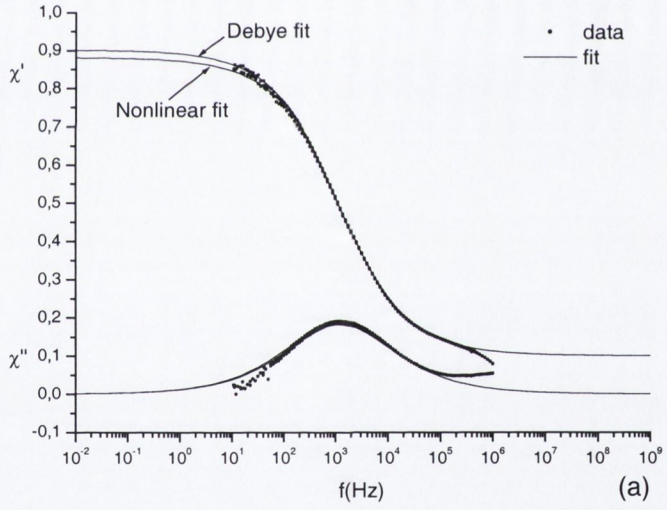

Figure 3.12 (a) The linear (Debye) and the nonlinear susceptibility curves when the biasing field is 750 A/m. Both curves are very close together, because we operate in the linear region.

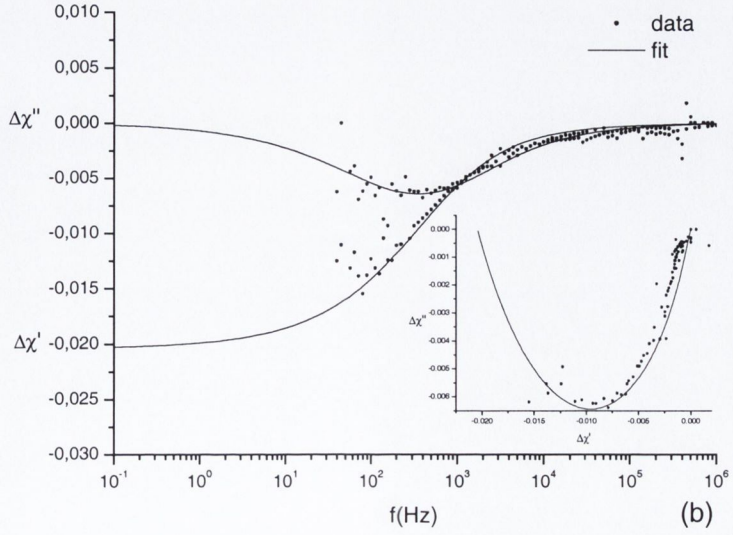

Figure 3.12 (b) The difference between the linear and the nonlinear susceptibility is derived by subtracting the two sets of data. The nonlinear increment $\Delta\chi$ can be very well fitted by Eq. (3.5.10) for α=0.45. The corresponding Cole-Cole diagram is presented in the inset.

(Continued).

Figure 3.12

Shows the data of the linear (unpolarised) and the nonlinear (polarised) susceptibility for various biasing fields.

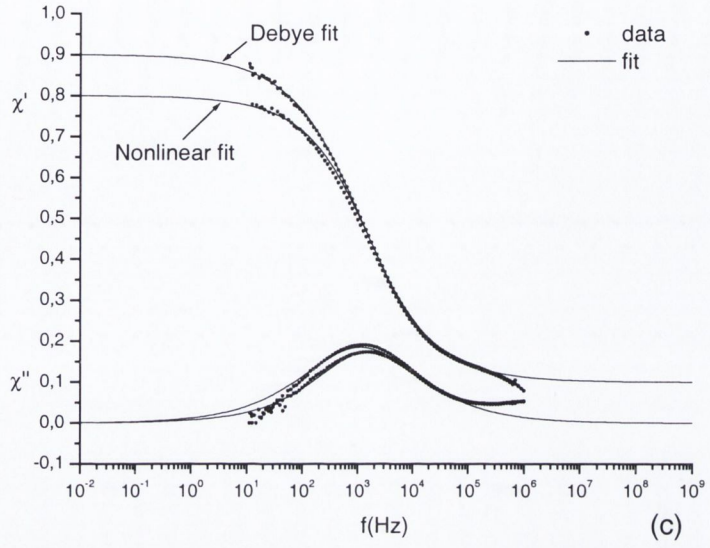

Figure 3.12 (c) The linear and the nonlinear susceptibility curves when the biasing field is 1.5 kA/m. The difference is more prominent than with the previous field (750 A/m).

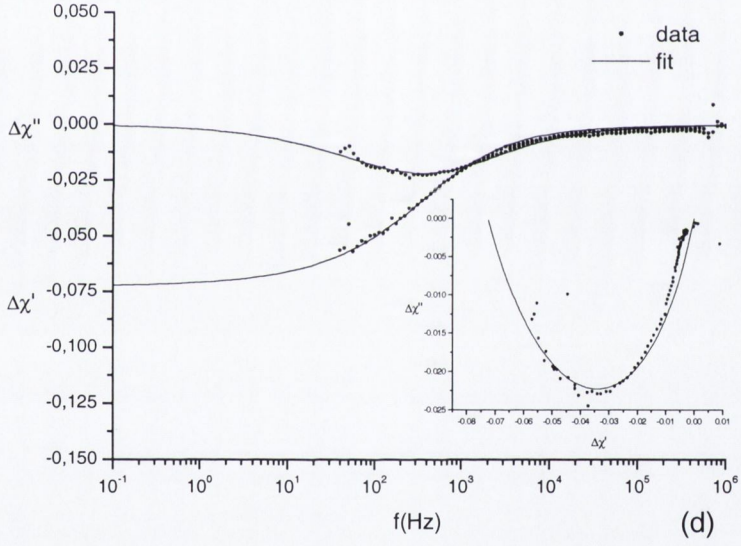

Figure 3.12 (d) The corresponding $\Delta\chi$ versus frequency and the Cole-Cole diagram.

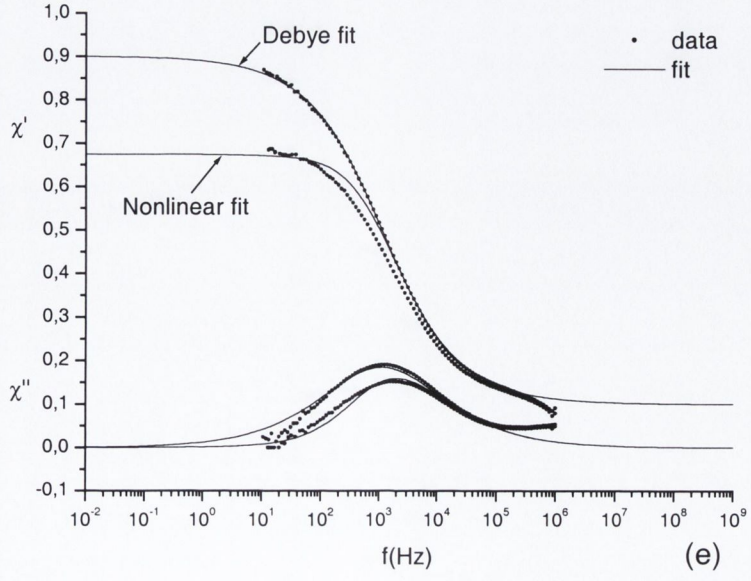

Figure 3.12 (e-f) The same, for H_s=2.25 kA/m.

(Continued).

Figure 3.12

Shows the data of the linear (unpolarised) and the nonlinear (polarised) susceptibility for various biasing fields.

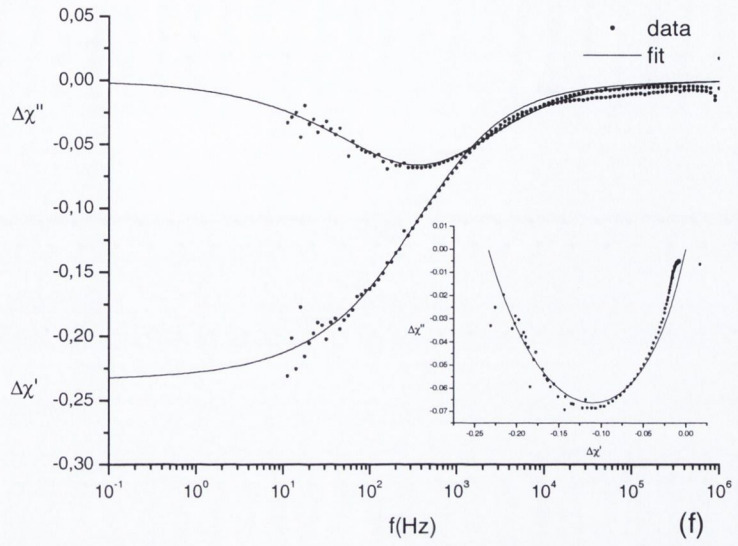

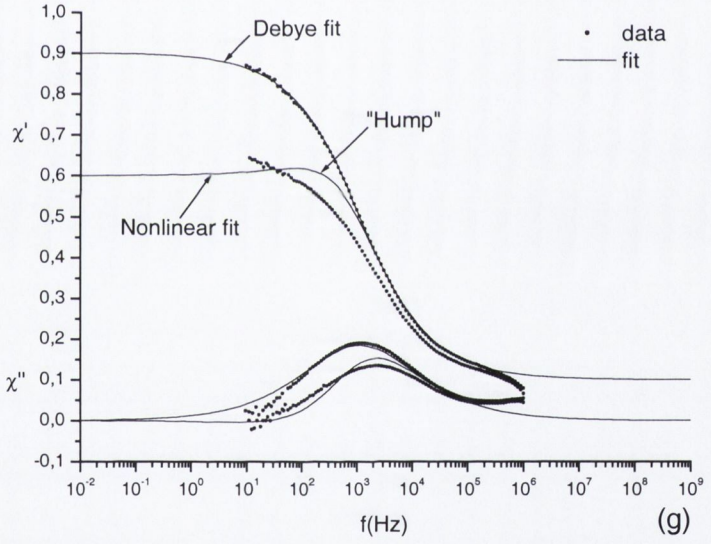

Figure 3.12 (g-h) The same, for H_s=3 kA/m. Here, because H_s is very strong, the nonlinear (second order) term in Eq. (3.5.11) become comparable to the linear and a hump appear on χ' component. Equation (3.5.11) is invalid to describe the effect.

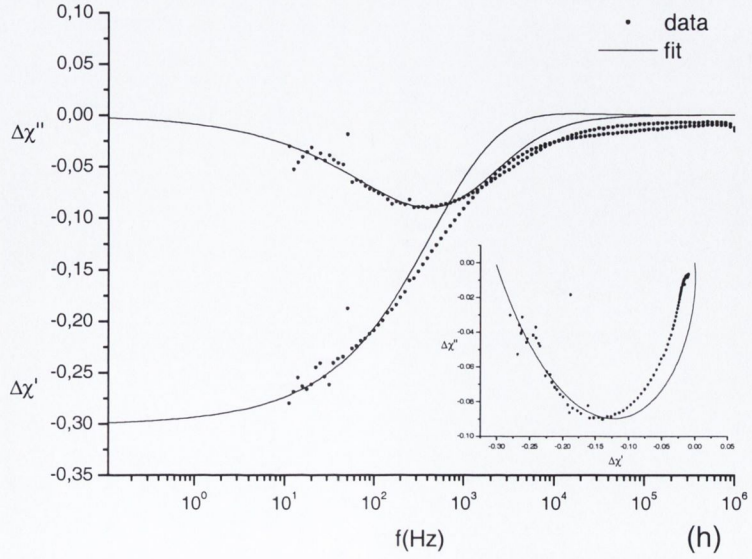

(Continued).

Figure 3.12

Shows the data of the linear (unpolarised) and the nonlinear (polarised) susceptibility for various biasing fields.

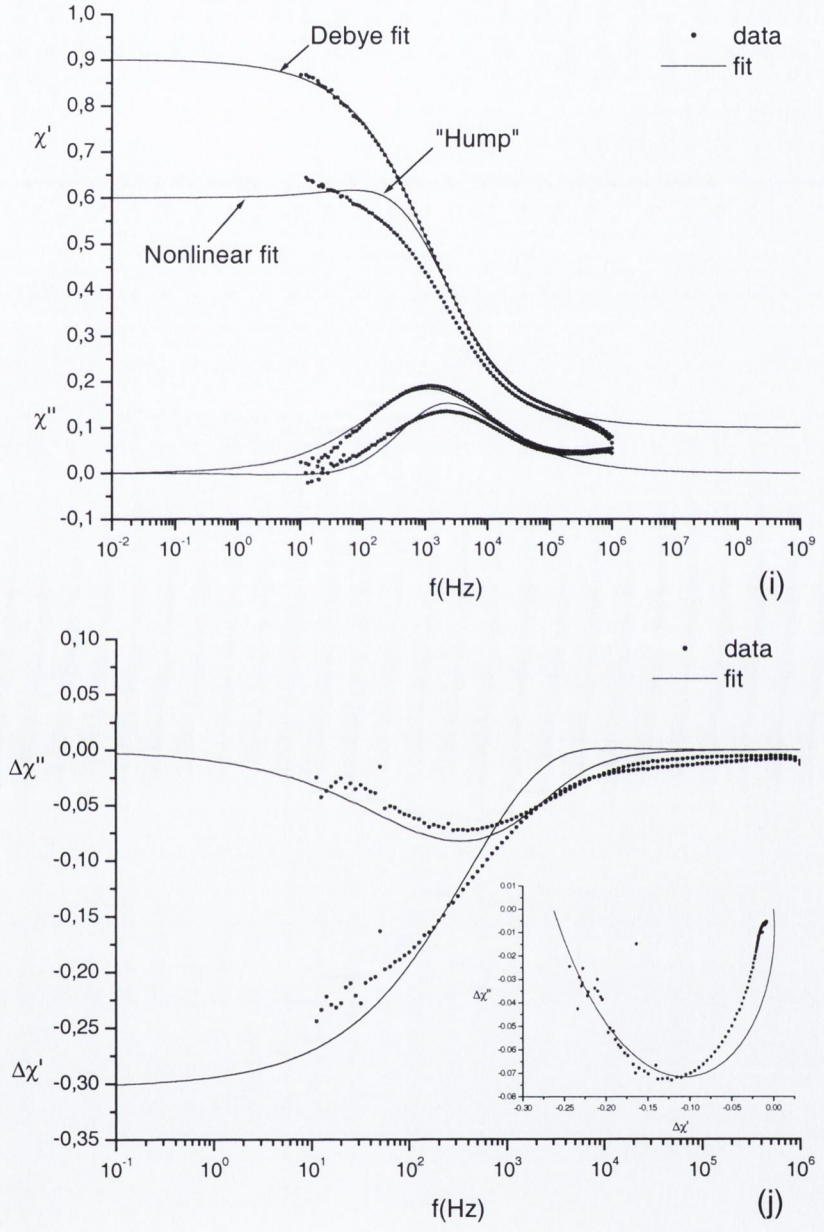

Figure 3.12 (i-j) The same, for H_s=3.75 kA/m. The deviation from the measured data is obvious and the fit is invalid.

Table 3.7 Fitting parameters when Eq. (3.5.11) is used to fit the nonlinear susceptibility data of Fig. (3.12). In all cases $\mu_m = 3\times10^{-24}$ Wb m.

Biasing field H_s (A/m)	Relaxation time τ_B (s)	Cole-Cole parameter α	Static nonlinear increment $\Delta\chi_0$	Validity of model [Eq. (3.5.11)]
750	1.3×10^{-4}	0.45	0.02	Valid
1,500	1.08×10^{-4}	0.45	0.1	Valid
2,250	8.03×10^{-4}	0.45	0.23	Valid
3,000	7.4×10^{-4}	0.45	0.42	Invalid
3,750	7.2×10^{-4}	0.45	0.66	Invalid

frequencies ($\omega \to 0$) the term $13\omega^2\tau_B^2$ is negligible and the nonlinear term of Eq. (3.5.1) is negative, but when the frequency increases the term $13\omega^2\tau_B^2$ becomes significant and results in a change of the sign of $\Delta\chi'$. This behaviour is reflected in the Cole-Cole diagram, in which some of the data points are on the right of the zero vertical axes as Fig. (3.11 d) shows. The same behaviour has been reported for polar dielectric liquids [21,22,23].

Case (b): The values of the constant polarizing fields used to shift the total field $H_s + h_a(t)$ to the nonlinear region, were 750 A/m, 1.5 kA/m, 2.25 A/m, 3 kA/m and 3.75 kA/m. The measured susceptibility is presented in Fig. (3.12), for each individual biasing field. For the first polarizing field (750 A/m) the susceptibility is very close to the unpolarised susceptibility (Fig. (3.12 a)) since we are still working in the linear region of the magnetization curve. In Fig. (3.12 a) the data are indicated by the dots and the fit is the solid line. The fit is obtained by using the model suggested by Coffey et al [1,32] and extended by Déjardin [33] to the susceptibility's nonlinear increment (Eq. (3.5.10)), which is combined with the Cole-Cole expression, Eq. (1.4.52). The form of the fitting equation is the same as Eqs. (3.5.5) and (3.5.6), with the Cole-Cole parameter α included (we also add in the high frequency susceptibility term, χ_∞),

$$\chi(\omega, H_s) = \frac{\chi_0 - \chi_\infty}{1 + (i\omega\tau_B)^{1-\alpha}}\left[1 - \left(\frac{\mu_m H_s}{k_B T}\right)^2 \frac{1 + (1 + (i\omega\tau_B)^{1-\alpha})(2 + \tfrac{1}{3}(i\omega\tau_B)^{1-\alpha})}{15(1 + (i\omega\tau_B)^{1-\alpha})(1 + \tfrac{1}{3}(i\omega\tau_B)^{1-\alpha})}\right] + \chi_\infty \quad (3.5.11)$$

We fit simultaneously the polarised curve (lower curve of Fig. (3.12 a)) with Eq. (3.5.11) and the unpolarised data with the usual Cole-Cole equation. The Brownian relaxation time of the unpolarised data was estimated to be $\tau_B = 1.3 \times 10^{-4}$ s and the α parameter was 0.45 (as in the fit of section 3.4, in Fig. (3.9), where we used the same magnetite sample). The incremental deviation of the static susceptibility, $\Delta\chi_0$, is calculated in terms of the biasing field, where

$$\Delta\chi_0 = -\frac{1}{5}\left(\frac{\mu_m H_s}{k_B T}\right)^2 \chi_0 \quad (3.5.12)$$

as is predicted from Eq. (3.5.10) for $\omega \to 0$. In this instance $\Delta\chi_0$ is calculated as $\Delta\chi_0 = -0.02$. The small deviation between the unpolarised data and the polarised data is plotted in Fig. (3.12 b), in which the fit for $\Delta\chi$ is obtained by use of Eq. (3.5.10). The corresponding Cole-Cole diagram is the inset graph.

The χ and $\Delta\chi$ curves which correspond to the second polarizing field (1.5 kA/m) are presented in Fig. (3.12 c-d). Now, we are fully into the nonlinear region. Here the increment $\Delta\chi_0 = -0.1$, which is larger than with the previous field (750 A/m). The α parameter and moment μ_m, used here, are the same as the previous field (see Table (3.7)). The relaxation time of the polarised data is $\tau_B = 1.08\times10^{-4}$ s, which is bigger than before, because τ_B is dependent on H_s according to Eq. (3.4.3). This is something which is not accounted for in Eq. (3.5.11) but it has to be considered since H_s is strong enough to shift the f_{max} point. From this, we conclude that Eq. (3.5.11) is good enough to predict $\Delta\chi_0$ but the relaxation time cannot be taken equal to the relaxation time of the unpolarized susceptibility.

Increasing the biasing field up to 2.2 kA/m the fit is still close to the data. A further increase ($H_s > 3$ kA/m) results in the polarised susceptibility deviating very much from the unpolarised susceptibility. In this case Eq. (3.5.11) cannot describe the nonlinear effect anymore, because the nonlinear term becomes comparable to the linear term. This is shown in Figs. (3.12 g-j) in which a "hump" appears as indicated by the arrows. The fitting parameters for each of the five cases are shown collectively in Table (3.7).

We conclude that it is possible to use Coffey and Paranjape's calculation modified by Déjardin to describe the nonlinear magnetic susceptibility as it is measured for both the (a) and (b) cases with the condition, for case (b), that the magnitude of the biasing field is such that the second order (nonlinear) term is not significant.

3.6 Application 1: Calculation of the loss factor tanδ from the susceptibility data.

The loss factor tanδ is a quantity measuring losses in a magnetic material. It is defined as [9]

$$\tan\delta = \frac{\mu''}{\mu'} = \frac{\chi''}{1+\chi'} \tag{3.6.1}$$

Substituting the values for χ' and χ'' from Eq. (1.4.47) have,

$$\tan\delta = \frac{\chi''(\omega)}{1+\chi'(\omega)} = \frac{(\chi_0 - \chi_\infty)\omega\tau_B}{(1+\chi_\infty)(1+\omega^2\tau_B^2) + \chi_0 - \chi_\infty} \tag{3.6.2}$$

tanδ is field dependent because the susceptibility is field dependent. This dependence have been studied theoretically in [1,7] where expressions for tanδ for both linear and nonlinear relaxation are given. We may distinguish between parallel tanδ, when both

biasing and alternating fields are in the same direction, and perpendicular tanδ, when the fields are in vertical orientations. In this section we present experimental evidence for the field dependence of parallel tanδ.

For the cobalt-ferrite in water sample, which was studied in section 3.4, tanδ is shown in Fig. (3.13 a) as a function of the frequency for various fields. The polarizing fields are those indicated in Table (3.5). tanδ increases gradually with the frequency up to a maximum and then decreases. Its magnitude is a decaying function of the biasing field. The fluid becomes less-lossy with increase of H_s. This is expected since χ, which defines tanδ, is a decaying function of the polarizing field. In the context of the application of magnetic fluids in the area of low-loss devices, this result is of significance as it indicates a possible technique of controlling such losses.

The maximum peak of tanδ differs from the maximum peak of χ''. We can estimate the frequency at which tanδ peaks simply by calculating the derivative of tanδ with respect to the angular frequency, ω, and equating to zero. Thus,

$$\frac{d(\tan\delta)}{d\omega} = \frac{d}{d\omega}\left(\frac{(\chi_0-\chi_\infty)\omega\tau_B}{(1+\chi_\infty)(1+\omega^2\tau_B^2)+\chi_0-\chi_\infty}\right)$$

$$= \frac{\tau_B(\chi_0-\chi_\infty)(1+\chi_\infty)\left(1-\omega^2\tau_B^2+\dfrac{(\chi_0-\chi_\infty)}{(1+\chi_\infty)}\right)}{[(1+\chi_\infty)(1+\omega^2\tau_B^2)+\chi_0-\chi_\infty]^2} \qquad (3.6.3)$$

By setting the derivative equal to zero, results in

$$\omega_{max} = \frac{1}{\tau_B}\sqrt{1+\frac{(\chi_0-\chi_\infty)}{(1+\chi_\infty)}} \qquad (3.6.4)$$

ω_{max} of tanδ differs from ω_{max} of χ'' (which equals $1/\tau_B$) by the square root factor. Setting χ_0=1 and χ_∞=0 we find $\omega_{max} = \sqrt{2}/\tau_B$. From the Table (3.5) f_{max}=794 Hz, for the unpolarised χ'', and from Fig. (3.13 a) f_{max}=1,240 Hz, for tanδ. Their ratio is $1.36 \cong \sqrt{2}$. Now, if we consider the field dependence of the parallel susceptibility we must substitute χ_0 by $3\chi_0 L'(\xi_m)$ into Eq. (3.6.4) and we get the field dependence of the parallel tanδ,

$$\omega_{max} = \frac{1}{\tau_B}\sqrt{1+\frac{(3\chi_0 L'(\xi_m)-\chi_\infty)}{(1+\chi_\infty)}} \qquad (3.6.5)$$

In Fig. (3.13 b) we show the dependence of tanδ on the biasing field for some individual frequencies, namely 100 Hz, 500 Hz, 1 kHz, 5kHz, 10 kHz, 50 kHz and 100

kHz. All curves decay with increasing polarising field. Their curvature is dependent on the frequency of measurement.

Figure 3.13

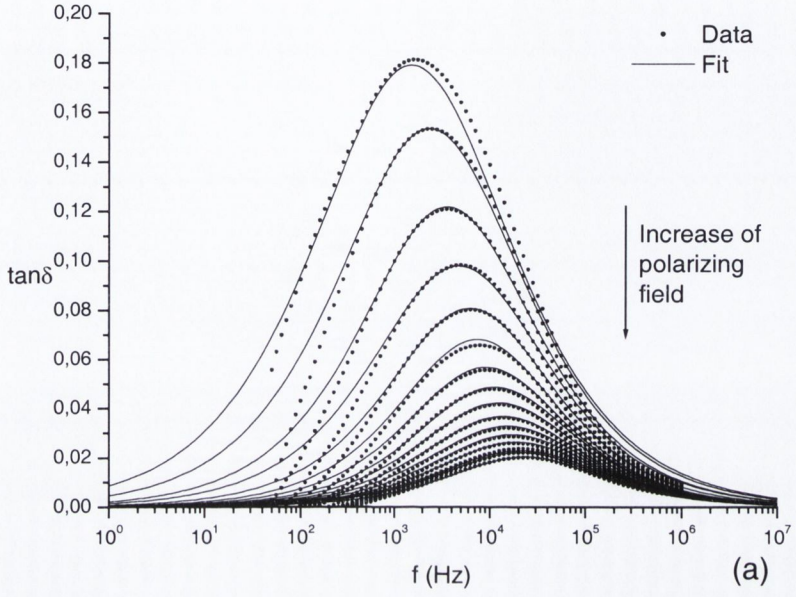

Figure 3.13 (a) The loss factor tanδ, of a 300 G cobalt-ferrite in water ferrofluid, as a function of the frequency for various polarizing fields. The fits (solid lines) are in accordance to the equations given in [7].

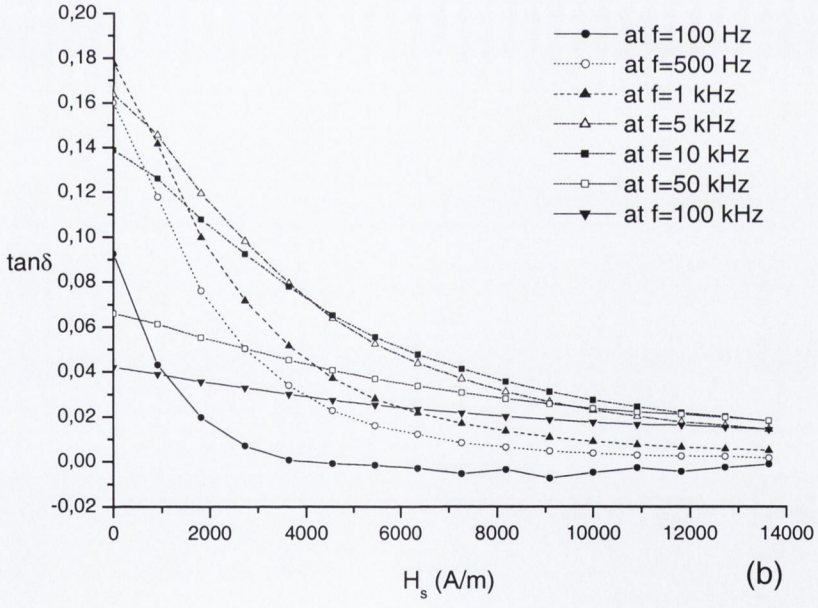

Figure 3.13 (b) The loss factor tanδ as a function of polarizing field for various frequencies.

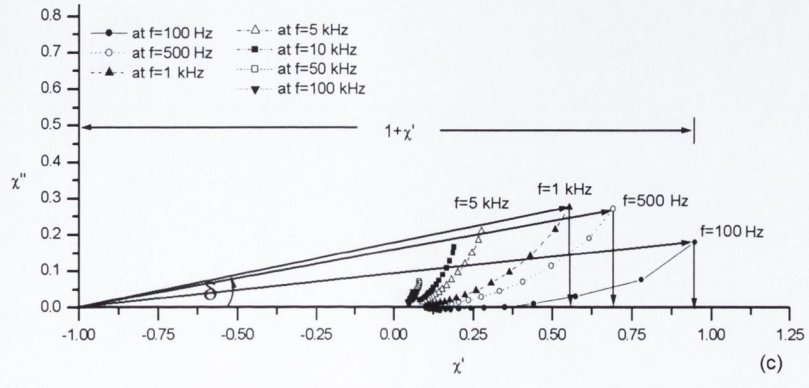

Figure 3.13 (c) A triangular representation of tanδ.

It is possible to plot the tanδ data in a Cole-Cole diagram in which the curves correspond to constant frequencies, in a manner similar of that in Fig. (3.8 d) [34]. In this diagram (Fig. (3.13 c)) the horizontal axis is extended back to –1, so each point's value represents the denominator of Eq. (3.6.1). Each data-point corresponds to a triangle from which tanδ is easily calculated from the lengths of the triangle's sides.

3.7 Application 2: Calculation of heat losses from susceptibility data.

It is possible to estimate the dissipated energy when current flows into a coil, which contains a ferrofluid. The energy loss is transformed into heat. The heat losses have been studied in detail by Rosensweig [35] who calculated the heating rates in several ferrofluids subjected to an alternating field (the magnetic work is converted into the internal energy of ferrofluid). In this section we estimate the heat when the sample is subjected to a biasing field H_s superimposed on an alternating field $h_a(t) = H_0 \cos(\omega t)$. The heat rate energy density is proportional to the loss component, χ'', of the magnetic susceptibility and it is given by [9,35]

$$U^{heat}(\omega) = \frac{1}{2}\omega\mu''(\omega)\mu_0 H_0^2 = \frac{1}{2}\omega\chi''(\omega)\mu_0 H_0^2 \qquad (3.7.1)$$

The heat produced per unit volume in the period of one cycle is [9]

$$U^{heat}(T) = \pi\chi''(\omega)\mu_0 H_0^2 \qquad (3.7.2)$$

The heat produced per unit volume in the period of one cycle is [9]

Tl $$U^{heat}(T) = \pi\chi''(\omega)\mu_0 H_0^2$$ toroid coil we use is

60 A/m.

Adapting the susceptibility data of the already measured 300 G cobalt-ferrite in water and 100 G magnetite in water samples (section 3.4), we can estimate the heat rate energy density, $U^{heat}(\omega)$, and the heat energy density per cycle, $U^{heat}(T)$. The heat losses for the cobalt-ferrite sample are shown in Fig. (3.14 a-b) which illustrate $U^{heat}(\omega)$ and $U^{heat}(T)$, respectively, for the various fields of Table (3.5). We see a decrease of both quantities as a function of H_s. $U^{heat}(\omega)$ increases with the frequency, while $U^{heat}(T)$ increases up to a maximum point and then decreases. We get analogous results for the magnetite sample as shown in Fig. (3.14 c-d).

Heating ferrofluids, to achieve hyperthermia, has important applications in medical treatments [36,37,38] as well as in electronic technology [39].

Figure 3.14

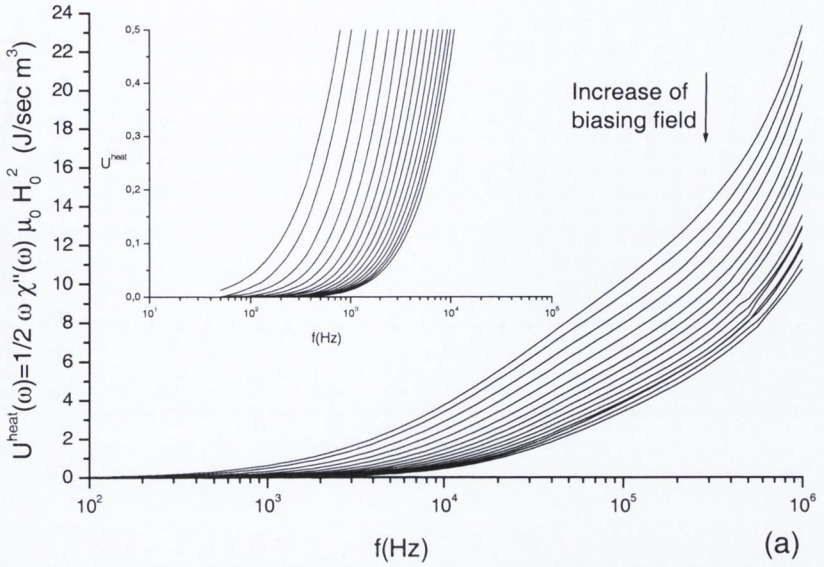

Figure 3.14 (a) The heat rate energy density of the 300 G cobalt-ferrite in water ferrofluid as a function of the frequency of the oscillating field. The heat rate is calculated by use of Eq. (3.7.1) for the various polarised susceptibility data. The inset shows the detail at the beginning of the frequency range.

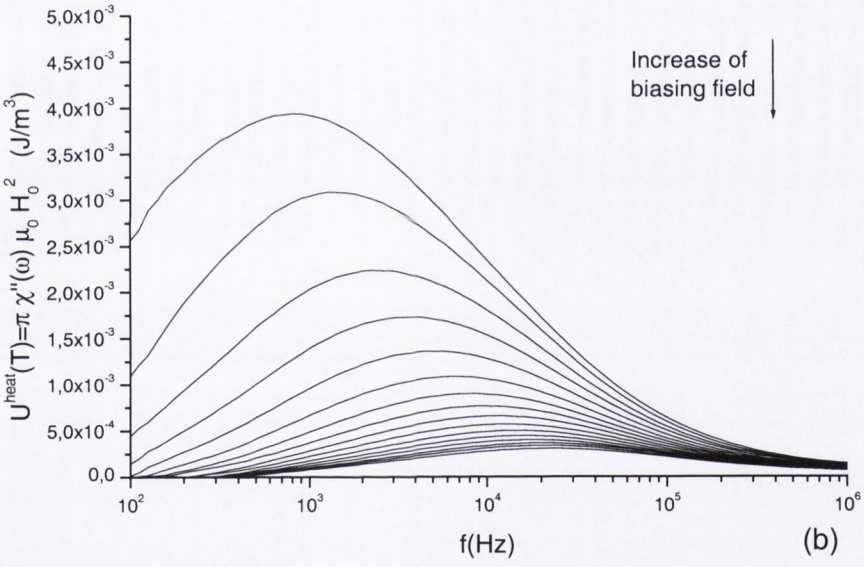

Figure 3.14 (b) The heat energy density given by Eq. (3.7.2).

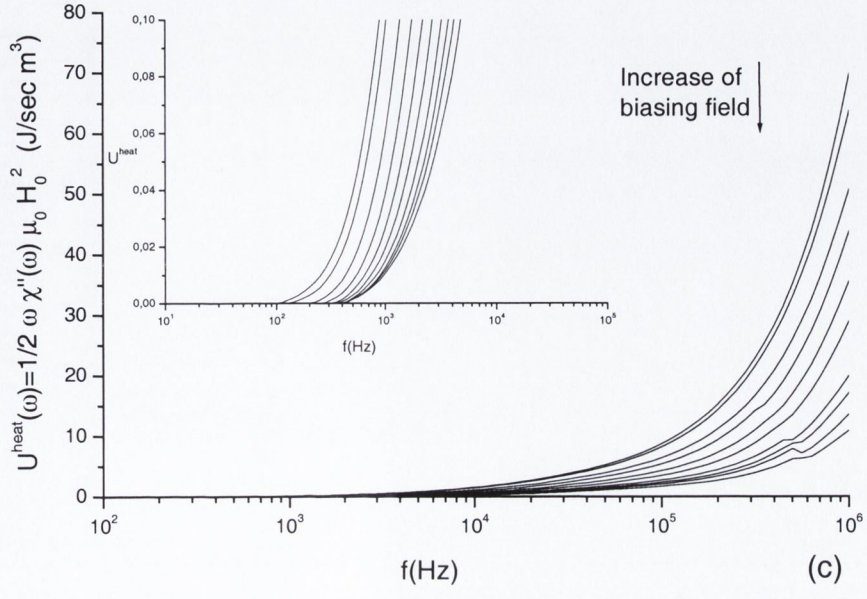

Figure 3.14 (c) The same as in (a), but for the 100 G magnetite in water sample.

(Continued).

Figure 3.14

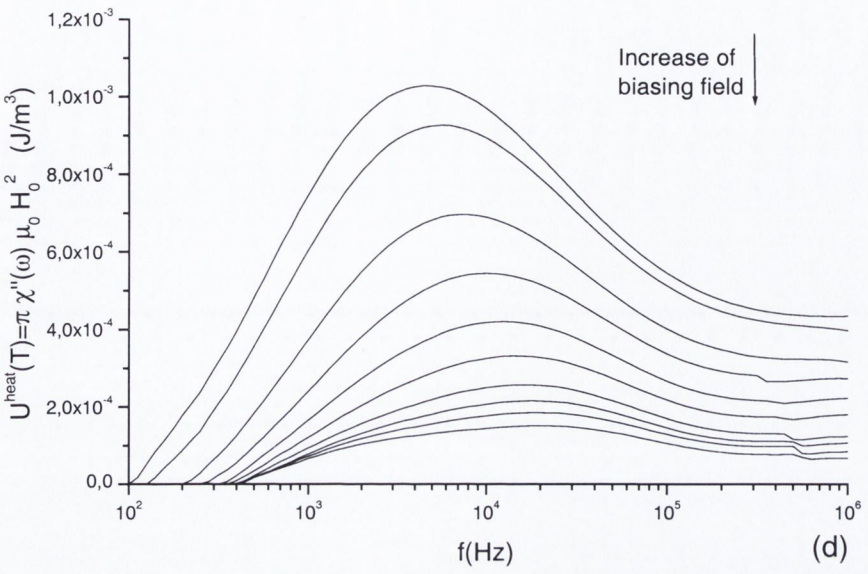

Figure 3.14 (d)
The same as in (b), but for the 100 G magnetite sample.

3.8 Conclusions and suggestions for future work.

Susceptibility measurements for frequencies below 1 MHz have been reported in both linear and nonlinear regions of the magnetization curve. Various techniques have been used, namely: (a) the constant frequency method (section 3.3.), (b) the polarizing technique with strong biasing field and weak alternating field, for linear susceptibility observation (section 3.4), and (c) the polarizing technique with strong biasing field and strong alternating field, for nonlinear susceptibility observation (section 3.5). The results are in accordance with the existing phenomenological relaxation theories, namely: (a) Martsenyuk et al [13] and Coffey et al [7], for the linear Brownian relaxation and (b) the extension of the Debye theory proposed by Coffey and Paranjape [1] to the nonlinear Brownian relaxation. Appropriate fits for both, (a) susceptibility's spectra and (b) relaxation times versus the biasing field, show the validity of these theories in the context of the explanation of the Brownian relaxation effect in ferrofluids. The fitting equations combine (in the susceptibility expressions) various distribution functions in order to account for the particle's poly-dispersion (studied in section 2.2). These are the first measurements on ferrofluids ever presented, to the best of our knowledge, which verify both Martsenyuk's theory for the increment of the relaxation time and the Debye theory as extended by Coffey at al for the linear and nonlinear relaxation.

Two applications of magnetic susceptibility measurements, have been presented: the first is the calculation of the loss factor tanδ as a function of the polarizing field and the second is the calculation of the heat energy density.

The separation of the fundamental frequency component from the third harmonic component in the nonlinear susceptibility data (case (a), section 3.4), is a task which can be performed in the future. Separation of the two frequency components has been achieved, in dielectric measurements, by sampling the electric displacement and afterwards decomposing it by means of the Fourier transform [24,25].

To date, little work has been done on the temperature dependence of linear and nonlinear relaxation in ferrofluids [40,41] and therefore this topic is also a suitable subject for future investigation.

References:

1. Coffey W.T., Paranjape B.V., *Proceedings of the Royal Irish Academy*, Vol. **78 A** No 3, 16, (1978).
2. O'Grady K., Bradbury A., *J. Magn. Magn. Mater.*, **39**, 91, (1983).
3. Nakagami M., *In "Statistical Methods of Radio Wave Propagation"*, Ed. by W.C., Hoffman, Pergamon Press (1960).
4. Bottcher C.J.F., Bordewijk P., *Theory of Electric Polarisation*, vol 2, Amsterdam, Elsevier Scientific Publishing Company, (1978).
5. Fröhlich H., *Theory of Dielectrics*, 2nd Ed., Oxford, Clarendon Press, (1958).
6. Fannin P.C., Scaife B.K.P., Giannitsis A.T., Charles S.W., *J. Phys. D: App. Phys.*, **35**, 1305, (2002).
7. Coffey W.T., Cregg P.J., Kalmykov Yu.P., *Advances In Chemical Physics*, **83**, 263, (1993).
8. Scaife B.K.P., *Complex Permittivity*, The English University Press, London, (1971).
9. Scaife B.K.P., *Principles of Dielectrics*, rev. Edn., Clarendon Press, Oxford (1998).
10. Chikazumi S., *Physics of Magnetism*, John Wiley, New York, (1964).
11. Snelling E.C., *Soft Ferrites Properties and Applications*, Iliffe Books, London, (1969).

12. Smith J., Wijn H., *Ferrites*, Philips, Eindhoven, (1969).
13. Martsenyuk M.A., Raikher Yu.L., Shliomis M.I., *Sov. Phys. JETP*, **38**, 413, (1974).
14. Shliomis M.I., Raikher Yu.L., *IEEE Trans. Magn.*, **MAG-16**, 237, (1980).
15. Morita A., *J. Phys. D*, **11**, 1357, (1978).
16. San Miguel M., Pesquara L., Rodriquez M.A., Hernandez-Machado A., *Phys. Rev. A*, **35**, 208, (1987).
17. Fannin P.C., Charles S.W., *J. Phys. D: App. Phys.*, **22**, 187, (1989).
18. Coffey W.T., Kalmykov Yu.P., Quinn K.P., *J. Chem. Phys.*, **96**, 5471, (1992).
19. Kalmykov Yu.P., *Phys. Rev. A*, **45**, 7184, (1992).
20. Cole K.S., Cole R.H., *J. Chem. Phys.*, **9**, 341, (1941).
21. DeSmet K., Hellemans L., Rouleau F.J., Courteau R., Bose T.K., *Physical Review E*, Vol **57** No2, 1384, (1998).
22. Jadzyn J., Kedziora P., Hellemans L., *Physics Letters A*, **251**, 49, (1999).
23. Kedziora P., Jadzyn J., DeSmet K., Hellemans L., Journal of Molecular Liquids, **80**, 19, (1999).
24. Fukurawa T., Matsumoto K., *Jpn. J. Appl. Phys.*, Vol. **31**, No. 3, 840, (1992).
25. Kodama H., Takahashi Y., Furukawa T., Jpn. J. Appl. Phys., Vol. **38**, No. 38, 3589, (1999).
26. Debye P., Polar Molecules, The Chemical Catalogue Co., New York (1929), Reprinted by Dover, New York.
27. Morita A., *Phys. Rev. A*, **34**, 1499, (1986).
28. Morita A., Watanabe H., Phys. Rev. A, **35**, 2690, (1987).
29. Raikher Y.L., Stepanov V.I., Burylov S.V., *J. Colloid Interface Sci.*, **144**, 308, (1991).
30. Déjardin J.L., Kalmykov Yu.P., *J. Chem. Phys.*, **112**, 2916, (2000).
31. Déjardin J.L., Kalmykov Yu.P., Déjardin P.M., *Adv. Chem. Phys.*, **117**, 275, (2001).
32. Coffey W.T., Kalmykov Yu.P., Titov S.V., *J. Chem. Phys.*, Vol **116**, No 15, 6422, (2002).
33. Déjardin J.L., *Physical Review E*, **68**, 031108, (2003).
34. Fannin P.C., Giannitsis A.T., *J. Molecular Liquids*, in press, (2004).
35. Rosensweig R.E., *Journal of Magnetism and Magnetic Materials*, **252**, 370, (2002).

36. Jordan A., Wust P., Fahling H., Hohn W., Hinz A., Felix R., *Int. J. Hyperthermia*, **9** 1, p. 51, (1993).

37. Hiergeist R., Andra W., Buske N., Hergt R., Hilger I., Richter U., Kaiser W., *J. Magn. Magn. Mater.*, **201**, 420, (1999).

38. Jordan A., Scholz R., Wust P., Schirra H., Schiestel T., Schmidt H., Felix R., *J. Magn. Magn. Mater.*, **194**, 185, (1999).

39. Raj K., in: *Magnetic Fluids and Applications Handbook*, Begell House Inc., New York, pp. 716–724, (1996), B. Berkovski (Ed.).

40. García-Palacios J.L., Jönsson P., Svedlindh P., *Phys. Rev. B*, **61**, 10, 6726, (2000).

41. Jönsson P., Jonsson T., García-Palacios J.L., Svedlindh P., *J. Mag. Mag. Matter.*, **222**, 219, (2000).

Chapter 4

Properties of ferrofluids at frequencies above 1 MHz and the dependence on the polarising field of the susceptibility.

4.1 Introduction

The experimental investigation of the properties of ferrofluids in the high frequency range (beyond 100 MHz) has been reported recently and involves: (a) the study of the dependence of the resonant frequency, f_{res}, on the biasing field [1], (b) the estimation, by use of $\chi(\omega)$ data, of the decay of the magnetization when a bias is suddenly removed (after-effect) [2] and (c) the temperature dependence of the susceptibility [3]. So far, there has been no detailed study of the variation of χ as a function of the field.

In this chapter we present magnetic susceptibility measurements as functions of both frequency and polarizing field. Two phenomenological expressions, Landau-Lifshitz (Eq. (1.5.39)) [4] and Coffey et al (Eq. (1.5.43)) [5], can be used. The first is suitable to describe the field dependence of χ, while the second is more appropriate to describe the frequency dependence of χ. A presentation of the data, in a Cole-Cole diagram of constant frequency curves, as a function of various fields and the corresponding fits, shows the validity of the Landau-Lifshitz equation.

With the possible use of nanoparticles as devices, such as switches, one is interested in the signal-to-noise ratio (SNR) of such systems. The usefulness of the availability of χ data comes to the fore since the SNR for a field-driven magnetization of a nanoparticle can be determined in terms of $|\chi|$.

4.2 A brief review on measurements of χ, in the RF and microwave frequency ranges.

There has been gradual progress in magnetic susceptibility measurements in the microwave frequency range, during the last decade. Fannin et al [6] upgraded the coaxial line technique by using network analysers. Moreover Fannin presented polarised susceptibility measurements up to 6 GHz [1] by means of the HP 8753C analyser and up to 20 GHz [7] with the HP 8722D analyser. He also presented measurements for the external field parallel and perpendicular to the plane of the sample [8]. An extensive

theoretical study by use of the expressions given in [5], combined with appropriate distribution functions in order to account for the particle poly-dispersion, is given by Fannin et al in [9].

To obtain polarised measurements in the microwave range, a biasing field H_s has to be applied to the sample as shown in Fig. (4.1). Figure (4.1) shows the relative direction of the alternating field, $\mathbf{h}_a(x,t) = \mathbf{H}_0 \cos(\omega t + 2\pi x/\lambda)$, which is combined with the polarising field, $\mathbf{H}_s$. The characteristic profile of the resonant absorption (see Fig. (4.2 a-b), which shows the susceptibility of a magnetite isoparaffin-based ferrofluid) shows a gradual decay of the χ'component as a function of the frequency and a prominent peak of the χ'' component at a frequency f_{max}, which is the frequency of the moment's precession for the case of undamped motion. The frequency at which χ' becomes negative is the resonance frequency, f_{res}, and it is associated with f_{max} according to Eq. (1.5.42). As is shown in the primary works of Fannin et al [1,6] f_{res} increases by applying an external polarising field, H_s. Also the magnitude of the susceptibility decreases on increasing H_s. By applying various polarising fields (see the values of H_s in Table 4.1 below) it is possible to show both (a) the dependence of f_{res} and f_{max} on the biasing field, and (b) the dependence of the magnitude of the susceptibility, with respect to a specific frequency, on the biasing field.

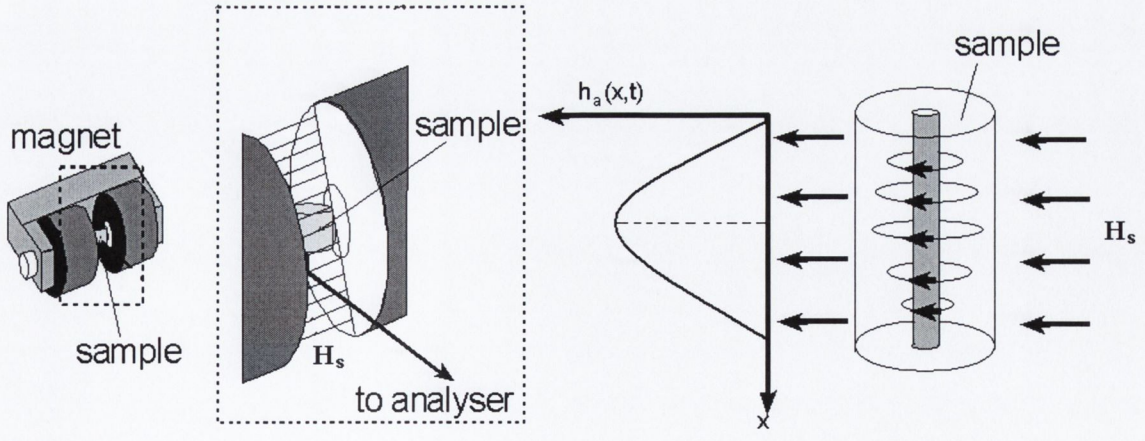

Figure 4.1 Experimental setup of the transmission line technique and relative orientation of the external polarising field, H_s, with respect to the sample. The oscillating field, $h_a(t)$, is always concentric with the inner conductor.

Experimental measurements of two ferrofluids, namely (a) 900 G (0.09 T) magnetite in isoparaffin sample (with mean particle hydrodynamic radius $r_p \cong 5$ nm [10]), and (b) a 400 G (0.04 T) cobalt ferroparticles in diester sample (with $r_p \cong 4$ nm) are presented in Figs. (4.2) and (4.3), respectively. The prominent peaks in χ'' between 10 MHz-100MHz in Figs. (4.2 b), (4.3 b) are purely due to Néel relaxation while above 100 MHz resonance is dominant. It is important to notice that Néel relaxation may appear throughout the whole spectrum, however in the majority of ferrofluids it is dominant only between 1 MHz-100 MHz. It is seen that for both samples (Figs. (4.2 a), (4.3 a)), on increasing the external field, the magnitude of $\chi'(\omega, H_s)$ at the lower frequency end of the plots is progressively reduced, whilst towards the higher frequencies the profile takes on more of a resonant character. The explanation of this reduction in $\chi'(\omega, H_s)$, is that the effect of the external field is to effectively increase the value of the anisotropy field, $\langle H_A \rangle$, and hence $\langle K \rangle$. The barrier to rotation of the magnetic moments now becomes $\langle V_A \rangle = \langle K \rangle v_m + \mu_m H_s$. This increase in the potential barrier reduces the rate at which Néel relaxation takes place, leading to a reduction in the magnitude of $\chi'(\omega, H_s)$ (indicative of a reduction in the real part of the relaxational component of $\chi(\omega)$) over the frequency range. In the corresponding plots of $\chi''(\omega, H_s)$, a similar reduction in the magnitude is observed at lower frequencies, whilst at higher frequencies the frequency of the maximum, f_{max}, increases with increasing external field, H_s. Two processes are responsible for the appearance of this loss peak, namely the Néel relaxation of the smallest particles in the distribution and resonance. Increasing H_s results in less spontaneous flipping of the magnetic moments (Néel relaxation) and the contribution to the loss peak from the Néel component is reduced whilst the contribution from the resonant component increases.

Important information can be derived from the resonant profile of a sample. That is:

(a) *The calculation of* γ, H_A *and* K: The dependence of f_{res} on the polarising field is linear. From the plot of f_{res} versus H_s it is possible to estimate the average equivalent internal field over the particle ensemble, $\langle H_A \rangle$, which is defined in Eq. (1.3.10). Knowing the saturation magnetization of the material of the ferroparticle, we are able to estimate the mean anisotropy constant, $\langle K \rangle$. The slope of f_{res} versus H_s defines the

gyromagnetic ratio, γ, (Eq. (1.5.36)). γ, $\langle H_A \rangle$ and $\langle K \rangle$ are microscopic quantities which characterise each ferrofluid sample. Kinsella [11] studied extensively the resonant profile of various ferrofluids, such as magnetite in water, manganese ferrite in isoparaffin and nickel-zinc in isoparaffin, and he estimated their $\langle H_A \rangle$ and γ. Table 4.3 shows the approximate values of γ, $\langle H_A \rangle$ and $\langle K \rangle$ for various ferrofluids. The wide range of values of γ and $\langle K \rangle$ for a particular fluid is due to the different proportion (stoichiometry) between the iron and the transition metal. For example, for manganese ferrite $Mn_{0.1}Fe_{0.9}Fe_2O_4$ we have measured $\gamma \cong 230{,}000$ m/A s and $\langle K \rangle \cong 6{,}000$ J/m^3, but for $Mn_{0.7}Fe_{0.3}Fe_2O_4$ we found $\gamma \cong 252{,}000$ m/A s and $\langle K \rangle \cong 2{,}400$ J/m^3.

For the two samples we are studying, the values of f_{res} for each biasing field are indicated in the Tables 4.1 and 4.2 and the corresponding graphs of f_{res} versus H_s are the Figs. (4.2 c) and (4.3. c). For the magnetite sample we found $\langle H_A \rangle$=40 kA/m, which is a typical value for magnetite, and for the cobalt sample we found $\langle H_A \rangle$=126 kA/m. Since M_s=0.4 T for the magnetite sample and M_s=1 T for the cobalt sample, we easily find (Eq. (1.3.10)) $\langle K \rangle$=9,740 J/m^3 and $\langle K \rangle$=63,000 J/m^3 respectively. The gyromagnetic ratio, γ, is defined as the slope of f_{res} versus H_s. In the case of magnetite, γ has been estimated to be 221,000 m/A sec, while for the cobalt sample γ was found to be 200,000 m/A sec.

(b) *The estimation of the ratio* f_{max}/f_{res}: From the spectrum of χ'' we can estimate f_{max}. The measured values of f_{max} for the two samples are shown in Tables 4.1 and 4.2 and the corresponding graphs are Figs. (4.2 d) and (4.3 d). As shown in [12] f_{max} versus H_s may be used to make a comparative measure of particle interactions in two magnetic fluid samples having the same particle composition but different fluid magnetisations. f_{max} is written in terms of the interaction field, H_R, as [12]

$$\omega_{max} = 2\pi f_{max} = \gamma\sqrt{1+\alpha_d^2}\,(H + H_R) \qquad (4.2.1)$$

Figure 4.2 Ferrofluid: 900 G (0.09 T) magnetite in isoparaffin.

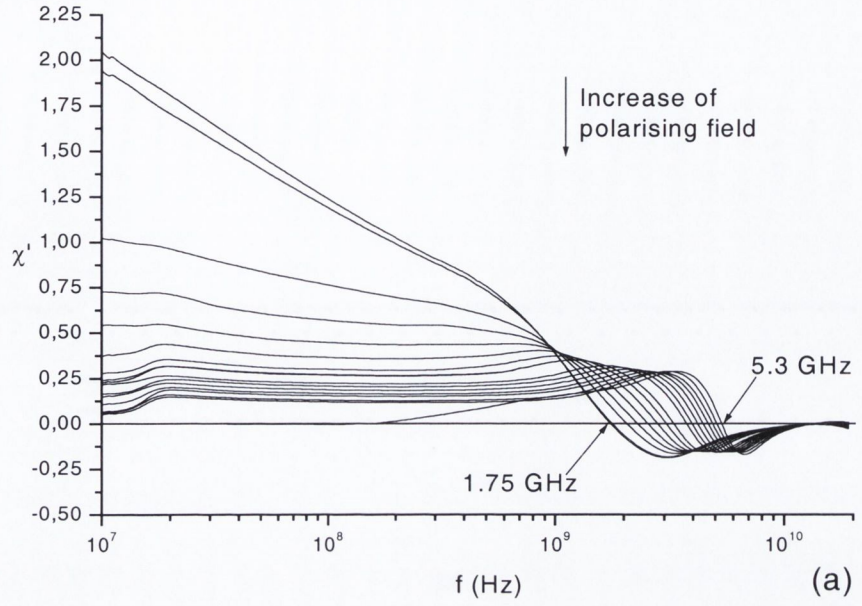

Figure 4.2 (a) χ' for the values of H_s in Table 4.1.

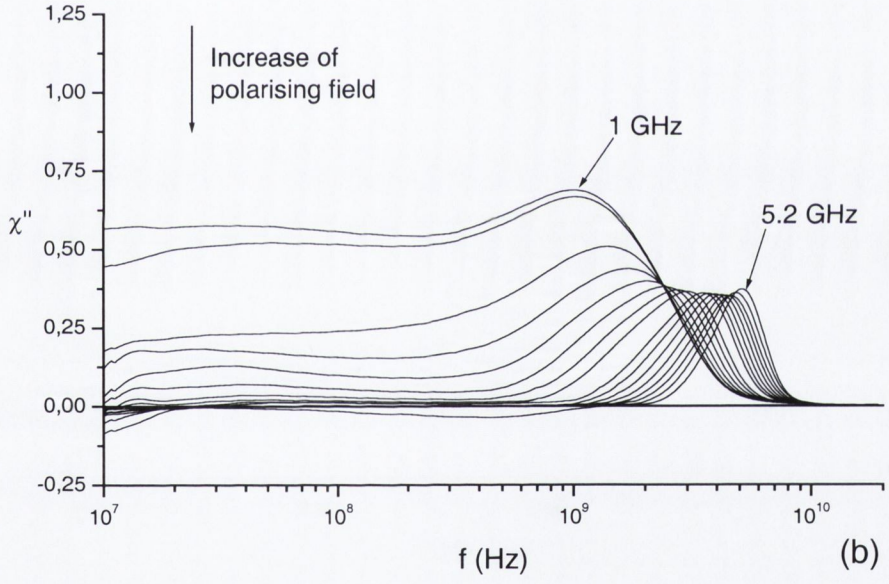

Figure 4.2 (b) χ'' for the same values of H_s.

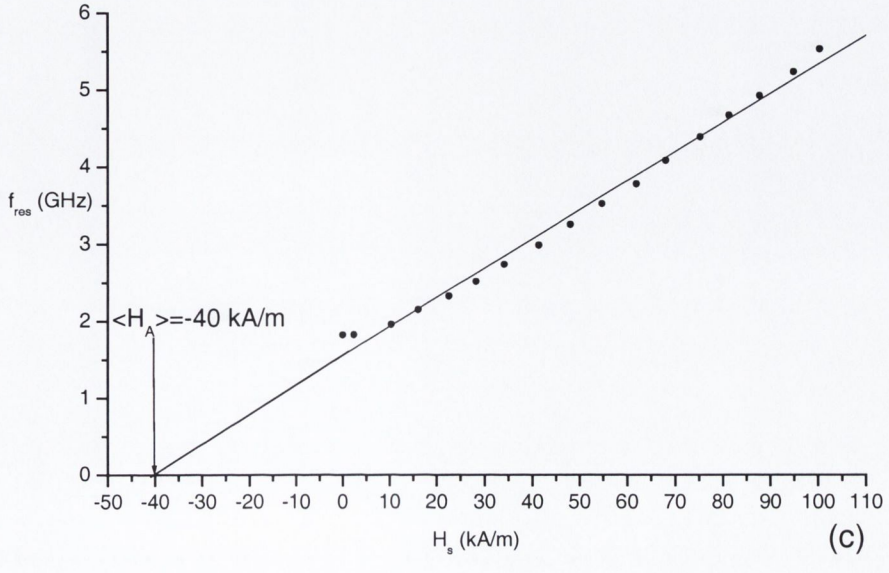

Figure 4.2 (c) f_{res} versus H_s. $\langle H_A \rangle$ is estimated from the point where the line cuts the horizontal axis. The value of 40 kA/m is typical for magnetite. The slope of the line defines γ.

(Continued).

Figure 4.2 Ferrofluid: 900 G (0.09 T) magnetite in isoparaffin.

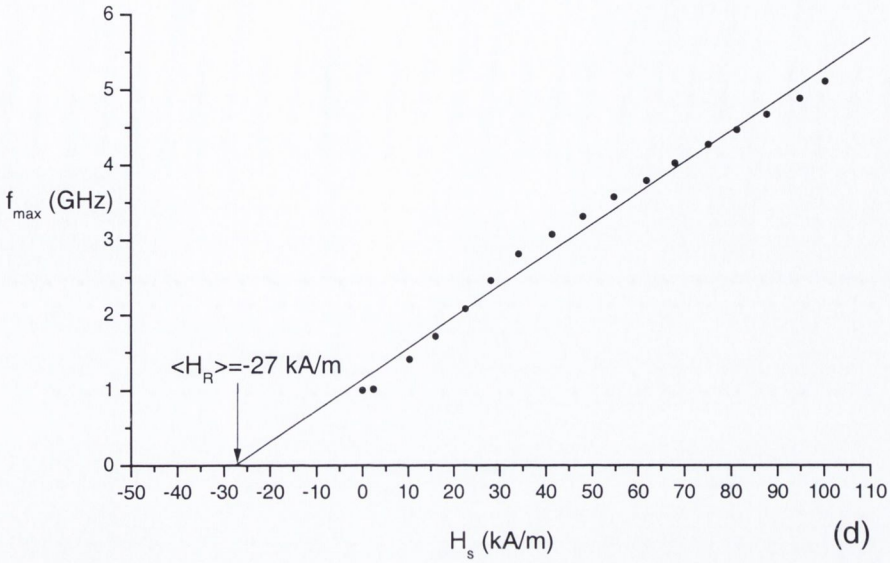

Figure 4.2 (d) f_{max} versus H_s.

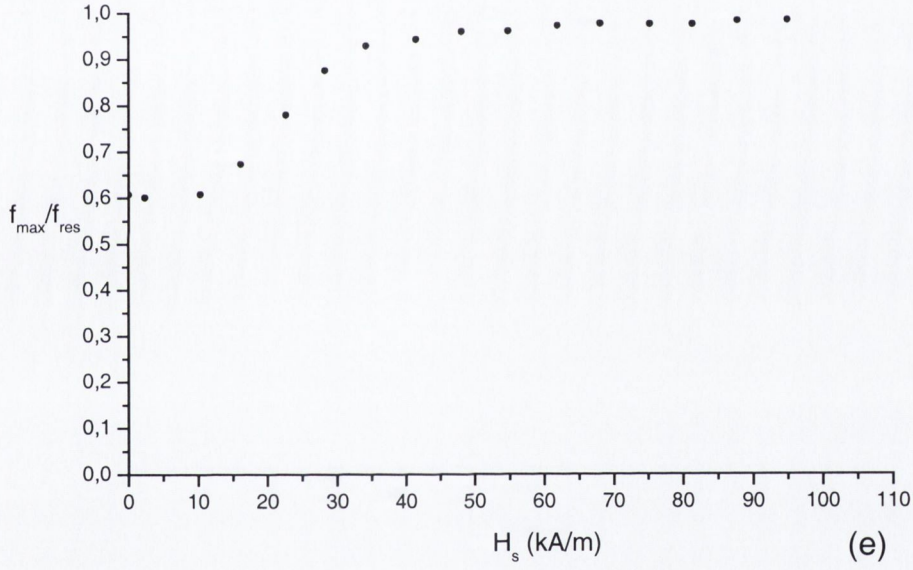

Figure 4.2 (e) f_{max}/ f_{res} versus H_s.

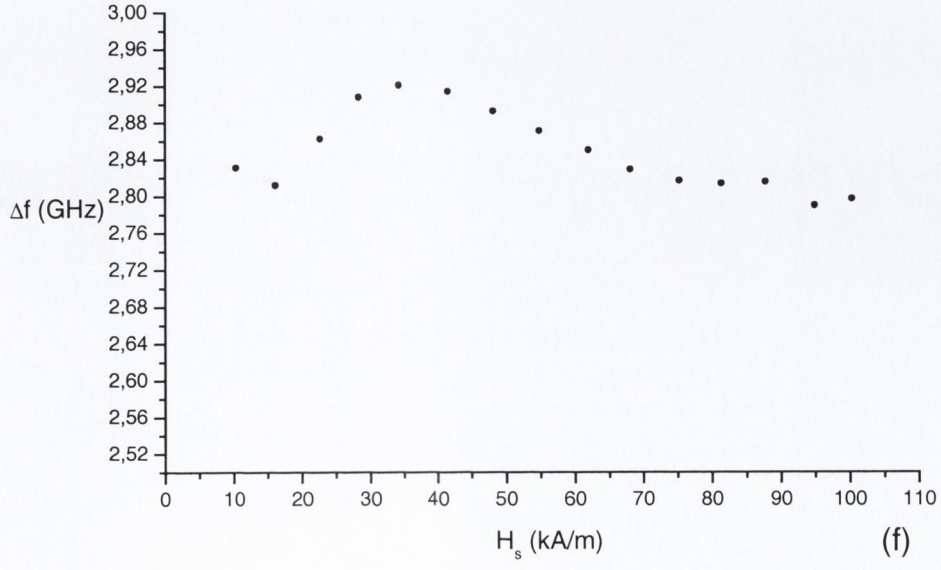

Figure 4.2 (f) The width parameter Δf versus H_s.

(Continued).

Figure 4.2 Ferrofluid: 900 G (0.09 T) magnetite in isoparaffin.

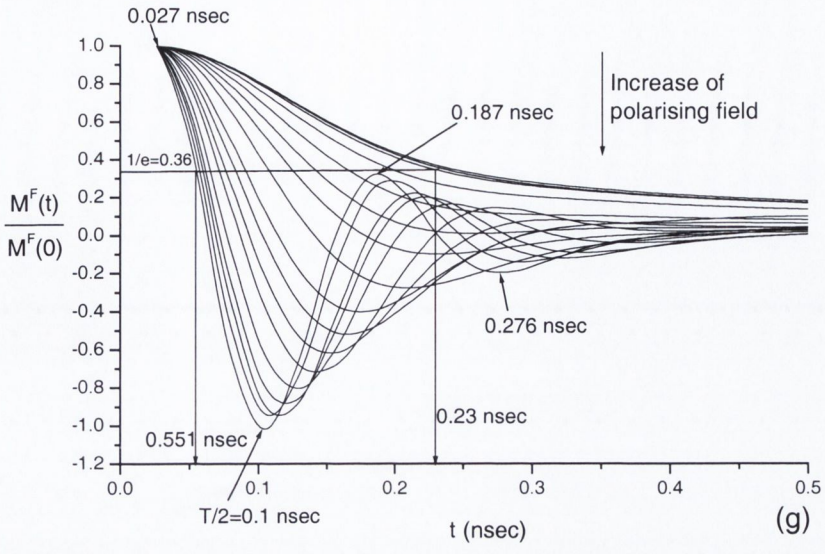

Figure 4.2 (g) The decay of magnetisation (after effect). Each curve refers to a separate H_s. The horizontal line corresponds to the value of magnetisation where the decay is the 1/e of the static value.

Figure 4.3 Ferrofluid: 400 G (0.04 T) cobalt ferroparticles in diester.

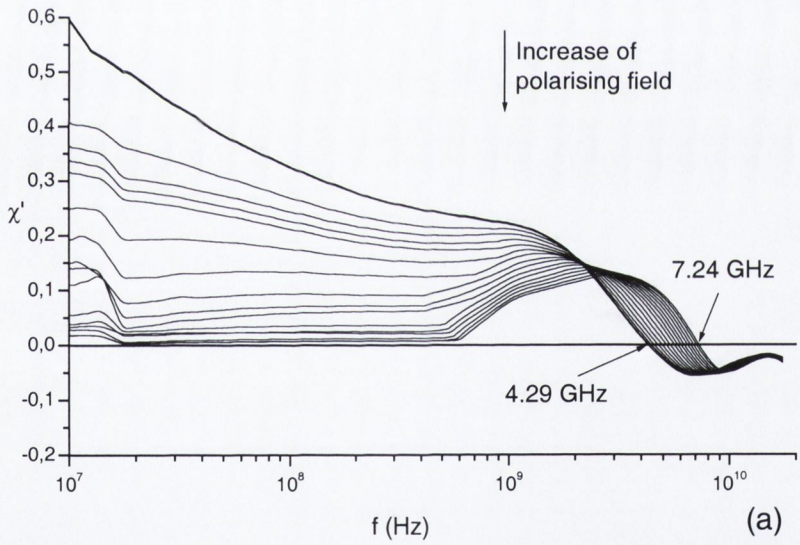

Figure 4.3 (a) χ' for the values of H_s in Table 4.1.

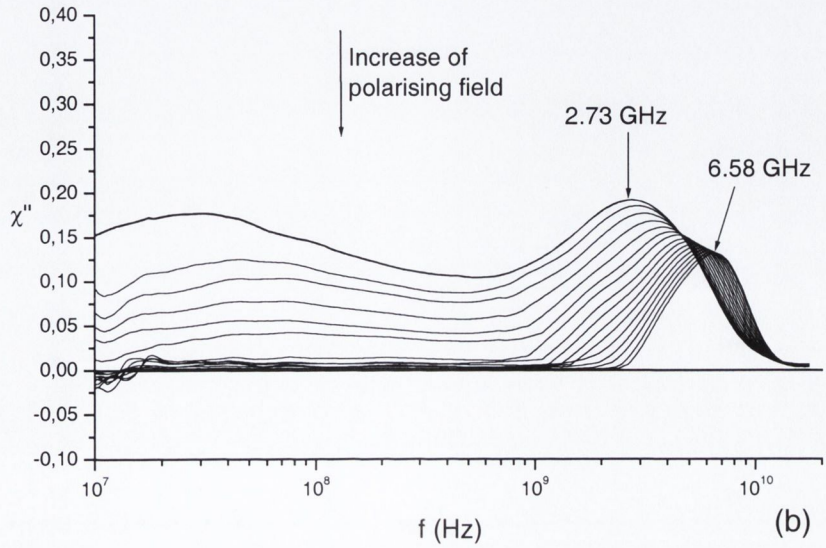

Figure 4.3 (b) χ'' for the values of H_s which are stated in Table 4.1.

(Continued).

Figure 4.3 Ferrofluid: 400 G (0.04 T) cobalt ferroparticles in diester.

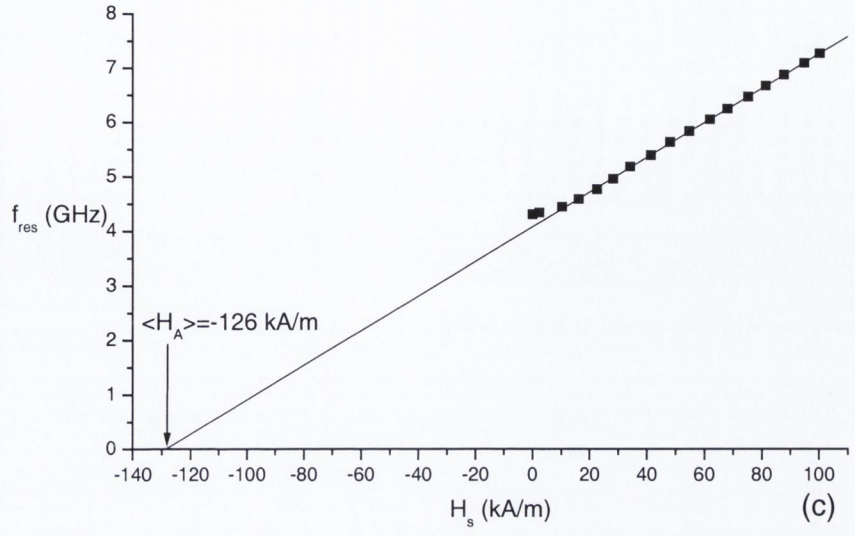

Figure 4.3 (c) f_{res} versus H_s. $<H_A>$ is estimated from the point where the line cuts the horizontal axis. The value of 126 kA/m is found here. The slope of the line defines γ.

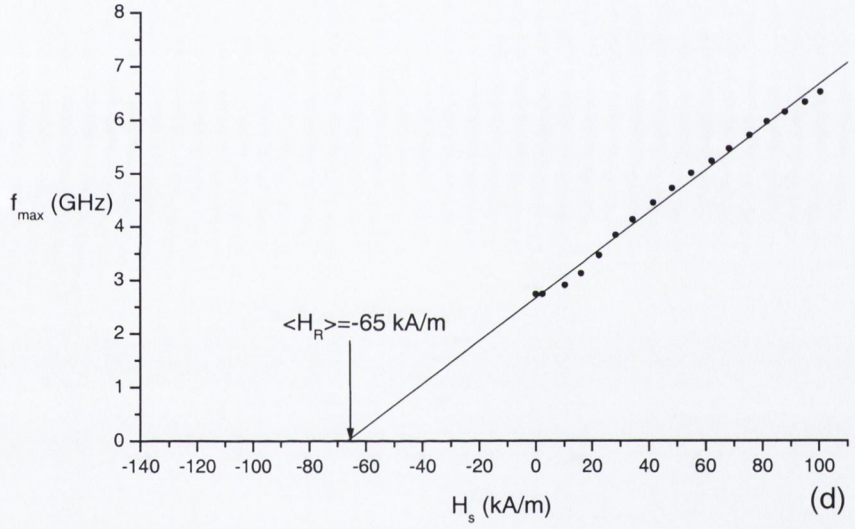

Figure 4.3 (d) f_{max} versus H_s.

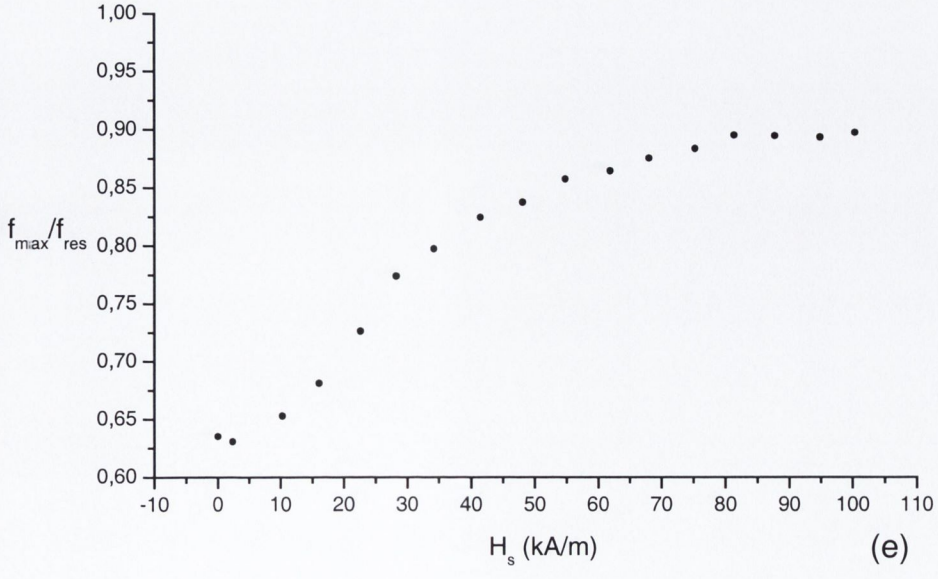

Figure 4.3 (e) f_{max}/f_{res} versus H_s.

(Continued).

Figure 4.3 Ferrofluid: 400 G (0.04 T) cobalt ferroparticles in diester.

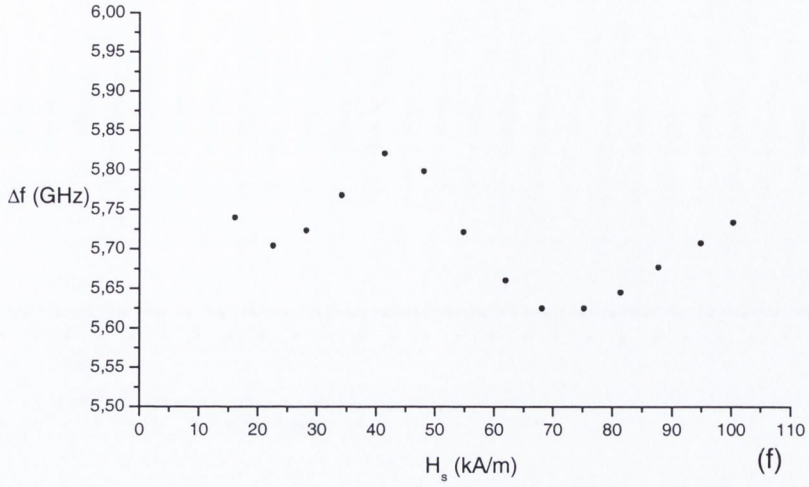

Figure 4.3 (f) The width parameter Δf versus H_s.

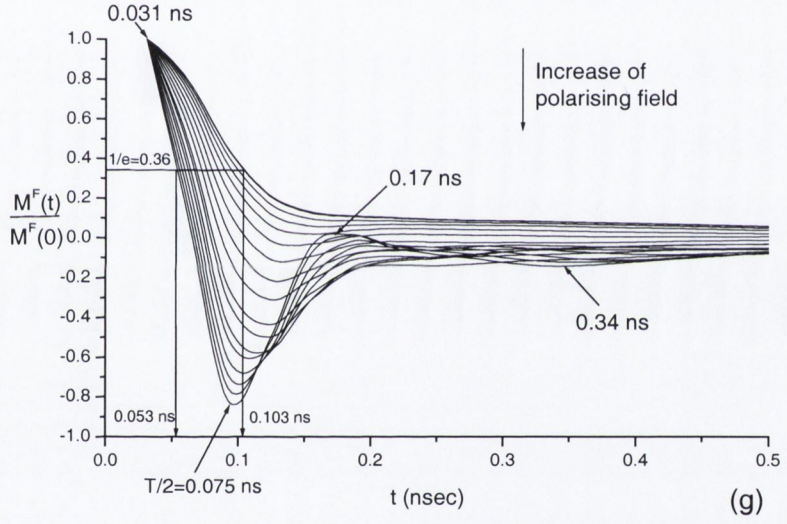

Figure 4.3 (g) The decay of magnetisation (after effect) for each individual H_s.

where the interaction field can be written in terms of the interaction parameter $I(r_p)$ and a dimensionless parameter b, which is a function of the orientation of the anisotropy axis, i.e.

$$H_R = bH_A + I \tag{4.2.2}$$

From Figs. (4.2 d) and (4.3 d) we can estimate that $\langle H_R \rangle = 27$ kA/m for the magnetite sample and $\langle H_R \rangle = 65$ kA/m for the cobalt sample. Since α_d is small, $\sqrt{1+\alpha_d^2} \cong 1$ and thus the slopes of Eqs. (1.5.36) and (4.2.1) should be equal when H_s takes on large

values. That is why the values of f_{res} and f_{max} are close, as Tables 4.1 and 4.2 indicate, for large values of H_s.

In Figs. (4.2 e) and (4.3 e) the ratio of f_{max}/f_{res} is plotted against H_s for both samples. The results obtained show a similar dependence to that predicted theoretically by Raikher and Shliomis [4]. The graphs show the effect of a gradual transition from relaxation (low σ, low H_s) to resonance (high σ, high H_s). This is explained by the increase of the anisotropy energy barrier, V_A, due to the increase of the biasing field.

(c) *The estimation of the width* Δf : The width is a measure of the broadness of the absorption ($\chi''(\omega)$) curve and it is strongly related to the distribution, both shape and size, of the particles. The width is approximated by [1]

$$\Delta\omega = 2\pi\Delta f \cong 2\alpha_p\omega_{res} \qquad (4.2.3)$$

It can easily be estimated by measuring the linewidth, Δf, which corresponds to a height at 1/2 of the vertical axis which passes through the peak of $\chi''(\omega)$.

On applying H_s one might expect a "texture" (partial alignment of the easy axis to appear, predominantly from the bigger particles which have σ, $\xi >> 1$). The overall extent of the texturing in the magnetite and cobalt particle systems we study here is known to be small at room temperature [13,14], even for fields sufficient to saturate the system. There are two processes taking place: (a) narrowing of the resonance line due to texturing and (b) the presence of Néel relaxation of the smallest particles. For an increase in H_s (i.e. an effective increase in σ), one would expect either an initial drop of Δf to occur due to the reduction in the contribution of the Néel relaxation followed by an approximately constant value ($\cong \gamma\langle H_A \rangle$) where texturing is small, or, a continuing decrease of Δf where texturing is important [1].

(d) *Estimation of the decay of the magnetisation*: It is possible by applying the inverse Fourier transform to the susceptibility data to derive the decay of the magnetisation, as a function of the time, after the switching off of the biasing field (after-effect). This is an easy method by which one can estimate $M^F(t)$ where the time interval of interest is of the order of nanoseconds. As H_s increases, the profile of $M^F(t)$ shows oscillatory behaviour. This should be expected since an increase in H_s results in an effective increase of σ, or in other words to an elimination of the thermal agitation. The

thermal agitation interrupts the oscillatory motion of the magnetic moment, $\boldsymbol{\mu}_m$, of the ferroparticles. When H_s is removed the decay type is exponential or oscillatory, depending on the magnitude of the field strength.

Table 4.1 The values of f_{res}, f_{max} and Δf for the 900 G (0.09 T) magnetite in isoparaffin sample for each individual applied field.

H_s (kA/m)	f_{res} (GHz)	f_{max} (GHz)	Δf (GHz)	H_s (kA/m)	f_{res} (GHz)	f_{max} (GHz)	Δf (GHz)
0	1.824	1.10	-*	54.7	3.52	3.38	2.87
2.3	1.825	1.10	-	61.9	3.77	3.67	2.84
10.3	1.96	1.19	2.83	68	4.07	3.98	2.82
16.1	2.15	1.44	2.81	75.2	4.38	4.28	2.81
22.6	2.32	1.81	2.86	81.3	4.66	4.55	2.81
28.2	2.51	2.2	2.9	87.7	4.91	4.83	2.81
34.1	2.73	2.53	2.92	94.8	5.22	5.14	2.78
41.4	2.98	2.81	2.91	100.3	5.52	5.58	2.79
48.1	3.25	3.11	2.89				

* Cannot be estimated

Table 4.2 The values of f_{res}, f_{max} and Δf for the 400 G (0.04 T) cobalt in diester sample for each individual applied field.

H_s (kA/m)	f_{res} (GHz)	f_{max} (GHz)	Δf (GHz)	H_s (kA/m)	f_{res} (GHz)	f_{max} (GHz)	Δf (GHz)
0	4.3	2.7	-*	54.7	5.8	5	5.72
2.3	4.3	2.7	-	61.9	6	5.2	5.66
10.3	4.4	2.9	-	68	6.2	5.4	5.62
16.1	4.5	3.1	5.73	75.2	6.4	5.7	5.62
22.6	4.7	3.4	5.7	81.3	6.6	5.9	5.64
28.2	4.9	3.8	5.72	87.7	6.8	6.1	5.67
34.1	5.1	4.1	5.76	94.8	7	6.3	5.7
41.4	5.3	4.4	5.82	100.3	7.2	6.5	5.73
48.1	5.6	4.7	5.79				

* Cannot be estimated

Table 4.3 Approximate values of γ, $\langle H_A \rangle$ and $\langle K \rangle$ for several types of ferrofluids.

Ferrofluid	γ (m/A sec)	$\langle H_A \rangle$ (A/m)	$\langle K \rangle$ (J/m^3)
Magnetite in water or in isoparaffin	220,000-235,000	40,000	7,500-11,000
Cobalt ferrite in isoparaffin	**	**	5,000
Cobalt in diester	200,000	126,000	63,000
Manganese ferrite in isoparaffin	230,000-255,000	20,000-40,000	4,000-6,000
Nickel-zinc ferrite in isoparaffin	250,000	5,000	3,000-3,500

** Have not been measured yet because its resonant frequency is outside the experimental frequency range.

The normalised magnetisation, $M^F(t)/M^F(t=0)$, versus time is plotted in Figs. (4.2 g), (4.3 g). Such a representation is called, the after-effect function. As expected, the greater the field the more pronounced the oscillation. The semi-period of the oscillation, for the magnetite sample at H_s=100.3 kA/m (strongest field), is estimated from the after-effect function graph and equals T/2=0.1 ns which corresponds to a frequency f=1/T=5 GHz which is approximately equal to f_{max}=5.2 GHz (frequency of precession). For the cobalt sample T/2=0.075 nsec, which corresponds to a frequency f=6.6 GHz which is very close to the frequency of the precession f_{max}=6.58 GHz. The same occurs for all other polarising fields. Now, the value of the time which corresponds to the 1/e of the decay of $M^F(t)$ (horizontal line drawn) is the Néel relaxation time (remember that the effective relaxation time corresponds to a decay of $M^F(t)$ by 1/e of its maximum value, and also in the RF band $\tau_{eff} \cong \tau_N$). A detailed description of the oscillating action of the ferropaticles and of the usefulness of the after-effect function is given by Fannin in [2,15].

To conclude, in this section we have reviewed the information which can be obtained from $\chi(\omega, H_s)$ measurements in the RF and microwave band. Both relaxation (mainly Néel) and resonance contribute to χ. The knowledge of $\chi(\omega, H_s)$ in that frequency range is a powerful tool by which one can calculate the microscopic parameters, such as γ, H_A and K, of a nanoparticle magnetic system. In addition it is possible to derive the decay of $M^F(t)$ (after-effect function) by applying the inverse Fourier transform to the frequency data.

4.3 The magnetic susceptibility as a function of biasing field in the microwave band.

As we extensively described in section 1.5, Raikher and Shliomis [4,16] have treated the resonance phenomena in terms of equations proposed by Landau-Lifshitz (Eq. (1.5.39)) [4], modified to include stochastic terms and derived expressions for the transverse susceptibility, $\chi_\perp(\omega)$, which is equivalent to the resonance susceptibility component. Their expressions were subsequently simplified by Coffey et al (Eq. (1.5.43)) [5]. The Landau-Lifshitz equation is suitable for describing the system only for large values of σ, which means that thermal agitation does not greatly affect the movement of the moment, or equivalently the internal barrier is very large ($Kv_m >> k_BT$), so that the

rotation of the moment with respect to the particle (Néel relaxation) does not change for long periods of time (i.e. we assume that $\boldsymbol{\mu}_m$ is blocked) and the only change of the direction of $\boldsymbol{\mu}_m$ is due to the precession within the particle. Hence all changes in orientation of $\boldsymbol{\mu}_m$ are determined by the rotational motion of the particle. For the kind of experiments we perform (i.e. polarised measurements where the effective σ becomes large) and for the frequencies of our interest (≥ 1 GHz), this approximation is tolerable. The simplicity of the Landau-Lifshitz equation, in contrast to the equation (1.5.43) of Coffey et al, makes the use of this equation appropriate.

Scaife [17] studied extensively the Landau-Lifshitz equation. He compared the Landau-Lifshitz type of absorption (also called ferromagnetic resonance absorption) with the Debye type and the Lorentz type of absorption. The difference between the Landau-Lifshitz absorption type and the Debye type is, as we already mentioned in Chapter 1, that the latter does not take account of the inertia which produces Larmor precession* about the magnetic axis. The Landau-Lifshitz absorption has many similarities, at low frequencies, with the Lorentz type of absorption, which is the resonance of a damped harmonic oscillator [17]. Scaife also estimated the value of τ_0, in Eq. (1.5.39), and he derived the following expression in terms of τ_B, τ_N and ω_{pre}

$$\frac{1}{\tau_0} = \frac{1}{\tau_B} + \frac{1}{2\tau_N} + \alpha_d \omega_{pre} \tag{4.3.1}$$

Here ω_{pre} is the frequency of the free (undamped) precession, while in [17] ω_{pre} is the frequency of the damped precession. For particles with large values of σ, the Néel relaxation time is much greater than the Brownian time, τ_B, which is much greater than the precession time constant $1/\alpha_d\omega_{pre}$. In these circumstances $\tau_0 \cong 1/\alpha_d\omega_{pre}$, which is in agreement with Eq. (1.5.13).

We are able now to fit the polarised susceptibility data of Fig. (4.2 a-b) of the *900 G magnetite in isoparaffin* sample by use of the Landau-Lifshitz equation, appropriately modified to include distributions for K and r_m. The use of a distribution is necessary, as explained in section 1.5, Fig. (1.7 c). We can use the normal distribution function to distribute both K and r_m. The time constant of the resonance is approximated by $\tau_0 \cong 1/\alpha_d\omega_{pre}$, as noticed previously. In Fig. (4.4) we present the fits of some of the

* Larmor precession is the undamped precession.

curves of Fig. (4.2 a-b). The polarising fields, H_s, used are: (a) 0 A/m (unpolarised), (b) 10.3 kA/m, (c) 22.6 kA/m, (d) 34.1 kA/m, (e) 48.1 kA/m and (f) 61.9 kA/m. For cases (a) and (b) the expression used for the total susceptibility was $\frac{1}{3}(\chi_{\parallel}(\omega,H_s)+2\chi_{\perp}(\omega,H_s))$, which combines both the relaxation, $\chi_{\parallel}(\omega,H_s)$, and the resonance, $\chi_{\perp}(\omega,H_s)$, components. This expression is valid for the case of small σ. When the externally applied magnetic field strength is strong the effective σ becomes large and only the resonance mechanism is present (Néel is blocked). The equation to fit the curves of Fig. (4.4 c-f) is the Landau-Lifshitz equation which is the resonance component, $\chi_{\perp}(\omega,H_s)$, of the total susceptibility. For all the fits we performed here: M_s=0.4 T, $\langle K\rangle$=9,000 J/m^3 with a standard deviation σ_K=0.7, $\langle r_m\rangle$=6 nm with standard deviation σ_r=0.55, γ=230,000 m/A s and α_d=0.25. The damping parameter, α_d, exceeded the usual values (0.01-0.1) which α_d typically takes*. The resonance frequency, $\omega_{res}=\gamma(H_s+\langle K\rangle/2M_s)$, is directly dependent on H_s and by increasing the latter we have a shift in the resonance point of the fit.

It is possible to study the polarised susceptibility data by means of Cole-Cole plots. This representation of the data was first introduced, for magnetic liquids, by Fannin et al in [15,18,19]. There are two individual formats and we should distinguish between them:

(a) *Type I Cole-Cole plot*: This is the usual Cole-Cole plot, introduced in Chapter 3. We plot χ'' versus χ' for each individual H_s. Each point on the Cole-Cole curve corresponds to an individual frequency. An example of this Cole-Cole plot is shown in Fig. (4.5 a-b) where theoretical curves are generated by the Landau-Lifshitz equation for several polarising fields, H_s. Each curve corresponds to a different H_s, while each point of the curve corresponds to an individual frequency. The $\omega_{pre}\tau_0$ parameter in the Landau-Lifshitz equation (see Eq. (1.5.39)) equals to $1/\alpha_d$ and it is directly related to the polarising field, since $\omega_{res}=\gamma(H_s+H_A)$.

* The limited range of values that α_d can take (0.01-0.1) was treated by Raikher and Shliomis [16] and applies only to their equation. For the Landau-Lifshitz equation, α_d may be lie between 0-1.

Figure 4.4

Fits (dotted lines) of the susceptibility data (solid lines) of the 900 G magnetite in isoparaffin sample. The fitting equation used here is the Landau-Lifshitz equation (1.5.39). These data are the sample susceptibility which is measured under the influence of various polarising magnetic fields, with strengths:

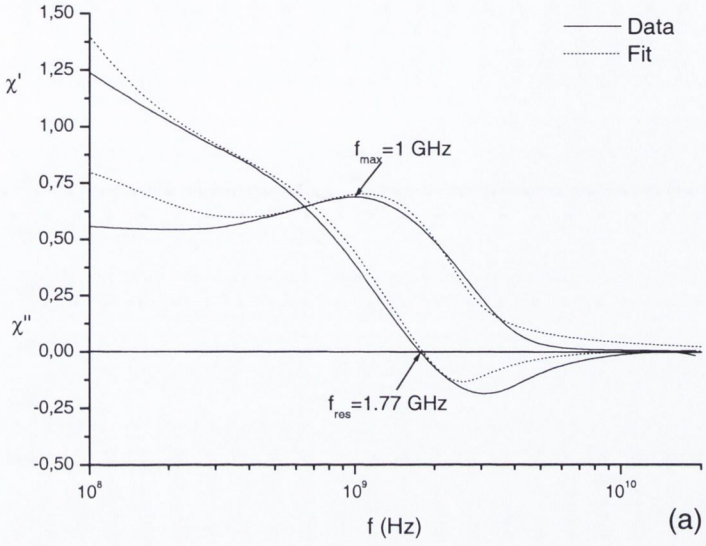

Figure 4.4 (a) 0 A/m (unpolarised),

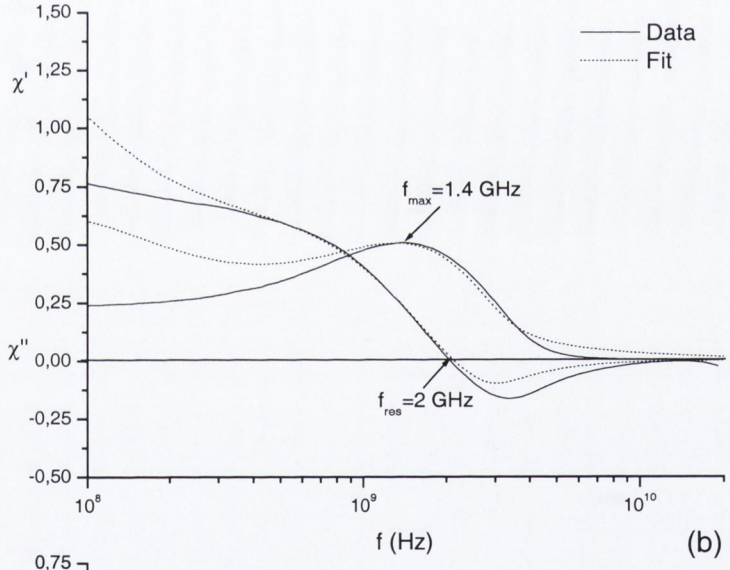

Figure 4.4 (b) 10.3 kA/m,

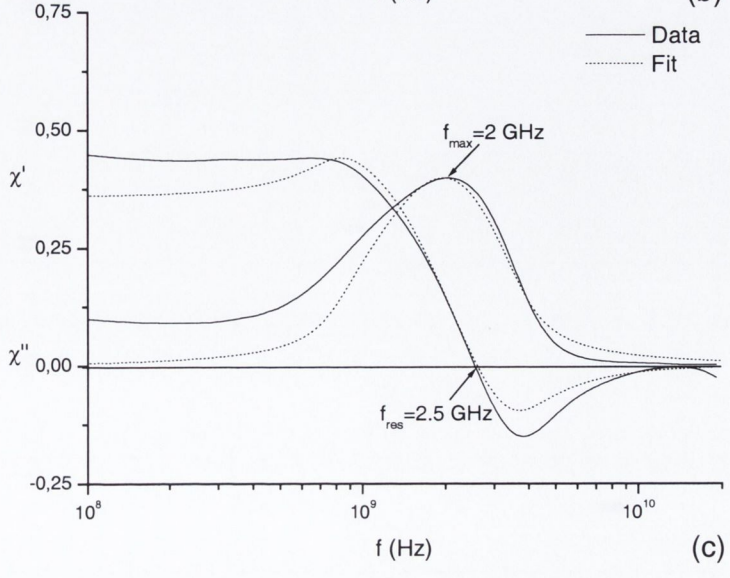

Figure 4.4 (c) 22.6 kA/m,

(Continued).

Figure 4.4

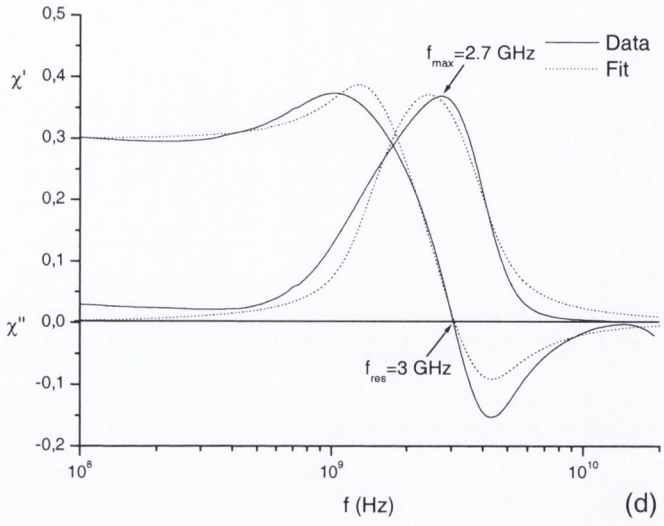

Figure 4.4 (d) 34.1 kA/m,

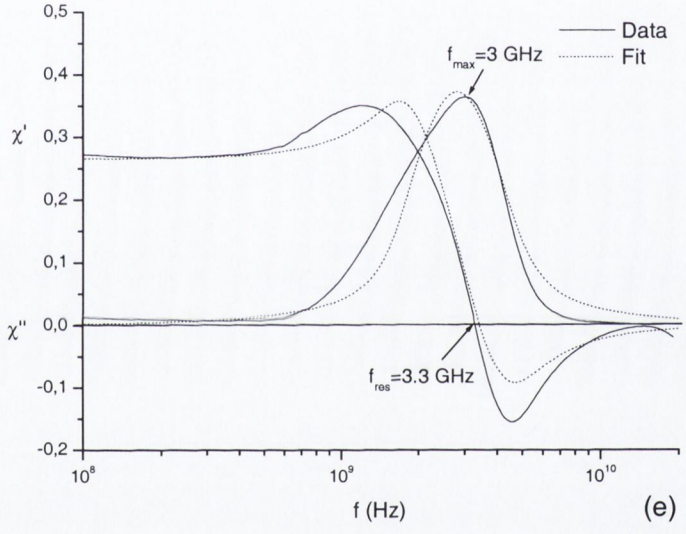

Figure 4.4 (e) 48.1 kA/m and

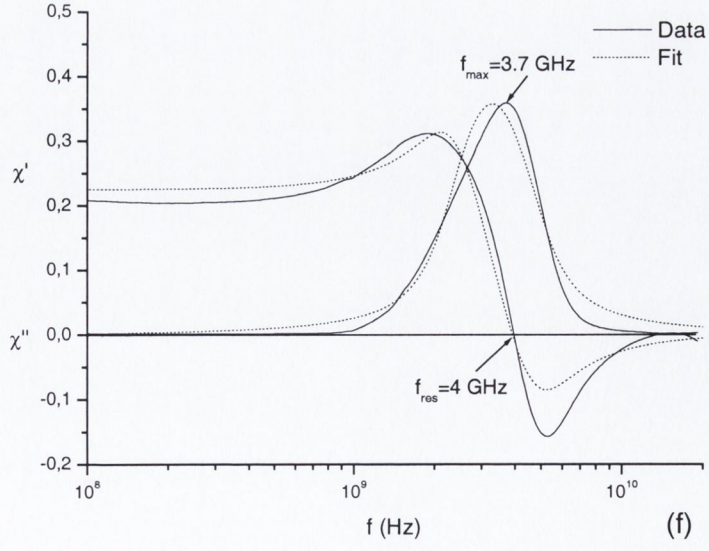

Figure 4.4 (f) 61.9 kA/m.

When the polarising field is zero or small, such as in cases (a) and (b), the effective σ is small so the Néel relaxation operates and the total susceptibility is given by $\frac{1}{3}(\chi_{\parallel}(\omega, H_s) + 2\chi_{\perp}(\omega, H_s))$. $\chi_{\perp}(\omega, H_s)$ is the resonance component (Landau-Lifshitz) and $\chi_{\parallel}(\omega, H_s)$ the relaxation component (Debye type). The inclination of the χ' curve below 1 GHz is due to the appearance of Néel relaxation at the radio frequency range. When the polarising field becomes strong σ is very large and in this event the Néel relaxation is blocked (cases (c)-(f)). The total susceptibility in this case equals $\chi_{\perp}(\omega, H_s)$.

Figure 4.5 A Cole-Cole representation of the Landau-Lifshitz profile:

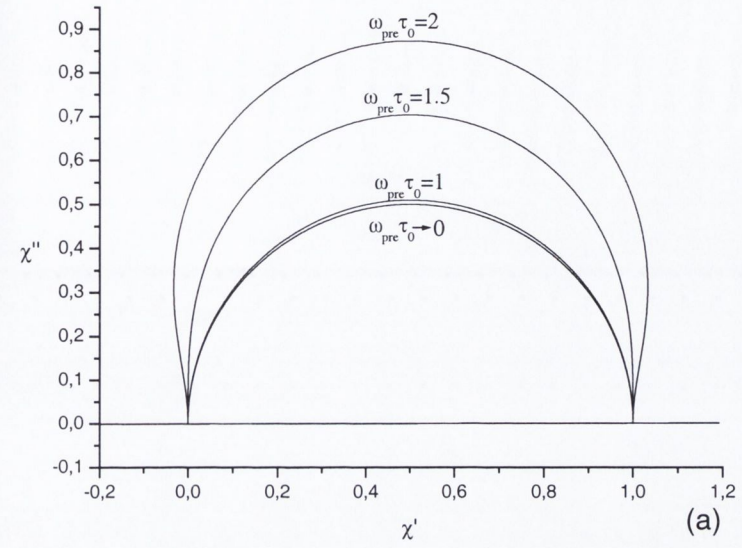

Figure 4.5 (a) Type I: Each curve corresponds to an individual polarising field. The value of $\omega_{pre}\tau_0$ is proportional to the polarizing field. For $\omega_{pre}\tau_0$ =0 the curve is a pure semicircle, i.e. a Debye profile. For $\omega_{pre}\tau_0 \neq 0$, the arcs always deviate from circular arcs at the points (0,0) and (1,0), due to Néel flipping. Each point on this graph corresponds to an individual frequency. To produce these theoretical curves the frequencies were taken over the range Hz to GHz,

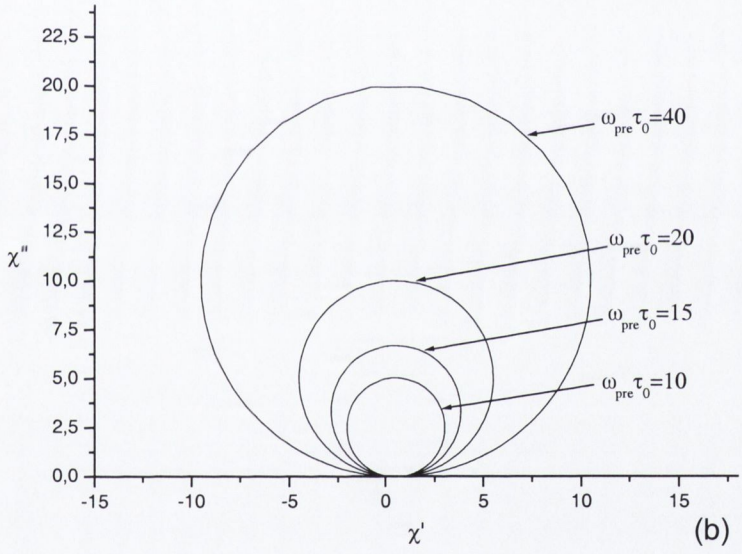

Figure 4.5 (b) Enlargement of the previous graph, in order to include larger values of $\omega_{pre}\tau_0$,

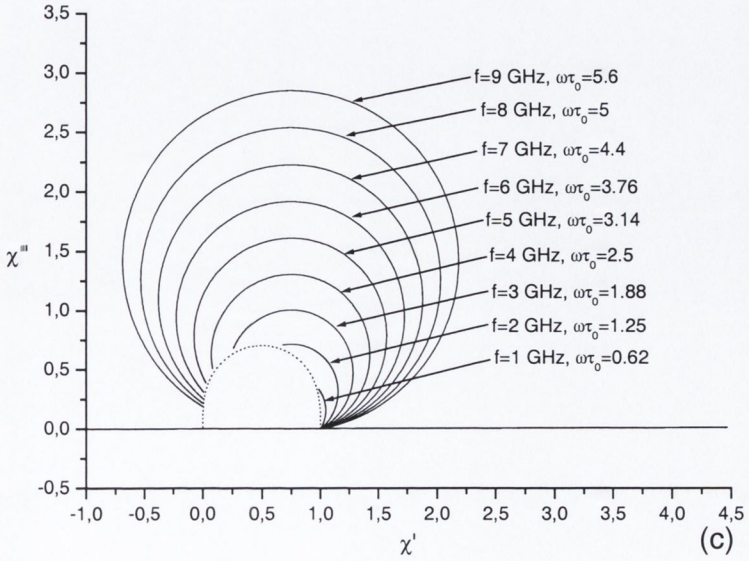

Figure 4.5 (c) Type II: Each curve corresponds to an individual frequency, which is directly related to the $\omega\tau_0$ term. Each point of the curve corresponds to an individual polarising field. These arcs are, for the Landau-Lifshitz absorption type, exact circular arcs. Here the polarising field range was extended from A/m up to kA/m.

Figure 4.6

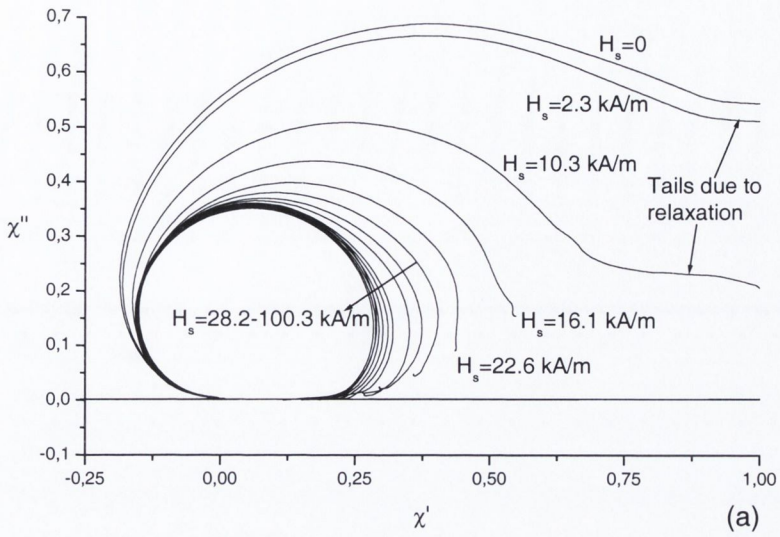

Figure 4.6 (a) Cole-Cole diagram (type I) of the resonant curve of the 900 G magnetite in isoparaffin sample. Each curve corresponds to a constant polarising field. The tail appearing on the right hand side of the first three curves is due to the relaxation contribution,

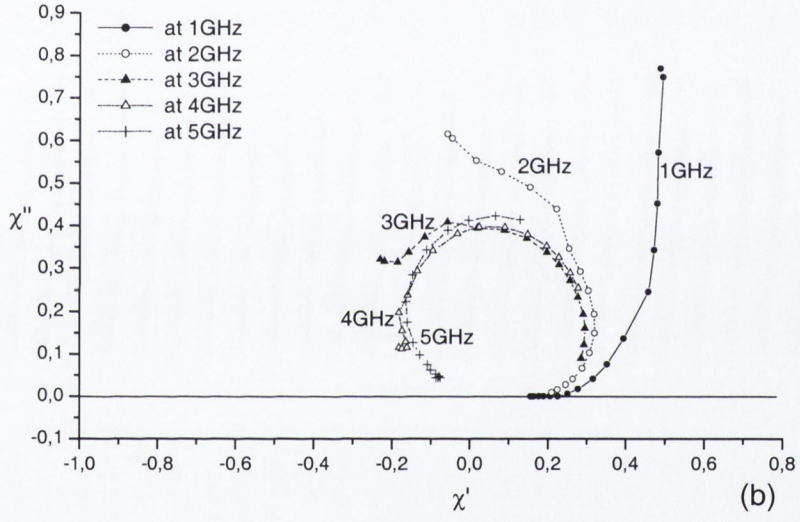

Figure 4.6 (b) Cole-Cole diagram (type II) of the same data where each curve corresponds to a constant frequency (i.e. 1, 2, 3, 4, 5 GHz). Each data point of each individual curve corresponds to a different polarising field,

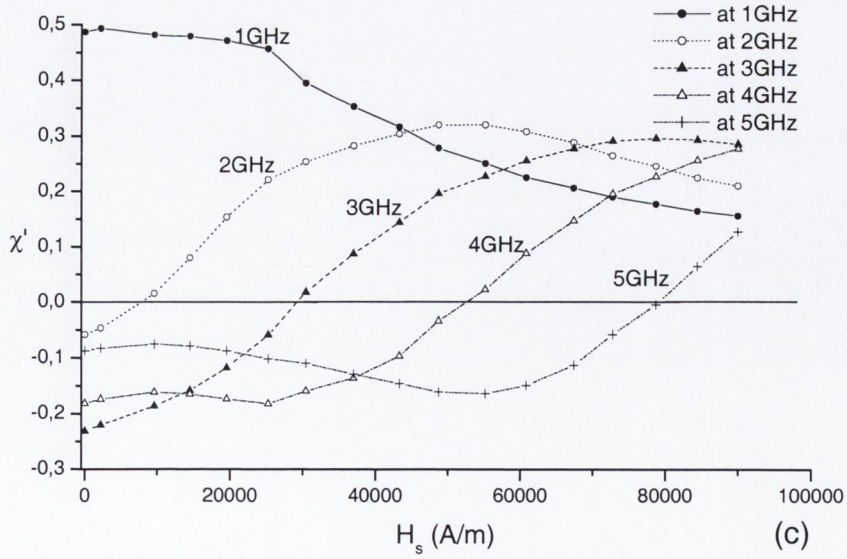

Figure 4.6 (c) Real susceptibility component as a function of the field and of the frequency,

(Continued)

Figure 4.6

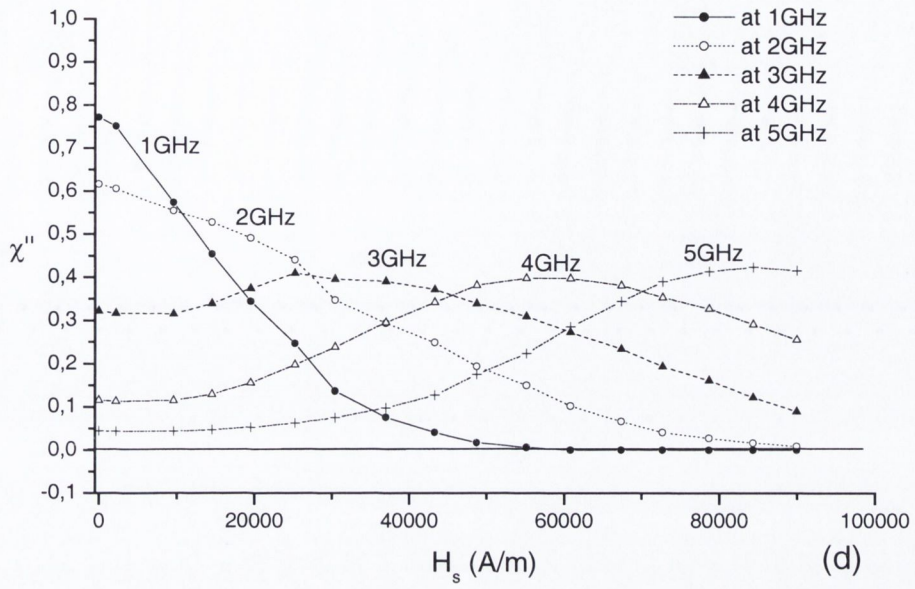

Figure 4.6 (d) Imaginary susceptibility component as a function of the field and of the frequency,

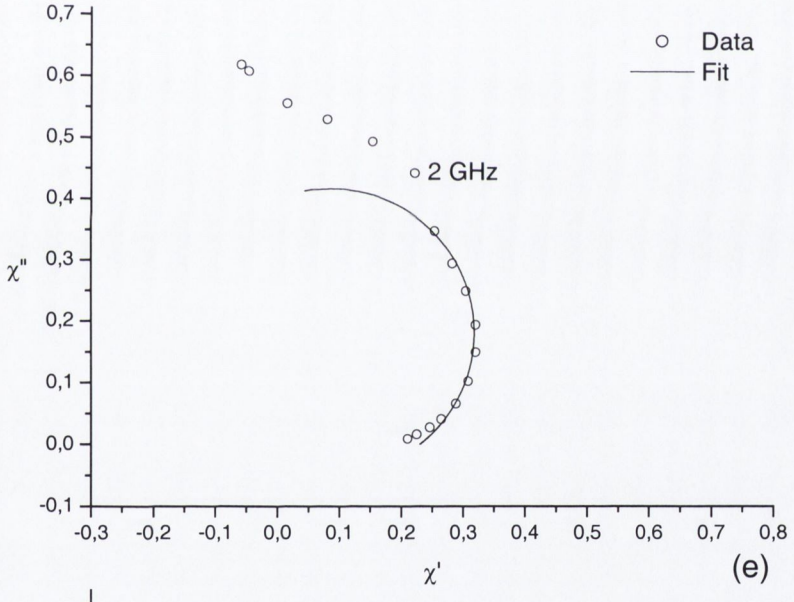

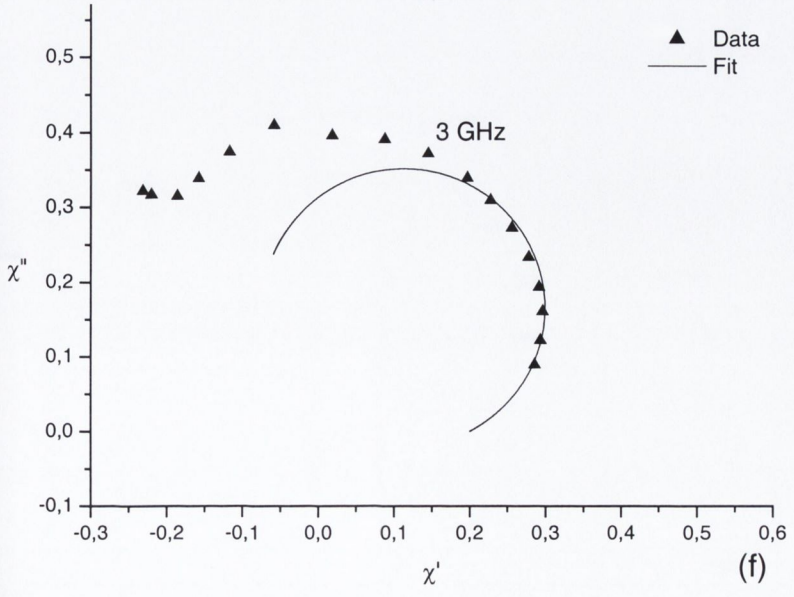

Figure 4.6 (e)-(h) Fits of the Cole-Cole curves of figure (b) by use of the Landau-Lifshitz equation. The fits are theoretical curves similar to those in Fig. (4.5 c). In all the four cases the fitting parameters used were the same. The parameters used were: M_s =0.4 T, K=9,000 J/m^3, γ =230,000 m/A sec, τ_0=2x10^{-10} sec. In each fit the frequency took its correspondent value, i.e. (e) 2 GHz, (f) 3 GHz, (g) 4 GHz, (h) 5 GHz.

(Continued)

Figure 4.6

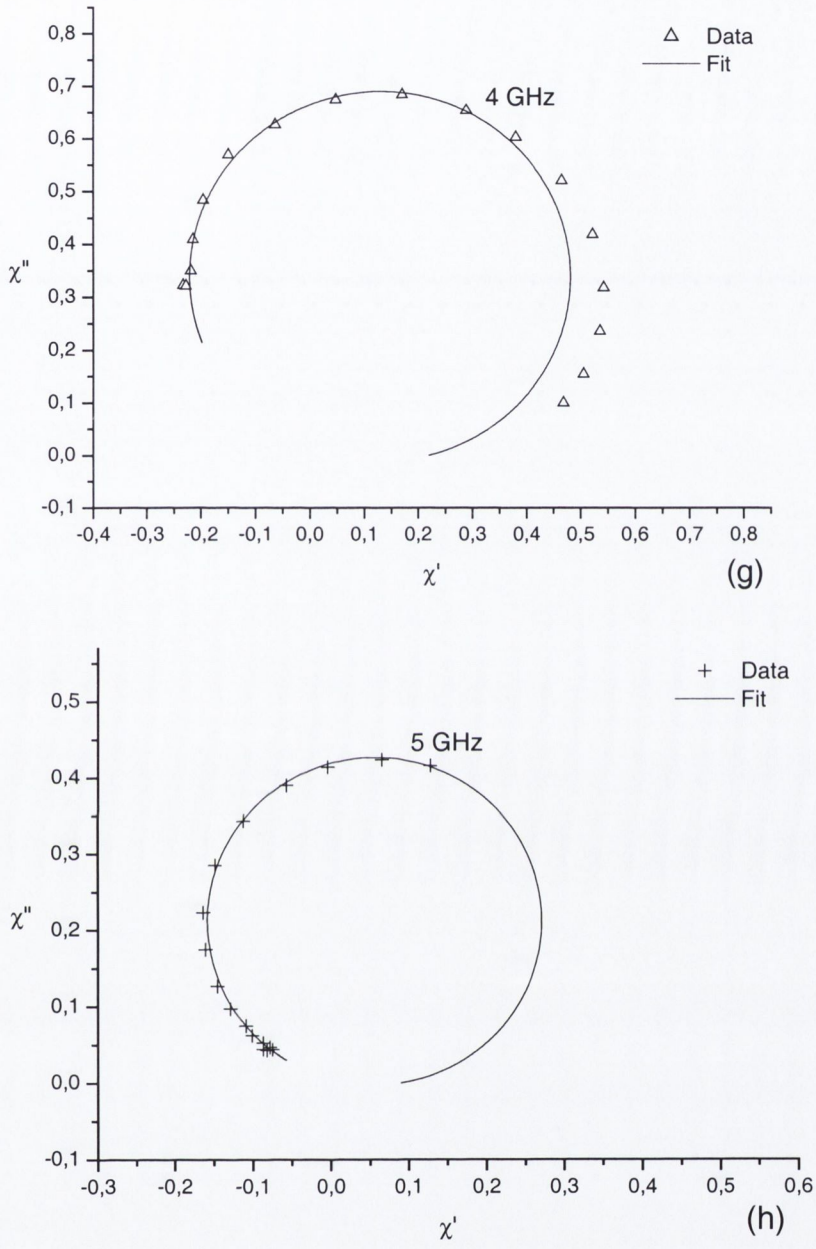

Figure 4.7 400 G cobalt sample in diester:

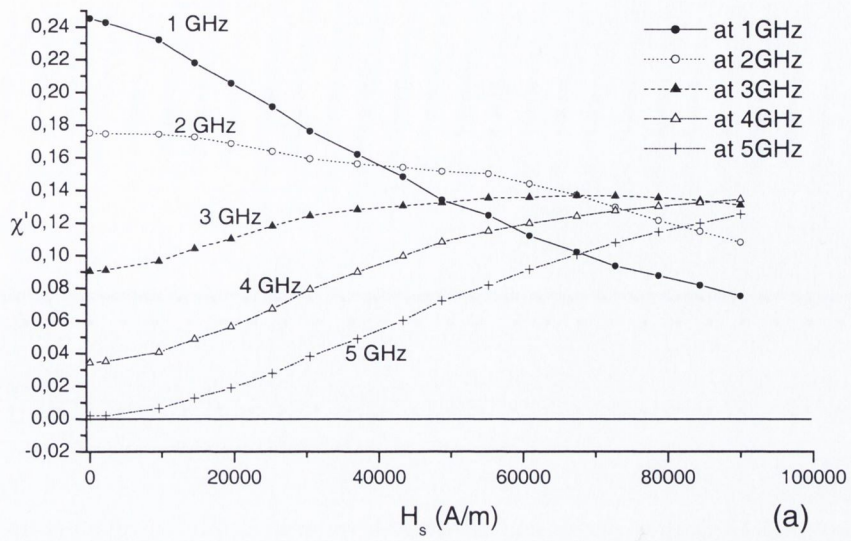

Figure 4.7 (a) χ' as a function of the field and frequency in the resonance range. The frequencies are picked from the resonance area,

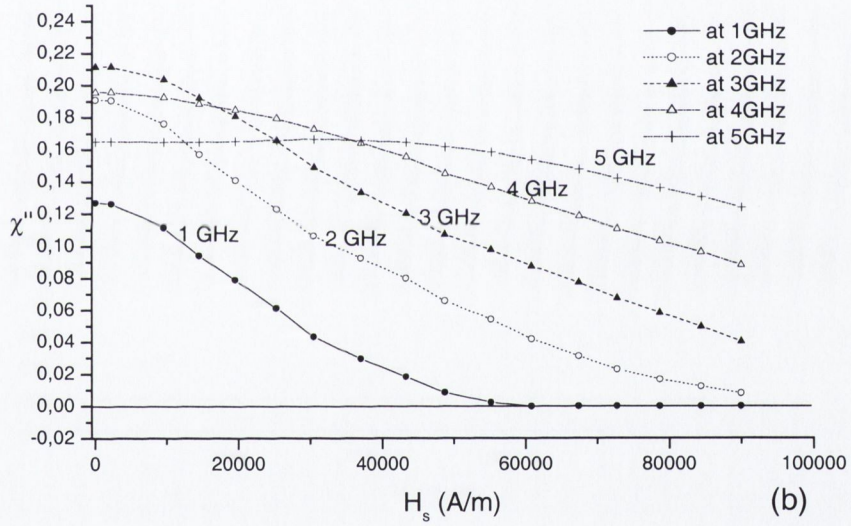

Figure 4.7 (b) the same as (a) but for the χ'' component,

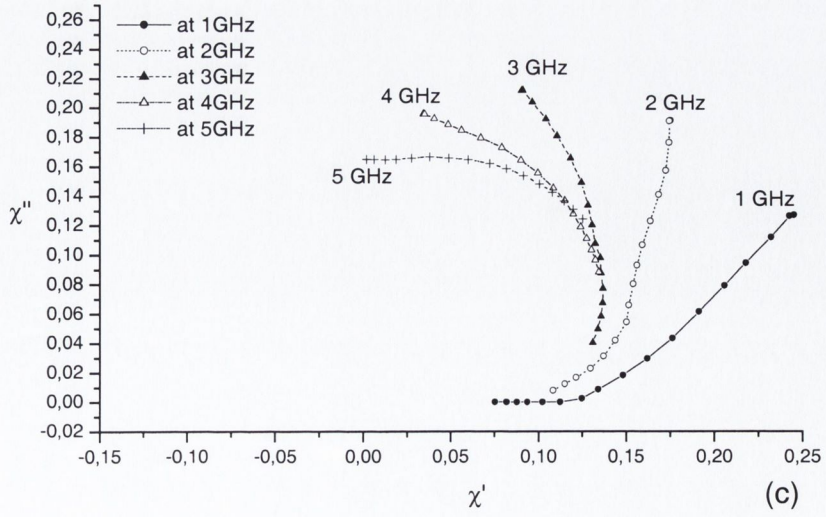

Figure 4.7 (c) Cole-Cole (type II) representation of the previous curves for each individual frequency. Each point corresponds to a separate polarising field,

(Continued)

Figure 4.7 400 G cobalt sample in diester:

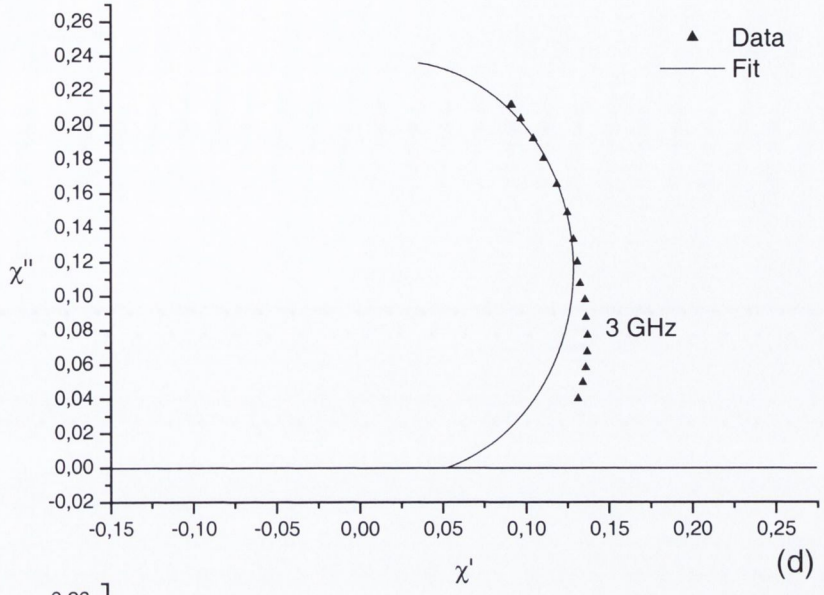

Figure 4.7 (d)

Fit (solid line) of the Cole-Cole data for f=3 GHz. The parameters used were: M_s =1 T, K=63,000 J/m^3, γ =200,000 m/A sec, τ_0=1.75x10^{-10} sec.,

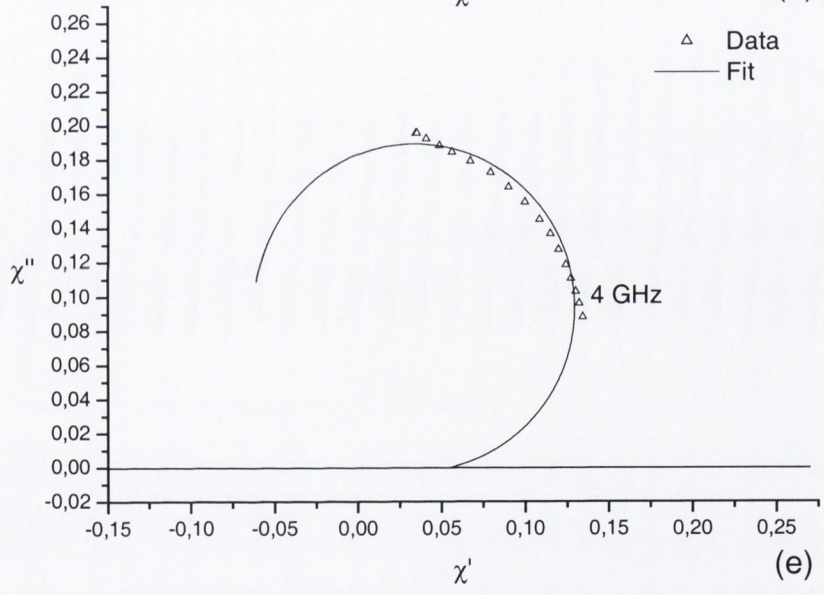

Figure 4.7 (e)

the same as (d) but for f=4 GHz,

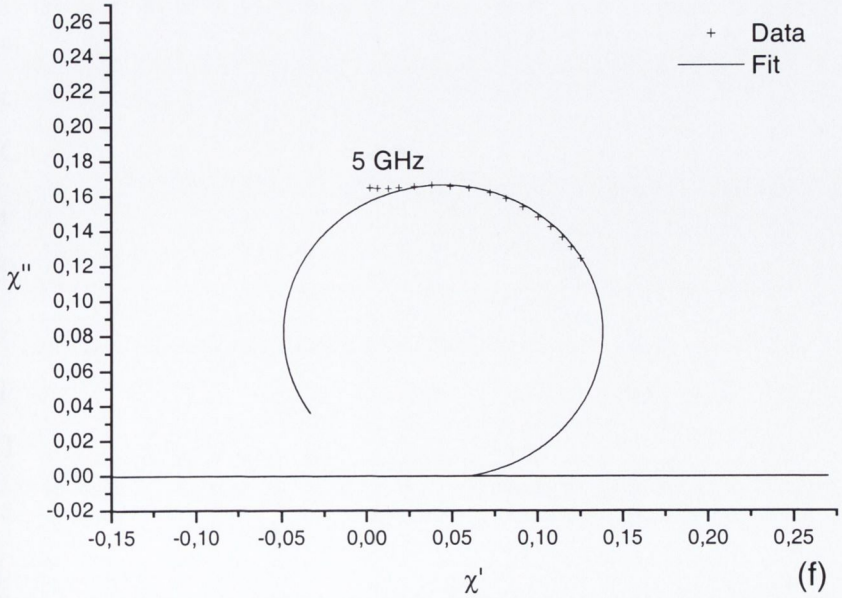

Figure 4.7 (f)

the same as (d) but for f=5 GHz.

When $\omega_{pre}\tau_0 \cong 0$ the Cole-Cole plot is a pure semicircle but when $\omega_{pre}\tau_0$ takes large values the Cole-Cole curve becomes, *almost*, a complete circle. The susceptibility values in the area under the semicircle, for which $\omega_{pre}\tau_0 \cong 0$, are invalid, because there $\omega_{res} \leq 0$ ($H_s \leq -H_A$). All (χ'',χ') pairs are outside this area.

(b) *Type II Cole-Cole plot*: Here we plot χ'' versus χ' for each individual frequency. In this type of Cole-Cole representation, which was first introduced by Scaife [17], each curve corresponds to a specific frequency, i.e. $\omega\tau_0$= constant, and each point of the curve corresponds to a particular polarizing field. An example of this Cole-Cole plot is shown in Fig. (4.5 c) where theoretical curves were created by use of the Landau-Lifshitz equation, for several frequencies. The arcs are *exact* circular arcs. The continuous values of H_s were extended from zero up to some kA/m. The left end points of the incomplete circles correspond to $H_s = -H_A$ ($\omega_{res} = 0$) and the right end points of the circles (i.e. points (0,1) on the chart) corresponds to $H_s \rightarrow \infty$ ($\omega_{res} \rightarrow \infty$). The points for which $H_s = H_A$ form a semicircle, which is denoted by a dotted line in Fig. (4.5 c). The area under this semicircle is invalid for susceptibility values.

Let us consider the experimental data of the *900 G magnetite in isoparaffin* sample which are presented in Figs. (4.2 a-b). We can plot these data in terms of the two types of Cole-Cole diagrams. The type I Cole-Cole diagram is presented in Fig. (4.6 a), in which each data curve corresponds to a different field. There are 17 curves, as many as the polarising fields which were used in this experiment. The values of the polarising fields used, are those indicated in Table 4.1. At lower fields (<16.1 kA/m) the effective σ is small and the relaxation mechanism is active. The relaxation is responsible for the appearance of the tails on the right hand side of the first three curves. The rest of the curves are normal circles and do not have tails. In Fig. (4.6 b) we present the type II Cole-Cole plot, in which each curve is associated with a constant frequency and each point of the curve with a particular field. Each curve consists of 17 points, as many as the polarising fields which were used in this experiment. To select the (χ', χ'') pairs we choose six frequencies from the resonance area of the spectra, i.e. 1, 2, 3, 4, 5, 6 GHz, we project them on $\chi'(\omega, H_s)$, $\chi''(\omega, H_s)$ curves and we take the intersected (χ', χ'') points. The values of the 17 χ' points are presented in Fig. (4.6 c) for each individual frequency and field. The 17 values of χ'' are presented in Fig. (4.6 d). We are now able to fit the

type II Cole-Cole curves of Fig. (4.6 b) with the Landau-Lifshitz equation for each selected frequency. The fits for f=2, 3, 4, 5 GHz are shown in Figs. (4.6 e-h) with solid lines. The same fitting parameters were used for all the fits; they were: M_s=0.4 T, K=9,000 J/m^3, γ=230,000 m/A s and $\tau_0=2\times10^{-10}$ sec. These are in full agreement with the fitting parameters used for the fits of Fig. (4.4). The resonance time constant, τ_0, corresponds here to an effective time constant which involves all polarising fields. This is due to the fact that each circle is a superposition of data, which are taken from several polarised $\chi(\omega,H_s)$ curves and all of them contribute to the circle. Thus τ_0 corresponds to an effective resonance frequency, $\omega_{res}=1/\alpha_d\tau_0$. We can see from the above fits that if we plot the data in a Cole-Cole graph it is easier to fit them and estimate the critical microscopic parameters M_s, K, γ and τ_0. This method is easier to apply than to perform fits such as those of Fig. (4.4).

With the same method we can fit the data of the *400 G cobalt in diester*, the spectra of which is shown in the previous Figs. (4.3 a-b). Figure (4.7 a) shows the χ' points for 17 biasing fields and 5 individual frequencies. The frequencies, again, are taken in the resonance region of the susceptibility spectra. Figure (4.7.b) shows the same thing but for χ''. Finally by plotting χ'' versus χ' we get the type II Cole-Cole diagram, which is shown in Fig. (4.7 c). The Figs. (4.7 d-f) show examples of the fitting of these Cole-Cole curves. The fitting parameters used were: M_s=1 T, K=63,000 J/m^3, γ=200,000 m/A s and $\tau_0=1.75\times10^{-10}$ sec. Here K and γ are in full agreement with the estimated, from f_{max} versus H_s plot of Fig. (4.3 c), values. M_s=1 T is typical for cobalt ferroparticles.

To conclude, in this section we introduced a more efficient method to fit the data by use of the type II Cole-Cole diagram. This method applies only four parameters, M_s, K, γ and τ_0. The fitting procedure appears to be easier and more accurate than the one described in the beginning of this section.

In the following sections we introduce two applications which involve power losses and signal-to-noise ratio in the resonance region of the susceptibility curve.

4.4 Application 1: Estimation of ferrofluid losses in the microwave frequency range.

The same definition for $\tan\delta$ which was given in section 3.6 (Eq. (3.6.1)), can be easily applied to the high frequency susceptibility. We recall that $\tan\delta$ is adapted from

circuit theory where it is used to describe power losses in devices. In the same manner we use the tan δ parameter to describe microwave absorption (losses) in magnetic systems and nanoparticle-based devices. Tan δ is both frequency and field dependent. As measurements show, tan δ decreases with increasing bias field and the frequency of the microwave signal.

Figure 4.8 900 G magnetite isoparaffin-based ferrofluid:

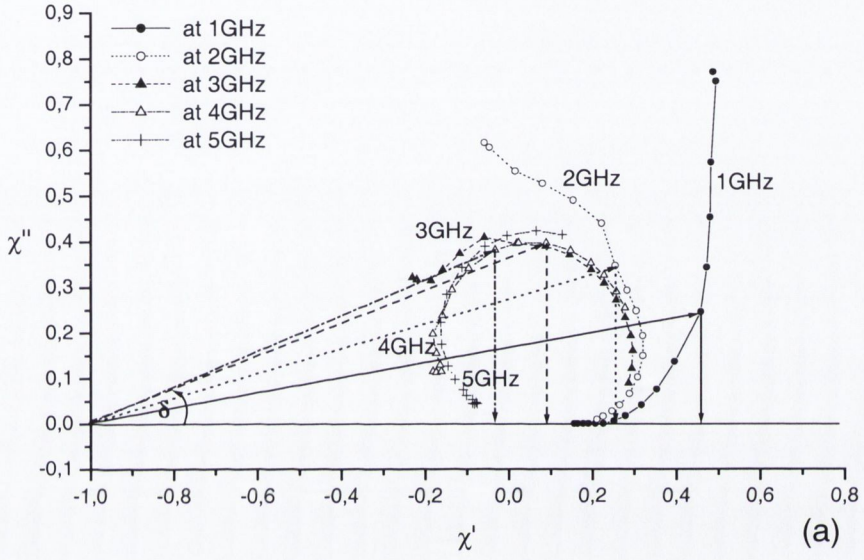

Figure 4.8 (a) Representation of tan δ in a type II Cole-Cole diagram. The horizontal edge of the drawn triangles equals $1+\chi'$ while the vertical edge equals to χ'',

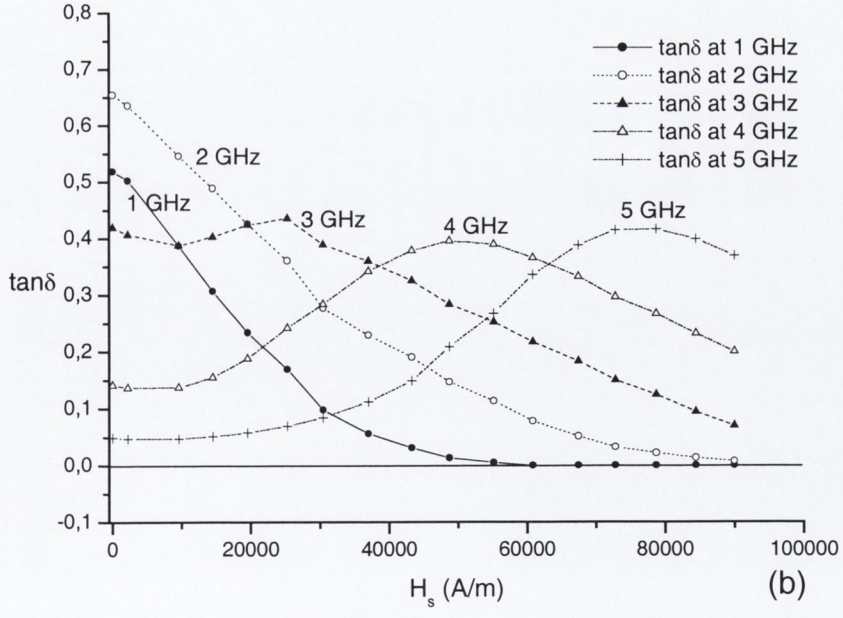

Figure 4.8 (b) tan δ as a function of frequency and polarising field.

Table 4.4 Variation of $\tan\delta$ of the 900 G magnetite, for several biasing fields and frequencies.

H_s (kA/m)	$\tan\delta$ at f=1 GHz	$\tan\delta$ at f=2 GHz	$\tan\delta$ at f=3 GHz	$\tan\delta$ at f=4 GHz	$\tan\delta$ at f= 5 GHz
0	0.518	0.654	0.419	0.141	0.048
2.3	0.503	0.635	0.406	0.136	0.047
10.3	0.387	0.546	0.387	0.137	0.047
16.1	0.306	0.488	0.402	0.154	0.051
22.6	0.234	0.425	0.424	0.188	0.057
28.2	0.169	0.360	0.435	0.241	0.069
34.1	0.097	0.276	0.389	0.283	0.084
41.4	0.056	0.229	0.359	0.341	0.111
48.1	0.031	0.190	0.324	0.378	0.148
54.7	0.013	0.146	0.283	0.395	0.208
61.9	0.004	0.113	0.252	0.389	0.267
68	0	0.078	0.217	0.365	0.335
75.2	0	0.051	0.182	0.332	0.387
81.3	0	0.032	0.149	0.295	0.413
87.7	0	0.022	0.124	0.266	0.415
94.8	0	0.013	0.094	0.231	0.398
100.3	0	0.007	0.069	0.199	0.368

To estimate $\tan\delta$ for the *900 G isoparaffin based magnetite* ferrofluid, we use the Cole-Cole representation of χ for this sample, see Fig. (4.6 b). The angle δ varies for each individual frequency and biasing field as Fig. (4.8 a) illustrates. This plot is analogous to Fig. (3.13 c) in section 3.6, where we studied losses at low frequencies. The value of $\tan\delta$ for each field and frequency is presented in Table 4.4. These values are plotted in Fig. (4.8 b).

From this plot we can see that, for the same H_s, $\tan\delta$ decreases as the frequency increases. At fields below 20 kA/m the biggest absorption appears for f=2 GHz. As the external magnetic strength increases, $\tan\delta$ increases up to a maximum and then decreases rapidly down to zero. This is opposite to what we discovered in section 3.6 in the low frequency case. There, $\tan\delta$ decreased uniformly with increase in H_s and the frequency was the main factor which affects the losses. In the resonance region, the opposite happens. The losses are mainly affected by the biasing field, rather than the frequency. A fuller explanation of this may be found in the nature of the relaxation and resonance absorption mechanisms. By polarising the sample, in the relaxation case the absorption peak, f_{max}, is not shifted as much as its counterpart is in the resonance case. In

terms of absorption, in the relaxation case the changes of the frequency have more effect than the changes of the field, whilst in the resonance case the opposite applies.

It is obvious that Fig. (4.8 b) consists of a chart which one can use to control the losses in magneto-electronic devices, by a simple change to the amplitude or the frequency of the intrinsic wave (alternating current).

4.5 Application 2: Estimation of the signal-to-noise ratio in ferrofluids.

The quality of a single-domain nanoparticle as a signal processing device is estimated with the aid of the signal-to-noise ratio (SNR) characteristic. The imposition of an external alternating field together with random noise, influences the magnetic switching within the magnetic particle and the SNR can be found in the framework of micromagnetic theory. The main material parameters essentially involved in the resulting expression are, the Néel relaxation time, τ_N, the precessional decay time, τ_0, and also the magnetic viscosity, η_m.

The description of the signal-to-noise ratio of a field-driven magnetisation of a fine ferroparticle is delivered by the theory of the superparamagnetic *stochastic resonance*[*]. The SNR is defined through the power spectral density function S(ω). In the framework of linear response theory, i.e., in terms of the dynamic susceptibility the corresponding expression is [21-23]:

$$S(\omega) = \pi\mu_0 H_0^2 \,|\chi(\omega)|^2\, \delta(\omega-\Omega) + \frac{4k_B T}{\omega}\chi''(\omega) \qquad (4.5.1)$$

where μ_0 is the permeability of free space. In the right-hand side of this formula, the first term corresponds to the signal. The delta-function refers to the fact that the system excited at the frequency Ω responds in a regular way at the same frequency; H_0 is the amplitude of the exciting alternating field. The second term in the right-hand side of Eq. (4.5.1) yields the noise component. The presence of the current frequency ω means that the system generates spontaneous noise at any frequency. By definition,

$$\mathrm{SNR} = \frac{\pi\mu_0\omega H_0^2\,|\chi(\omega)|^2}{4k_B T\chi''(\omega)} \qquad (4.5.2)$$

[*] Fox [20] defines the stochastic resonance as "noise-induced signal-to-noise ratio enhancement". The main model in the stochastic resonance theory is an overdamped bistable oscillator in a thermal bath.

This quantity turns out to have dimensions of frequency due to the fact that the delta-function has been omitted (this is in line with common practice). The way in which formula (4.5.2) is written, implies that the SNR is evaluated at the frequency of excitation. Hence, in the following analysis we set $\omega = \Omega$ and do not distinguish between these frequencies.

In our experiments the power of the microwave is set, by the analyser**, to 20 dbm which is equal to 100 mW. In the microwave frequency range (GHz) the period, T, of the microwave signal is of the order of 10^{-9} s and thus the energy of the microwave signal (power×time) is approximately 10^{-10} J. Since the transmission line is shorted, only the magnetic field is present in the cell. The energy density of the microwave can be calculated from electromagnetic theory by integrating the magnetic field, $h_a(t) = H_0 \cos(\omega t)$ over the period T, which gives $\mu_0 H_0^2 / 2$ (J/m^3). The volume of the sample is approximately equal to 4.7×10^{-8} m^3, for 1.5 mm cell depth. Thus the energy density of the microwave in the GHz range is approximately equal to 10^{-10}/ 4.7×10^{-8} J/m^3= 21×10^{-4} J/m^3. By equating $\mu_0 H_0^2 / 2$ with 21×10^{-4} J/m^3 yields H_0=60 A/m (=7.5×10^{-5} T), which is the amplitude of the alternating magnetic field which is used in this experiment. Equation (4.5.2) applies directly to the susceptibility data and gives the SNR.

Figures (4.9 a-b) show a set of theoretical curves of χ' and χ'' with both the Néel relaxation and resonance present. Curve 1 was created without considering any polarising field, curve 2 was created by considering a small effective biasing field and curves 3, 4, 5, 6 were created by stronger fields. In curves 1 and 2 the Néel relaxation is present, while in the rest of the curves it disappears, due to the presence of high σ. The signal-to-noise ratio is plotted in linear and logarithmic scale in Figs. (4.9 c) and (4.9 d) respectively. From the graphs we see that below 400 MHz, when no relaxation is present (curves 3, 4, 5, 6), the SNR appears constant while when relaxation operates (curves 1, 2) there is a curvature. The latter is visible in logarithmic scale, as Fig. (4.9 d) demonstrates. Now, in the resonance region, at above 4 GHz, there is a rapid increase of SNR for all curves. The reason that SNR goes high is the zeroing of χ''. At this point, discontinuity appears and SNR cannot be defined.

** The user can set up the power of the microwave signal. Both HP 8753C and HP 8722D analysers support a wide range of powers.

Figure 4.9

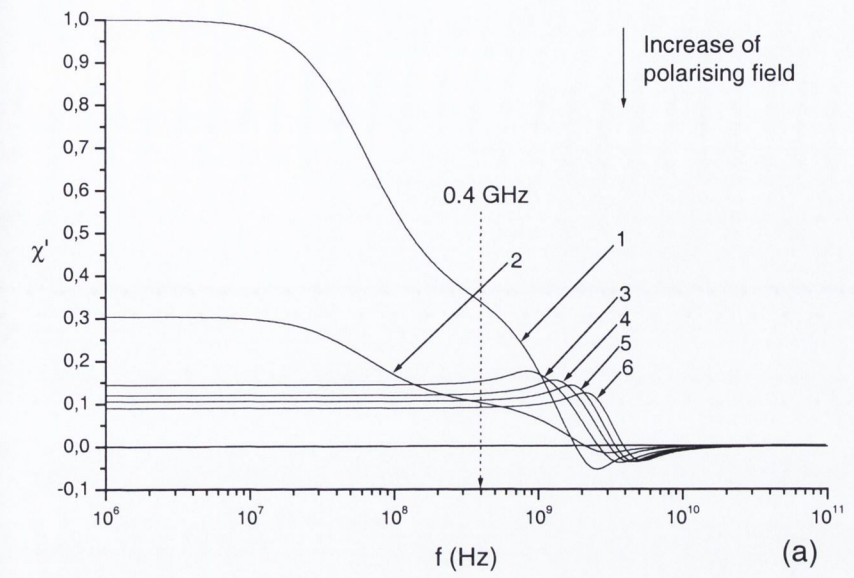

Figure 4.9 (a)
Theoretical curves of χ' produced by use of the Landau-Lifshitz equation. The curves are produced for various biasing fields. Below 400 MHz the Néel relaxation is dominant, while above 400 MHz resonance is pronounced. When the biasing field is large the effective σ is large and Néel relaxation disappears, as the curves 3, 4, 5, 6 show. The vertical dotted line shows the point of change from the relaxation profile to resonance,

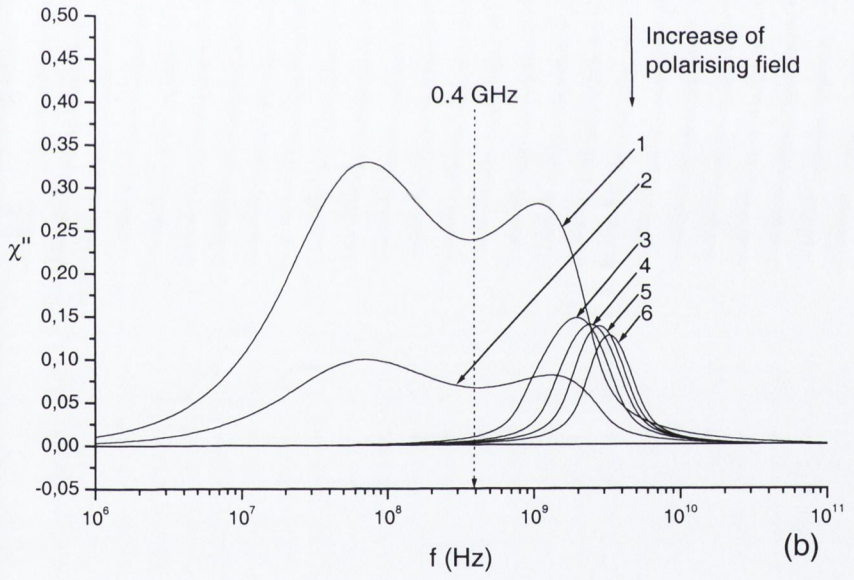

Figure 4.9 (b)

Same as (a) but for χ'',

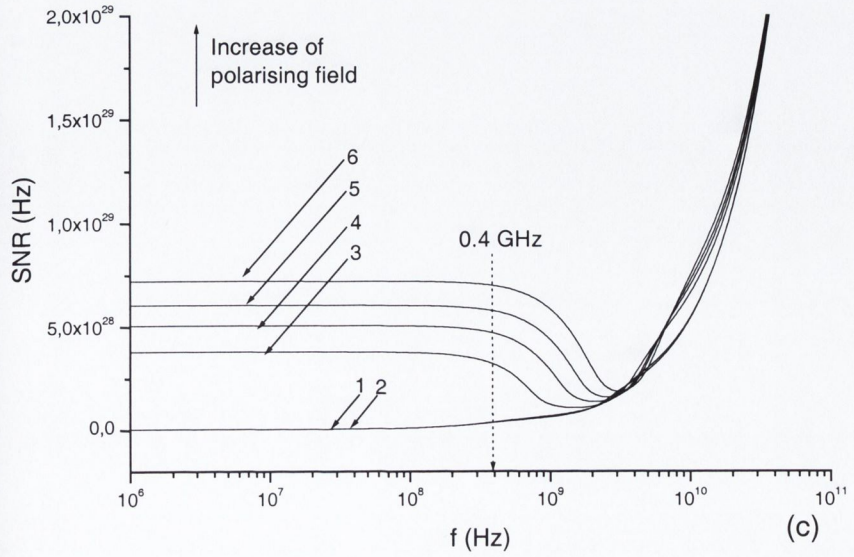

Figure 4.9 (c)

Signal-to-noise ratio as a function of the frequency. The SNR curves were created by use of the definition, Eq. (4.5.2), which applied to the theoretical curves of (a)-(b). It is easy to distinguish between the two different profiles, i.e. when both relaxation and resonance are present and when only resonance appears,

Figure 4.9

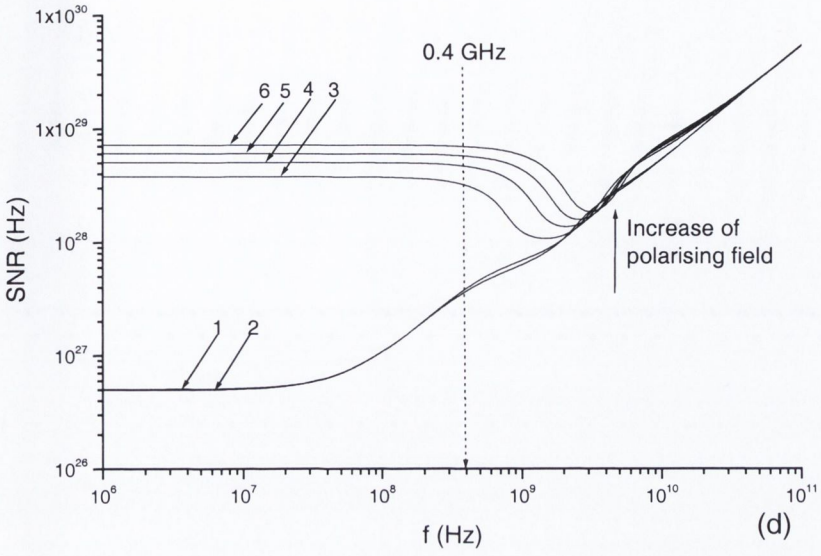

Figure 4.9 (d)

The same as in (c) but in logarithmic scale.

Figure 4.10

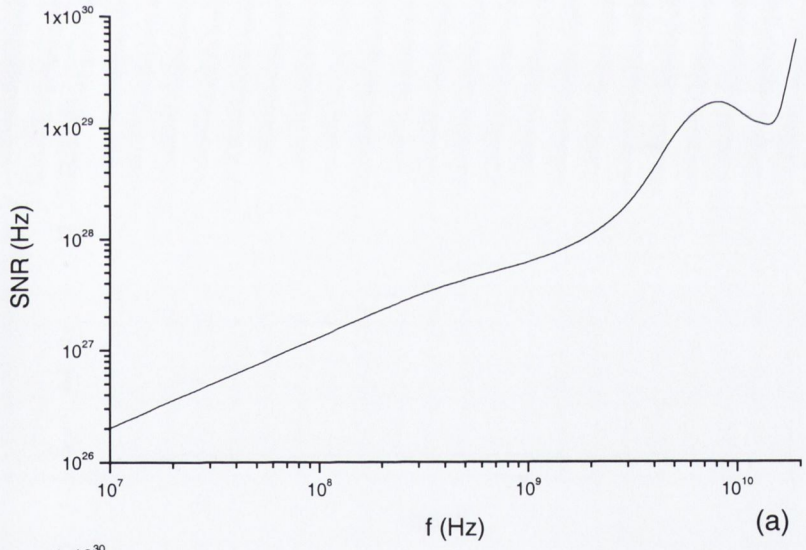

Figure 4.10 (a)

Signal-to-noise ratio of the magnetite in isoparaffin sample (unpolarised),

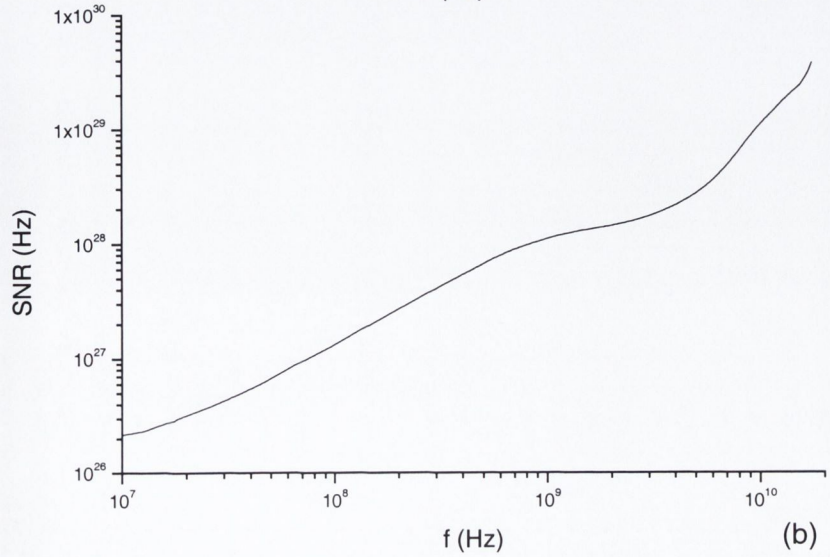

Figure 4.10 (b)

Signal-to-noise ratio of the cobalt in diester sample (unpolarised).

In Figs. (4.10 a), (4.10 b) we plot the SNR of the magnetite and cobalt samples respectively, which are calculated by applying Eq. (4.5.2) to the unpolarised data of those ferrofluids. Since relaxation exist in these unpolarised data, the SNR, as expected, has the same profile as curve 1 of Fig. (4.9 d).

It is of interest to explore Eq. (4.5.2) when only the longitudinal, $\chi_{\parallel}$, component contributes to the SNR. $\chi_{\parallel}$ is given by the Debye equation for susceptibility (Eq. (1.4.47) where χ_{∞}=0). Using the real and imaginary parts and then arranging them in the expression for the modulus $|\chi(\omega)|$, one finds that

$$\mathrm{SNR} = \frac{\pi\mu_0 H_0^2 \chi_0}{4k_B T\tau_{\parallel}} \tag{4.5.3}$$

where $\tau_{\parallel}$ stands for the effective relaxation (longitudinal) time, which in these circumstances is equal to the Néel relaxation time ($\tau_{\parallel} = \tau_N$). Note that in the considered frequency range the SNR is independent of frequency. Setting the value of χ_0 from Eq. (1.4.48), assuming for the relaxation time $\tau_{\parallel}$ the simple form of τ_N which is Eq. (1.5.19), and substituting η_m (Eq. (1.5.18)) in the expression for τ_D' (Eq. (1.5.17)) and remembering that for the Néel prefactor $\tau_0 = \tau_D'$ holds, one finds that the signal-to-noise ratio can be written in the form

$$\mathrm{SNR} = \frac{\pi(M_s H_0)^2}{36\eta_m K}\sigma^2 \exp(-\sigma) \tag{4.5.4}$$

Therefore, if possible parametric temperature dependencies of the material parameters K, M_s and η_m, are neglected, the explicit temperature behaviour of the SNR in Eq. (4.5.4) is rendered by the remaining term $\sigma^2\exp(-\sigma)$. At small σ, the function $\sigma^2\exp(-\sigma)$ increases in order of σ^2. At large σ, the function $\sigma^2\exp(-\sigma)$ decreases approximately exponentially. From the fact that $\sigma^2\exp(-\sigma)$ reduces for both $\sigma \to 0$ and $\sigma \to \infty$, it follows that there exists a maximum somewhere at finite σ. This σ-induced maximizing of the signal-to-noise ratio is termed *the magnetic stochastic resonance*. In the framework of linear response theory which yields Eq. (4.5.3), the actual location of the maximum SNR(σ) is very close to σ = 2.5 [23,24], and is almost independent of whether $\tau_{\parallel}$ ($=\tau_N$) is determined by Eq. (1.5.19) or by Eq. (1.5.21). The above consideration shows that for optimizing the signal processing properties of a single-domain particle (or an assembly of

such particles), knowledge of the effective anisotropy constant, K, and the damping parameter, α_d, which enters the magnetic viscosity, η_m, (see Eq. (1.5.18)) is of paramount importance. An estimation of the SNR for various ferrofluids by use of expression (4.5.4) can be found in [25,26].

4.6 Conclusions and suggestions for future work.

In this chapter we introduced measurements in the RF and microwave frequency range of the magnetic susceptibility of two samples, namely magnetite in water and cobalt in diester. Both samples show Néel relaxation and resonance absorption, manifested by two prominent peaks on the spectrum of χ''. Both samples were polarised with external biasing fields, H_s, created by an electromagnet. The magnetic susceptibility was measured for 17 individual values of the polarising field (Table 4.1), which shows a gradual elimination of the Néel relaxation effect due to the effective increase of $\sigma = Kv_m / k_B T$ parameter. The characteristic profile of the polarised susceptibility is shown in Figs. (4.2 a-b), (4.3 a-b). From there it is possible to estimate a range of microscopic parameters which characterises the material, namely $\langle K \rangle$, $\langle H_A \rangle$, and γ. An easy and reliable method, by which one can derive the after-effect function of the magnetisation of a ferrofluid, is by simply applying the inverse Fourier transform to the susceptibility data. The $M^F(t)$ function can be derived for time intervals down to nanoseconds, making this method really preferable in the research of nanoparticle systems.

The Landau-Lifshitz equation proved to be well suited (for the polarised high frequency measurements we perform) to describe resonance in ferrofluids, due to its simplicity and easiness to fit the data (Fig. (4.4)). Other proposed models [5] may also be suitable. The Landau-Lifshitz equation can easily be presented in a Cole-Cole diagram (type II) where χ'' is plotted versus χ' for a number of selected frequencies. This kind of representation aids very much the study of polarised data. It is also very easy, with this format, to fit directly the experimental data by use of the M_s, K, γ and τ_0 parameters. Examples of fitting were presented in Figs. (4.6) and (4.7).

The magnetic susceptibility spectra is a powerful tool for practical applications. With the increased interest in the use of ferrofluids in magneto-electronics applications involve the estimation of power losses and noise effects in magnetic devices. The tanδ characteristic is proposed here as a quantitative parameter by which one can measure

losses at RF and microwave frequencies. Since tanδ is both field and frequency dependent, this dependence can consist of a map to control the losses by adjustment of the amplitude and the frequency of the signal.

The concept of using superparamagnetic particles in a signal processing environment is discussed. A plausible quantitative criterion for that is the signal-to-noise ratio (SNR). The SNR is an essential characteristic of a nanoparticle as a signal processing device. The SNR can aid to qualify a magneto-device and it is simply defined by the ratio of the signal to the thermal noise. The random noise influences the magnetic switching of $\boldsymbol{\mu}_m$. By use of the available susceptibility data and Eq. (4.5.2) one can estimate the SNR throughout the RF and microwave frequency range as is shown in Fig. (4.10), which shows the SNR for the two ferroparticle systems we measured, i.e. magnetite and cobalt. Other simplified estimations of SNR entail the use of microscopic parameters, i.e. τ_N, τ_0 and η_m, as is shown in [25,26].

In the context of using ferroparticles as magnetic switches, our current research involves applications of the resonance effect by mixing two ferrofluids with different resonant frequencies. The result is that f_{res} of the composite appears between the f_{res} values of the two constituent ferrofluids. Composite f_{res} is controlled by adjusting an external field to certain levels. This result is important for the design of microwave attenuators or microwave absorbers based on ferromagnetic resonance absorption. Both experimental and theoretical research is currently undertaken on this subject.

References:

1. Fannin P.C., Charles S.W., Relihan T., *J. Mag. Mag. Mat.*, **162**, 319, (1996).
2. Fannin P.C., Kinsella L., Charles S.W., *J. Phys. D: Appl. Phys.*, **30**, 533, (1997).
3. Fannin P.C., Kinsella L., Charles S.W., *J. Mag. Mag. Mater.*, **201**, 91, (1999).
4. Raikher Yu.L., Shliomis M.I., *Sov. Phys. JETP*, **40**, No 3, 526, (1974).
5. Coffey W.T., Kalmykov Y.P., Massawe E.S., *Adv. Chem. Phys.*, **85**, 704, (1993).
6. Fannin P.C., Relihan T., Charles S.W., *J. Phys. D: App. Phys.*, **28**, 2003, (1995).
7. Fannin P.C., Perov P.A., Charles S.W., *J. Phys. D: App. Phys.*, **32**, 1583, (1999).

8. Fannin P.C., Perov P.A., Charles S.W., *J. Phys. D: Appl. Phys.*, **32**, No 18, 2367 (1999).
9. Fannin P.C., Relihan T., Charles S.W., *Physical Review B*, Vol **55**, No 21, 14423, (1997).
10. FerroTec Data Table, EMG Ferrofluids, (1998).
11. Kinsella L., *MSc thesis*, Univ. of Dublin-Trinity College Library, Dublin (1998).
12. Fannin P.C., Martin C.N., Socoliuc V., Istratuca G.M., Giannitsis A.T., *J. Phys. D: Appl. Phys.*, **36**, 1227, (2003).
13. Tari A., Popplewell J., Charles S.W., *J. Magn. Magn. Mater.*, **15**, 1125, (1980).
14. Charles S.W., Wells S., *Magnetohydrodynamics*, **26**, 288, (1990).
15. Fannin P.C., *Advances in Chemical Physics*, **104**, 181, (1998).
16. Shliomis M.I., Raikher Yu.L., *IEEE Trans. Magn.*, **MAG-16**, 237, (1980).
17. Scaife B.K.P., *Adv. Chem. Phys.*, **109**, 1, (1999), and private communication.
18. Fannin P.C., Scaife B.K.P., Charles S.W., *J. Phys. E: Sci. Instrum.*, **19**, 238, (1986).
19. Fannin P.C., Scaife B.K.P., Charles S.W., *J. Magn. Magn. Mater.*, **85**, 54, (1990).
20. Fox R.F., *Phys. Rev. A*, **39**, 4148, (1989).
21. Dykman M.I., Mannella R., McClintock P.V.E., Stocks N.G., *Phys. Rev. Lett*, **65,** 2606, (1990).
22. Dykman M.I., Luchinsky D.G., Mannella R., McClintock P.V.E., Stein N. D., Stocks N. G. , *Nuovo Cimento*, **17D,** 661, (1995).
23. Raikher Yu.L., Stepanov V.I., *Phys. Rev.*, **B 52**, 3493, (1995).
24. Raikher Yu.L., Stepanov V.I., *J. Phys. C: Condens. Matter*, **6**, 4137, (1994).
25. Fannin P.C., Raikher Yu.L., *J. Phys. D.*, **34**, 1612, (2001).
26. Fannin P.C., Raikher Yu.L., Giannitsis A.T., Charles S.W., *J. Mag. Mag. Mater.*, **252**, 114, (2002).

Chapter 5

Electrical equivalent circuits for Debye, Cole-Cole and Landau-Lifshitz equations.

5.1 Introduction

It is convenient to model the frequency dependence of the complex permittivity, permeability and susceptibility by means of electric circuits of ideal (that is frequency independent and linear) resistors, inductors, and capacitors.

The usefulness of using the equivalent electrical circuits is due to the ease of representing absorbers with single electrical circuit components. This may help researchers to study in depth the nature of the relaxation and resonance phenomenon in both dielectric materials and ferrofluids.

The first attempts to describe the relaxation and resonance effects were made for polar liquids, however similar electrical circuits can be used to describe the behavior of magnetic materials. As it is more convenient to deal with capacitors and resistors and because in the literature most applications involve dielectric measurements, first we will introduce the equivalent circuits for the dielectric case and after we will adapt them to the magnetic case. Some modifications, when one changes from one case to the other, are necessary, namely: (a) to replace the capacitors with inductors, and (b) to replace the parallel circuitry with series circuitry and vice versa.

In the following analysis three types of equivalent electrical circuits are presented: (a) the Debye relaxation absorber (section 5.2), (b) the Cole-Cole relaxation absorber (section 5.3) and (c) the resonance absorber which is described by the Landau-Lifshitz equation (section 5.4). The Debye relaxation absorber has been extensively studied for the dielectric case [1,2] as well as the resonance absorber [3,4]. The aim is to modify the dielectric equivalent circuit to a magnetic circuit made by inductive and resistive components. The Cole-Cole absorber can be realized in terms of the *constant phase element* (CPE) [5].

The application involves examples of the ferrofluid's permittivity (permeability has been already studied in the previous chapters), in which the ferrofluid's composites (carrier and surfactant) can be approximated by two capacitors in series. Based on this equivalent

circuit we can write the overall permittivity of a ferrofluid in terms of the permittivities of its composites, ε_1 (carrier) and ε_2 (surfactant) and of their fractional volumes, v_1 and v_2. The conductivity, σ, can be calculated as a function of the frequency from the permittivity spectra ($\sigma(\omega) = \omega\varepsilon''(\omega)\varepsilon_0$).

5.2 Equivalent electrical circuits for the Debye equation.

Let us consider the simplest possible case of an electrical circuit, which is a RC parallel combination. We will see that it is possible to model the Debye equation (1.4.43), in its simplest form where $\varepsilon_\infty = 0$, with the parallel RC combination, however some of its properties do not make this circuitry the best possible circuit. When an empty ideal capacitor with capacitance $C_0 \propto \varepsilon_0$ is filled with a dielectric it will have an admittance of $\omega(\varepsilon'(\omega) - i\varepsilon''(\omega))C_0$. Because the permittivity is complex this admittance can be simulated by a capacitance $\varepsilon'(\omega)C_0$ in parallel with a resistance $1/\omega\varepsilon''(\omega)C_0$ (Fig 5.1 (a)). This can easily be seen by equating the equivalent total parallel admittance $\omega(\varepsilon'(\omega) - i\varepsilon''(\omega))C_0$, corresponding to an equivalent total parallel capacitance $C_p^{tot}(\omega) = (\varepsilon'(\omega) - i\varepsilon''(\omega))C_0$, with the admittance given from circuit theory

$$Y_p(\omega) = G_p(\omega) + iB_p(\omega) = i\omega C_p^{tot}(\omega)$$

$$\frac{1}{R_p(\omega)} + i\omega C_p(\omega) = i\omega(\varepsilon'(\omega) - i\varepsilon''(\omega))C_0 = i\omega\varepsilon'(\omega)C_0 + \omega\varepsilon''(\omega)C_0 \qquad (5.2.1)$$

from where

$$R_p(\omega) = \frac{1}{\omega\varepsilon''(\omega)C_0}, \quad C_p(\omega) = \varepsilon'(\omega)C_0, \quad \varepsilon'(\omega) = \frac{C_p(\omega)}{C_0}, \quad \varepsilon''(\omega) = \frac{1}{\omega R_p(\omega)C_0} \qquad (5.2.2)$$

The resistance, R_p, is related directly to ε'' which is proportional to absorption and the capacitance, C_p, which involves energy storage, is related to ε'. In this parallel circuitry, the voltage is externally controlled and the current is measured. The impedance and the admittance will be frequency dependent. It is important to notice that only C_0 is frequency independent and since the permittivity is frequency dependent its combinations with frequency $R_p(\omega)$ and $C_p(\omega)$ should be constant for low ω.

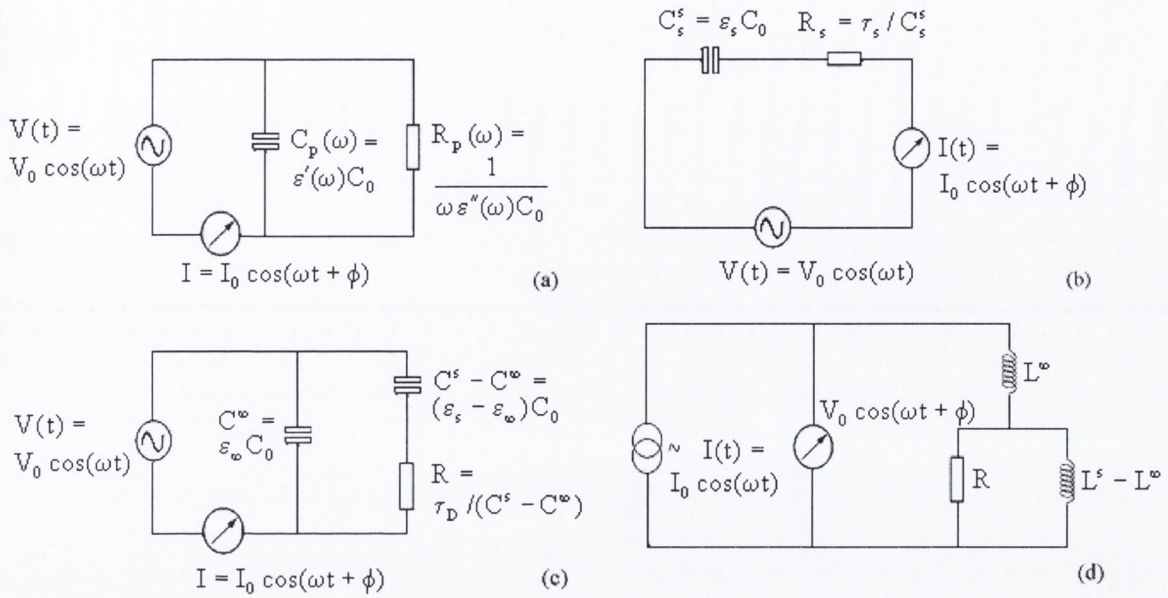

Figure 5.1 Equivalent electrical circuits describing the Debye equation for a dielectric (a-c) and a magnetic material (d). (a) Parallel arrangement: the real permittivity is represented by the parallel capacitor and the imaginary by the parallel resistance, (b) Series arrangement: the static permittivity is represented by the series capacitor and the series resistor evaluates the time constant, (c) By adding a parallel capacitance to the previous circuitry it is possible to represent the permittivity at high frequencies, (d) The same as (c) but for the magnetic case. It is required to replace the capacitances with the equivalent inductors representing permeability. The series circuitry has to become parallel and the parallel to be changed to series. The constant current represents the magnetic field. The cases (c) and (d) are the best possible to represent the Debye equation with equivalent electrical circuits.

This RC circuit has a time constant of

$$\tau_p(\omega) = R_p(\omega)C_p(\omega) = \frac{\varepsilon'(\omega)}{\omega\varepsilon''(\omega)} \tag{5.2.3}$$

which is in general a function of the frequency and this is the main reason why we do not consider τ_p directly equivalent to the Debye relaxation time τ_D since we need a constraint (i.e. the combination of $R_p(\omega)$ with $C_p(\omega)$ constant). This is one reason why this circuitry is not optimal. The phase angle between voltage, $V(t) = V_0\cos(\omega t)$, and current, $I(t) = I_0\cos(\omega t + \phi)$, is given by $\phi_p(\omega) = \tan^{-1}(\omega R_p(\omega)C_p(\omega))$. The impedance is expressed in terms of the $R_p(\omega)$, τ_p values as

$$Z_p(\omega) = \frac{1}{Y_p(\omega)} = \frac{1}{\frac{1}{R_p(\omega)} + i\omega C_p(\omega)} = \frac{R_p(\omega)}{1 + i\omega R_p(\omega)C_p(\omega)} = \frac{R_p(\omega)}{1 + i\omega\tau_p},$$

$$Z_p(\omega)=\frac{R_p(\omega)(1-i\omega\tau_p)}{(1+\omega^2\tau_p^2)},\qquad Z_p'(\omega)=\frac{R_p(\omega)}{(1+\omega^2\tau_p^2)},\quad Z_p''(\omega)=-\frac{R_p(\omega)\omega\tau_p}{(1+\omega^2\tau_p^2)} \tag{5.2.4}$$

This circuit has some very characteristic properties: (a) the admittance diverges at higher frequencies (impedance nullifies), (b) it conducts dc current, (c) the phase angle is positive, meaning that the current (dependent variable) leads the voltage. The reasons that this RC circuit cannot describe perfectly Eq. (1.4.43) are: (a) parallel resistance (dissipation) is not proportional to ε''(energy absorption) but inversely proportional, (b) it doesn't represent ε_s, ε_∞, (c) the considered time constant is frequency dependent (only under constraints may not be).

It is also possible to simulate Eq.(1.4.39) with series circuitry (Fig 5.1 (b)), in which again the voltage, but not the current division, is externally controlled. This suits better the simulation of the Debye equation since the series capacitance may be constant by representing the static permittivity ($C_s^s=\varepsilon_s C_0=\text{const.}$), thus the time constant will be somewhat independent of frequency as is τ_D, but it still cannot represent the ε_∞ component. The series impedance is

$$Z_s(\omega)=R_s-\frac{i}{\omega C_s^s}$$

and the series admittance

$$Y_s(\omega)=\frac{1}{Z_s(\omega)}=\frac{1}{R_s-\dfrac{i}{\omega C_s^s}}=\frac{i\omega C_s^s}{1+i\omega R_s C_s^s}=i\omega C_s^{tot}(\omega)$$

from where

$$C_s^{tot}(\omega)=\frac{C_s^s}{1+i\omega R_s C_s^s} \tag{5.2.5}$$

Dividing by C_0, gives

$$\varepsilon(\omega)=\frac{\varepsilon_s}{1+i\omega R_s C_s^s}=\frac{\varepsilon_s}{1+i\omega\tau_s} \tag{5.2.6}$$

which is the simplified Debye equation with time constant $\tau_s=R_sC_s^s=\text{const.}$, which is directly equivalent to τ_D. From the latter expressions we may write,

$$Y_s'(\omega) = \frac{\omega^2\tau_s^2}{R_s(1+\omega^2\tau_s^2)}, \qquad Y_s''(\omega) = \frac{C_s^s\omega}{(1+\omega^2\tau_s^2)}, \tag{5.2.7}$$

$$\varepsilon'(\omega) = \frac{C_s^s}{(1+\omega^2\tau_s^2)C_0}, \qquad \varepsilon''(\omega) = \frac{C_s^s\omega\tau_s}{(1+\omega^2\tau_s^2)C_0} \tag{5.2.8}$$

In the series arrangement impedance converges at higher frequencies but it doesn't allow the passage of dc (fails at low frequencies). The phase is positive, i.e. the current (dependent variable) leads the voltage. The parallel and series two-component circuits are complementary models and contain the same information in ideal systems.

The most advanced circuit model is a combination of parallel and series circuitry (Fig. (5.1 c)) by adding a capacitance $C^\infty = \varepsilon_\infty C_0$ in parallel to the previous series RC and reducing the series capacitance to $C_s^s - C^\infty = C^s - C^\infty = (\varepsilon_s - \varepsilon_\infty)C_0$. Here the admittance of the series part is

$$\frac{1}{R - \dfrac{i}{\omega(C^s - C^\infty)}} = \frac{i\omega(C^s - C^\infty)}{1 + i\omega R(C^s - C^\infty)}$$

For the whole arrangement

$$Y(\omega) = i\omega C^\infty + \frac{i\omega(C^s - C^\infty)}{1 + i\omega R(C^s - C^\infty)} = i\omega\left(C^\infty + \frac{(C^s - C^\infty)}{1 + i\omega R(C^s - C^\infty)}\right) = i\omega C^{tot}(\omega)$$

where $C^{tot}(\omega)$ is the total equivalent capacitance of the device and is given by,

$$C^{tot}(\omega) = C^\infty + \frac{(C^s - C^\infty)}{1 + i\omega R(C^s - C^\infty)} \tag{5.2.9}$$

with time constant $\tau_D = R(C^s - C^\infty) = \text{const.}$, from which we define the series resistance $R = \tau_D/(C^s - C^\infty)$. Now the Debye equation is easily derived from Eq. (5.2.9) by dividing by the capacitance, C_0, of the empty capacitor, giving

$$\varepsilon(\omega) = \frac{C^{tot}(\omega)}{C_0} = \frac{C^\infty}{C_0} + \frac{(C^s - C^\infty)}{(1 + i\omega R(C^s - C^\infty))C_0} \tag{5.2.10}$$

$$\varepsilon'(\omega) = \frac{C^\infty}{C_0} + \frac{(C^s - C^\infty)}{(1+\omega^2R^2(C^s - C^\infty)^2)C_0}, \qquad \varepsilon''(\omega) = \frac{\omega R(C^s - C^\infty)}{(1+\omega^2R^2(C^s - C^\infty)^2)C_0} \tag{5.2.11}$$

In this model the permittivity (total capacitance) is not zero at high frequencies (parallel $C^{\infty} = \varepsilon_{\infty} C_0$ prevents that), the time constant is suitable to represent the Debye relaxation time, none of the components are frequency dependent even when filled with dielectric material, ε'' is related to R (dissipative part) and ε' to the capacitance. Expression (5.2.9) giving $C^{tot}(\omega)$ is the Debye equation. Consider now an instant charge of the system with a step voltage at time t=0, the polarisation immediately jumps (due to the capacitance C^{∞}) to the value

$$P_{\infty} = \varepsilon_0(\varepsilon_{\infty} - 1)E \tag{5.2.12}$$

where E is the electrical field of the circuit. This is followed by a further increase of the polarization given by

$$P(t) = P_{\infty} + \varepsilon_0(\varepsilon_s - \varepsilon_{\infty})(1 - \exp(-t/\tau_D))E \tag{5.2.13}$$

For times greatly in excess of τ_D, P(t) is constant at a value $P_s(t) = \varepsilon_0(\varepsilon_s - \varepsilon_{\infty})E$. If discharge starts there is first an abrupt fall in P(t) from P_s to $P_s - P_{\infty}$, then the polarisation decays exponentially so that

$$P(t) = (P_s - P_{\infty})\exp(-t/\tau_D) \tag{5.2.14}$$

The presence of the capacitance C^{∞} allows for part of the polarisation to respond instantly to any changes in the applied field.

The above theory of equivalent circuits for dielectrics can easily be applied to the magnetic case by considering a constant amplitude current (equivalent to a constant magnetic field external excitation) feeding a RL combination (Fig. (5.1 d)) where the capacitors have been replaced by inductors, the parallel arrangement with series and the series with parallel. The permeability is related to the full inductance, L(ω), and the empty inductance, L_0 ,by

$$L(\omega) = \mu(\omega)L_0 = (\mu'(\omega) - i\mu''(\omega))L_0 \tag{5.2.15}$$

The impedance of the parallel part of the circuit of Fig. (5.1 d) is

$$\frac{1}{\frac{1}{R} + \frac{1}{i\omega(L^s - L^{\infty})}} = \frac{i\omega R(L^s - L^{\infty})}{R + i\omega(L^s - L^{\infty})} = \frac{i\omega(L^s - L^{\infty})}{1 + i\omega\frac{L^s - L^{\infty}}{R}}$$

and the total impedance

$$Z(\omega) = i\omega L^{\infty} + \frac{i\omega(L^{s} - L^{\infty})}{1 + i\omega\dfrac{L^{s} - L^{\infty}}{R}} = i\omega L^{tot}(\omega) \tag{5.2.16}$$

where

$$L^{tot}(\omega) = L^{\infty} + \frac{(L^{s} - L^{\infty})}{1 + i\omega\dfrac{L^{s} - L^{\infty}}{R}} \tag{5.2.17}$$

is the equivalent inductance of the whole device. By dividing by L_0 and setting $\tau_D = (L^s - L^\infty)/R$ as the time constant, we derive the Debye equation (1.4.49) for the magnetic case.

5.3 Equivalent electrical circuits for the Cole-Cole equation.

It is important now to find what is the equivalent to the Cole-Cole equation (1.4.52) for both the dielectric and magnetic case. We introduce the constant phase element (CPE) circuitry for the parallel case (Fig. (5.1 a)) which is when the combination of B_p and G_p gives a constant phase, ϕ_p^{CPE}, where

$$\phi_p^{CPE} = \tan^{-1}\left(\frac{B_p^{cpe}(\omega)}{G_p^{cpe}(\omega)}\right) \tag{5.3.1}$$

that is when the ratio in the brackets is constant. This may be realized when $B_p^{CPE}(\omega)$, $G_p^{CPE}(\omega)$ are frequency dependent in the same way, such that

$$G_p^{CPE}(\omega) = G^p_{\omega\tau=1}(\omega\tau_p)^{\alpha}, \qquad B_p^{CPE}(\omega) = B^p_{\omega\tau=1}(\omega\tau_p)^{\alpha}, \qquad 0 \le \alpha \le 1 \tag{5.3.2}$$

where τ_p is considered as a scale factor and $G^p_{\omega\tau=1}$ and $B^p_{\omega\tau=1}$ are constants. Thus the phase angle becomes constant with

$$\phi_p^{CPE} = \tan^{-1}\left(\frac{B^p_{\omega\tau=1}}{G^p_{\omega\tau=1}}\right) \tag{5.3.3}$$

The parallel admittance, of the RC combination, is given by

$$Y_p^{CPE}(\omega) = (\omega\tau_p)^{\alpha}(G^p_{\omega\tau=1} + iB^p_{\omega\tau=1}) = (\omega\tau_p)^{\alpha}\left(\frac{1}{R^p_{\omega\tau=1}} + i\omega C^p_{\omega\tau=1}\right) \tag{5.3.4}$$

with an equivalent capacitance of $C_p^{CPE} = C^p_{\omega\tau=1}(\omega\tau_p)^{\alpha-1}$ decreasing with increasing frequency (important since C_p is proportional to ε', see Eq. (5.2.2)). We may now correlate the exponent α with the phase: $\phi_p^{CPE} = \alpha\pi/2$. It is possible to write the admittance in terms of $G^p_{\omega\tau=1}$ [5]

$$Y_p^{CPE}(\omega) = G^p_{\omega\tau=1}(i\omega\tau_p)^{\alpha} = G^p_{\omega\tau=1}(\omega\tau_p)^{\alpha}(\cos(\alpha\pi/2) + i\sin(\alpha\pi/2)) \qquad (5.3.5)$$

since $i^{\alpha} = \cos(\alpha\pi/2) + i\sin(\alpha\pi/2)$. For $\alpha = 1$ we get $\phi_p^{CPE} = \pi/2$, $Y_p^{CPE} = i\omega\tau_p G^p_{\omega\tau=1}$ (ideal capacitor with capacitance $\tau_p G^p_{\omega\tau=1}$) and for $\alpha = 0$ we get $\phi_p^{CPE} = 0$, $Y_p^{CPE} = G^p_{\omega\tau=1}$ (ideal conductance). The corresponding impedance will be

$$Z_p^{CPE}(\omega) = \frac{1}{Y_p^{CPE}(\omega)} = \frac{R^p_{\omega\tau=1}}{(i\omega\tau_p)^{\alpha}} = \frac{R^p_{\omega\tau=1}}{(\omega\tau_p)^{\alpha}}(\cos(\alpha\pi/2) - i\sin(\alpha\pi/2)) \qquad (5.3.6)$$

The factor $(\omega\tau)^{\alpha}$ implies Cole-Cole behavior. The impedance, series version, is calculated similarly (for phase not correlated to α) as,

$$Z_s^{CPE}(\omega) = \frac{1}{(\omega\tau_s)^{\alpha}}(R^s_{\omega\tau=1} + iX^s_{\omega\tau=1}) = \frac{1}{(\omega\tau_s)^{\alpha}}(R^s_{\omega\tau=1} + i\frac{1}{\omega C^s_{\omega\tau=1}}) \qquad (5.3.7)$$

with equivalent capacitance $C_s^{CPE}(\omega) = C^s_{\omega\tau=1}(\omega\tau_s)^{\alpha-1}$ and phase of

$$\phi_s^{CPE} = \tan^{-1}\left(\frac{X^s_{\omega\tau=1}}{R^s_{\omega\tau=1}}\right) \qquad (5.3.8)$$

The choice between parallel and series representation is not important for a constant phase element, since both explain the behaviour of the material equally well.

In order to see what needs to be altered in the arrangement of Fig. (5.1 c) which describes the Debye process, so to allow one to use the Cole-Cole model, it is necessary to work backwards. The equivalent of Eq. (5.2.9) for the Cole-Cole case is

$$C^{tot}(\omega) = C^{\infty} + \frac{(C^s - C^{\infty})}{1 + (i\omega R(C^s - C^{\infty}))^{1-\alpha}} \qquad (5.3.9)$$

or, remembering that $i^{1-\alpha} = i(\cos(\alpha\pi/2) - i\sin(\alpha\pi/2))$,

$$C^{tot}(\omega) = C^{\infty} + \frac{(C^s - C^{\infty})}{1 + i(\omega R(C^s - C^{\infty}))^{1-\alpha}(\cos(\alpha\pi/2) - i\sin(\alpha\pi/2))} \qquad (5.3.10)$$

corresponding to an admittance of

$$Y(\omega) = i\omega C^{tot}(\omega) = i\omega C^{\infty} + \frac{i\omega(C^{s} - C^{\infty})}{1 + i(\omega R(C^{s} - C^{\infty}))^{1-\alpha}(\cos(\alpha\pi/2) - i\sin(\alpha\pi/2))} \tag{5.3.11}$$

The impedance of the series RC part would be the inverse of the second term of the right side of Eq. (5.3.11) leading us to

$$\frac{1 + i(\omega R(C^{s} - C^{\infty}))^{1-\alpha}(\cos(\alpha\pi/2) - i\sin(\alpha\pi/2))}{i\omega(C^{s} - C^{\infty})} =$$

$$= \frac{1}{i\omega(C^{s} - C^{\infty})} + R^{1-\alpha}\omega^{-\alpha}(C^{s} - C^{\infty})^{-\alpha}(\cos(\alpha\pi/2) - i\sin(\alpha\pi/2)) \tag{5.3.12}$$

The second term of Eq.(5.3.12) is the impedance of the element which is necessary to connect in series with the capacitor $(C^{s} - C^{\infty})$ in the circuit of Fig. (5.1 c) by replacing the resistor R. This is a constant phase element with required impedance of

$$Z^{CPE}(\omega) = \frac{R}{\omega^{\alpha} R^{\alpha}(C^{s} - C^{\infty})^{\alpha}}(\cos(\alpha\pi/2) - i\sin(\alpha\pi/2))$$

$$= \frac{R(\cos(\alpha\pi/2) - i\sin(\alpha\pi/2))}{\omega^{\alpha}\tau_{D}^{\alpha}} \tag{5.3.13}$$

time constant $\tau_{D} = R(C^{s} - C^{\infty})$ and capacitance

$$C^{CPE}(\omega) = \frac{(C^{s} - C^{\infty})}{\omega^{1-\alpha} R^{1-\alpha}\sin(\alpha\pi/2)} = \frac{\tau_{D}^{\alpha}}{\omega^{1-\alpha} R\sin(\alpha\pi/2)} \tag{5.3.14}$$

which is derived by equating Eq. (5.3.13) to an equivalent capacitance. The nature of the circuitry for the CPE is found by comparing its impedance Eq. (5.3.13) with the impedances of the CPEs described above. It is obvious that Eq. (5.3.13) is identical to Eq. (5.3.6), hence the CPE consists of a parallel capacitor and resistor.

For the magnetic case, since the Debye equivalent is a parallel inductance $L^{s} - L^{\infty}$ with a resistor $(L^{s} - L^{\infty})/\tau_{D}$ in series with an inductor L^{∞}, a constant phase element will replace the resistor (inductors remain as they are). This constant phase element will consist of an inductor and resistor in series thereby verifying the constraint for constant phase Eqs. (5.3.2), (5.3.3). Working as before by multiplying the Debye equation for permeability with L_{0} and equating to the equivalent total inductance, one gets,

$$Z(\omega) = i\omega L^{tot}(\omega) = i\omega \left(\frac{(L^s - L^\infty)}{1 + \left(i\omega \frac{L^s - L^\infty}{R} \right)^{1-\alpha}} + L^\infty \right) \tag{5.3.15}$$

The term $i\omega L^\infty$ is the series impedance of L^∞, so the remainder is the impedance of the CPE with the inductor $(L^s - L^\infty)$. The total admittance of the parallel part is then,

$$Y(\omega) = \frac{1 + \left(i\omega \frac{L^s - L^\infty}{R} \right)^{1-\alpha}}{i\omega(L^s - L^\infty)} = \frac{1}{i\omega(L^s - L^\infty)} + \frac{\left(\frac{L^s - L^\infty}{R} \right)^{1-\alpha}}{(i\omega)^\alpha (L^s - L^\infty)} \tag{5.3.16}$$

The first term of Eq.(5.3.16) is the admittance of the $(L^s - L^\infty)$ inductor and the second the admittance of the CPE which is finally written as

$$Y^{CPE}(\omega) = \frac{1}{\omega^\alpha R \left(\frac{L^s - L^\infty}{R} \right)^\alpha (\cos(\alpha\pi/2) - i\sin(\alpha\pi/2))}$$

$$= \frac{1}{\omega^\alpha \tau_D^\alpha R(\cos(\alpha\pi/2) - i\sin(\alpha\pi/2))} \tag{5.3.17}$$

and thus the impedance

$$Z^{CPE}(\omega) = \frac{1}{Y^{CPE}(\omega)} = \omega^\alpha \tau_D^\alpha R(\cos(\alpha\pi/2) - i\sin(\alpha\pi/2)) \tag{5.3.18}$$

This is a CPE with series inductor and resistor R.

Concluding, the equivalent circuits proposed in the latter two sections simulate the two important relaxation expressions, i.e. the Debye model, Eqs. (5.2.9), (5.2.17), and the Cole-Cole model, Eqs. (5.3.9), for both dielectric and magnetic case. The Debye equation is described with the circuit of (Figs. 5.1 (c, d)) for the dielectric and magnetic cases respectively. The Cole equation is the same circuit gained by (a) replacing the resistance with a constant phase element with impedance described by Eq. (5.3.6) for the dielectric case and (5.3.18) for the magnetic case, and (b) under the constraint for the phase as described in Eqs. (5.3.2), (5.3.3).

5.4 Equivalent electrical circuits for the Landau-Lifshitz equation.

It is possible, as in the case of the Debye and Cole-Cole equations, to describe the Landau-Lifshitz equation (1.5.39) by means of an equivalent electrical circuit. The complexity of Coffey's equation (1.5.43) prohibits this, so we direct our attention to model the Landau-Lifshitz equation which is, as is stated before, the limit of Coffey's equation for large σ. Macdonald and Brachman [3] proposed the circuitry shown in Fig. (5.2 a) for the dielectric resonance absorption described by the Van Vleck and Weisskopf [4] equation

$$\varepsilon(\omega) = \varepsilon_\infty + (\varepsilon_s - \varepsilon_\infty)\frac{1+\omega_{pre}^2\tau_0^2 + i\omega\tau_0}{1+\omega_{pre}^2\tau_0^2 - \omega^2\tau_0^2 + i2\omega\tau_0} \tag{5.4.1}$$

which is of the same form as the Landau-Lifshitz equation for magnetism. To describe the resonance it is essential to include capacitor and inductor components in the same circuit. To express the Landau-Lifshitz equation for permeability we simply replace capacitors with inductors and parallel circuitries with series and vice versa. The electrical model, which is proposed by Scaife [6], is that of Fig. (5.2 b). In this figure μ_∞, which is the equivalent to ε_∞, is omitted since it is not considered in the Landau-Lifshitz equation (1.5.39).

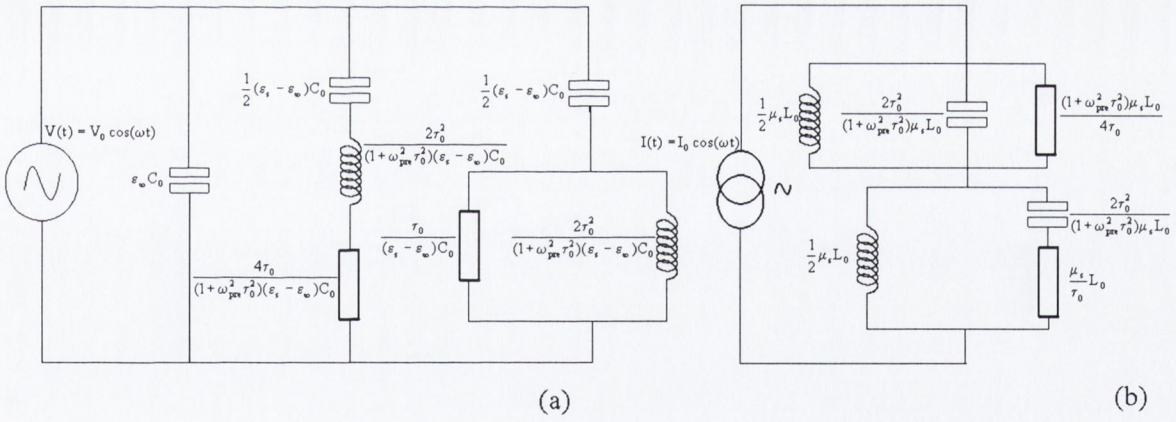

Figure 5.2 (a) Shows the equivalent electrical circuit proposed by Macdonald and Brachman, which can sufficiently describe the Van Vleck and Weisskopf equation (5.4.1) for dielectric resonance, (b) Shows the equivalent circuit which describes the Landau-Lifshitz equation (1.5.39) for ferromagnetic resonance.

5.5 Application 1: Permittivity measurement of ferrofluids.

The equivalent electric circuits, as presented in the previous sections, for both the magnetic and dielectric case assist us greatly in the study and modelling of ferrofluids. The

magnetic properties have been studied extensively in Chapters 3 and 4. In this section we will present examples of permittivity measurements for some magnetic fluids, in which the relaxation absorption is prominent. Resonant absorption in dielectrics occurs beyond the frequency range of the network technique, thus it is not included in our studies. Hence we will concentrate our attention on the relaxation absorption in ferrofluids, which can be measured in the GHz frequency range.

Since ferrofluids are colloidal suspensions of ferroparticles dispersed in a carrier liquid and coated by an organic surfactant, the three components, namely the carrier liquid, the surfactant and the particle material, contribute to the permittivity, ε, of the colloid. In general the contribution of the free surfactant in the polarizability of a ferrofluid is much larger than the polarizability of the ferroparticles themselves. Thus, hereafter, we will consider the free surfactant as the only composite which, together with the carrier, affects the overall permittivity.

We compare the relative permittivity of pure isoparaffin liquid, shown in Fig. (2.6 a), which has a value of 2.3, and the permittivity of an isoparaffin-based ferrofluid, such as the one shown in Fig. (2.8) which has a value of 4.25 between 1 MHz-10 MHz. The difference in the value of ε, of the two cases, is due to the influence of the polar molecules consisting of (a) the carrier liquid and of (b) the free surfactant in the solution (the free surfactant in the solution usually arises from incomplete coverage of the ferroparticles during the preparation process and usually exists in a majority of ferrofluids).

The difference in ε between pure isoparaffin and the isoparaffin-based ferrofluid shows that the surfactant contributes significantly to the effective permittivity of the solution. The opposite happens with aqueous solutions. There the polarizability, in the diluted solutions, is mostly due to the water molecules (relative permittivity for water is approximately 80) rather than the surfactant and ferroparticles.

The surfactant, in the majority of ferrofluids, is a straight-chained aliphatic organic compound namely cis-9-octadecanoic acid ($C_{17}H_{33}COOH$) or commonly known as oleic acid*. Although this fatty acid is insoluble in water and in paraffin, it is very soluble in ethanol and other organic solvents. The chemical structure of the oleic acid is shown in Fig.

* Oleic acid is manufactured from olive oil and can be found in candles, oilsolive, almond and liver. It is a clear, colorless liquid with a molecular weight of 282.52, a melting point of 16.3 ^{o}C and a boiling point of 286 ^{o}C.

(5.3 a-b). Its polarity is small and this is explained by the small electronegativity of the C-H bonds and from its structural geometry**. The small polarity explains the low value of the permittivity of isoparaffin ($\cong 2.5$).

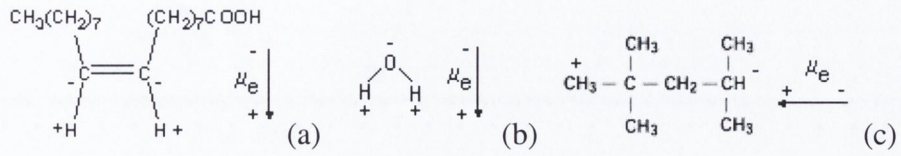

Figure 5.3 (a) The chemical structure of the oleic acid (cis-9-octadecanoic acid, $C_{17}H_{33}COOH$). Note that the double bond is *cis* (H atoms on the same side of the double bond) which is the common natural configuration. μ_e of the Oleic Acid is relatively small because of the small electronegativity of the C-H bond, thus its polarity is small, which explains its low permittivity ($\cong 2.5$), (b) The chemical structure of the water molecule. μ_e of water is large due to the high electronegativity of the H-O bond. This explains its high polarity and permittivity ($\cong 80$), (c) The chemical structure of the isoparaffin (2,2,4-trimethylpentane, C_8H_{18}). The geometry of this type of isoparaffin is responsible for the appearance of μ_e. The permittivity of this molecule ($\cong 2.2$) is comparable to oleic acid's since its polarity arises from the same type of bond (C-H).

Water (H_2O), which is the most commonly used carrier liquids in ferrofluids, is a polar dielectric (Fig. (5.3 c)), the large polarity of which is explained by the large electronegativity of the O-H bond and the angle between H-O-H. Its large polarity gives rise to its high permittivity ($\cong 80$).

The other commonly used carrier, in ferrofluid manufacture, is the isoparaffin 2,2,4-Trimethylpentane (C_8H_{18}), the molecular structure of which is shown in Fig. (5.3 d). This arrangement gives rise to paraffin's electric dipolar moment, μ_e. Due to the weak electronegativity of the C-H bonds its permittivity is low ($\cong 2.2$).

As we do not know the amount of surfactant in a ferrofluid, we cannot accurately assess the precise individual contribution of the magnetite particles and surfactant to the overall permittivity. However, an approximate quantitative estimation of the contribution of the surfactant in the polar solution may be obtained by considering the dielectric as an equivalent circuit with two capacitors in series. We denote the equivalent capacitance of the carrier by C_1 and the equivalent capacitance of the particles and the oleic acid together by C_2, thus

** In chemistry, the molecule's structural geometry is explained by the *valence-shell electron-pair repulsion* theory, or commonly known as VSEPR.

Figure 5.4

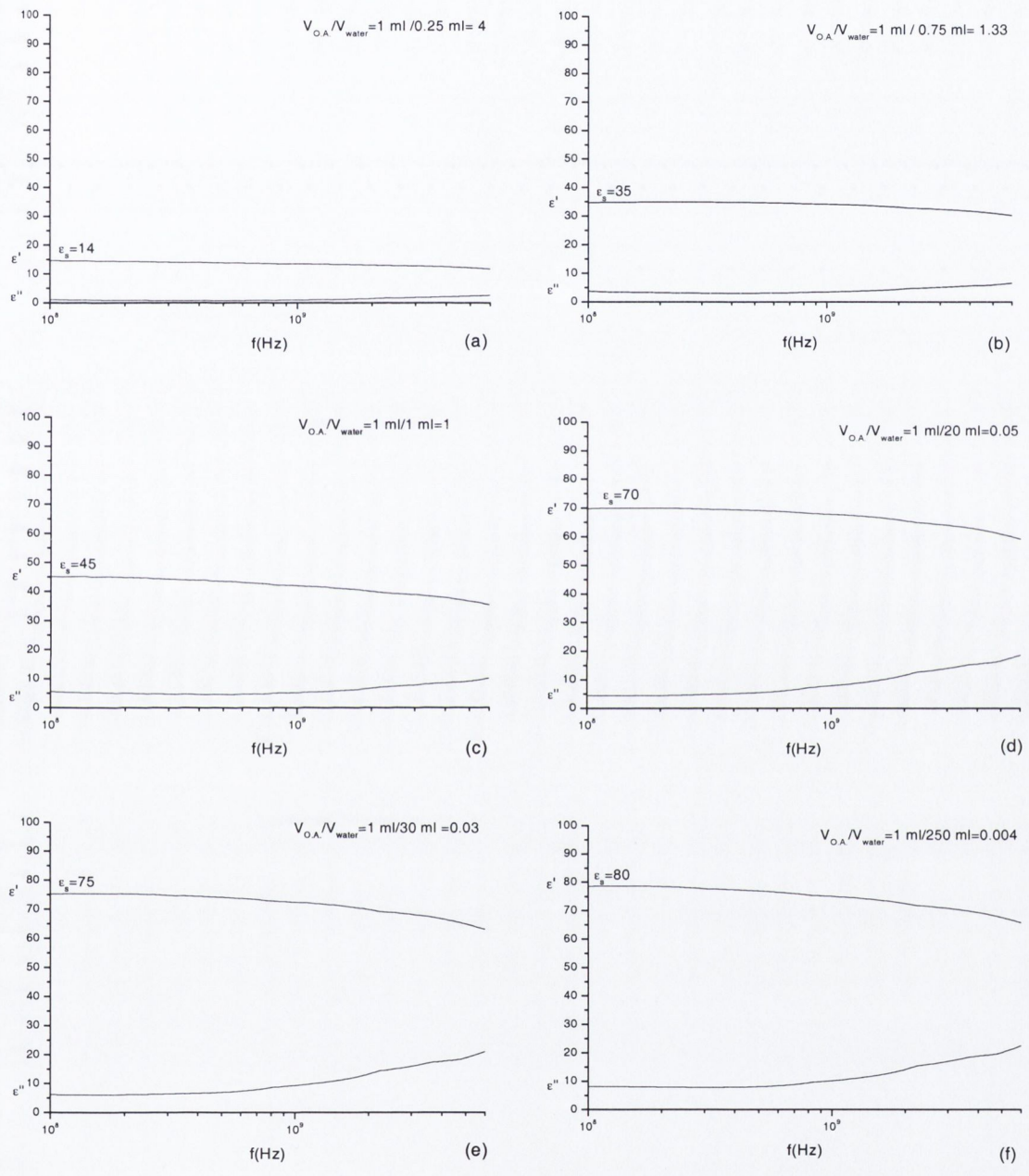

Figure 5.4 Permittivity of diluted oleic acid in a water solution, for several values of the ratio of the fractional volume $V_{O.A.}/V_{water}$: (a) 4, (b) 1.33, (c) 1, (d) 0.05, (e) 0.03, (f) 0.004.

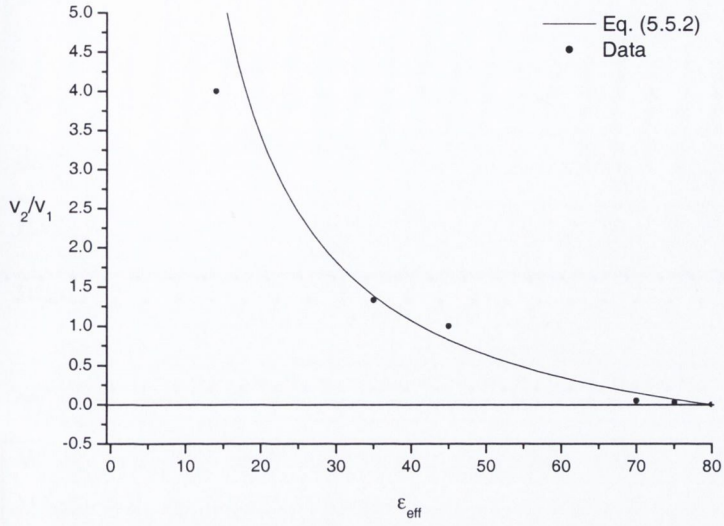

Figure 5.5 Plot of Eq. (5.5.2) (solid line) normalised to the data (dots), for the values of the ratio v_2 / v_1 reported in the Table (5.1), against ε_{eff}. In Eq. (5.5.2) ε_1=80 (water) and ε_2=2.5 (isoparaffin) were read.

$$\frac{1}{C_{eff}(\omega)} = \frac{1}{C_1(\omega)} + \frac{1}{C_2(\omega)} \Rightarrow \frac{l_1 + l_2}{\varepsilon_0 \varepsilon_{eff}(\omega) A_p} = \frac{l_1}{\varepsilon_0 \varepsilon_1(\omega) A_p} + \frac{l_2}{\varepsilon_0 \varepsilon_2(\omega) A_p}$$

$$\Rightarrow \frac{(v_1 + v_2)}{\varepsilon_{eff}(\omega)} = \frac{v_1}{\varepsilon_1(\omega)} + \frac{v_2}{\varepsilon_2(\omega)} \qquad (5.5.1)$$

where $v_1 = l_1 A_p$, $v_2 = l_2 A_p$ are the fractional volumes of the carrier liquid and the free surfactant respectively. ε_{eff} is the overall (effective) real permittivity of the ferrofluid and ε_1, ε_2 are the carrier and surfactant actual permittivities. The same equation, got from another approach, is given in [1].

To verify the validity of the equivalent circuit we do a simple experiment in which we dilute isoparaffin (surfactant) into water (carrier) for several volume ratios of the surfactant volume to the water volume (v_2 / v_1) as is described in Table 5.1. The measured permittivity is shown in Fig. (5.4 a-f). The region of interest is that in which the permittivity curve appears constant. This is below 100 MHz. The value of the permittivity at 100 MHz approximates its static, ε_s, value. In the same table we record the measured ε_{eff} (at 100 MHz) from Fig. (5.4).

We may solve Eq. (5.5.1) for v_2 / v_1. It gives

$$\frac{v_2}{v_1} = \frac{\varepsilon_2(\varepsilon_1 - \varepsilon_{eff})}{\varepsilon_1(\varepsilon_{eff} - \varepsilon_2)} = \text{const}\frac{(\varepsilon_1 - \varepsilon_{eff})}{(\varepsilon_{eff} - \varepsilon_2)} \qquad (5.5.2)$$

The latter expression for the volume ratio is to be plotted as a function of ε_{eff}, and to be compared with the measured ε_{eff} from Table (5.1). Figure (5.5) shows a normalized plot of Eq. (5.5.2) and the ε_{eff} data from Table (5.1) and it is seems to vary in the same way as a function of ε_{eff}.

Table 5.1 Dilution of isoparaffin in water for various volume ratios.

Water's fractional volume v_1 (ml)	Isoparafin's fractional volume v_2 (ml)	Fractional volume ratio v_2 / v_1	Overall permittivity ε_{eff} measured at (100 MHz) $\cong \varepsilon_s$
0.25	1	4	14
0.75	1	1.33	35
1	1	1	45
20	1	0.05	70
30	1	0.03	75
250	1	0.004	80

5.6 Application 2: Estimation of the conductivity of a ferrofluid.

The conductivity, σ, can be calculated from the permittivity and can be expressed by the Debye relaxation time, τ_D. The conductivity is frequency dependent and is defined by

$$\sigma(\omega) = \omega\varepsilon''(\omega)\varepsilon_0 \qquad (5.6.1)$$

By substituting ε from Eq. (1.4.38) and assuming that ε_∞, which is the permittivity at frequencies well below the optical dispersion region, is negligible the latter expression for σ takes the form

$$\sigma(\omega) = \frac{\omega^2\tau_D\varepsilon_0\varepsilon_s}{1+\omega^2\tau_D^2} \qquad (5.6.2)$$

A normalised theoretical plot of Eq. (5.6.2), for a dielectric material described by the Debye equation, is shown in the following Fig. (5.6). In this figure, the Debye equation is drawn with a solid line, while σ is shown by dotted lines.

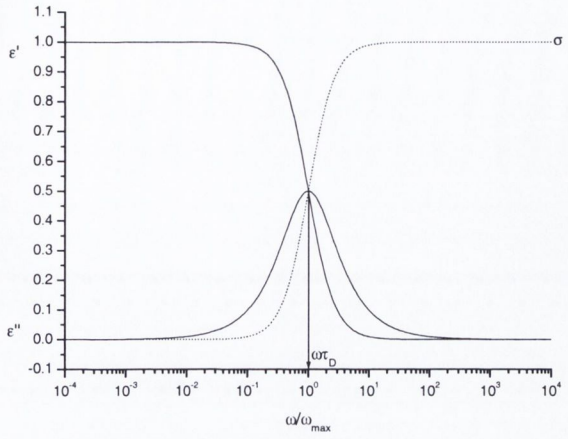

Figure 5.6 A normalised Debye plot for ε (solid line) and a normalised conductivity plot (dashed line).

We are able now to calculate σ from ε″ data by importing the data into a computer program. For example the conductivity of the ferrofluid, the permittivity of which is shown in Fig. (2.8) for the wideband frequency range 1MHz-6GHz, is plotted in the following Fig. (5.7).

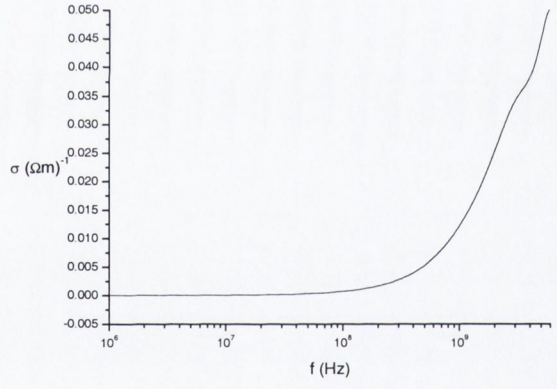

Figure 5.7 The conductivity of the 525 G magnetite in isoparaffin, the permittivity of which is presented in Fig. (2.8). The conductivity, here, has been calculated from the permittivity data by use of Eq. (5.6.1).

The above graph represents a typical conductivity curve for those materials which are subject to Debye dispersion. The critical range is between 100 MHz to 6GHz where σ makes a huge increase. This corresponds approximately to the region $0.1 \leq \omega\tau_D \leq 1$ of the theoretical plot (see Fig. (5.6)) where the most prominent increase of σ takes place. This is the frequency interval which interests us.

In the following the dielectric permittivity of two magnetic fluids consisting of suspensions of magnetite in isoparaffin of magnetisation 760 G (0.076 T) and 327 G (0.0327 T) is measured between 100 MHz-6 GHz. The first liquid has 2.3 times larger magnetization

and thus 2.3 times bigger concentration. In Figs. (5.8) and (5.9) we show the data for ε and σ. As expected, the sample with the largest packing fraction and hence the larger component of magnetite (and surfactant) has the largest value of overall permittivity.

Figure 5.8

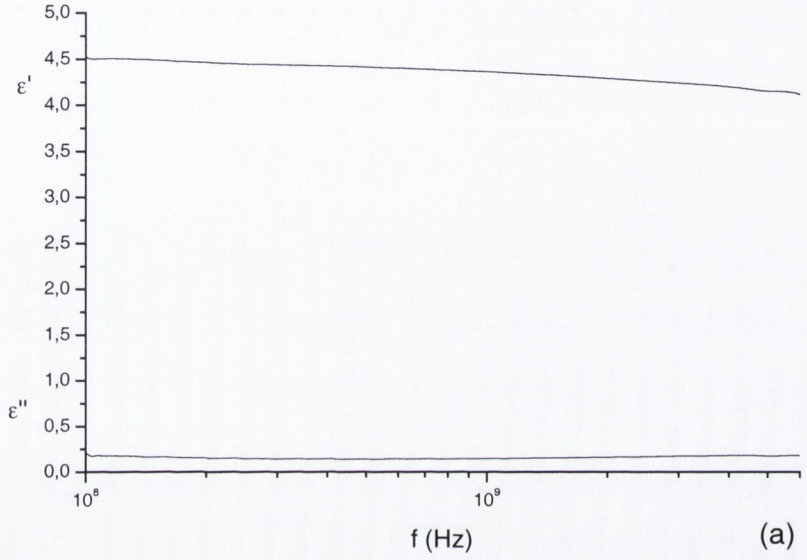

Figure 5.8 (a) Permittivity of a magnetite in isoparaffin ferrofluid (760 G).

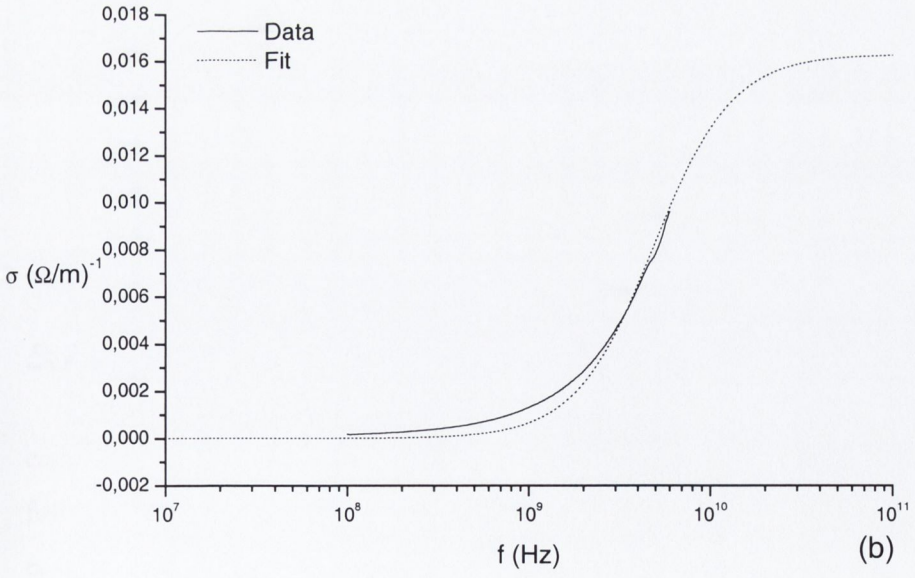

Figure 5.8 (b) the corresponding conductivity (solid line) and fit (dotted line). The fit is obtained by use of Eq. (5.6.2), where $\tau_D = 4.36 \times 10^{-11}$ s.

Figure 5.9

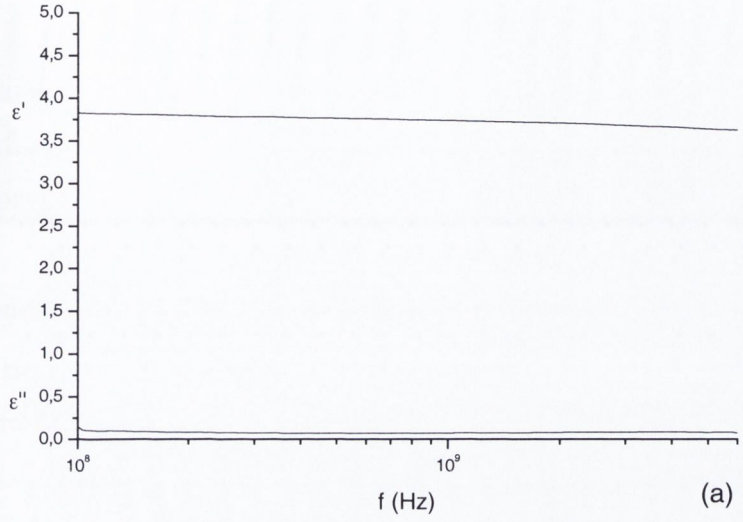

Figure 5.9 (a) Permittivity of a magnetite in isoparaffin ferrofluid (327 G),

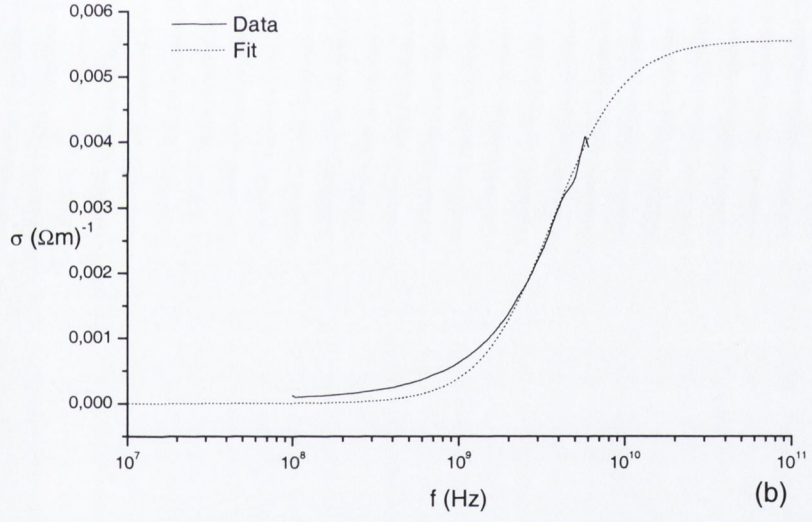

Figure 5.9 (b) the corresponding conductivity (solid line) and fit (dotted line). The fit is obtained by use of Eq.(5.6.2).

5.7 Conclusions

Equivalent electrical circuits may be used to describe the Debye and Landau-Lifshitz equations and to aid the researcher with a more familiar representation. The Debye equation for permeability is represented by the circuit of Fig.(5.1 d). The equivalent Cole-Cole equation is signified by replacing the parallel circuitry of Fig.(5.1 d), with a constant phase element the impedance of which is described by Eq.(5.3.18). The Landau-Lifshitz equation is

represented by the electrical circuit of Fig.(5.2 b). Coffey's equation (1.5.43) is very complex and there is no equivalent circuit representation.

By using a combination of two capacitors in series we are able to explain the components of the permittivity of a ferrofluid. Since a ferrofluid consists of carrier and surfactant, it is of interest to estimate their volume ratio in the liquid. Equation (5.5.2) is appropriate.

Another application involves the estimation of conductivity from permittivity data. Conductivity is defined by Eq. (5.6.1) and can be expressed in terms of the Debye time, τ_D, as Eq. (5.6.2) states. A typical conductivity plot is shown in Fig. (5.6) and some examples of ferrofluid's conductivity are given in Figs. (5.8) and (5.9).

References:

1. Scaife B.K.P., *Principles of Dielectrics*, Oxford Publications, (1998).
2. Cole K.S., Cole R.J., *Journal of Chemical Physics* , **9**, 341, (1941).
3. Macdonald J.R., Brachman M.K., *Reviews of Modern Physics*, **28**, 393, (1956).
4. Van Vleck J.H., Weisskopf V.F., *Reviews of Modern Physics*, **17**, 227, (1945).
5. Grimnes S., Martinsen Ø.G., *Bioimpedance and Bioelectricity Basics*, Academic Press, (2000).
6. Scaife B.K.P., Private communication, (2003).

Appendix A

Calculation of the magnetic susceptibility using the toroidal technique, and estimation of the susceptibility and permittivity using the transmission line technique.

A.1 Introduction

In this appendix we present a detailed calculation of the susceptibility and permittivity in terms of impedances, which are measured by means of the following techniques:

(a) The toroid coil technique, in which a relation of the permeability is derived in terms of the geometrical characteristic of the toroid and the impedance which is measured with the toroid's slit full and empty ($R_{cut}^{full}, X_{cut}^{full}, R_{cut}^{empty}, X_{cut}^{empty}$). [1]

(b) The transmission line technique [2,3], in which permeability and permittivity can be calculated individually or to be correlated in one relation. The latter gives results which are almost independent of the wavelength restriction.

A.2 Calculation of susceptibility by means of the toroidal technique.

To measure the permeability, μ, of a ferrofluid with the toroidal technique, it is necessary to perform two impedance measurements: one with the slit of the toroid empty and one with the slit of full. In this section a calculation of μ is derived in terms of impedance measurements (empty and full) and the geometrical characteristic of the toroid. In the toroid coil of Fig. (2.4) the slit's length, L_1, is small in comparison to the remaining length, L_2, of the circumference ($\gamma_g = L_1 / L_2 << 1$). If the toroid has N_t turns and I(t) is the alternating current conducting through the winding, the current produces a magnetic force, H, of

$$H = \frac{N_t I(t)}{L_1 + L_2} \qquad (A.2.1)$$

in A/m units. If Φ_B is the flux (in webers) and A_{cs} is the cross-sectional area of the toroid, then

$$\Phi_B = B_{toroid} A_{cs} = B_{gap} A_{cs} = \mu_0 H_{gap} A_{cs} \tag{A.2.2}$$

since the flux is the same throughout the core.

Hence

$$B_{toroid} = \mu_t \mu_0 H_{toroid} = \mu_0 H_{gap} \tag{A.2.3}$$

where μ_t is the relative permeability of the toroidal core. $H(L_1 + L_2) = N_t I$ (ampere-turns) is always the same across the core and the slit. Therefore we may write,

$$H(L_1 + L_2) = N_t I = H_{gap} L_1 + H_{toroid} L_2 = H_{gap} (L_1 + L_2 / \mu_t) \tag{A.2.4}$$

The effective (equivalent) flux density across the toroid is calculated by combining Eqs. (A.2.2), (A.2.4), thus

$$B_{eff} = \frac{\Phi_B}{A_{cs}} = \mu_{eff} \mu_0 \frac{N_t I(t)}{L_1 + L_2} = \mu_0 \frac{N_t I(t)}{(L_1 + L_2 / \mu)} \tag{A.2.5}$$

Consequently the effective relative permeability is equal to,

$$\mu_{eff} = \frac{1 + (L_1 / L_2)}{1/\mu_t + (L_1 / L_2)} \tag{A.2.6}$$

Since $L_1 / L_2 << 1$ the latter equation is simplified to,

$$\mu_{eff} = \frac{1}{1/\mu_t + (L_1 / L_2)} = \frac{\mu_t}{1 + \mu_t (L_1 / L_2)} \tag{A.2.7}$$

Let L_{nocore} be the inductance of the excitation winding without any material in the toroid, that is, the inductance of N_t turns uniformly around the periphery of the toroid, then

$$L_{nocore} = \frac{\mu_0 N_t^2 A_{cs}}{L_1 + L_2} \cong \frac{\mu_0 N_t^2 A_{cs}}{L_2} \tag{A.2.8}$$

Let L_{nocut} be the inductance of the toroid without a cut, then

$$L_{nocut} = \frac{\mu_0 \mu_t N_t^2 A_{cs}}{L_1 + L_2} \cong \frac{\mu_0 \mu_t N_t^2 A_{cs}}{L_2} \tag{A.2.9}$$

If L_{cut}^{empty} denotes the inductance of the toroid with an empty cut, and by using Eqs. (A.2.7), (A.2.9),

$$L_{cut}^{empty} = \frac{\mu_0 \mu_{eff} N_t^2 A_{cs}}{L_1 + L_2} \cong \frac{\mu_0 \mu_t N_t^2 A_{cs}}{(1 + \mu_t L_1 / L_2)(L_1 + L_2)} = \frac{L_{nocut}}{1 + \mu_t L_1 / L_2} \tag{A.2.10}$$

So, from Eq. (A.2.8),

$$L_{cut}^{empty} = \frac{L_{nocore}}{1/\mu_t + L_1/L_2} \tag{A.2.11}$$

Thus, the impedance of the coil on the core with a cut is

$$Z_{cut}^{empty} = R_w + i\omega L_{cut}^{empty} = R_w + \frac{i\omega L_{nocore}}{\left(\frac{1}{\mu_t' - i\mu_t'} + \frac{L_1}{L_2}\right)} \tag{A.2.12}$$

where R_w is the dc resistance of the wire. The latter equation is written in a compact format, as

$$Z_{cut}^{empty} = R_w + \frac{i\omega L_{nocore}(\mu_t' - i\mu_t')}{1 + \gamma_g(\mu_t' - i\mu_t')} \tag{A.2.13}$$

($\gamma_g = L_1/L_2 << 1$). Insertion of a ferrofluid of relative permeability μ into the gap gives

$$L_{cut}^{full} = \frac{\mu_0 N_t^2 A_{cs}}{\frac{L_1}{\mu} + \frac{L_2}{\mu_t}} = \frac{\mu_0 N_t^2 A_{cs}}{\frac{L_2}{\mu_t}\left(1 + \gamma_g \frac{\mu_t}{\mu}\right)} = \frac{\mu_0 N_t^2 A_{cs}}{\frac{L_2}{\mu_t}\left(1 + \gamma_g \frac{\mu_t' - i\mu_t''}{\mu' - i\mu''}\right)} = \frac{L_{nocore}(\mu_t' - i\mu_t'')}{1 + \gamma_g \frac{\mu_t' - i\mu_t''}{\mu' - i\mu''}} \tag{A.2.14}$$

The impedance corresponding to the toroid with filled slit is, equivalently, given by

$$Z_{cut}^{full} = R_w + i\omega L_{cut}^{full} = R_w + \frac{i\omega L_{nocore}(\mu_t' - i\mu_t'')}{1 + \gamma_g \frac{\mu_t' - i\mu_t''}{\mu' - i\mu''}} \tag{A.2.15}$$

From Eq. (A.2.13)

$$Z_{cut}^{empty} - R_w = \frac{i\omega L_{nocore}(\mu_t' - i\mu_t'')}{1 + \gamma_g(\mu_t' - i\mu_t'')} \tag{A.2.16}$$

Form Eq.(A.2.15)

$$Z_{cut}^{full} - R_w = \frac{i\omega L_{nocore}(\mu_t' - i\mu'')}{1 + \gamma_g \frac{\mu_t' - i\mu_t''}{\mu' - i\mu''}} \tag{A.2.17}$$

By dividing and calling $Z_r = \left(\frac{Z_{cut}^{full} - R_w}{Z_{cut}^{empty} - R_w}\right)^{-1}$ we obtain

$$\frac{(\mu' - i\mu'') + \gamma_g(\mu_t' - i\mu_t'')}{\mu' - i\mu''} = Z_r[1 + \gamma_g(\mu_t' - i\mu_t'')] \tag{A.2.18}$$

Solving for $\mu' - i\mu''$ we obtain

$$\mu' - i\mu'' = \frac{-\gamma_g(\mu_t' - i\mu_t'')}{1 - Z_r[1 + \gamma_g(\mu_t' - i\mu_t'')]} \tag{A.2.19}$$

From Eq. (A.2.13) by solving for $\mu_t' - i\mu_t''$ we get

$$\mu_t' - i\mu_t'' = \frac{Z_{cut}^{empty} - R_w}{i\omega L_{nocore} + \gamma_g R_w - \gamma_g Z_{cut}^{empty}} \tag{A.2.20}$$

Consequently

$$\mu' - i\mu'' = \frac{-\gamma_g\left(\dfrac{Z_{cut}^{empty} - R_w}{i\omega L_{nocore} + \gamma_g R_w - \gamma_g Z_{cut}^{empty}}\right)}{1 - Z_r\left[1 + \gamma_g\left(\dfrac{Z_{cut}^{empty} - R_w}{i\omega L_{nocore} + \gamma_g R_w - \gamma_g Z_{cut}^{empty}}\right)\right]} =$$

$$= \frac{-\gamma_g(Z_{cut}^{empty} - R_w)}{i\omega L_{nocore} + \gamma_g R_w - \gamma_g Z_{cut}^{empty} - Z_r i\omega L_{nocore}} \tag{A.2.21}$$

Substituting for Z_r yields

$$\mu' - i\mu'' = \frac{-\gamma_g(Z_{cut}^{empty} - R_w)(Z_{cut}^{full} - R_w)}{(Z_{cut}^{full} - R_w)(i\omega L_{nocore} + \gamma_g R_w - \gamma_g Z_{cut}^{empty}) - (Z_{cut}^{empty} - R_w)i\omega L_{nocore}} \tag{A.2.22}$$

Considering the denominator of the latter equation:

$$(Z_{cut}^{full} - R_w)(i\omega L_{nocore} + \gamma_g R_w - \gamma_g Z_{cut}^{empty}) - (Z_{cut}^{empty} - R_w)Z_r i\omega L_{nocore}$$

$$= (R_{cut}^{full} - R_w - iX_{cut}^{full})(i\omega L_{nocore} + \gamma_g R_w - \gamma_g R_{cut}^{empty} - i\gamma_g X_{cut}^{empty}) - (R_{cut}^{empty} - R_w - iX_{cut}^{empty})i\omega L_{nocore} \tag{A.2.23}$$

The real part of the latter equation is equal to

$$-\omega L_{nocore} X_{cut}^{full} + \gamma_g R_w R_{cut}^{full} - \gamma_g R_w^2 - \gamma_g R_{cut}^{empty} R_{cut}^{full} + \gamma_g R_w R_{cut}^{empty} + \gamma_g X_{cut}^{empty} X_{cut}^{full} + \omega L_{nocore} X_{cut}^{empty} \tag{A.2.24}$$

and the imaginary part is equal to

$$i\gamma_g R_w X_{cut}^{full} - i\gamma_g R_{cut}^{empty} X_{cut}^{full} - i\gamma_g R_{cut}^{full} X_{cut}^{empty} + i\gamma_g R_w X_{cut}^{empty} + i\omega L_{nocore} R_{cut}^{full} - i\omega L_{nocore} R_{cut}^{empty} \tag{A.2.25}$$

Let

$$\tilde{A} = \gamma_g(R_{cut}^{empty} R_{cut}^{full} + R_w^2 - R_w R_{cut}^{full} - R_w R_{cut}^{empty} - X_{cut}^{empty} X_{cut}^{full} \tag{A.2.26}$$

$$\tilde{B} = \gamma_g(-R_w X_{cut}^{empty} - R_w X_{cut}^{full} + R_{cut}^{full} X_{cut}^{empty} + R_{cut}^{empty} X_{cut}^{full}) \tag{A.2.27}$$

$$\tilde{U} = \gamma_g R_w R_{cut}^{full} + \gamma_g R_w R_{cut}^{empty} + \gamma_g X_{cut}^{full} X_{cut}^{empty} - \gamma_g R_w^2 - \gamma_g R_{cut}^{full} R_{cut}^{empty} + \omega L_{nocore}(X_{cut}^{empty} - X_{cut}^{full})$$

(A.2.28)

$$\tilde{V} = \gamma_g R_w X_{cut}^{full} - \gamma_g R_{cut}^{empty} X_{cut}^{full} - \gamma_g R_{cut}^{full} X_{cut}^{empty} - \gamma_g R_w R_{cut}^{empty} + \omega L_{nocore}(-R_{cut}^{empty} + R_{cut}^{full}) \quad (A.2.29)$$

It is obvious that $\tilde{A}$, $\tilde{B}$, $\tilde{U}$, $\tilde{V}$ can be evaluated by measuring $R_{cut}^{full}, R_{cut}^{empty}, X_{cut}^{full}, X_{cut}^{empty}$ and by knowing γ_g, L_{nocore} which are given by the geometrical characteristics of the toroid, that is L_1, L_2, N_t, and A_{cs}. Finally, permeability is written in terms of $\tilde{A}$, $\tilde{B}$, $\tilde{U}$, $\tilde{V}$ as

$$\mu' - i\mu'' = \frac{(-\tilde{A} - i\tilde{B})(\tilde{U} - i\tilde{V})}{\tilde{U}^2 + \tilde{V}^2} \quad (A.2.30)$$

Therefore,

$$\mu' = -\frac{\tilde{A}\tilde{U} + \tilde{B}\tilde{V}}{\tilde{U}^2 + \tilde{V}^2}, \qquad \mu'' = \frac{\tilde{B}\tilde{U} + \tilde{A}\tilde{V}}{\tilde{U}^2 + \tilde{V}^2} \quad (A.2.31)$$

Susceptibility will be given, then, as

$$\chi' = \mu' - 1 = -\frac{\tilde{A}\tilde{U} + \tilde{B}\tilde{V}}{\tilde{U}^2 + \tilde{V}^2} - 1, \qquad \chi'' = \mu'' = \frac{\tilde{B}\tilde{U} + \tilde{A}\tilde{V}}{\tilde{U}^2 + \tilde{V}^2} \quad (A.2.32)$$

By importing the measured data $(R_{cut}^{full}, R_{cut}^{empty}, X_{cut}^{full}, X_{cut}^{empty})$ into a computer program the susceptibility's components can be determined.

A.3 Calculation of permeability by means of the short circuit transmission line technique.

Let us consider the transmission line of Fig. (2.7). We want to express the input impedance in terms of the propagation constant $\gamma_0 = \alpha_0 + i\beta_0$ (α_0 is the attenuator factor and $\beta_0 = 2\pi/\lambda$ is the phase coefficient), the characteristic impedance Z_0 and the input impedance Z_R of the load. The impedance Z_R is the input impedance of the cell with the sample in it (part of length l). The input impedance of the whole arrangement, at distance x from the load Z_R, is given by the following equation [4]

$$Z_{in} = \frac{V_{in}}{I_{in}} = \frac{V_R \cosh(\gamma_0 x) + Z_0 I_R \sinh(\gamma_0 x)}{I_R \cosh(\gamma_0 x) + \frac{V_R}{Z_0} \sinh(\gamma_0 x)} \quad (A.3.1)$$

where V_R =voltage across the coaxial cell, I_R =current through the conductors of the cell. Because the line is low-loss, α_0 =0, the propagation constant is written as $\gamma_0 = i\beta_0$ and by using the fact that $\cosh i\beta_0 x = \cos\beta_0 x$ and $\sinh i\beta_0 x = i\sin\beta_0 x$, Eq. (A.3.1) takes the form,

$$Z_{in} = Z_0 \frac{Z_R \cos(\beta_0 x) + iZ_0 \sin(\beta_0 x)}{Z_0 \cos(\beta_0 x) + iZ_R \sin(\beta_0 x)} \tag{A.3.2}$$

By dividing above and below by $\cos\beta_0 x$ we obtain,

$$Z_{in} = Z_0 \frac{Z_R + iZ_0 \tan(\beta_0 x)}{Z_0 + iZ_R \tan(\beta_0 x)} \tag{A.3.3}$$

In the special case where the load is a short circuit (Z_R =0 and V_R =0), the input impedance is

$$Z_{in} = iZ_0 \tan(\beta_0 x) \tag{A.3.4}$$

We want to derive, now, an expression for μ as function of $Z_{in} = R_{in} + iX_{in}$ for the case of the shorted cell. This model will not take into account the dielectric characteristics of the material. A combined theory, which includes μ and ε together, will be studied in section A.5. The part of the line (cell) filled by the sample will have a characteristic impedance and propagation constant different to those of the unfilled part of the line. Say that this impedance and propagation constant are Z_1 and γ_1 respectively. In this case this part of the line has losses, so the general Eq. (A.3.1) has to be used. Since the line is shorted, as Eq. (A.3.4) states, Z_R becomes

$$Z_R = Z_1 \tanh(\gamma_1 l) \tag{A.3.5}$$

The intrinsic impedance Z_{sample} of the medium is given by [4]

$$Z_{sample} = \frac{i\omega\mu\mu_0}{\gamma_1} = \sqrt{\frac{\mu\mu_0}{\varepsilon\varepsilon_0}} \tag{A.3.6}$$

since the propagation factor is $\gamma_1 = i\omega\sqrt{\varepsilon\varepsilon_0\mu\mu_0}$. The characteristic impedance Z_1 of the part of the line filled with the material is related to the geometrical characteristics of the coaxial line and the intrinsic impedance [5]

$$Z_1 = \frac{Z_{sample}}{2\pi} \ln\frac{R_2}{R_1} \tag{A.3.7}$$

where R_1, R_2 are the inner and outer radius of the cylindrical conductors. Combining Eqs. (A.3.5), (A.3.6), (A.3.7) we get,

$$Z_R = \frac{1}{2\pi}\frac{i\omega\mu\mu_0}{\gamma_1}\tanh(\gamma_1 l)\ln\frac{R_2}{R_1} \tag{A.3.8}$$

A significant simplification can now be made if we assume that the sample depth is much less than the wavelength of electromagnetic radiation, which means $\gamma_1 l << 1$. Under this condition $\tanh(\gamma_1 l) \cong \gamma_1 l$, and the previous equation can be simplified to,

$$Z_R = \frac{1}{2\pi} i\omega\mu\mu_0 \ln\frac{R_2}{R_1} l \tag{A.3.9}$$

This result gives the load impedance in terms of the permeability of the sample medium. Returning to Eq. (A.3.3) for the input impedance at a distance x from the front end of the sample face and substituting for Z_R, one obtains,

$$Z_{in} = Z_0 \frac{i\omega\mu\mu_0 \ln(R_2/R_1)l/2\pi + iZ_0\tan(\beta_0 x)}{Z_0 - i\omega\mu\mu_0 \ln(R_2/R_1)l\tan(\beta_0 x)/2\pi} \tag{A.3.10}$$

From this equation by solving for μ, one obtains,

$$\mu\mu_0 = Z_0 \frac{Z_{in} - iZ_0\tan(\beta_0 x)}{i\omega\ln(R_2/R_1)lZ_0/2\pi + Z_{in}\omega\ln(R_2/R_1)l\tan(\beta_0 x)/2\pi} \tag{A.3.11}$$

The next step is to eliminate the geometrical parameters R_1 and R_2, so that one does not have to include the dimensions of the coaxial line. The inductance of the line is given by Eq. (A.3.5). By substituting Eq. (A.3.5) into Eq. (A.3.11) and extracting L and writing ω in terms of the wavelength λ, we finally derive,

$$\mu = \frac{\lambda}{2\pi l}\frac{Z_{in}/Z_0 - i\tan(\beta_0 x)}{Z_{in}/Z_0\tan(\beta_0 x) + i} \tag{A.3.12}$$

By replacing $Z_{in} = R_{in} + iX_{in}$ and separating into real and imaginary part, we find

$$\mu' = \frac{\lambda}{2\pi l}\frac{R_{in}^2\tan(\beta_0 x) + (X_{in} - Z_0\tan(\beta_0 x))(X_{in}\tan(\beta_0 x) + Z_0)}{(R_{in}\tan(\beta_0 x))^2 + (X_{in}\tan(\beta_0 x) + Z_0)^2} \tag{A.3.13}$$

and

$$\mu'' = \frac{\lambda}{2\pi l}\frac{R_{in}(X_{in}\tan(\beta_0 x) + Z_0) - (X_{in} - Z_0\tan(\beta_0 x))R_{in}\tan(\beta_0 x)}{(R_{in}\tan(\beta_0 x))^2 + (X_{in}\tan(\beta_0 x) + Z_0)^2} \tag{A.3.14}$$

The above equations are valid when the calibration plane is in an arbitrary position, x, far from the actual port. In our setup the calibration plane is the upper face of the cell, thus $x = -l$. Note that $Z_{in} = R_{in} + iX_{in}$ is the impedance measured by the instrument on the calibration plane, since the rest of the line is part of the port.

A.4 Calculation of permittivity by means of the open circuit transmission line technique.

By following a similar procedure to that of section A.3 we are able to derive an expression of ε, uncorrelated to μ. The termination of the cell is open. This ensures that the electric field is large and the magnetic field is small within the sample, provided that the wavelength within the sample is much greater than the sample thickness. As before, we express the load impedance in terms of the filled cell's characteristic impedance. In this case this is,

$$Z_R = Z_1 \coth(\gamma_1 l) \tag{A.4.1}$$

The intrinsic impedance of the sample medium can be written as

$$Z_{sample} = \frac{\gamma_1}{i\omega\varepsilon\varepsilon_0} \tag{A.4.2}$$

Using the relation between characteristic impedance of filled cell and intrinsic impedance, Eq. (A.3.7), one obtains the following,

$$Z_R = \frac{1}{2\pi}\frac{\gamma_1}{i\omega\varepsilon\varepsilon_0}\coth(\gamma_1 l)\ln\frac{R_2}{R_1} \tag{A.4.3}$$

Again making the assumption that the sample depth is much less than the wavelength in the sample so that $\coth(\gamma_1 l) \cong 1/\gamma_1 l$ then Eq. (A.4.3) becomes,

$$Z_R = \frac{\gamma_1}{2\pi i\omega\varepsilon\varepsilon_0 l}\ln\frac{R_2}{R_1} \tag{A.4.4}$$

Substituting the latter equation into Eq. (A.3.3) yields the following expression for the input impedance,

$$Z_{in} = Z_0\frac{\gamma_1 \ln(R_2/R_1)/(2\pi i\omega\varepsilon\varepsilon_0 l) + iZ_0\tan(\beta_0 x)}{Z_0 + \tan(\beta_0 x)\gamma_1 \ln(R_2/R_1)/(2\pi i\omega\varepsilon\varepsilon_0 l)} \tag{A.4.5}$$

Rearranging the latter equation one obtains the permittivity as,

$$\varepsilon\varepsilon_0 = \frac{\ln(R_2/R_1)}{2\pi\omega l Z_0}\left(\frac{Z_0/Z_{in} - i\tan(\beta_0 x)}{Z_0/Z_{in}\tan(\beta_0 x) + i}\right) \tag{A.4.6}$$

The capacitance of an empty cylindrical capacitor is given by Eq. (2.6.5). Using the fact that $Z_0 = \sqrt{L/C}$ and $\omega = 2\pi/(\lambda\sqrt{L/C})$, Eq. (A.4.6) becomes,

$$\varepsilon = \frac{\lambda}{2\pi l}\left(\frac{Z_0/Z_{in} - i\tan(\beta_0 x)}{Z_0/Z_{in}\tan(\beta_0 x) + i}\right) \tag{A.4.7}$$

Separating into real and imaginary parts the latter equation gives the complex components of ε, as,

$$\varepsilon' = \frac{\lambda}{2\pi l}\frac{(Z_0 + X_{in}\tan(\beta_0 x))(Z_0\tan(\beta_0 x) - X_{in}) - R_{in}^2\tan(\beta_0 x)}{(R_{in}\tan(\beta_0 x) - X_{in})^2 + R_{in}^2} \tag{A.4.8}$$

and

$$\varepsilon'' = \frac{\lambda}{2\pi l}\frac{(Z_0 + X_{in}\tan(\beta_0 x))R_{in} + (Z_0\tan(\beta_0 x) - X_{in})R_{in}\tan(\beta_0 x)}{(R_{in}\tan(\beta_0 x) - X_{in})^2 + R_{in}^2} \tag{A.4.9}$$

A.5 Calculation of both μ and ε by means of the short and open circuit transmission line technique.

To correlate μ and ε in one relation it is necessary to take two sets of impedance measurements: one with the sample short circuited and one with the sample open circuited. For the short circuit termination the load impedance is given by Eq. (A.3.5), i.e.

$$Z_R^{short} = Z_1\tanh(\gamma_1 l) \tag{A.5.1}$$

and for the open circuit termination the load impedance, given by Eq. (A.4.1) is

$$Z_R^{open} = Z_1\coth(\gamma_1 l) \tag{A.5.2}$$

Substituting these into Eq. (A.3.1) for the input impedance and with the characteristic impedance, $Z_1 = \sqrt{\varepsilon\varepsilon_0\mu\mu_0}\,\ln(R_2/R_1)/2\pi$, one obtains the following,

$$Z_{in}^{short} = Z_0\frac{\tanh(\gamma_1 x)\sqrt{\varepsilon\varepsilon_0\mu\mu_0}\,\ln(R_2/R_1)/2\pi + Z_0\tanh(\gamma_0 x)}{Z_0 + \tanh(\gamma_1 x)\tanh(\gamma_0 x)\sqrt{\varepsilon\varepsilon_0\mu\mu_0}\,\ln(R_2/R_1)/2\pi} \tag{A.5.3}$$

and

$$Z_{in}^{open} = Z_0\frac{\coth(\gamma_1 x)\sqrt{\varepsilon\varepsilon_0\mu\mu_0}\,\ln(R_2/R_1)/2\pi + Z_0\tanh(\gamma_0 x)}{Z_0 + \coth(\gamma_1 x)\tanh(\gamma_0 x)\sqrt{\varepsilon\varepsilon_0\mu\mu_0}\,\ln(R_2/R_1)/2\pi} \tag{A.5.4}$$

which represent the input impedance with short and open circuit terminations respectively. From the last two equations one can obtain two expressions containing $\sqrt{\mu\mu_0/\varepsilon\varepsilon_0}$ namely:

$$\sqrt{\frac{\mu\mu_0}{\varepsilon\varepsilon_0}}\tanh(\gamma_1 l) = \frac{Z_0^2\tanh(\gamma_0 x) - Z_{in}^{short} Z_0}{Z_{in}^{short}\tanh(\gamma_0 x)\ln(R_2/R_1)/2\pi - Z_0\ln(R_2/R_1)/2\pi} \tag{A.5.5}$$

and

$$\sqrt{\frac{\mu\mu_0}{\varepsilon\varepsilon_0}}\coth(\gamma_1 l) = \frac{Z_0^2\tanh(\gamma_0 x) - Z_{in}^{open} Z_0}{Z_{in}^{open}\tanh(\gamma_0 x)\ln(R_2/R_1)/2\pi - Z_0\ln(R_2/R_1)/2\pi} \tag{A.5.6}$$

These equations can be further simplified by knowing that the characteristic impedance of the lossless part of the line is given by,

$$Z_0 = \frac{1}{2\pi}\ln\left(\frac{R_2}{R_1}\right)\sqrt{\frac{\mu_0}{\varepsilon_0}} \tag{A.5.7}$$

On using Eq. (A.5.7) in Eqs.(A.5.5) and (A.5.6) the geometrical parameter $\ln(R_2/R_1)/2\pi$ cancels out and dividing across by $\sqrt{\mu_0/\varepsilon_0}$ leaves

$$\sqrt{\frac{\mu}{\varepsilon}}\tanh(\gamma_1 l) = \frac{Z_0\tanh(\gamma_0 x) - Z_{in}^{short}}{Z_{in}^{short}\tanh(\gamma_0 x) - Z_0} \tag{A.5.8}$$

and

$$\sqrt{\frac{\mu}{\varepsilon}}\coth(\gamma_1 l) = \frac{Z_0\tanh(\gamma_0 x) - Z_{in}^{open}}{Z_{in}^{open}\tanh(\gamma_0 x) - Z_0} \tag{A.5.9}$$

If the last two equations are multiplied by each other one obtains μ/ε, where say

$$\frac{\mu}{\varepsilon} = \tilde{P} + i\tilde{Q} \tag{A.5.10}$$

where $\tilde{P}$ and $\tilde{Q}$ denote the real and the imaginary parts of the multiplication of the right hand sides of Eqs.(A.5.8), (A.5.9). When Eq. (A.5.8) is divided by Eq. (A.5.9) we have

$$\tanh^2(\gamma_1 l) = \tilde{R} + i\tilde{S} \tag{A.5.11}$$

with $\tilde{R}$ and $\tilde{S}$ denoting the real and imaginary parts of the division exercise. Since we know that $\gamma_1 = i\omega\sqrt{\varepsilon\varepsilon_0\mu\mu_0}$ then Eq. (A.5.11) becomes,

$$\tanh(i\omega l\sqrt{\varepsilon\varepsilon_0\mu\mu_0}) = \sqrt{\tilde{R} + i\tilde{S}} \tag{A.5.12}$$

Now $\tanh(i\psi)=i\tan\psi$ so that Eq. (A.5.12) can be rewritten as

$$i\tan(\omega l\sqrt{\varepsilon\varepsilon_0\mu\mu_0}) = \sqrt{\tilde{R}+i\tilde{S}} \qquad (A.5.13)$$

Dividing across by i and solving for με, gives

$$\varepsilon\mu = \frac{[\tan^{-1}(-i\sqrt{\tilde{R}+i\tilde{S}})]^2}{\varepsilon_0\mu_0\omega^2 l^2} = \tilde{X}+i\tilde{Y} \qquad (A.5.14)$$

where $\tilde{X}$ and $\tilde{Y}$ represent the real and imaginary parts of the right hand side of Eq. (A.5.14). By combining Eqs. (A.5.10) and (A.5.14) one can solve for ε and μ. First if Eq. (A.5.10) is multiplied by Eq. (A.5.14), ε cancels out and one can solve for μ, i.e.

$$\mu = \sqrt{(\tilde{P}+i\tilde{Q})(\tilde{X}+i\tilde{Y})} \qquad (A.5.15)$$

If Eq.(A.5.14) is divided by Eq.(A.5.10) then μ cancels out and solving for ε gives,

$$\varepsilon = \sqrt{\frac{\tilde{X}+i\tilde{Y}}{\tilde{P}+i\tilde{Q}}} \qquad (A.5.16)$$

Here we have two equations for the complex permittivity and permeability, all the parameters $\tilde{P}$, $\tilde{Q}$, $\tilde{X}$ and $\tilde{Y}$ can be determined from the impedance measurements.

References:

1. Fannin P.C., Scaife B.P.K., Charles S.W., *J. Phys. E., Sci. Instrum.*, **19**, 238, (1986).
2. Roberts S., von Hippel A.R., *J. App. Phys.*, **17**, 610, (1946).
3. Fannin P.C., Relihan T., Charles S.W., *J. Phys. D, App. Phys.*, **28**, 2003, (1995).
4. Kraus J.D., *Electromagnetics*, McGraw-Hill, 4th Edition, (1992).
5. Henson C.S., *Solutions of Problems in Electronics and Telecommunications, Pitman Press*, London, (1969).

Appendix B

Computational and fitting programs.

B.1 Introduction.

This work is supported by a number of computational and fitting programs developed in Matlab and created by me. Matlab is a high-performance language for technical computing [1,2]. It integrates computation, visualisation and programming in an easy to use environment. Typical uses include math and computation, algorithm development, modelling, simulation, data analysis, visualisation, scientific and engineering graphs.

There were two reasons to choose Matlab as the main programming language of this work. The first is the simplicity of programming using this language and the other reason is to remain compatible with the previous programs which were created by the previous researchers/students who worked in the laboratory.

In the following sections we will introduce the programs used in this work, by analysing their structure and code. We may distinguish between computational and fitting programs because they perform different kinds of work. We will describe their structure by the use of block diagrams, also called flow diagrams. Examples of Matlab code are presented below in `courier` typescript. Due to the extensive length of the code of each program, we will only present the parts of the code which perform specific operations and routines. These routines are included in most of the programs, so there is no need to explain the structure of each program individually. We start the presentation by describing the exercises that computational and fitting programs are involved in and afterwards we describe how they work.

B.2 Computational and fitting programs.

There are two kinds of programs which support this work:

(a) The *computational programs*, are those which calculate the magnetic susceptibility, $\chi(\omega)$, or the permittivity, $\varepsilon(\omega)$, from the impedance data. The impedance data, recognised as *double* numbers, are downloaded from the analysers via the GP-IB interface to the computer (controller) and are saved in a tabular array in .DAT formatted files. The computational program opens the data file, performs calculations, plots and saves in a .DAT output file the

values of susceptibility and permeability, as functions of frequency or field. Each experimental technique (i.e. toroid technique, cylindrical coil, transmission line, cylindrical capacitor) requires a specific computational program which, depending on the exercise, can use: (i) the equations which were described in sections 2.5 and A.2, for the case of magnetic measurements with cylindrical or toroidal coils, (ii) the equations which were introduced in sections 2.7 and A.5, for the transmission line technique, by which one calculates $\chi(\omega)$ and $\varepsilon(\omega)$ and (iii) the equations which were introduced in section 2.6 and which give $\varepsilon(\omega)$ for the case where dielectric measurements are performed with a plate or cylindrical capacitor. Other classes of program, which perform secondary operations, such as calculation of the tangent of a curve, or search for peaks on a curve, can be considered in this category. The program which combines two data curves into one curve is also a kind of computational program (it is necessary combine curves when data are taken by different experimental techniques (i.e. toroid method and transmission line) or when one uses the same technique for different cell depths).

(b) The *fitting programs*, are those which fit the experimental $\chi(\omega)$ or $\varepsilon(\omega)$ curves to theoretical curves. The theoretical curves (fits) are created by use of the proposed models, such as the Debye and Cole-Cole equations for relaxation-profile curves, or the Landau-Lifshitz and Coffey et al equations for resonance-profile curves. These equations are modified to include distribution functions to account for the particle's polydispersion. There is an optimum value for each fitting parameter which gives the best possible approximation to the data curve. If n is the number of the free (fitting) parameters, x_i, i=1, 2,…,n and m is the number of the dependent parameters y_j, j=1, 2,…,m , (i.e. frequency or field) we define the function $f(x_1, x_2, ..., x_n, y_1, y_2, ..., y_m)$ as function of both dependent and independent variables. This function represents the theoretical curve (fit). The function $f(x_1, x_2, ..., x_n, y_1, y_2, ..., y_m)$ may be split into real and imaginary components which correspond to the real and imaginary components of $\chi(\omega)$ or $\varepsilon(\omega)$. Let us call $g(y_1, y_2, ..., y_m)$ the function which represents the data curve. We are looking for the optimum set of x_i, i=1, 2,…,n values which gives the minimum difference between f and g,

$$D(x_1, x_2, ..., x_n) = f(x_1, x_2, ..., x_n, y_1, y_2, ..., y_m) - g(y_1, y_2, ..., y_m) = \min \qquad \text{(B.2.1)}$$

The problem may equivalently be expressed as the zeroing of the gradient ∇_x with respect to x_i parameters, thus we can write

$$\nabla_x D(x_1, x_2, ..., x_n) = \nabla_x f(x_1, x_2, ..., x_n, y_1, y_2, ..., y_m) - \nabla_x g(y_1, y_2, ..., y_m) = 0 \qquad \text{(B.2.2)}$$

This minimization may be realised by applying mathematical algorithms such as the Mean Square Error (MSE) or the Simplex method [3,4] or by visual fitting. The realisation of the MSE algorithm, in a program, is easy but can only be applied for the case of one only free parameter (n=1). If more than one parameter is involved, the procedure may take a very long computational time. For more than one free parameter the Simplex method is suitable, it is an automatic method by which it is only required to declare the field in which each x_i parameter takes its values. Unfortunately, to realise such an algorithm in a program causes difficulties due to its complexity. Matlab has embodied functions which perform optimisation [5] by using Simplex or other relevant algorithms, but again the programming complexity and the computational time restricted our use of these functions. The visual fitting procedure is the one which is commonly used in this work.

In Eq. (B.2.2) the y_j variables represent the two common free variables, which are the frequency, ω, and the polarising field, H_s. Thus we write $y_1 = \omega$, $y_2 = H_s$ and m=2. Depending on the equation we want to fit, the x_i parameters may correspond to the following parameters:

(i) For the Debye equation when a distribution function is applied, $x_1 = M_s$, $x_2 = \langle r_m \rangle$, $x_3 = \chi_0$, $x_4 = \chi_\infty$ and x_5=distribution function parameter, such as σ_r, β, α, x_{max}/x_{min} (depends on the distribution we use, see section 3.2). Thus n=5.

(ii) For the Cole-Cole equation, $x_1 = \chi_0$, $x_2 = \chi_\infty$ and $x_3 = \alpha$, so n=3.

(iii) For the Landau-Lifshitz equation, $x_1 = M_s$, $x_2 = \langle r_m \rangle$, $x_3 = \langle K \rangle$, $x_4 = \chi_0$, x_5=parameter of the distribution of K and x_6= parameter of the distribution of r_m. So in this situation n=6.

(iv) For the Coffey et al equation we have the same parameters as in the previous case.

The computational programs are relatively simple programs. The fitting programs are quite more complicated due to the use of distributions which require the use of repeatable loops and multidimensional arrays to store the values. Before we describe the structures of

the computational and fitting programs, it is useful to make a brief introduction to the Matlab environment and how to program with this powerful tool.

B.3 Programming in Matlab.

Matlab is an interactive system whose basic data element is an array that does not require dimensioning. This allows one to solve many technical computing problems, especially those with matrix and vector formulations, in a fraction of the time it would take to write a program in a scalar noninteractive language such as Basic, C or Fortran.

Matlab features a family of application specific solutions called *toolboxes*. Toolboxes are comprehensive collections of Matlab functions (called M-files) that extend the Matlab environment to solve particular classes of problems.

The Matlab system consists of four main parts, namely [2]:

(a) *the Matlab language*, which is a high level matrix/array language with control flow statements, functions, data structures, input/output and object-oriented programming features. The syntax of the commands is very similar to the well-known C programming language.

(b) *the Matlab working environment*, which includes facilities for managing the variables in the workspace and importing and exporting data. It also includes tools for developing, managing, debugging and profiling M-files, Matlab's applications.

(c) *the Matlab graphics system*, which includes high-level commands for two-dimensional and three dimensional data visualization, image processing, animation and presentation graphics.

(d) *the Matlab mathematical function library*, which is a vast collection of computational algorithms ranging from elementary functions like sum, sine, cosine and complex arithmetic, to more sophisticated functions like matrix inverse, matrix eigenvalues and fast Fourier transforms.

Table B.1 consists of a quick reference to the most common in used Matlab commands, which can help one to understand the code which is presented in the next sections. Further details can be found in [6]. In Table B.1 the argument A can be an array (matrix) of arbitrary dimensions, but in our programming it is usually a single element (1×1), a row ($1\times n$) or column ($n\times1$) vector, or a two dimensional ($n\times m$) array. In Matlab, the mathematical functions and arithmetic operators can apply directly to each individual element of A. The arithmetic operators, the logical operators, and the flow control commands have the same

Table B.1 Quick reference to the commonly used Matlab commands (alphabetic order).

Command syntax	Operation	Function type
`+, -, *, /, \, ^, '`	Matrix and array operation (e.g. `A+B`, `A*B`, etc).	Arithmetic operators
`.*, ./, .\, .^, .'`	Element by element operation.	Arithmetic operators
`<, >, ==`	Element by element comparison.	Relational operators
`&, |`	Logical operations.	Logical operators
`[], (), =, !`	Special operations	Special characters
`:`	Create vectors, matrix subscripting, and `for` iterations.	Special operator
`;`	Declares the end of a command line.	Special character
`%`	Declares the start of a comment line.	Special character
`abs(A)`	Absolute value of the elements of A.	Math
`asin(A),acos(A),atan(A)` `asinh(A),acosh(A)`	Inverse trigonometric functions of the elements of A.	Math
`break`	Break out of control structures.	Flow control
`ceil(A)`	Rounds the elements of A to the nearest integers $\geq$ A.	Math
`clear`	Clear all variables.	Variable control
`cos(A), cosh(A)`	Cosine and hyperbolic cosine.	Math
`cumsum(A)`	Cumulative sum of the elements of A, over each column.	Math
`else(Statement)`	Conditionally execute statements.	Flow control
`elseif(Statement)`	Conditionally execute statements.	Flow control
`end`	Terminate `for`, `while` and `if` statements.	Flow control
`exp(A)`	Exponential, operates element-wise to A.	Math
`eval('String')`	Interpret string containing expressions.	Evaluation
`floor(A)`	Rounds the elements of A to the nearest integers $\leq$ A.	Math
`for Expression(Statem.)`	Create loops: repeat statements a specific number of times (e.g. `for i=1:10 Statements end`).	Flow control
`gamma(A)`	Gamma function evaluated at the elements of A.	Math
`i, j`	Imaginary unit	Numeric
`if Expression(Statem.)`	Conditionally execute statements.	Flow control
`imag(A)`	Imaginary part of the elements of A.	Math
`inf`	Provide infinity.	Numeric
`input('String')`	Request user to input a number.	Input/output
`input('String','s')`	Request user to input a string.	Input/output
`length(A)`	Length of vector A.	Array dimension
`linspace(Num1,Num2,Num)`	Generate linear spaced vector with Num elements, between the values Num1-Num2.	Create array
`load filename.extension`	Load ASCII file.	Input/output
`log(A)`	Natural logarithm of the elements of A.	Math
`log10(A)`	Common logarithm of the elements of A	Math
`logspace(Num1,Num2,Num)`	Generate logarithmically spaced vector with Num elements, between the values 10^{Num1}-10^{Num2}.	Create array
`max(A)`	Maximum elements of A.	Math
`mesh(A,B,C)`	3 dimensional plot. The arrays A, B, C defines the points in the space.	Plot
`min(A)`	Minimum elements of matrix A.	Math
`pi`	Provide π.	Numeric
`plot(A,B,'Linetype')`	2 dimensional plot with the values of vector B versus the values of vector A.	Plot
`quad('Function',Num1, Num2)`	Numerical integration of a function between the limits Num1 and Num2, by use of Simpson's rule.	Math
`quad8('Function',Num1, Num2)`	Numerical integration of a function between the limits Num1 and Num2, by use of Newton-Cotes 8 rule.	Math
`real(A)`	Real part of the elements of A.	Math
`save filename`	Save workspace arrays to a file in ASCII format.	Input/output

Table B.1 (continues)

Command syntax	Operation	Function type
`semilogx(A,B)`	2 dimensional plot with the values of vector B versus the values of vector A. Horizontal axis in log scale.	Plot
`sin(A), sinh(A)`	Sine and hyperbolic sine of the elements of A.	Math
`size(A)`	Returns the dimensions of matrix A.	Array dimension
`sqrt(A)`	Square root of the elements of A.	Math
`std(A)`	Standard deviation of the elements of each column of A.	Math
`sum(A)`	Sum of the elements of each column of A.	Math
`tan(A), tanh(A)`	Tangent and hyperbolic tangent of the elements of A.	Math
`title('String')`	Graph title.	Plot
`while Expression (Stat)`	Create loops: repeat statements a specific number of times (e.g. `while i>1 Statements end`).	Flow control
`xlabel('Text')`	Graph's x-axis label.	Plot
`ylabel('Text')`	Graph's y-axis label.	Plot
`zlabel('Text')`	Graph's z-axis label.	Plot

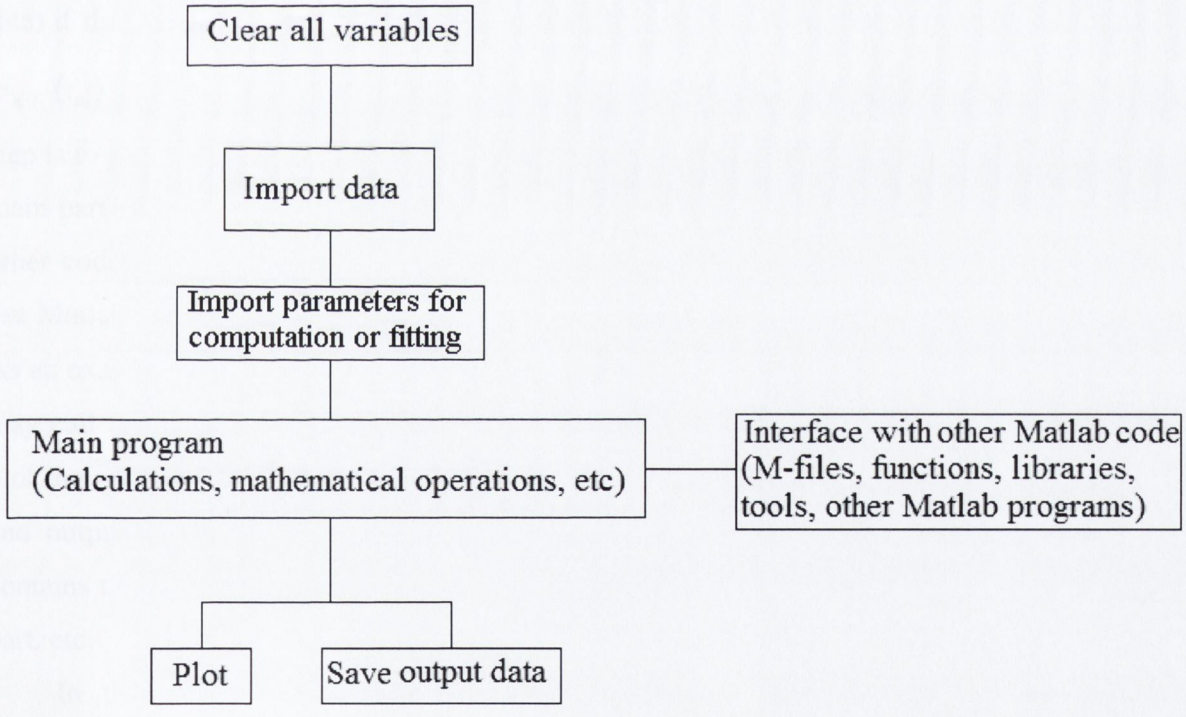

Figure B.1 Basic flow diagram of a Matlab program.

syntax and operation as in C language. The math functions can operate element-by-element to the elements of a matrix. This unique advantage of Matlab saves the user from creating repeatable loops in order to make mathematical operations between the elements of different matrices. Also, Matlab automatically recognises the type of variables, arrays, structures, strings, etc so there is no need to define in the beginning of the program any identification (single, double, integer, character etc), as is required in other languages. These simplifications in the Matlab code can make a Matlab program much shorter and easier-to-develop, compared with other languages.

Figure (B.1) illustrates a flow diagram of a basic Matlab program. The first task is to clear the variables. This is performed with the command `clear` which is a standard command on the top of each program's code. The next is to import the data (impedance measurements, or $\chi(\omega)$, $\varepsilon(\omega)$) from a file. The next is to import the parameters which are required for computation (i.e. the geometrical characteristics of a toroid or of a transmission line) if the program is a computational program, or the fitting parameters (such as M_s, $\langle K \rangle$, σ_K, $\langle r_m \rangle$, σ_r, α_d, H_s, relaxation times, etc) if the program is a fitting program. The next step is to perform calculations or fitting. This is realized by the main part of the program. The main part of the program may be used in combination with Matlab's embodied functions, or other code which performs specialized jobs. These are usually the M-files (.m files) which use Matlab's interface to communicate with the main program when the program calls them. As an example, the main program may call the function `quad` which performs integration, or may call another function which has been defined by the programmer. The final step is to plot the result and to save the output data to an ASCII file for further future use. The input and output files must contain ASCII data in a tabular format in which the first column contains the frequencies or the fields, the second column the real part, the third the imaginary part, etc.

In the following example is described analytically how to perform some basic operations such as to import data, import parameters, save the output data and to plot graphs.

(a) *Import data from a file*: One has to define a parameter, call it for example `filein`, which contains the name of the file which is to be imported. The syntax can be

```
filein=input('enter name of data file','s');
```

where the command `input('String','s')` is used for entering strings. Next is to use the command `load filename.extension` which loads files. This is a *high-level* command, but there are two restrictions: (i) the input file can be called only from the same directory from where the user runs the program and (ii) the data in the input file has to be arrayed in columns which are separated by the *tab* separator. The syntax of the command `load` is as follows,

```
eval(['load',filein,'.dat']);
```

In this example the extension .dat is used because our data files have .dat extensions. The command `eval` evaluates the statement in the parentheses, which is the string `['load',filein,'.dat']`. At this stage the data have been loaded in but we have to define an array which will represent them. So we define a matrix, call it `data`, which keeps the data in its structure for later use. The syntax is given as

```
data = eval(filein);
```

The whole code for importing data is the following three lines,

```
filein=input('enter name of data file', 's');
eval(['load',filein,'.dat']);
data = eval(filein);
```

(b) *Import parameters*: This is realized by the single command `input`. For example, to import a number for the saturation magnetization, M_s, we write

```
Ms=input('Enter value of saturation magnetization in Tesla:');
```

where the command `input`, with this syntax, passes a number into `Ms`. `Ms`, hereafter, symbolizes in the program the parameter M_s.

(c) *Save output data to a file*: The user has to give first a filename for the output file and after to export the data by using the command `save` which performs the opposite operation to that of the `load` command. The code that outputs the data, which are contained in an $n \times m$ array called `E`, into a file is as follows,

```
fileout = input('Enter name of output file ','s');
eval(['save',fileout,'.dat E /ascii']);
```

The output file will be saved into the same directory from where the user runs the program.

(d) *Plot data*: Matlab supports some high-level commands for graphics. For a two-dimensional plot, where the horizontal x-axis is in logarithmic scale, the command which should be used is `semilogx`. For example:

```
figure(1);semilogx(E(:,1),E(:,2),'r',E(:,1),E(:,3),'r',data(:,
1),data(:,2),'b.',data(:,1),data(:,3),'b.');
```

In this example we plot the data of the susceptibility which are contained in the n×3 array `data` (n=number of data, 3 is the number of columns; the 1st column contains the frequencies, the 2nd column the real part and the 3rd the imaginary part), and the corresponding fit which is contained in the n×3 array `E`. The specifiers `'r'` and `'b.'` specify the line's style. `'r'` is for red solid line (fit) and `'b.'` is for blue dotted line (data). The statement `figure(1)` identifies the graph with a number in order to distinguish it from other graphs which can possibly be created by the same program.

To plot a two-dimensional curve in a linear spaced axis, Matlab supports the command `plot`. In the following example we plot a probability distribution function, `pdf`, against the particle radius, `r`:

```
figure(2);plot (r(:), pdf(:));
```

To plot a three dimensional surface, as these of Fig. (3.5), the command `mesh` is used:

```
figure(3); mesh(E1(:,:),r (:,:),E2(:,:));
```

In the argument of `mesh` the three matrices, `E1`, `r`, and `E2`, contain the points which form the three dimensional surface.

After this brief introduction of the main features of Matlab's environment, we can describe, in general lines, the basic structure of the computational and fitting programs. In section B.4, which follows, we will present the basic code of the program which executes the computations which are required for the calculation of the susceptibility from impedance measurements, which were performed by using the constant frequency method (see section 3.3). In section B.5 we will present the code of two fitting programs: (i) one which uses the Debye equation and (ii) another which uses the Landau-Lifshitz equation.

B.4 An example of a computational program.

As an example of a computational program we will present here the code of the program which was used to execute calculations concerned with the constant frequency method. As was mentioned in section 3.3, this method involves inserting the sample in a cylindrical coil and polarising it with an electromagnet in two different directions, parallel and perpendicular, to the coil's major axis. The data of the parallel and perpendicular

measurements are saved in a number of files, each one for a different polarising field. These files are imported, afterwards, into the main program.

When the data are imported they are saved in four arrays, which in this example are called `Ze`, `Zf`, `Ze2`, `Zf2` (`Z`, `e`, `f`, `2` stand for impedance, empty, full and perpendicular respectively), and then split into eight vectors (`Repar`, `Xepar`, `Rfpar`, `Xfpar`, `Reper`, `Xeper`, `Rfper`, `Xfper`) which present the real and imaginary values of the impedance of the full and empty coil:

```
Repar(:) = Ze(:,2);
Xepar(:) = Ze(:,3);
Rfpar(:) = Zf(:,2);
Xfpar(:) = Zf(:,3);
Reper(:) = Ze2(:,2);
Xeper(:) = Ze2(:,3);
Rfper(:) = Zf2(:,2);
Xfper(:) = Zf2(:,3);
```

We then perform the calculations of the susceptibility. The susceptibility in terms of the full and empty impedance values is given by $\chi' = (X_{full} - X_{empty})/X_{empty}$ and $\chi'' = (R_{full} - R_{empty})/X_{empty}$ (section 2.5). This calculation is performed by the following code:

```
[row,col] = size(Ze);
```
, defines the number of rows and columns of the inserted files,

```
for i = 1:row
```
, defines the number of repeatable loops (equals the number of rows),

```
f(i) = Ze(i,1)*1e3;
```
,change frequency from kHz to Hz (HP4192A reads only kHz)

```
w(i) = 2*pi*f(i);
```
, calculate angular frequency,

```
X1par(i) = ((Xfpar(i)-Xepar(i))/Xepar(i));
```
, calculate $\chi'_{\parallel}$,

```
X2par(i) = ((Rfpar(i)-Repar(i))/Xepar(i));
```
, calculate $\chi''_{\parallel}$,

```
X1per(i) = ((Xfper(i)-Xeper(i))/Xeper(i));
```
, calculate $\chi'_{\perp}$,

```
X2per(i) = ((Rfper(i)-Reper(i))/Xeper(i));
```
, calculate $\chi''_{\perp}$,

```
end
```
, end of loop.

In the following we pass the field values, contained in `field`, and the susceptibility values to a common matrix, `X`. To pass the field values to `X` we write:

```
X(:,1) = field(:,1);
```

To pass to `X` the susceptibility values at the frequency of 10 kHz, which is the n-th element of the vector array, we write:

```
X(:,2) = X1par(1,n)';
X(:,3) = X2par(1,n)';
X(:,4) = X1per(1,n)';
X(:,5) = X2per(1,n)';
X(:,6) = X1per(1,n)'-X1par(1,n)'; , in this line we calculate χ'⊥ − χ'∥.
```

At the end we plot $\chi'_{\perp}$, $\chi'_{\parallel}$ and $\chi'_{\perp} - \chi'_{\parallel}$ in one graph:

```
semilogx(X(:,1),X(:,2),X(:,1),X(:,3),'g.',X(:,1),X(:,4),X(:,1)
,X(:,5),'g.',X(:,1),X(:,6));
```

and we save the data to a file:

```
fileout=input('Enter name of output file to store data ','s');
eval([' save ',fileout,'.dat X /ascii']);
```

With a similar procedure we can perform the calculations which are required for the toroid technique and the transmission line technique.

B.5 Examples of fitting programs.

First we will present the code of a fitting program which is used to fit Debye-profile data. This fit applies the Cole-Cole equation (1.4.52). The program automatically searches for the optimum value of the Cole-Cole parameter, α, by repeating 1000 iterations and estimates the Mean Square Error (MSE) for each iteration. The optimum value of α is that which causes the smallest error. χ_0 and χ_∞ can be imported by the user. The MSE is defined by the following expression,

$$\mathrm{MSE}=\frac{\sqrt{\sum_{i=1}^{N}(\chi_i^{\mathrm{Fit}}-\chi_i^{\mathrm{Data}})^2}}{N} \qquad \text{(B.5.1)}$$

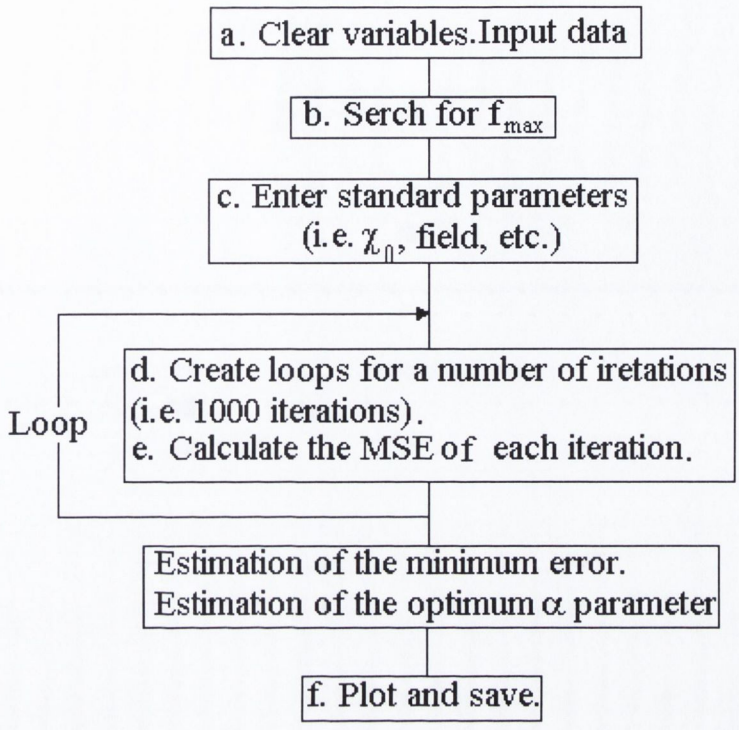

Figure B.2 Flow diagram of the fitting program which performs a Debye fit. The program searches automatically for the optimum Cole-Cole parameter α, by applying the mean square error algorithm.

where χ_i^{Data} is the value of the i-th data point, χ_i^{Fit} is the respective value of the created fit point and N is the number of the data points. The program stores the MSE of all the iterations, which are created for a different value of α, and makes at the end a comparison and estimates the optimum α. The number of iterations can be adjusted by the user but in this fitting procedure a number of 1000 iterations is enough. Thus the program starts from α=0 and uses a step of 0.001 to go up to α=1. The flow diagram of this program is shown in Fig. (B.2). Here follows the structure of the fitting program:

(a) First the program clears up all the parameters, inputs the data (susceptibility or permittivity) into a matrix called `data` and defines the size of the matrix:

```
clear;
filein = input('Enter name of input data file','s');
eval(['load',filein,'.dat']);
data = eval(filein);
[m,n] = size(data);
```

(b) The program searches for the frequency f_{max} of the absorption peak:

`[chmax1,I]=max(data);`, finds the maximum value of each column of `data`. The `chmax1` vector contains the maximum value of each column (all four together) and the vector `I` contains the positions of the maximums in the matrix `data`. The fourth column is the one we are interested in because it contains the χ'' values.

`fmax=data(I(1,4),1);` , this gives the frequency f_{max} which corresponds to the maximum of χ''.

`tau=1/(2*pi*fmax);` , estimates the relaxation time.

(c) Enter χ_0 and χ_∞ (the user can easily predict these two values from the data curves):

```
chi0 = input('Enter value of Chi(0): ');
chiinf = input('Enter value of Chi(inf): ');
```

It is also possible to ask the user to enter the value of the polarising field if the data involves polarised measurements, as in the fits of Figs. (3.8 a-b), (3.9 a-b). In this case both `chi0` and `tau` are field dependent and must be expressed in terms of Eqs. (3.4.1) and (3.4.3) respectively.

(d) The program creates 1000 iterations for each value of $\alpha = 0-1$ with step 0.001:

`bindex=0;` , create a counter which counts the number of the repeatable loops. `Bindex` will be used to indicate which of the 1000 available curves gives the minimum MSE.

`for alpha=0:0.001:1` , create 1000 iterations,

`for bindex=bindex+1` , the counter increments by 1 each time a loop terminates,

`for i = 1:m` , creates a nested loop. The number of repeatability is equal to the number of the individual frequencies, m, of the experiment,

`f1(i) = data(i,1);` , `f1` contains the list frequency,

`w1(i) = f1(i)*2*pi;` , `w1` contains the values of the circular frequency,

`ch(i)=(chi0-chiinf)/(1+(j*w1(i)*tau)^(1-alpha))+chiinf;` , creates a Debye curve for the current value of α,

`ch1(i)=real(ch(i));`

`ch2(i)=-imag(ch(i));` , split to real part and imaginary part.

```
end                                    , end of the nested loop.
U(:,1) = f1';
U(:,2) = ch1';
U(:,3) = ch2';                         , saves the current fit (frequencies, real, imaginary) in U matrix.
```

(e) The following estimates the MSE given by Eq. (B.5.1) for the real (MSE1) and the imaginary (MSE2) components, for the current Debye curve:

```
for i=1:m
    SQR1(i)=U(i,2)^2;
    SQR2(i)=U(i,3)^2;
    SQR3(i)=U(i,4)^2;
    SQR4(i)=U(i,5)^2;
    difference1(i)=U(i,2)-U(i,4);
    difference2(i)=U(i,3)-U(i,5);
    differe1(i)=abs(difference1(i));
    differe2(i)=abs(difference2(i));
    diff1(i)=SQR1(i)-SQR3(i);
    diff2(i)=SQR2(i)-SQR4(i);
    dif1(i)=abs(diff1(i));
    dif2(i)=abs(diff2(i));
end
MSE1(bindex)=sum(dif1)/m;
MSE2(bindex)=sum(dif2)/m;
end
end
```

The following code calculates the mean of MSE1 and MSE2 , makes a comparison and selects the minimum error. The optimum value of α is given in the parameter alpha1 at the end:

```
D=0:0.01:1;
Z(:,1)=D';
Z(:,2)=MSE1';
Z(:,3)=MSE2';
Z(:,4)=(Z(:,2)+Z(:,3))/2;              , average value of MSE1, MSE2,
[E,L]=min(Z);                          , finds the minimum of the average,
y=L(1,4);
```

`alpha1=Z(y,1);` , `alpha1` contains the optimum value of α.

(f) Afterwards, the program plots the optimum curve on the same graph with the data curves and saves the result in a file:

```
semilogx(Q(:,1),Q(:,2),'b.',Q(:,1),Q(:,3),'b.',Q(:,1),Q(:,4),'
r+',Q(:,1),Q(:,5),'r+');
fileout = input('Enter name of output file containing the fit:
','s');
eval(['save',fileout,'.dat Q /ascii']);
```

where `Q` is a new matrix which contains the values of the fit.

A more sophisticated fitting program is one which applies distributions to a number of parameters. As explained in the beginning of this Appendix it is not easy to apply optimisation because the number of parameters is large. Optimisation, such the MSE algorithm, can be applied for one or two parameters at the most. When a function depends on, at least, five parameters, it is a very difficult and time consuming task to minimise such a function. For example, using the simplest search algorithm (numerical calculation of each parameter) with a step of 1000 iteration for each parameter and a time of 0.05 sec to calculate the function for each set of parameters, we can estimate the period of time required to complete these calculations. This simple evaluation shows that we will need approximately $1000^5 = 10^{15}$ iterations or 5×10^{13} sec, which is nearly 1.6 million years. In order to reduce the time required for calculations, the number of step points can be decreased but this will impact on the precision of the model. At the end we prefer to perform a visual fitting where the user himself repeat the fits and checks visually the accuracy of the fit.

In the following analysis we will present, as example of a fitting program, the program which applies the Landau-Lifshitz equation (1.5.39) in which K and r_m are distributed. There are options in this program to select which distribution to use. The user can choose between normal, log-normal and Nakagami for K or r_m. It is also possible to apply no distribution. In order to perform the best fit with the Landau-Lifshitz basic equation, when σ is relatively low (i.e. unpolarised data), it is necessary to add a relaxation term. The same program can perform either a Landau-Lifshitz fit for constant field, i.e. the fits of Fig. (4.4), or a Cole-Cole type II fit as those of Figs. (4.6), (4.7). The flow diagram of this program is shown in Fig. (B.3). The steps are as follows:

(a) The first is to decide which kind of fit we want to do. The program can perform a constant frequency fit or a constant field fit:

```
clear;
option=input('Do you want to obtain a constant field fit or a
constant frequency?(1/2): ');
if option==1
```

(b) If the decision is for constant frequency fit, the next step is to enter the fitting parameters, i.e. M_s, $\langle K \rangle$, r_m, H_s, α_d, γ, and some constants, i.e. T, k_B, η_h:

```
Ms=input('Enter value of saturation magnetization (Tesla): ');
Kmean=input('Enter mean value of anisotropy constant (J/m^3)
:');
rmean = input('Enter mean radius (m): ');
Xo = input('Enter value of static susceptibility:  ');
y = input('Enter gyromagnetic ratio (m/A*sec): ');
H = input('Enter value of polarising field(A/m): ');
a = input('Enter value of damping constant: ');
kb=1.380658e-23;
T=300;
vis=1e-4;
```

We also calculate the mean of v_m, ω_{pre}, τ_0, τ_N and τ_B:

```
Vmean = (4*pi*(rmean^3))/3;
womean=y*(H+2*Kmean/Ms);
tau0mean = 1/(a*womean);
taudmean = Ms*Vmean/(2*a*y*kb*T);
taubmean =3*vis*Vmean/(kb*T);
```

The user has, in addition, to declare from which frequency the fitting points start and to which frequency they end. In this example a vector with 500 log-spaced frequencies is created:

```
NoPts=500;
fstart=input('enter start frequency for the fit (Hz): ');
fend=input('enter end frequency for the fit (Hz): ');
f=logspace(log10(fstart),log10(fend),NoPts);
```

The vector `f` will be the x-axis.

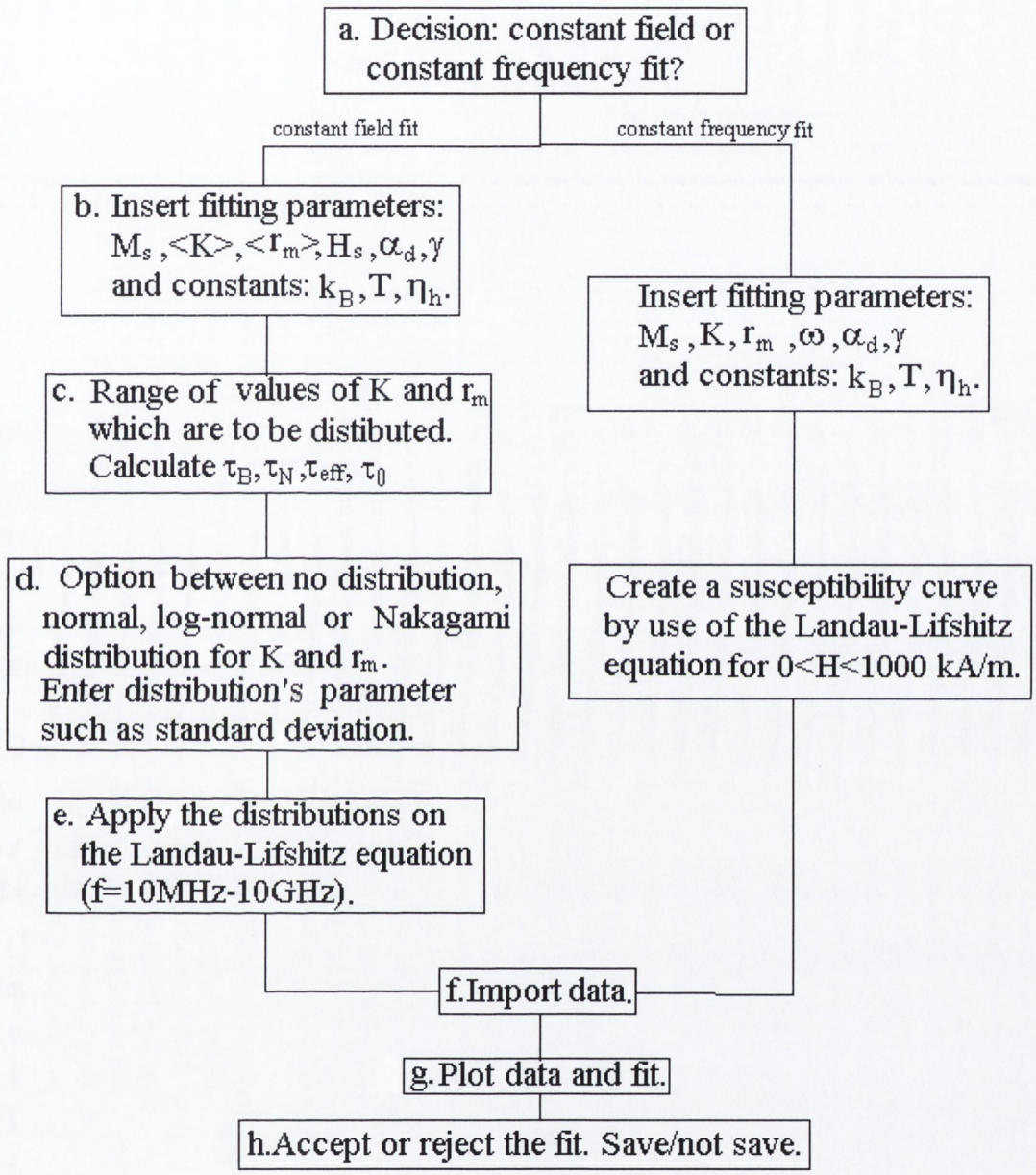

Figure B.3 Flow diagram of the program which performs a Landau-Lifshitz fit, for constant field or constant frequency.

(c) In the subsequent portion, the program creates two vectors which contain the values of the K and r_m which will be used in the distribution. The number of points for each distribution was taken as 200.

For the radius:

```
NoDis=200;
logrmean=floor(log10(rmean));
scaler=2*(rmean-10^(logrmean-1))/NoDis; ,
```

here we estimated the step of increase of the radius, which is two orders less than $\langle r_m \rangle$. So, if the mean radius is 5 nm, the step of increase will be 0.05 nm. This ensures that the distribution will be evaluated in a wide range of radii. The subsequent code creates a vector, `r0`, with the values of r_m and displays on Matlab's *command window* the start, `rstart`, and end, `rend`, value of the distribution:

```
No2=NoDis/2;
for ii=1:No2
r1(ii)=rmean-(No2-ii)*scaler;
r2(ii)=rmean+ii*scaler;
end
r0(1:No2,1)=r1';
r0(No2+1:NoDis,1)=r2';
rstart=r0(1)
rend=r0(NoDis)
```

The pertinent vector, `K0`, for K is created in the same way:

```
logKmean=floor(log10(Kmean));
scaleK=2*(Kmean-10^(logKmean-1))/NoDis;
for ii=1:No2
K1(ii)=Kmean-(No2-ii)*scaleK;
K2(ii)=Kmean+ii*scaleK;
end
K0(1:No2,1)=K1';
K0(No2+1:NoDis,1)=K2';
Kstart=K0(1)
Kend=K0(NoDis)
```

It is necessary now to estimate the range of the relaxation times. It should be noticed that τ_B is dependent on $v_m = 4/3\pi r_m^3$ and τ_N is dependent on $\sigma = Kv_m/k_BT$. It is obvious that both relaxation times are distributed; τ_B is directly dependent on the distribution of $v_m \propto r_m^3$ and τ_N is dependent on the distribution of σ which combines distribution of K and $v_m \propto r_m^3$. Thus the resultant $\tau_{\parallel}^{eff} = \tau_B\tau_N/(\tau_B + \tau_N)$ is distributed in a complex way which involves a distribution of K and r_m. $\tau_{\perp}$ is taken equal to the precession time constant, $\tau_0 = 1/\alpha_d\omega_{pre}$, and involves distribution of K only. This is because $\omega_{pre} = \gamma(H_s + 2K/M_s)$. The code which calculates the range of values of the relaxation times is the following:

```
for i=1:NoDis
V(i)=4/3*pi*r0(i)^3;
```
, estimation of v_m for each value of r_m,

```
sigma(i)=K0(i)*Vmean/(kb*T);
```
, estimation of σ for each value of K,

```
wo(i)=y*(H+2*K0(i)/Ms);
```
, estimation of ω_{pre} for each value of K,

```
tau0(i)=1/(a*wo(i));
```
, estimates τ_0 for each value of K,

```
sigma1=sigma(i);
```
, stores the current value of σ,

```
DawsonINLINE=inline('exp(sigma1.^2)','sigma1');
```
, constructs an object for $\exp(\sigma^2)$ function,

```
q1(i) = quad(DawsonINLINE,0,sqrt(sigma(i)));
```
, solves the integral $\int_0^{\sqrt{\sigma}} e^{t^2} dt$ for each value of σ,

```
D1(i)=exp(-sigma(i))*q1(i);
```
, estimates the Dawson integral for each value of σ,

```
tauNeel(i)=2*taudmean*(sqrt(sigma(i))D1(i))/(D1(i)*(1+2*sigma
(i))-sqrt(sigma(i)));
```
, estimates τ_N (Eq. (1.5.21)) in terms of the Dawson integral,

```
taub(i)=3*vis*V(i)/(kb*T);
```
, estimates τ_0 for each value of v_m,

```
taupar(i)=tauNeel(i)*taub(i)/(tauNeel(i)+taub(i));
```
,estimation of $\tau_{\parallel}^{eff}$

```
end
```
, end of loop.

(d) At this point of the program one has the option to choose a distribution for K and a distribution for r_m. The option is between normal, log-normal or Nakagami distribution. To perform this option it is necessary to use the conditional commands `if`, `else` and `elseif`.

Options for the distribution of K:

```
option1=input('Do you want to use Normal, Log Normal or
Nakagami PDF for K distribution?(1/2/3):'); , the user choose between
                                                the 3 options,
if option1==1 || option1==2                    , if one of options 1 or 2 is true,
sK=input('enter normalised standard deviation of K: ');
                                               , the user enters the standard deviation,
elseif option1==3                              , if the 3rd option is true,
WK=sum(K0.^2)/NoDis;                           , calculate the Nakagami W parameter,
betaK=input('enter NAKAGAMI parameter beta: ');, ask for parameter β,
else
disp('improper selection!!!');                 , in case of invalid option,
break;                                         , the program stops,
end
```

The code is exactly the same for the options in the distribution of r_m (here, we added one more option for no distribution).

In the subsequent section we define the normal, log-normal and Nakagami distributions of K:

```
for n1=1:NoDis
if option1==1
pdf(n1)=((sK*sqrt(2*pi))^-1)*exp(-0.5*((abs(K0(n1))-Kmean)/
(Kmean*sK))^2);                                , normal distribution,
elseif option1==2
sKL=log(1+sK^2);
KL=log(Kmean/sqrt(sK^2+1));
pdf(n1)=1/sqrt(2*pi*sKL)*exp(-0.5*(log(abs(K0(n1)))-
KL)^2/sKL);                                    , log-normal distribution,
elseif option1==3
```

```
pdf(n1)  =  2*sqrt(WK)*(betaK^betaK)*(K0(n1)^(2*betaK-1))*exp(-
betaK*(K0(n1)^2)/WK)/(gamma(betaK)*(WK^betaK)), Nakagami distribution,
end
```

The same code is used for the distributions of r_m.

(e) In the following division of the code, the program calculates the susceptibility by using the Landau-Lifshitz equation. $\chi_{\parallel}$ and $\chi_{\perp}$ are calculated for each value of the relaxation times that they are related with. Each susceptibility value is multiplied with the probability distribution function (PDF), which plays the role of a weight function.

```
j=sqrt(-1);                                   , imaginary unit,
for i=1:NoPts     , nested loop: create 500 iterations, as many as the frequencies taken,
w(i)=2*pi*f(i);                               , circular frequency,
Xoper(n1)=Xo*tanh(sigma(n1))/sigma(n1);, realises Eq. (1.5.34),
Xopar(n1)=3*Xo*(1-2/3*tanh(sigma(n1))/sigma(n1));realises Eq. (1.5.31)

chiper(n1,i)=(Xoper(n1)*(1+(wo(n1)*tau0(n1))^2+j*w(i)*tau0(n1)
)/(1+(wo(n1)*tau0(n1))^2-(w(i)*tau0(n1))^2+2*j*w(i)*tau0(n1)))
                                                        *pdf(n1);
                                                , realises χ⊥×PDF(K),

chipar(n1,i) = Xopar(n1)/((1 + j*w(i)*taupar(n1)))*pdf(n1);
                                                , realises χ∥×PDF(K),

chi(n1,i)=1/3*(chipar(n1,i)+2*chiper(n1,i));, applies χ = (1/3)(χ∥ + 2χ⊥),

rechi(n1,i)=real(chi(n1,i));                  , separate real,
imchi(n1,i)=-imag(chi(n1,i));                 , separate imaginary,
end                                           , end of the nested loop,
end                                 , end of the loops involved with the distributions,
rechi1(:,:)=cumsum(rechi(:,:)); , summates (integrates) all the individual χ′,
imchi1(:,:)=cumsum(imchi(:,:)); , summates (integrates) all the individual χ″,
```

Redo the same work, but for the distribution function of r_m:

```
for ii=1:NoDis
```

```
for i=1:NoPts
rechi20(ii,i)=rechi1(NoDis,i)*pdfr(ii);
```
, realises $\chi' \times \mathrm{PDF}(r_m)$,
```
imchi20(ii,i)=imchi1(NoDis,i)*pdfr(ii);
```
, realises $\chi'' \times \mathrm{PDF}(r_m)$,
```
end
end
rechi200(:,:)=cumsum(rechi20(:,:));
```
, second integration,
```
imchi200(:,:)=cumsum(imchi20(:,:));
rechi2(1,:)=rechi200(NoDis,:);
imchi2(1,:)=imchi200(NoDis,:);

ratio=Xo/rechi2(1,1);
```
, adjust the scale of the y-axis,

Saves everything in the array `E`:

```
E(:,1)=f';
E(:,2)=rechi2'*ratio;
E(:,3)=imchi2'*ratio;
```

Saves the fitting parameters to the 4th column of the array:

```
E(1,4)=Ms;
E(2,4)=a;
E(3,4)=Xo;
E(5,4)=y;
E(6,4)=Kmean;
E(7,4)=K0(1);
E(8,4)=K0(NoDis);
E(9,4)=rmean;
E(10,4)=r0(1);
E(11,4)=r0(NoDis);
E(12,4)=womean;
E(13,4)=H;
if option1==1 || option1==2
E(14,4)=sK;
elseif option1==3
E(14,4)=betaK;
E(15,4)=WK;
```

```
    end
    if option2==1 || option2==2
    E(16,4)=sr;
    elseif option2==3
    E(16,4)=betar;
    E(17,4)=Wr;
```

(f) Opens the file with the susceptibility data which are to be fitted:

```
filein = input('Enter name of data file:  ','s');
eval([' load ',filein,'.dat']);
data = eval(filein);
```

(g) Plots data and fit together and add labels on the graph:

```
figure(1):semilogx(E(:,1),E(:,2),'r',E(:,1),E(:,3),'r',data(:,
1),data(:,2),'b.',data(:,1),data(:,3),'b.');
legend('Fit','Fit','Data','Data');
xlabel('f (Hz)');
ylabel('x``        x`');
```

Plots the distribution of K and add labels on the graph:

```
figure(2): plot(K0(:),pdf(:),'b.');
legend('PDF for K');
xlabel('K (J/m^3)');
ylabel('PDF(K)');
```

Plots the distribution of r_m and add labels on the graph:

```
figure(3): plot(r0(:),pdfr(:),'r.');
legend('PDF for r');
xlabel('r (m)');
ylabel('PDF(r)');
```

(h) Lets the user decide to save or to reject this fit:

```
y=1;
n=0;
yn=input('do you want to save this fit?(y/n): ');
```

```
if yn==y
fileout = input('Enter name of output file ','s');
sDir=[pwd,'\'];
filename=[sDir, fileout];
eval([' save ',fileout,'.dat E /ascii']);
end
```

The user can rerun the program and use a different set of fitting parameters, if desired.

If one chooses the option to perform a constant frequency fit, the program must take care to vary the field. The program creates a vector of 5000 log-spaced elements, which represent the field values,

```
NoPts=5000;
Hstart=input('enter start value of H(A/m) : ');
Hend=input('enter end value of H(A/m): ');
H=logspace(log10(Hstart),log10(Hend),NoPts);  ,
```

and calculates the susceptibility by use of the Landau-Lifshitz equation,

```
j=sqrt(-1);
for i=1:NoPts
```

wo(i)=y*(H(i)+2*K/Ms);,here ω_{pre} is given as a function of H_s and takes 5000 values

```
chi(i)=Xo*(1+(wo(i)*tau)^2+j*w*tau)/(1+(wo(i)*tau)^2-
(w*tau)^2+2*j*w*tau);
```

, the Landau-Lifshitz equation,

```
rechi(i)=real(chi(i));
imchi(i)=-imag(chi(i));
end
```

Finally the program plots the fit and the data in a Cole-Cole diagram,

```
figure(1):
plot(rechi(:),imchi(:),'r',data(:,2),data(:,3),'b.');
legend('Fit','Data');
xlabel('x``');
ylabel('x`');
```

It is supposed that the data, in this case, have been imported in a tabular format where the first column contains the values of χ' and the second column the values of χ''.

B.6 Conclusions.

A basic description of the Matlab environment was presented in section B.2. Matlab is the programming language by which we developed the computational and fitting programs to support this work. A summary of the commands used in the programs is offered in Table B.1. The flow diagram and the code of a computational program is given in section B.4, while in section B.5 we present, as examples of fitting programs, the full code of the Debye and the Landau-Lifshitz fitting programs. On the same basis we developed the programs performing fits by using Eq. (1.5.50) and Eqs. (3.3.1)-(3.3.3).

The techniques used here to execute the mathematical evaluations are simple and do not require special programming skills. More about how to use the mathematical techniques in Matlab is given in [7].

References

1. Pärt-Enander E., Sjöberg A., Melin B., Isaksson P., *The Matlab handbook*, Addison-Wesley, (1996).
2. Matlab, The language of technical computing, The Math Works Inc., Revised for Matlab 5.3 (Release 11), (1999).
3. Nelder J.A., Mead R., *Computer Journal*, **7**, 308, (1965)
4. Press W.H., Teukolsky S.A., Vettering W.T., Flannery B.P., *Numerical receipts in C*, Cambridge University Press, (1992).
5. Branch M.A., Grace A., *Matlab optimisation toolbox, user's guide*, (for Matlab V.5), The Math Works Inc., (1996).
6. Matlab, High-performance numeric computation and visualisation software, The Math Works Inc., Reference guide, (1992).
7. Harman T.L., Dabney J., Richert N., *Advanced engineering mathematics using Matlab V.4*, PWS Publishing Co, Boston, 1997.

APPENDIX C: Demagnetising Factor Chart

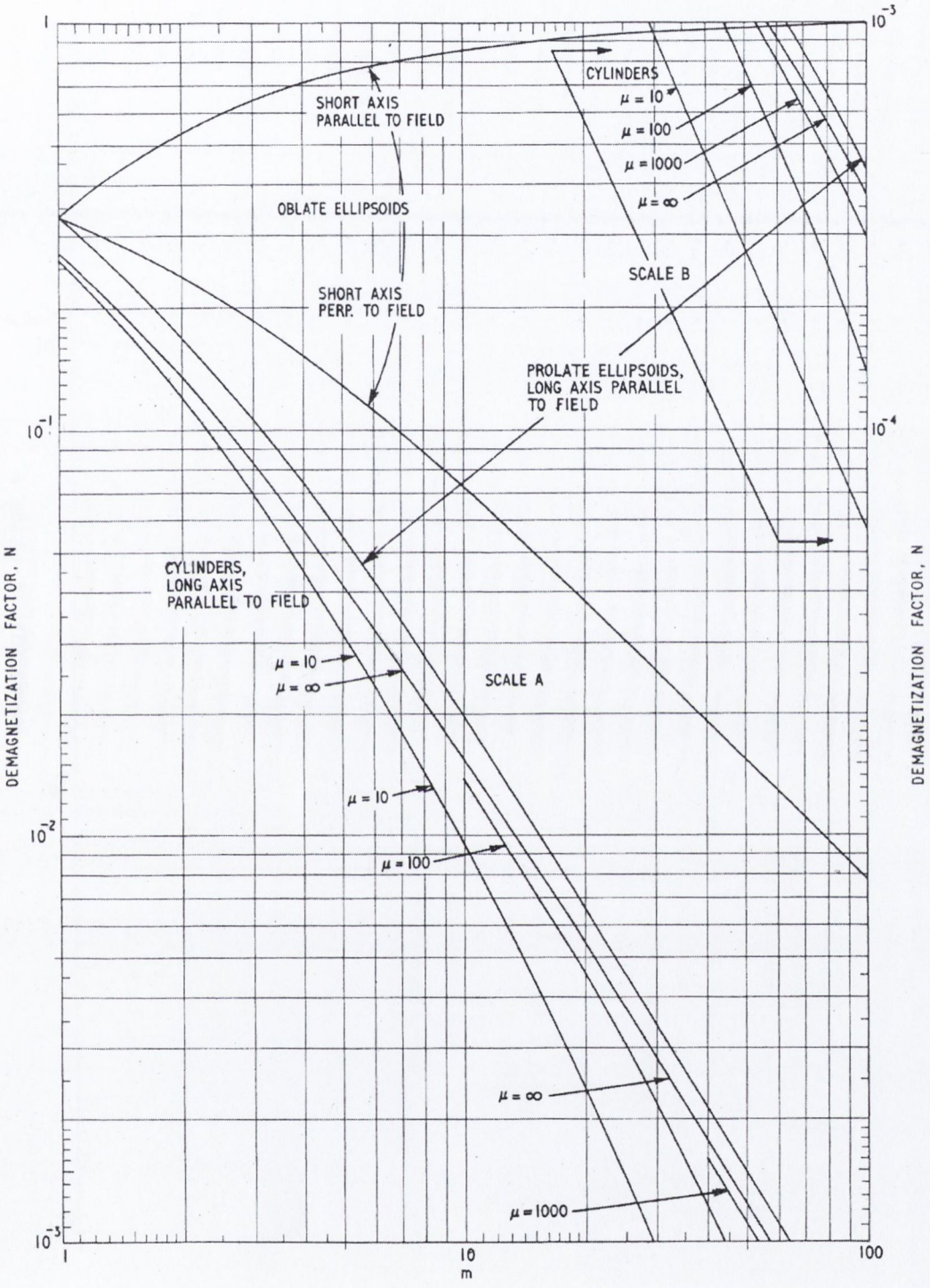

Figure C.1 Demagnetising factors for ellipsoids and cylinders as functions of m(=long axis/short axis for ellipsoids and length/diameter for cylinders). The values of demagnetising factor are appropriate to S.I. units. Chart is taken from: Snelling E.C., *Soft Ferrites Properties and Applications*, Iliffe Books, London, (1969).

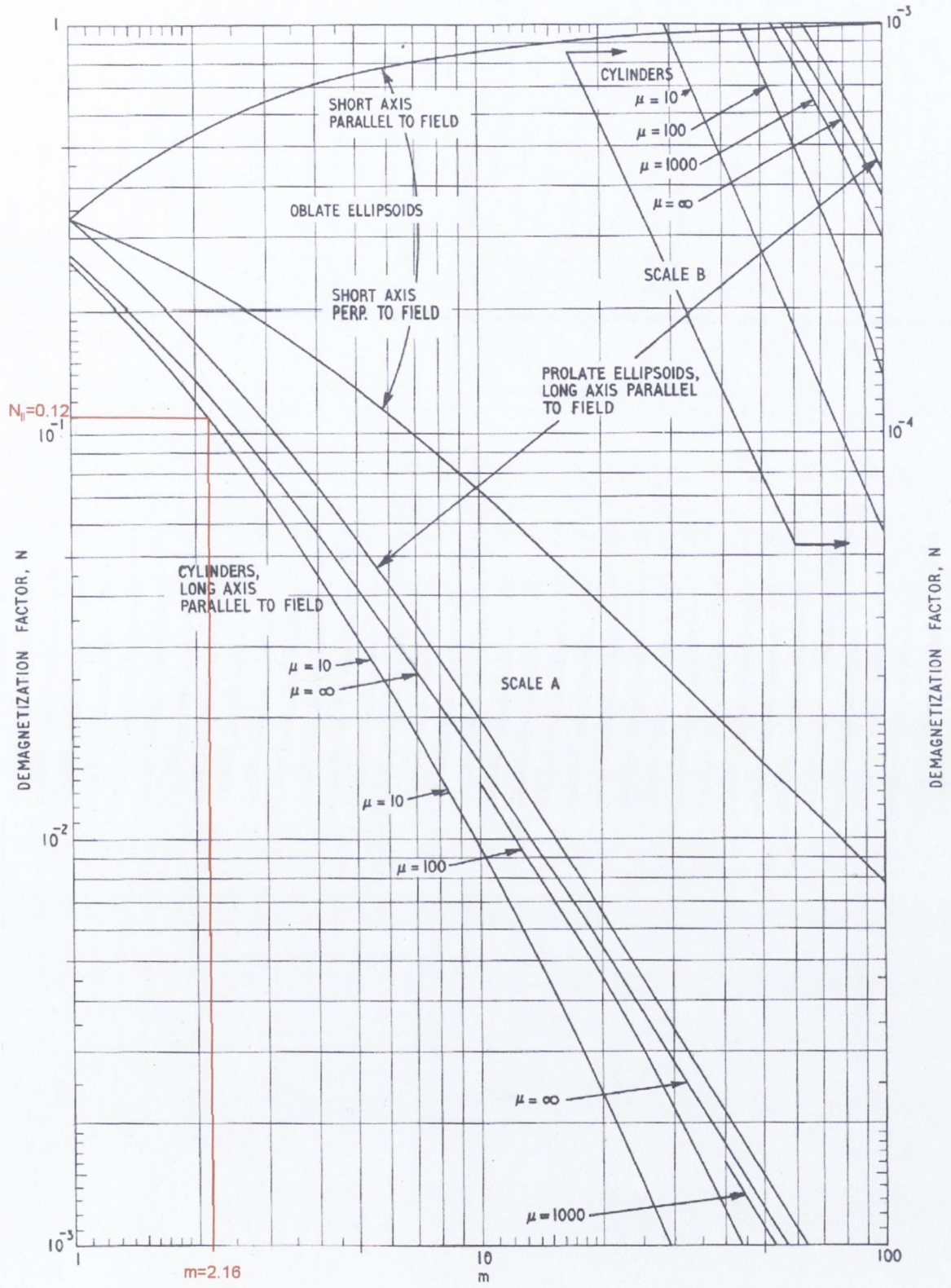

Figure C.2 Estimation of the parallel demagnetising factor for a cylindrical sample holder with long axis 2.6 cm and diameter 1.2 cm. These dimensions give m=2.16. Projecting to the curve which corresponds to low permeability (μ=10) we find $N_{\parallel}$=0.12.